Development of $Al_{93}Fe_3Cr_2Ti_2$/ Nano-size γ-Al_2O_3 Nanocomposite by Ball Milling Process

Weiyue XU

Linacre College

A thesis submitted for the degree of

Doctor of Philosophy

Department of Materials, University of Oxford

Trinity, 2017

Table of Contents

Acknowledgements

I would like to thank my supervisors Prof. Marina Galano and Prof. Fernando Audebert for their guidance and supports. They are very critical as well as very open to creative ideas and research plans. During my DPhil, they guided me from a fresh student to an independent and rigorous researcher. I am especially grateful to Prof. Marina Galano, as she continued working on my thesis during her maternity leave. I would like to thank my parents for their supports and care when I was abroad. I am also thankful to Dr. Zuliang Hong for trainings on the ball miller and glovebox, Philip Holdway for helping me in XRD, Dr. Asad Hameed for the support in the extrusion, Peter Flaxman for the compression sample preparations, and Igor Dyson for the compression tests. I would like to thank Dr. Neil Young, Fay Chicken, Dr. Jing Hu for the TEM training, Dr. Gareth Hughes for the FIB training, Gabriella Chapman for the SEM training and Graham Wyatt for the maintenance of all the electron microscopes. I am grateful to Prof. Richard Todd for density measurements. I would like to thank Dr. Lewys Jones, Dr Gerardo Martinez Alanis and Prof. Peter Nellist for the HRTEM imaging on quasicrystals.

Finally, I would like to especially thank my girlfriend for the accompany and encouragement during my hard days. I would also like to thank all my friends and colleagues, especially Xiaochen Wang, Ran XU, Asad Hameed, Rashid Bhatti, Khushbu Dash, Xia Jiang, Guo Wu, Stella Pedrazzini, Julian Malisano and others for their help.

Thank you!

Abstract

The strength of conventional aluminium alloys decreases rapidly above 150°C, which limits their applications at elevated temperature. Rapid solidified (RS) nanoquasicrystalline $Al_{93}Fe_3Cr_2Ti_2$ (at.%) alloy has previously shown outstanding mechanical performance and microstructural stability at elevated temperatures (>300°C). In order to obtain an outstanding Al-based material with very high strength in a broad range of temperature, it is proposed to produce a nanocomposite consisting of nano-size ceramic particles homogenously distributed in a nanoquasicrystalline alloy matrix. The main challenges of processing nanoquasicrystalline nanocomposites in ball milling are to prevent the metastable quasicrystalline phase from decomposition and to avoid the agglomerations of nano-size γ-Al_2O_3.

In order to produce high strength nanocomposite material with a nanoquasicrystalline alloy matrix, it is required to understand deeply the microstructure evolution and interactions between the nanoquasicrystalline alloy matrix and the nano-size ceramic reinforcements. Thus, in this work in-depth study has been performed assessing the microstructure evolution, the stability and the strengthening mechanisms in the $Al_{93}Fe_3Cr_2Ti_2$/12.9vol.% γ-Al_2O_3 nanocomposite milled powders in comparison with the $Al_{93}Fe_3Cr_2Ti_2$ alloy milled powders.

Five batches of nanoquasicrystalline $Al_{93}Fe_3Cr_2Ti_2$ (at.%) alloy powders (particle size: 25-50 μm) with 12.9 vol.% γ-Al_2O_3 (20-50 nm) powders as reinforcement, as well as two batches of nanoquasicrystalline $Al_{93}Fe_3Cr_2Ti_2$ alloy powders were processed through mechanical milling with different milling time and speeds. The powders with suitable milling conditions were extruded to produce a bar. The powder particle sizes were

measured using Mastersizer. The microstructure of powders and the bar were characterised using X-ray diffraction, differential scanning calorimetry, scanning electron microscopy, focused ion beam, transmission electron microscopy, energy dispersive X-ray spectroscopy and scanning transmission electron microscopy. The hardness of the powder was measured with Vickers hardness microindenter.

For the $Al_{93}Fe_3Cr_2Ti_2$ alloy atomised powder, the quasicrystal particles locate either inside the aluminium grains or on the grain boundaries before milling. The two-fold zone axes of icosahedral quasicrystal particles follow a crystallographic relationship with the [200] and [022] axes of α-Al and Al_3Ti intermetallics. During the milling, the quasicrystals break and the volume fraction of the quasicrystals decreases with milling time. The solute content of Ti, Cr, Fe elements in the α-Al grains increase from 0.42%, 0.27% and 0.04% to 1.66%, 1.66% and 2.57% respectively from 0 to 30 hours of milling. These supersaturated elements precipitate during heat treatment at 405°C, probably controlled by the diffusion. Before milling, the lattice diffusion is probably the controlling mechanism for decomposition of the quasicrystals. During ball milling, diffusion through grain boundaries and dislocations is involved, which decrease the activation energy of quasicrystalline phase from 297±20 kJ/mol to ~175 kJ/mol after ball milling.

For the $Al_{93}Fe_3Cr_2Ti_2$/12.9vol.% γ-Al_2O_3 nanocomposite powders, it was observed that higher milling time and/or milling speeds could improve the nano-size γ-Al_2O_3 particles distribution. The homogeneous distribution of γ-Al_2O_3 particles was obtained after 20 hours of milling at 250 rotates per minute.

For both the nanoquasicrystalline alloy and the nanocomposite powders, the α-Al crystallite size decreases and hardness increases with milling time and speeds. The smallest crystallite size (14 nm) and the highest hardness value (638 HV_{10g}) were obtained for the nanocomposite after 30 hours of milling at 250 rotates per minute. Quasicrystals could help refine crystallites by particle stimulate nucleation. Nanosize γ-Al_2O_3 may increase the grain refinement rate by inhibiting the dislocations. With the same milling speed, the nanoquasicrystalline $Al_{93}Fe_3Cr_2Ti_2$/γ-Al_2O_3 nanocomposites have smaller α-Al crystallites than the nanoquasicrystalline $Al_{93}Fe_3Cr_2Ti_2$ alloy powders after 10 hours of milling. As the α-Al crystallite size is the main change in the microstructure during the ball milling process, the changes in the hardness of the milled powders were found to follow a Hall-Petch type relation with an exponent of 0.25.

The $Al_{93}Fe_3Cr_2Ti_2$/γ-Al_2O_3 powders after 4 hours of milling at 250rpm and 5 hours of milling at 200rpm using a 500ml vessel were extruded at 450°C. The relative density of the extruded bar is 99%. The crystallite size is 97nm. Compression tests were performed at 25°C and 250°C at a strain rate of 0.001 s^{-1}. The compressive yield stress and the compression strength at room temperature are 673MPa and 925MPa respectively. The compressive yield strength and compression strength at 250°C are relative lower, 573MPa and 424MPa respectively.

The work in this thesis promotes understandings on processing nanocomposites by ball milling using matrix powders containing metastable phases. The ultrafine crystallite size and superior compression strength give the $Al_{93}Fe_3Cr_2Ti_2$/γ-Al_2O_3 nanocomposites a considerable respect for industry applications.

The following figures in this thesis were reprinted with permission from the respective publishers.

Figure No.	Publisher	License No.
Figure 2.1	Elsevier	4126591216624
Figure 2.2 (b) and (c)	American Physical Society	4126561232623
Figure 2.3	American Physical Society	4126561455089
Figure 2.4 (a)	American Physical Society	4126570071230
Figure 2.4 (b)	American Physical Society	4126570675274
Figure 2.5	Elsevier	4126570798242
Figure 2.6	Elsevier	4126571022929
Figure 2.7 (a)	Elsevier	4126571133698
Figure 2.7 (b)	Cambridge University Press	4126580122677
Figure 2.8 (a) and (b)	Cambridge University Press	4126580265768
Figure 2.8 (c)	Elsevier	4126580501803
Figure 2.9	Elsevier	4126580702503
Figure 2.10	Elsevier	4126580815880
Figure 2.13	Elsevier	4126580501803
Figure 2.14	Elsevier	4126581214154
Figure 2.16	Elsevier	4126581469455
Figure 2.17	Elsevier	4126581016886
Figure 2.18	John Wiley and Sons	4126590116546
Figure 2.19	Elsevier	4126590230714
Figure 2.20	Elsevier	4126590459485
Figure 2.21	Elsevier	4126590682984
Figure 2.22	Elsevier	4126590782621
Figure 7.7	Elsevier	4126591334631
Figure 7.8	Elsevier	4126560349885

1. Introduction

The commercial aluminium alloys have outstanding properties of light weight, high strength stiffness to weight ratio, and good formability, which give them a considerable prospect for automotive and aerospace applications (Miller, Zhuang et al. 2000). However, the yield strength of these conventional alloys decreases rapidly above ~150°C (Inoue and Kimura 2001). For light weight applications at elevated temperatures (>200°C), titanium alloys are the most commonly used materials. Compared with aluminium with a density of 2.7g/cm^3, titanium is heavier with a density of 4.5g/cm^3 (Polmear 1995). Besides, the price of titanium (11500$/tonne) is also more expensive than that of aluminium (1600$/tonne)[1].

Recent developments in novel advanced aluminium based alloys with nanoscale dispersed particles made them very attractive lightweight materials to be used for elevated temperature applications below 300°C~350°C (Inoue 1998, Kimura, Sasamori et al. 2000). The rapid solidified $Al_{93}Fe_3Cr_2Ti_2$ alloy, with nanoquasicrystalline particles (<200nm in diameter) dispersed in fine Al grains, has a yield strength of 530MPa at room temperature and 330MPa at 300°C (Inoue and Kimura 1999). With superior mechanical properties, such alloy has a considerable prospect for industry applications at elevated temperatures (Kimura, Sasamori et al. 2000). However, the yield strength of such alloy is still lower than that of the conventional Ti alloys, for example, Ti-6Al-4V alloy with yield strength values of 969MPa at room temperature and ~600MPa at 300°C (Wang, Wei et al. 2003, Balasubramanian, Balakrishnan et al. 2011).

[1] Commercially pure grade 1 ingot price of Ti is from www.metalprices.com (April 2016)
Aluminium price is from London metal exchange www.lme.com (April 2016)

Galano et al. (Galano, Marsh et al. 2015) processed nanoquasicrystalline $Al_{93}Fe_3Cr_2Ti_2/\gamma\text{-}Al_2O_3$ nanocomposites with ball milling. The microhardness of the nanocomposite is significantly harder than both the unreinforced quasicrystalline alloy and crystalline aluminium nanocomposites reported in literature (Todd, Chlup et al. 2004, Knowles, Jiang et al. 2014). However, the mechanisms for the microstructure evolution and mechanical behaviours were not deeply investigated. Therefore, a better understanding of the nanoquasicrystalline nanocomposites is required for processing high strength materials with a homogeneous distribution of reinforcement particles and the metastable quasicrystalline phase maintained.

In this thesis, quasicrystalline $Al_{93}Fe_3Cr_2Ti_2$ alloy instead of conventional Al alloys was used as matrix powder in the ball milling process. The effects of quasicrystals on the microstructure evolution in the ball milling process were studied for the first time. The effects of ball milling on the decomposition of quasicrystalline phase were also investigated. This improves understandings this and other nanocomposite systems containing a metastable microstructure matrix.

In this work, the nanoquasicrystalline nanocomposites were processed with different milling time (0 to 30 hours) and speeds (150 rotates per minute to 250 rotates per minute). Powders with suitable milling conditions were extruded. The distribution of the reinforcement particles, the microstructure evolution and the strengthening mechanisms of the nanocomposites were investigated. This helps determining suitable milling conditions for processing nanoquasicrystalline nanocomposites with a homogeneous distribution of reinforcements and outstanding strength.

The outline of the thesis is as follows: chapter two contains literature review and chapter three describes the experimental methods employed in this research. Chapter four provides the particle size, morphology, phase components, microstructure, reinforcement distribution, thermal stability and the hardness of the unmilled powders, the ball milled quasicrystalline $Al_{93}Fe_3Cr_2Ti_2$ alloy powders and the nanoquasicrystalline $Al_{93}Fe_3Cr_2Ti_2$/12.9vol.% γ-Al_2O_3 nanocomposite powders at a milling speed of 250 rotates per minute. Chapter five discusses the effects of the milling speeds on the nanoquasicrystalline nanocomposites. Chapter six reports processing powders for extrusion and the properties of the extruded bar. Chapter seven relates the observations and the findings from previous chapters and has a general discussion about the behaviours of the ball milled nanocomposite powders and the extruded bar. Chapter eight concludes the thesis and proposes routines for future work.

References

Balasubramanian, T., et al. (2011). "Influence of welding processes on microstructure, tensile and impact properties of Ti-6Al-4V alloy joints." Transactions of Nonferrous Metals Society of China **21**(6): 1253-1262.

Galano, M., et al. (2015). "Nanoquasicrystalline Al-based matrix/γ-Al_2O_3 nanocomposites." Journal of Alloys and Compounds **643**: S99-S106.

Inoue, A. (1998). "Amorphous, nanoquasicrystalline and nanocrystalline alloys in Al-based systems." Progress in materials science **43**(5): 365-520.

Inoue, A. and H. Kimura (1999). "High elevated-temperature strength of Al-based nanoquasicrystalline alloys." Nanostructured Materials **11**(2): 221-231.

Inoue, A. and H. Kimura (2001). "Fabrications and mechanical properties of bulk amorphous, nanocrystalline, nanoquasicrystalline alloys in aluminum-based system." Journal of light metals **1**(1): 31-41.

Kimura, H. M., et al. (2000). "Al–Fe-based bulk quasicrystalline alloys with high elevated temperature strength." Journal of Materials Research **15**(12): 2737-2744.

Knowles, A., et al. (2014). "Microstructure and mechanical properties of 6061 Al alloy based composites with SiC nanoparticles." Journal of Alloys and Compounds **615**: S401-S405.

Miller, W., et al. (2000). "Recent development in aluminium alloys for the automotive industry." Materials Science and Engineering: A **280**(1): 37-49.

Polmear, I. (1995). "Light alloys, metallurgy of the light alloys." Metallurgy and Materials Science, Arnold, Great Britain: 168-195.

Todd, I., et al. (2004). "The influence of processing variables on the structure and mechanical properties of nano-quasicrystalline reinforced aluminium alloys." Materials Science and Engineering: A **375**: 1235-1238.

Wang, S., et al. (2003). "Tensile properties of LBW welds in Ti–6Al–4V alloy at evaluated temperatures below 450°C." Materials Letters **57**(12): 1815-1823.

2. Literature review

2.1 Introduction

With the increasing demands for energy conservation, scientists are trying to discover structural materials with higher strength and lower density (Ma, Lavernia et al. 2017). Aluminium alloys, with the property of high strength to weight ratio, high ductility, recyclability and heat treatability (Davies 1993), can potentially address these issues. The 7000 series aluminium alloys have the highest strength at room temperature among all the series and are widely used in aircraft structures (Ma, Lavernia et al. 2017). The aluminium-copper alloys containing magnesium (2000 series) have higher strength, damage tolerance and good fatigue crack growth resistance (Dursun and Soutis 2014). However, the yield strength of these conventional alloys are usually less than 600MPa and decreases rapidly above ~150°C (Inoue and Kimura 2001). In order to manufacture aluminium alloys with higher strength at elevated temperature, new strategies need to be explored.

One way of enhancing the performance of aluminium alloys is though the presence of quasicrystalline phase in the face centred cubic (FCC) Al matrix (Inoue 1998). Quasicrystals are extremely hard and brittle due to the difficulty of dislocation movement in the quasiperiodic lattice without long range periodicity (Inoue 1998). Therefore, the nanoquasicrystalline particles can act as a resistant medium against the deformation, enhancing the tensile strength (Inoue, Kimura et al. 2000).

Aluminium metal matrix composite is another type of light-weight material processed by adding hard ceramic particles into the alloys (Kainer 2006). In this situation, usually high strength is achieved at the cost of ductility (Doel and Bowen 1996). It has been reported that by decreasing the particle size to nanoscale the loss of ductility can also be reduced

and the strengthening effects can be improved (Doel and Bowen 1996, Hassan and Gupta 2006). This literature review explains the progress so far in the production and properties of quasicrystalline aluminium alloys and aluminium composites. The mechanical milling and extrusion, which are two common routines for processing nanocomposites, are also discussed.

2.2 Structure and properties of the quasicrystalline phases

2.2.1 The quasicrystalline phases

Quasicrystals are a subclass of the aperiodic crystals with long range orientation symmetry and experimentally discrete diffraction patterns (Shechtman, Blech et al. 1984). Quasicrystals have rotation symmetries, but cannot be assigned to a conventional lattice (Cahn, Shechtman et al. 1986). One typical structure of the quasicrystal is Penrose diagram in 3 dimensions (Penrose 1979). Figure 2.1 is a 2D analogy of the 3D structure of quasicrystals made of rhombuses with 36°- 144° and 72°-108° (Akdeniz and Vignolo 2017). The quasicrystalline alloys can be divided into four kinds of icosahedral, decagonal, dodecagonal, and octagonal phases. However, quasicrystals which are composed of a single phase are limited to icosahedral and decagonal phases (Inoue 1998). Among them, icosahedral quasicrystals are of interest in this literature review.

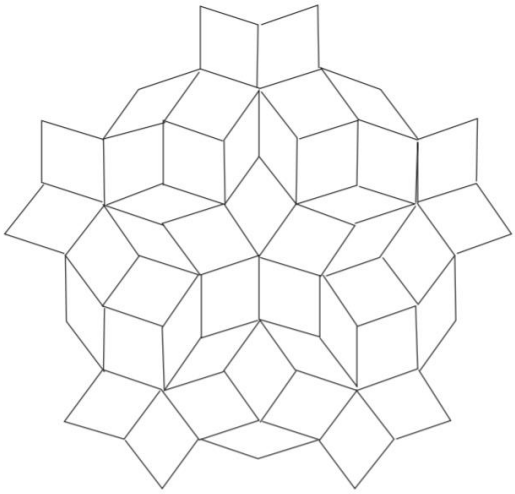

Figure 2.1: The rhombus Penrose tilting (Akdeniz and Vignolo 2017)

2.2.2 A one-dimensional quasicrystal

One natural way to generate quasi-periodic lattices is to use projections from a higher dimensional periodic lattices for obtaining quasicrystal packings of unit cells (Kramer and Neri 1984, Duneau and Katz 1985, Elser 1985). The procedure of generating one dimensional quasiperiodic lattice is shown in Figure 2.2. Assuming $\mathbb{Z}^2$ is the two-dimensional integer square lattice, e^1 and e^2 are the standard basis vectors in the two-dimensional lattice, as shown in Figure 2.2(a). Inside the $\mathbb{Z}^2$ space, another two-dimensional coordinate system is built up: $X_{//}$ is an axis with the slope of tanα, and $X_{\perp}$ is vertical to $X_{//}$. The projections of e^1 and e^2 on $X_{\perp}$ form two vectors, $e_{\perp}^1$ and $e_{\perp}^2$. Similarly, projections of e^1 and e^2 on $X_{//}$ form two vectors, $e_{\parallel}^1$ and $e_{\parallel}^2$.

Long and short intervals (marked as L and S in Figure 2.2(b)) could be formed when projecting lattice points from $\mathbb{Z}^2$ space on $X_{//}$ axis, as shown in Figure 2.2(b), provided that the slope of $X_{//}$ tanα is irrational (Elser 1986).

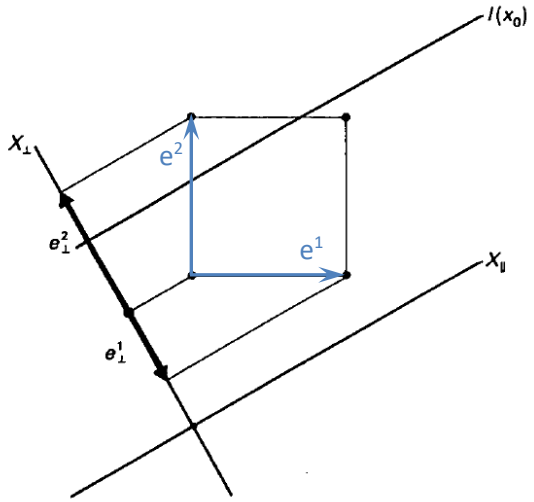

(a)

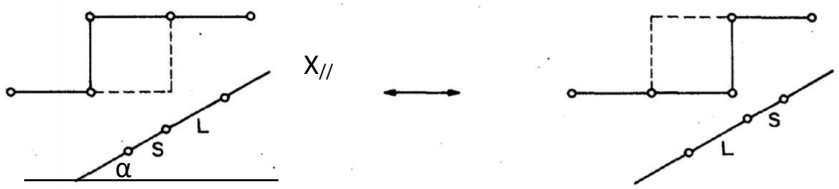

(b)

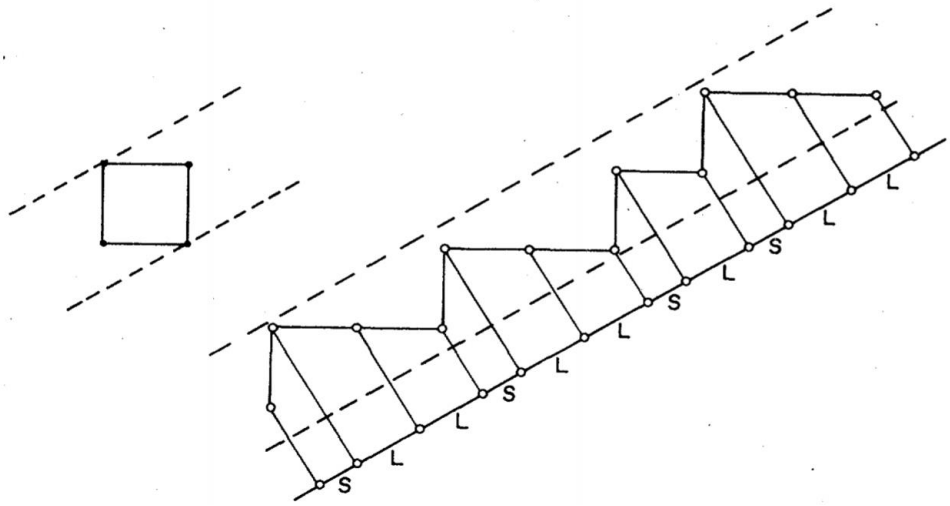

(c)

Figure 2.2: (a) Projection of a unit into vertical axis, **(b)** An elementary step transformation generating one dimension short and long intervals from two-dimensional unit, **(c)** By choosing the separation between the dashed lines, a Fibonacci sequence of short and long intervals is formed (Elser 1986).

A subset of points in $\mathbb{Z}^2$ with projections on the $X_\perp$ axis locating inside the projection of one unit cell are selected, as shown in Figure 2.2(c):

$$\boldsymbol{\mathcal{T}(x_0) = \{n \in \mathbb{Z}^2 \big| P_\perp(n) \in C_\perp(x_0)\}} \quad \text{----------} \quad \text{Equation 1}$$

where $\mathcal{T}(x_0)$ describes the subset of vertices, $P_\perp(n)$ is the projected position in $X_\perp$ axis from a lattice point n. $C_\perp(x_0)$ describes a segment in $X_\perp$ axis projected by a unit cube in $\mathbb{Z}^2$ space. The length of $C_\perp(x_0)$ equals to the sum length of $e_\perp^1$ and $e_\perp^2$.

Projecting all the points in $\mathcal{T}(x_0)$ to the $X_{//}$ axis, a sequence of long and short intervals (……SLLSLLSLSLL……) could be generated (Elser 1985), as shown in Figure 2.2(c). If the angle between the $X_{//}$ and the e^1 is α, and tanα equals to 1/τ (τ is the golden ratio), the sequence follows the order of Fibonacci chain (Cahn, Shechtman et al. 1986, Levine and Steinhardt 1986). The ends of the intervals in the Fibonacci chain form a one-dimensional quasi-periodic lattice.

2.2.3 The icosahedral quasi-lattice

Similar to the one-dimensional example, the icosahedral quasilattice can be obtained by projecting a subset of the six-dimensional lattice $\mathbb{Z}^6$ onto a special three dimensional hyperplane $X_{//}$ (Elser 1986). If the basis vectors $e_\parallel^1, e_\parallel^2, \ldots, e_\parallel^6$ coincide with the six vertex axes of an icosahedron, the projected lattices will have an icosahedral symmetry (Elser 1985, Elser 1986).

The following set defines a triacontahedron (Coxeter 1973) obtained from the projection of a six-dimensional unit cell to a three-dimensional hyperplane $X_\perp$ (Elser 1986):

$$\boldsymbol{C_\perp = \left\{\sum_{i=1}^{6} x^i e_\perp^i \middle| x^i \in [0,1),\ i = 1,2,3,4,5,6\right\}} \quad \text{------} \quad \text{Equation 2}$$

Analogous to Equation 1, all the lattices in six-dimensional space $\mathbb{Z}^6$ with projections onto the three-dimensional hyperplane $X_\perp$ falling inside $C_\perp$ can also form a three-dimensional quasi-periodic lattice when projected on special three-dimensional hyperplane $X_{//}$. Figure 2.3 is a section of the three-dimensional tiling orthogonal to a fivefold axis.

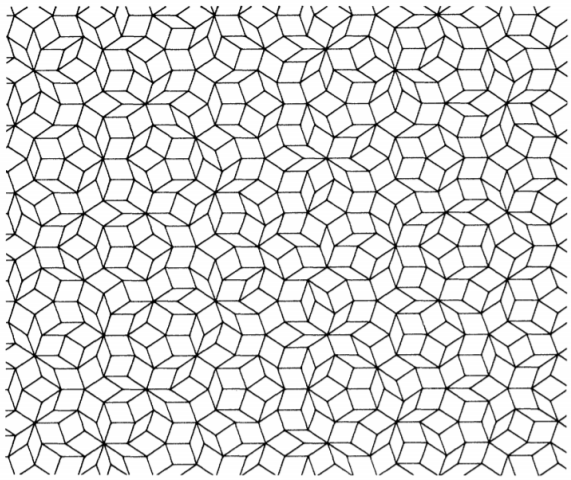

Figure 2.3: A section of the three-dimensional tiling orthogonal to a fivefold axis (Duneau and Katz 1985)

The Fourier transform of a quasiperiodic tiling can form diffraction patterns, as shown in Figure 2.4(a). The simulated diffraction pattern is similar to the electron diffraction images obtained by *Shechtman* et al. (Shechtman, Blech et al. 1984), as shown in Figure 2.4(b).

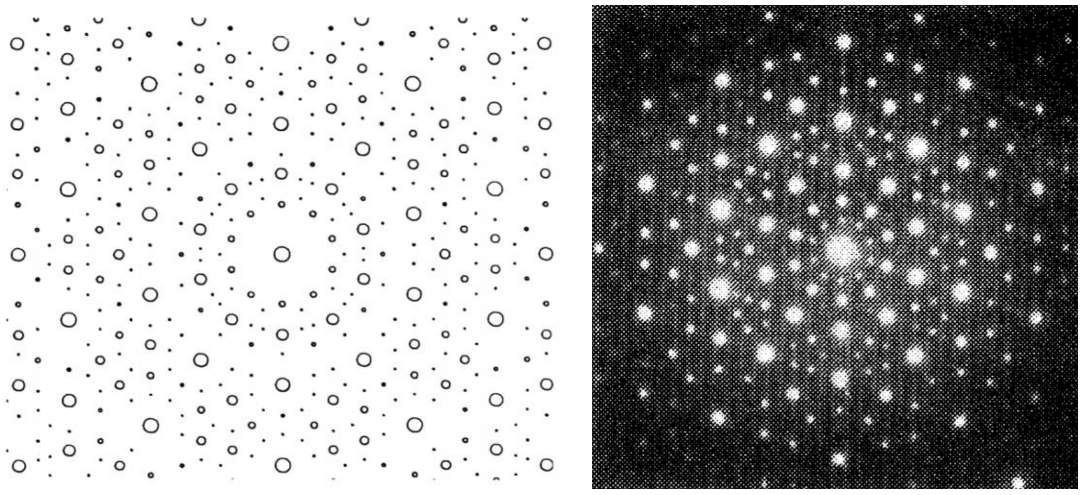

(a) (b)

Figure 2.4: (a) Fourier transform in a quasiperiodic plane orthogonal to a fivefold axis. (Duneau and Katz 1985), **(b)** the fivefold diffraction pattern of quasicrystals in $Al_{86}Mn_{14}$ alloy (Shechtman, Blech et al. 1984)

In 1986, *Cahn* et al. (Cahn, Shechtman et al. 1986) developed a method based on a three dimensional cubic coordinate system using icosahedral symmetry for icosahedral quasicrystals. In their system, a coordinate system aligned along three perpendicular twofold axes of the icosahedron was selected for indexing in reciprocal spaces. The diffraction spots in quasilattice in three-dimensional reciprocal space could be expressed as:

$$\boldsymbol{Q} = \sum_{\boldsymbol{i=1}}^{\boldsymbol{6}} \boldsymbol{n_i}\, \boldsymbol{q_i} \qquad \text{----------} \qquad \text{Equation 3}$$

Where the n_i are integers and the q_i are the vectors along the [1τ0] fivefold zone axes in icosahedron[1]:

$$\begin{aligned} \boldsymbol{q_1} &= (\mathbf{1/0\ \ 0/1\ \ 0/0}),\\ \boldsymbol{q_2} &= (\mathbf{0/1\ \ 0/0\ \ 1/0}),\\ \boldsymbol{q_3} &= (\mathbf{0/0\ \ 1/0\ \ 0/1}),\\ \boldsymbol{q_4} &= (\mathbf{\bar{1}/0\ \ 0/1\ \ 0/0}),\\ \boldsymbol{q_5} &= (\mathbf{0/1\ \ 0/0\ \ \bar{1}/0}), \end{aligned} \qquad \text{Equation 4}$$

[1] In Equation 4, a/b represents a+bτ (τ is the golden ratio). For example, (1/0 0/1 0/0) = (1 τ 0)

$$\boldsymbol{q_6 = (0/0\ \bar{1}/0\ 0/1)},$$

There are 384 ways for choosing q_i's. From Equation 3 and Equation 4, Q could be expressed as:

$$\boldsymbol{Q = ((n_1 - n_4)/(n_2 + n_5)\,, (n_3 - n_6)/(n_1 + n_4), (n_2 - n_5)/(n_3 + n_6))}$$

---------- Equation 5

Then the six-dimensional vector (n_1, n_2, n_3, n_4, n_5, n_6) could be converted to the six-index three-dimensional vector (h/h', k/k', l/l').

$$\begin{aligned} \boldsymbol{h = n_1 - n_4,} \quad & \boldsymbol{h' = n_2 + n_5} \\ \boldsymbol{k = n_3 - n_6,} \quad & \boldsymbol{k' = n_1 + n_4} \\ \boldsymbol{l = n_2 - n_5,} \quad & \boldsymbol{l' = n_3 + n_6} \end{aligned} \quad \text{----------} \quad \text{Equation 6}$$

For the purpose of simplicity, the square of Q is of the form:

$$\boldsymbol{Q^2 = N + M\tau} \quad \text{----------} \quad \text{Equation 7}$$

Where:

$$\boldsymbol{N = h^2 + k^2 + l^2 + h'^2 + k'^2 + l'^2} \quad \text{----------} \quad \text{Equation 8}$$

$$\boldsymbol{M = h'^2 + k'^2 + l'^2 + 2(hh' + kk' + ll')} \quad \text{----------} \quad \text{Equation 9}$$

The letters N and M can be used to index the quasicrystalline phases in X-ray diffractograms (Galano, Audebert et al. 2009).

2.3 Nanoquasicrystalline Aluminium alloys

2.3.1 Different types of Nanoquasicrystalline aluminium alloys

Quasicrystals have been found in aluminium alloys as well as several other alloy systems since their discovery by *Shechtman* et al. (Shechtman, Blech et al. 1984, Rao, Fidler et al. 1986, Niikura, Tsai et al. 1994, Inoue 1998), but it is nanoquasicrystalline aluminium alloys that are of interest in this literature review. The nanoquasicrystalline aluminium

alloys could be split into three categories according to their properties (Inoue 1998, Inoue and Kimura 2000, Inoue and Kimura 2001):

(1) High strength: Al-Mn-Ln, Al-Cr-Ln-TM (TM=transition metal, Ln=lanthanide metal)

(2) High ductility: Al-Mn-Cu-TM, Al-Cr-Cu-TM

(3) High elevated temperature strength: Al-Fe-Cr-TM

These alloys are normally produced by rapid solidification (melt-spinning or gas atomisation) and contain icosahedral quasicrystalline particles with typically size under 500 nm (Inoue 1998, Kimura, Sasamori et al. 2000, Galano, Audebert et al. 2004). Among them, the quasicrystalline alloys with high elevated temperature strength are of interest in this literature review. *Inoue* (Inoue 1998) processed the $Al_{93}Fe_3Cr_2Ti_2$ alloy by extruding sub 26μm powders (all proportions in this thesis are at.% unless otherwise noticed). As shown in Figure 2.5, the yield strength of quasicrystalline $Al_{93}Fe_3Cr_2Ti_2$ alloy is 420-520MPa at 473K and 320-350Mpa at 573K. In comparison, the 7000 series of age hardenable alloys have yield strengthen exceed 500 MPa at room temperature if aged to the T6 condition, but the strength of these alloys decrease rapidly to about 100 MPa if exposed to the temperatures exceeding 473K (Polmear and Couper 1988, Inoue and Kimura 2000). The 2000 series have relative higher strength than 7000 at elevated temperature, but still less than 300 MPa at 473K and less than 200 MPa at 573K. This indicates quasicrystalline alloys could become the potential light alloys for automotive engine industries.

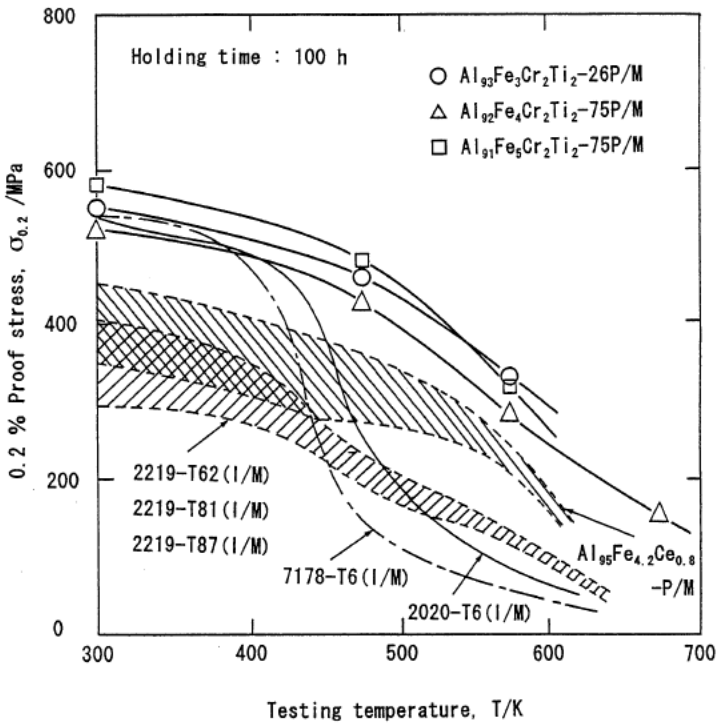

Figure 2.5: Temperature dependence of 0.2% yield stress as a function of testing temperature for the extruded bulk $Al_{91\text{-}93}Fe_{3\text{-}5}Cr_2Ti_2$ alloys produced by the powder metallurgy technique (Inoue and Kimura 2000).

2.3.2 Phases and microstructure

The microstructure of nanoquasicrystalline alloys is crucial in investigating their thermal stability and the mechanical properties. *Galano* et al. (Galano, Audebert et al. 2009) processed the $Al_{93}(Fe_3Cr_2)_7$ ribbon using melt spinning. Based on their X-ray diffractograms, α-Al, icosahedral quasicrystal and θ-$Al_{13}(Cr,Fe)_{2,4}$ are the main phases in the ribbons. According to previous researchers (Manaila, Florescu et al. 1989, Audebert, Colaco et al. 1999), the distorted θ-$Al_{13}(Cr,Fe)_{2\text{-}4}$ phase is a metastable phase with an undetermined composition and lattice parameter between those of the stable monoclinic phases $Al_{13}Fe_4$ and $Al_{13}Cr_2$ that have been observed in rapid solidified samples. This phase is metastable and will decompose into the $Al_{13}Fe_4$ and the $Al_{13}Cr_2$ phase if heat-treated

beyond 450°C (Galano, Audebert et al. 2009). The transmission electron microscope (TEM) bright field (BF) images show that most of the quasicrystal particles in the $Al_{93}(Fe_3Cr_2)_7$ ribbon are spherical, and have a diameter of about ~200nm (Galano, Audebert et al. 2004, Galano, Audebert et al. 2009), as shown in Figure 2.6.

Galano et al. (Galano, Audebert et al. 2009) also processed the $Al_{93}Fe_3Cr_2Ti_2$ alloy via melt spinning. The TEM BF images were shown in Figure 2.7. Only α-Al, icosahedral quasicrystal and θ-$Al_{13}(Cr,Fe)_{2,4}$ were detected in their X-ray diffractograms. Some authors also detected other intermetallics in the melt spinning $Al_{93}Fe_3Cr_2Ti_2$ alloy. *Inoue* et al. (Inoue and Kimura 1999) found one type of Al-Ti intermetallic in $Al_{93}Fe_3Cr_2Ti_2$ melt spun ribbons which they named as $Al_{23}Ti_9$. This Al-Ti phase was confirmed to be Al_3Ti (Audebert, Prima et al. 2002, Galano, Audebert et al. 2009). The melt spun quaternary $Al_{93}Fe_3Cr_2Ti_2$ alloy has quasicrystals with 100nm in diameter, as shown in Figure 2.7(a), 50% smaller than the quasicrystals in $Al_{93}(Fe_3Cr_2)_7$.

The fraction and the size of the quasicrystal change with the proportion of elements in Al-Fe-Cr-Ti alloys. The $Al_{93}Fe_3Cr_2Ti_2$ alloy shown in Figure 2.7(a) has 42vol.% of quasicrystals (Audebert, Prima et al. 2002). *Audebert* et al. (Audebert, Prima et al. 2002) processed the $Al_{91}Fe_5Cr_2Ti_2$ melt spun ribbon with a uniform distribution of small near-spherical quasicrystalline particles of 10-20nm in diameter (Audebert, Prima et al. 2002). The volume fraction of quasicrystals in $Al_{91}Fe_5Cr_2Ti_2$ is larger than that in the $Al_{93}Fe_3Cr_2Ti_2$ alloy. The quasicrystals in the $Al_{93}Fe_3Cr_2Ti_2$ have about 84.6 at.% of Al, 7.0 at.% of Fe, 6.0 at.% of Cr and 2.4 at.% of Ti (Kimura, Sasamori et al. 2000). When the proportions of the Al, Fe, Cr and Ti in the alloy are close to the atom percentage in the quasicrystal particle, the fraction of the quasicrystal particles increases dramatically. As

shown in Figure 2.7(b), the $Al_{84.2}Fe_{7.0}Cr_{6.3}Ti_{2.5}$ alloy has ~97% percentages of quasicrystals (Kimura, Sasamori et al. 2000). The quasicrystal particles in $Al_{93}Fe_3Cr_2Ti_2$ and $Al_{84.2}Fe_{7.0}Cr_{6.3}Ti_{2.5}$ alloys are spherical. The aluminium grain sizes for $Al_{93}Fe_3Cr_2Ti_2$ and $Al_{91}Fe_5Cr_2Ti_2$ are not uniform, 0.2-0.6μm for the former and 0.5-2.0μm for the latter (Audebert, Prima et al. 2002, Galano, Audebert et al. 2009).

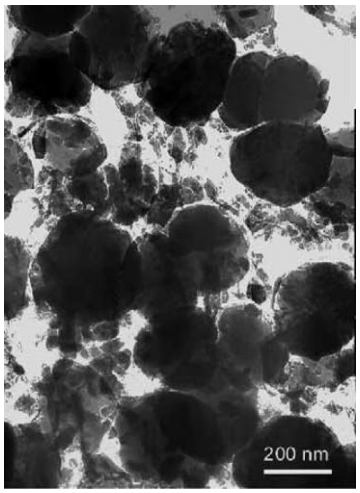

Figure 2.6: The TEM BF images of the $Al_{93}(Fe_3Cr_2)_7$ ternary melt spun alloy (Galano, Audebert et al. 2004)

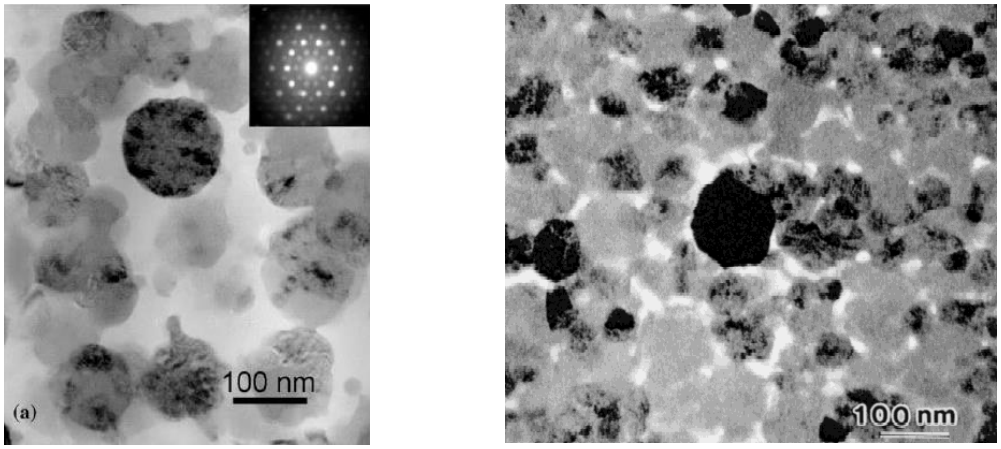

(a) (b)

Figure 2.7: The TEM BF images of melt-spun nanoquasicrystalline Al-Fe-Cr-Ti alloy **(a)** $Al_{93}Fe_3Cr_2Ti_2$ (Galano, Audebert et al. 2009), **(b)** $Al_{84.2}Fe_{7.0}Cr_{6.3}Ti_{2.5}$ (Kimura, Sasamori et al. 2000)

The gas atomised $Al_{93}Fe_3Cr_2Ti_2$ powder contains quasicrystal of size 380nm in the <26µm size powders and of 420nm in the <125µm size powders, as shown in Figure 2.8(a) and (b). Compared with the melt spun alloys, the gas atomised Al-Fe-Cr-Ti powder has larger quasicrystal size. Nanoquasicrystalline particles are also formed in the $Al_{92.5}Fe_{2.5}Cr_{2.5}Ti_{2.5}$ alloy by high-pressure argon-gas atomisation of arc melted mixtures of pure metals (Yamasaki, Nagaishi et al. 2007). As shown in Figure 2.8 (c), the spherical quasicrystals in the $Al_{92.5}Fe_{2.5}Cr_{2.5}Ti_{2.5}$ alloy have similar spherical morphology with the $Al_{93}Fe_3Cr_2Ti_2$ in Figure 2.8(a) and (b). The Al grain size of the $Al_{92.5}Fe_{2.5}Cr_{2.5}Ti_{2.5}$ ranges from 0.05µm to 0.4 µm. Table 2.1 is a summary of the microstructure of the Al-Fe-Cr-Ti alloys found in literature.

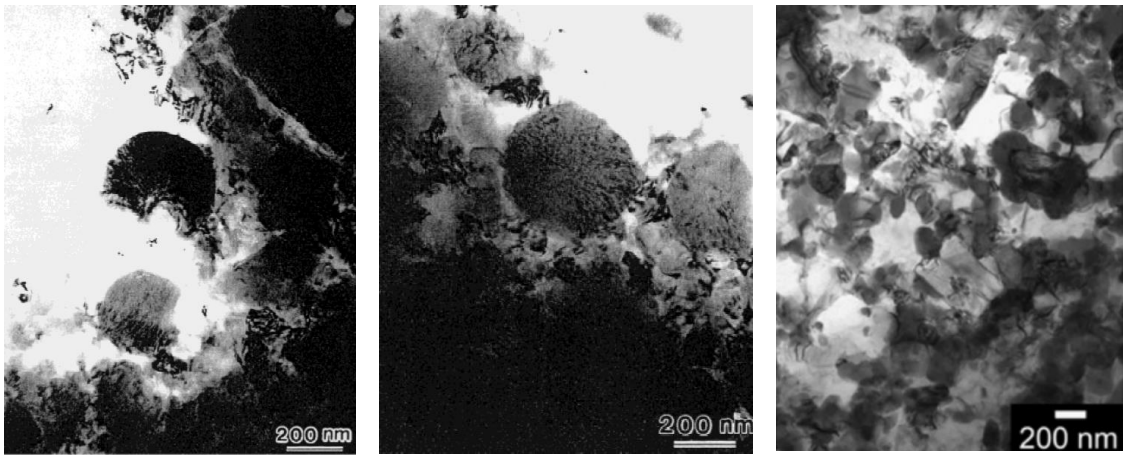

(a) (b) (c)

Figure 2.8: The TEM BF images of gas atomised powder **(a)** $Al_{93}Fe_3Cr_2Ti_2$, < 26µm (Kimura, Sasamori et al. 2000), **(b)** $Al_{93}Fe_3Cr_2Ti_2$, < 125µm (Kimura, Sasamori et al. 2000), **(c)** $Al_{92.5}Fe_{2.5}Cr_{2.5}Ti_{2.5}$, as consolidated state for powders < 38µm (Yamasaki, Nagaishi et al. 2007)

Components	Processing Routine	d_Q (nm)	f	d_{Al} (µm)	Ref.
$Al_{93}(Fe_3Cr_2)_7$	Melt spinning	200	-		[1]
$Al_{93}Fe_3Cr_2Ti_2$	Melt spinning	100	0.42	0.2-0.6	[1,2]
$Al_{84.2}Fe_{7.0}Cr_{6.3}Ti_{2.5}$	Melt spinning	~100	0.97	0.25	[3,4]
$Al_{91}Fe_5Cr_2Ti_2$	Melt spinning	10-20	>0.42	0.5-2	[2]
$Al_{93}Fe_3Cr_2Ti_2$	Gas atomisation (<25µm)	380	0.45	-	[3,4]
$Al_{93}Fe_3Cr_2Ti_2$	Gas atomisation (<125µm)	420	0.45	-	[3,4]
$Al_{92.5}Fe_{2.5}Cr_{2.5}Ti_{2.5}$	As consolidated (<38µm)	~300	-	0.05-0.4	[5]

Table 2.1: A summary of the microstructure of the nanoquasicrystalline Al-Fe-Cr(-Ti) alloys. d_Q is the diameter of the quasicrystal particle, f is the volume fraction of the quasicrystal and d_{Al} is the grain size of the α-Al. Ref. [1] (Galano, Audebert et al. 2009) [2] (Audebert, Prima et al. 2002) [3] (Kimura, Sasamori et al. 2000) [4] (Kimura, Sasamori et al. 2000) [5] (Yamasaki, Nagaishi et al. 2007)

2.3.3 Thermal stability of the quasicrystalline Al-Fe-Cr-Ti alloys

The metastable phases present in the nanoquasicrystalline Al-Fe-Cr-Ti alloys decompose and transform into intermetallics at elevated temperature (Inoue 1998, Vojtěch, Michalcová et al. 2012). Investigating the stability of the Al-Fe-Cr-Ti alloys is crucial for understanding the mechanical properties at elevated temperature.

Todd et al. (Todd, Chlup et al. 2004) investigated gas atomised $Al_{93}Fe_3Cr_2Ti_2$ powder with different particle sizes using differential scanning calorimetry, as shown in Figure 2.9. The main exothermal peak at about 527°C (800K) was related to the decomposition of the quasicrystal. The peak height increased with the decrease in the powder particle size. This should be related to the increasing degree of metastability in smaller powder particles due to a higher cooling rate in atomisation (Todd, Chlup et al. 2004). *Prima* et al. (Prima, Tomut et al. 2004) suggested that the icosahedral particle was less stable at elevated temperature if quenching from high melting temperature or high quenching rate, due to that a larger initial degree of disorder leads to a greater metastability and an increased

driving force for ordering. This could explain that the powders with larger particle size in Figure 2.9 have higher peak temperature.

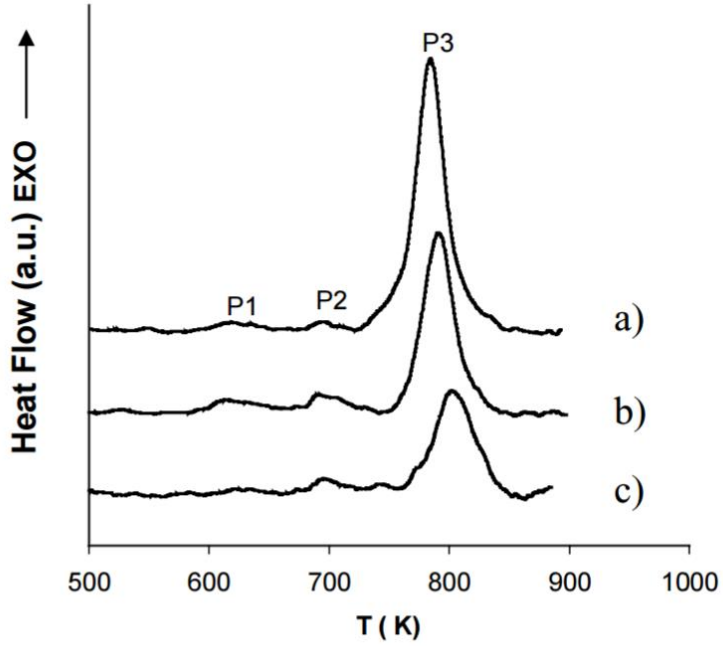

Figure 2.9: (a) DSC curves for $Al_{93}Fe_3Cr_2Ti_2$ powder with size range **(a)** <25µm, **(b)** 25-50µm and **(c)** 50-100µm, heated at 20Kmin (Todd, Chlup et al. 2004)

The $Al_{93}Fe_3Cr_2Ti_2$ alloy processed through gas atomisation and extrusion can maintain its icosahedral phase after heat treatment at 300°C for 1000h (Inoue and Kimura 2001). *García-Escorial* et al. (García-Escorial, Natale et al. 2015) performed a 1000h heat treatment on bulk nanoquasicrystalline $Al_{93}Fe_3Cr_2Ti_2$ alloy at 400°C. Based on their X-ray diffractograms the quasicrystals have been decomposed into Al_3Ti, $Al_{13}Fe_4$, $Al_{13}Cr_2$ and metastable Al_6Fe intermetallics. *Galano* et al. (Galano, Audebert et al. 2009) processed melt spun nanoquasicrystalline $Al_{93}Fe_3Cr_2Ti_2$ ribbons and performed 30min heat treatment at different temperatures. The quasicrystal could be detected in the samples

after heat treatment at 355°C and 400°C. After heat treatment at 550°C the icosahedral phase decomposed to rectangle shape intermetallics, as shown in Figure 2.10.

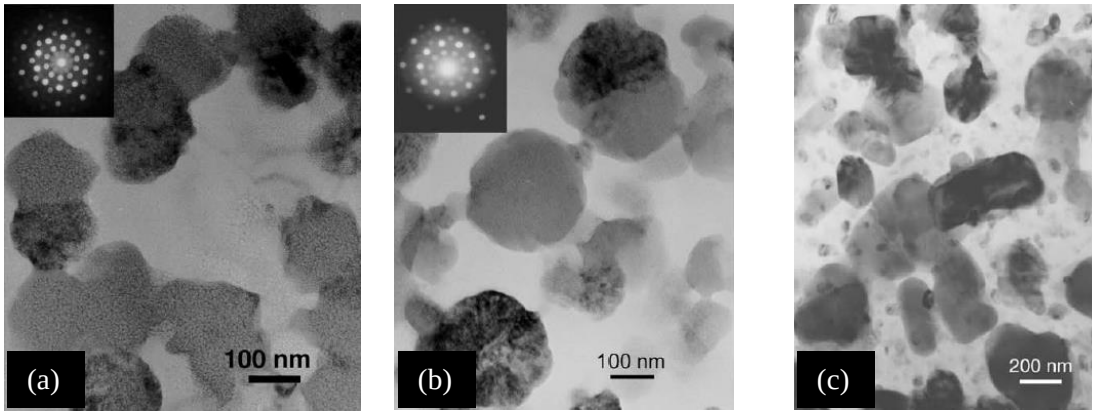

(a) (b) (c)

Figure 2.10: BF TEM images of melt spun nanoquasicrystalline $Al_{93}Fe_3Cr_2Ti_2$ alloy after 30min heat treatment at **(a)** 355°C **(b)** 450°C **(c)** 550°C (Galano, Audebert et al. 2009)

Recently, *Galano* et al. (Galano, Marsh et al. 2015) milled the nanoquasicrystalline $Al_{93}Fe_3Cr_2Ti_2$ nanocomposites. This is the first time that metastable quasicrystalline alloys were ball milled. They found that ball milling could increase the free energy of the quasicrystalline phase and decrease its decomposition temperature. In their study, before ball milling, the powder had only one exothermal peak (corresponds to decomposition of quasicrytal) in the differential scanning calorimetry. After long milling hours, two exothermal peaks appeared and the quasicrystalline phase began to decompose. However, it is still unclear what phase transformations the two exothermal peaks corresponded to, and it is unknow if any new phases formed after the decomposition of quasicrystal. Consequently, the understanding of the diffusion of transition atoms and the activation energy for the decomposition of the quasicrystal during the ball milling process are still to be developed.

2.3.4 Mechanical properties of quasicrystalline Al-Fe-Cr-Ti alloys

In the atomised powders, the power size is relevant to the mechanical properties. As shown in Figure 2.9, the powders with smaller particle sizes have higher exothermal peaks. This shows that powders with smaller sizes have larger proportions of quasicrystals, probably due to the higher cooling rates. These particles also have higher hardness. The nanoquasicrystalline $Al_{93}Fe_3Cr_2Ti_2$ processed powders with particle sizes of <25μm, 25-50μm and 50-100μm have microhardness of approximately 200, 183, 162 μHV_{25} respectively (Todd, Chlup et al. 2004).

The powder sizes also influence the mechanical properties of extruded bars. Figure 2.11 gives an overall view of $Al_{93}Fe_3Cr_2Ti_2$ alloy extruded at 400°C (673K) with different powder sizes. In general, the small powder sizes, having a higher hardness, also owned high ultimate tensile strength after extrusion. It can be noticed that Kimura's bars extruded with sub 125 μm powder had a higher ultimate tensile strength than Todd et al.'s 50-100 μm powder with the same composition, probably because there is no minimum size limit in Kimura's bar (Inoue and Kimura 1999, Todd, Chlup et al. 2004).

Figure 2.12 illustrates a series mechanical results of samples with different extrusion conditions. RX means bars with extrusion ratio of X. It is clear that bars extruded at higher temperature have lower yield stress. The extrusion ratio does not have severe influence on the final strength of the material.

The Al-Fe-Cr-Ti quasicrystalline alloys can retain strength when annealing at limited temperature. For example, the icosahedral based $Al_{93}Fe_3Cr_2Ti_2$ alloy experiences no significant hardness change after annealing at 300°C (573K) for 1000 hours, and the hardness value is ~190 HV_{100} (George, Kashyap et al. 2005). For the $Al_{92.5}Fe_{2.5}Cr_{2.5}Ti_{2.5}$

alloy, the yield strength dropped slightly from ~260MPa to ~220MPa after annealing for 100h at 300°C (573K) (Yamasaki, Nagaishi et al. 2007).

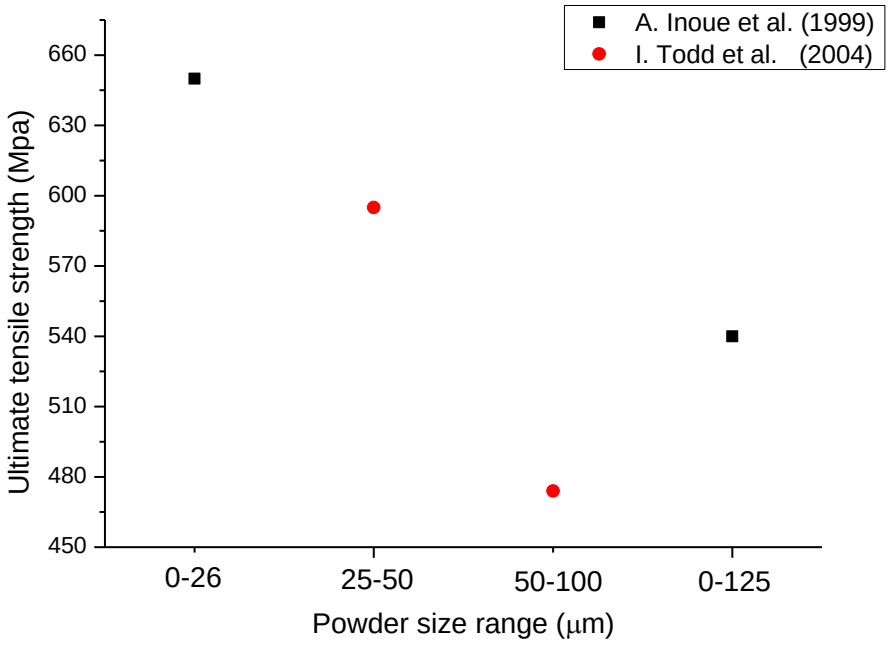

Figure 2.11: The ultimate tensile strength of bars of $Al_{93}Fe_3Cr_2Ti_2$ alloy extruded with different powder sizes. All the bars were extruded at 673K with an extrusion ratio of 10 (Inoue and Kimura 1999, Todd, Chlup et al. 2004)

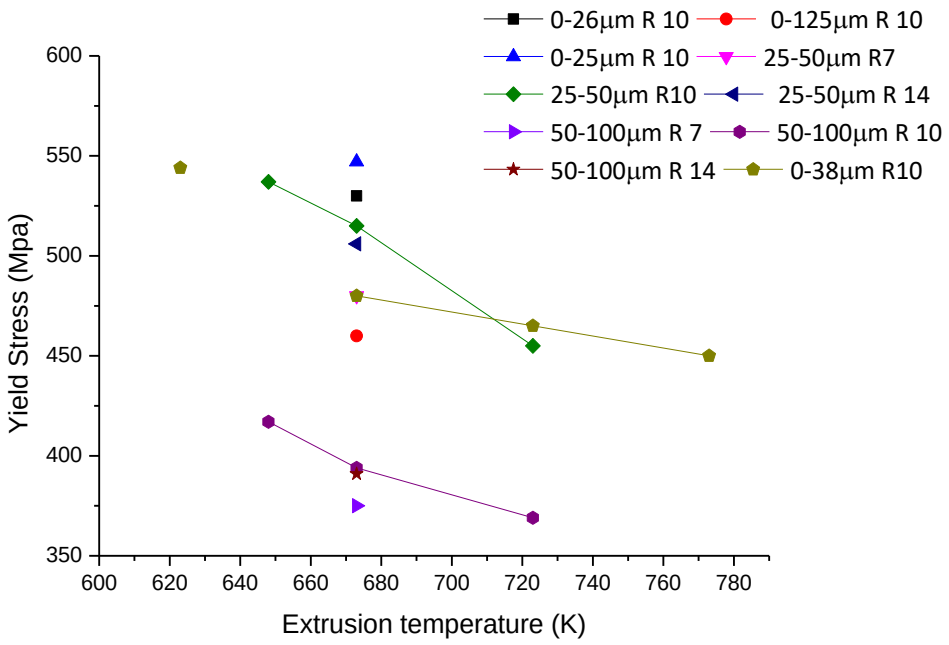

Figure 2.12: Effects of extrusion conditions on the yield strength of bars: 0-26µm R10 & 0-125µm R10 is of $Al_{93}Fe_3Cr_2Ti_2$ (at%) alloy (Kimura, Sasamori et al. 2000), 0-38µm R10 is of $Al_{92.5}Fe_{2.5}Cr_{2.5}Ti_{2.5}$ alloy (Yamasaki, Nagaishi et al. 2007), other data is of $Al_{93}Fe_3Cr_2Ti_2$ alloy (Todd, Chlup et al. 2004). The powder size and extrusion ratio are listed in the graph. (RX means bars with extrusion ratio of X)

The high strength at room and elevated temperature of the Al-Fe-Cr-Ti alloys could be due to three reasons:

- The precipitate strengthening from intermetallics. The intermetallics such as Al_3Ti, if homogeneously dispersed in the intermetallic matrix, can provide precipitate hardening especially at room temperature (Yamasaki, Nagaishi et al. 2007).

- The Orowan strengthening from the icosahedral particles. The icosahedral particles are so hard that they are impenetrable by dislocations. As a result, Orowan strengthening mechanism resulted from the encountering of the dislocations and the hard icosahedral particles contributes to the high strength of the alloys. (Galano,

Audebert et al. 2009).

- The icosahedral quasicrystal could inhibit the growth of α-Al grains. *Yamasaki* et al. (Yamasaki, Nagaishi et al. 2007) processed melt spun $Al_{92.5}Fe_{2.5}Cr_{2.5}Ti_{2.5}$ alloy and annealed the samples at 573K for 1000h. As shown in Figure 2.13, the Al crystallites enclosed by the icosahedral phase, and the two-fold axis of the icosahedral phase was along the <112> axis of the FCC Al. They found some other orientation relationships between the icosahedral phases and the Al grains but the one listed above occupied more than 80%. Such relationship could suppress the Al grain coarsening even after long time annealing (Yamasaki, Nagaishi et al. 2007).

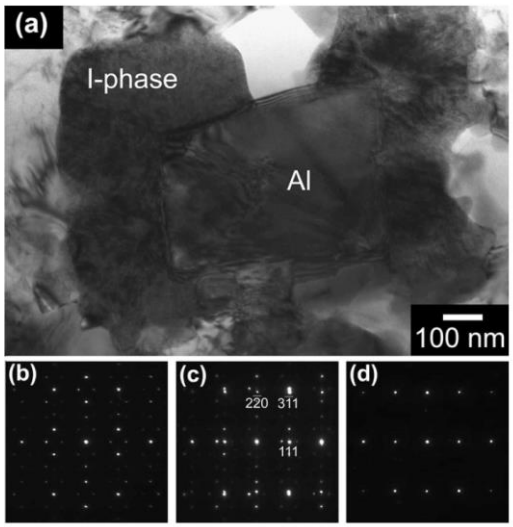

Figure 2.13: (a) TEM image of melt spun $Al_{92.5}Fe_{2.5}Cr_{2.5}Ti_{2.5}$ samples after annealing at 573K for 1000h. Selected area diffraction patterns taken from **(b)** icosahedral, **(c)** both icosahedral and Al grain and **(d)** Al phases. Diffraction spots were indexed by a FCC Al crystal (Yamasaki, Nagaishi et al. 2007)

2.4 Aluminium based composites

2.4.1 Introduction to composites

The composites usually mean a combination of two or more materials that can have the properties not obtainable with either component alone (Kelly 1985). Reinforced metal matrix composites are materials fabricated by adding reinforcements into a ductile metal matrix. Reinforcements can be classified into three types (Nair, Tien et al. 1985): (i) long, continuous or unbroken fibres of a high strength material; (ii) whisker, a substantially defect-free high strength material having a much smaller diameter than the fibres; (iii) particulates, or equiaxed particles of high strength. Among all the composites, particle reinforced composites, also known as discontinuous reinforced composites, with low cost, high modulus and strength and high wear resistance have attract extensive interests (Ma, Lavernia et al. 2017). Metal matrix composites have been used in aerospace, recreation and infrastructure industry (Miracle 2005). Commonly, when the reinforcement size is less than 500nm (Knowles, Jiang et al. 2014), the composite is called nanocomposite. Nanocomposites with Al or Al alloys as matrix are of interest in this literature. There are several aspects that can affect the properties of the composites, as discussed in the following sections.

2.4.2 Effects of reinforcement particle sizes

Reinforcement size is a main factor influencing the mechanical properties of the composites. *Kang* et al. (Kang and Chan 2004) divided the reinforcement particle sizes into three categories: Large particles (>1500 nm) act as micro-concentrators of stress and give rise to cleavage in the particle. Medium size particles can lead to the formation of cavities or pits through the loss of interphase cohesion. The smallest particles (below 200

nm) are usually well bonded to the matrix and do not initiate cavities in the particles. Therefore, studying the behaviours of nanocomposites is crucial.

When the particles are homogeneously distributed, decreasing the particle size reduces the mean free path between the particles, leading to more interactions between the matrix and particles (Chung, He et al. 2003). Therefore, the dislocation accumulation speed is faster (Khakbiz and Akhlaghi 2009). *Saberi* et al. (Saberi, Zebarjad et al. 2009) processed an Al-2.5vol.%SiC composite with reinforcement sizes of about 50nm and 5μm with ball milling. According to their results in Figure 2.14, after 10hs of milling, the grain size of the nanocomposite was ~30nm, much finer than that of the micro-reinforced composite 50nm. However, there was no much difference on grain size after 2 hours milling. This was probably because the nanoparticles agglomerated easily and it took longer time to break the mechanical interlocking than that for the micro-size particles (Hesabi, Simchi et al. 2006). The nanocomposites have advantages over the composites with respect to their mechanical properties. *Hosseini* et al. (Hosseini, Karimzadeh et al. 2010) compared Al6061-3vol.%Al_2O_3 composites with different alumina sizes 30nm, 1μm and 60μm processed through mechanical alloying and hot pressing. Figure 2.15 gives a description of hardness of the three samples tested with a load of 10kg (Hosseini, Karimzadeh et al. 2010). It is shown that with increasing alumina size the hardness dropped dramatically. The strengthening mechanisms between composites and nanocomposites will be discussed in detail in section 2.4.7 in this Chapter.

Several authors also compared the mechanical properties of composites with micro-size and nano-size reinforcements of different types. Figure 2.16 (Kang and Chan 2004) shows the tensile strength and the elongation of Al-Al_2O_3 nanocomposites as well as the

microsized SiC reinforced composites. It is clear that the tensile strength of the nanocomposite with 3 vol.% 25nm of added Al_2O_3 is higher than that of the 10 vol.% 13μm SiC composite. However, this can be due to that the Al_2O_3 has stronger interface bonding with aluminium than that of SiC, which *Kang* et al. did not consider. In literature, if processed with the same conditions, the strength of the Al-SiC composites is usually higher than the Al-Al_2O_3 composites with the same size and volume fraction of reinforcements (Nieh and Chellman 1984), although the mechanical properties of particulate SiC and Al_2O_3 are similar (Girot, Quenisset et al. 1987). The particulate cracking of SiC in Al-SiC composites has been found to be more predominant than interfacial debonding (Janowski and Pletka 1990). In Al-Al_2O_3 composite, significant interfacial debonding occurs (Lee, Subramanian et al. 1994). This indicates the bonding between Al and SiC is stronger than the bonding between Al and Al_2O_3. Therefore, from Figure 2.16, it is reasonable to say nanosize reinforcements have stronger strengthening effects in the study of *Kang* et al.

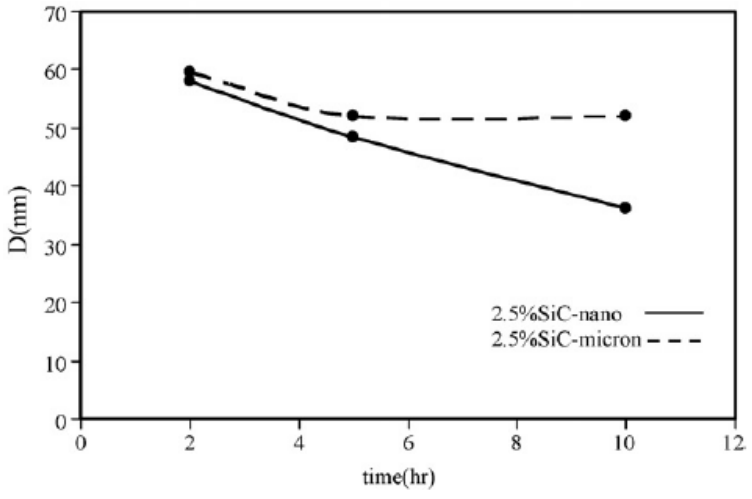

Figure 2.14: Grain size of Al-SiC composites and nanocomposites after ball milling (Saberi, Zebarjad et al. 2009)

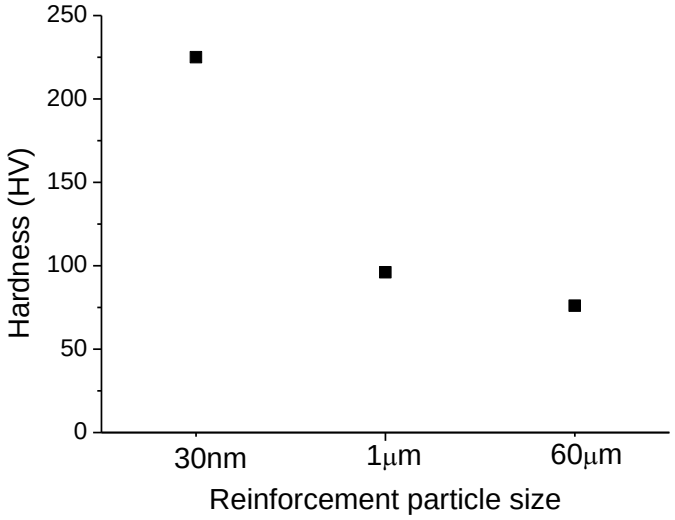

Figure 2.15: The hardness of Al6061-3vol.%Al_2O_3 composites (Hosseini, Karimzadeh et al. 2010)

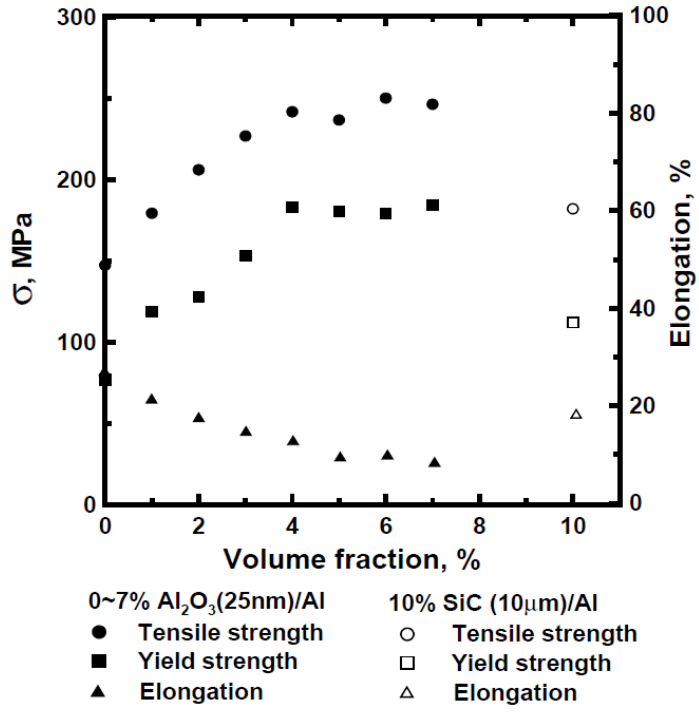

Figure 2.16: Tensile properties of Al-based nanocomposites (Kang and Chan 2004)

2.4.3 Effects of reinforcement particle volume fraction

The particle volume fraction is a dominant factor influencing the mechanical properties of the nanocomposites. It is believed that nano-sized reinforcement particles can prevent the movement of dislocations in pure aluminium matrix through dispersion strengthening mechanism (Poirier, Drew et al. 2010). If the reinforcements are homogeneously distributed, increasing the volume fraction can lower the inner particle distance and cause an enhancement in the required stress for the dislocation movements. As a result, the material strength is improved at the cost of ductility (Mohammad Sharifi, Karimzadeh et al. 2011).

Table 2.2 illustrates the mechanical properties of Al5083-B_4C nanocomposites processed using mechanical alloying and hot pressing (Mohammad Sharifi, Karimzadeh et al. 2011). Hardness tests were conducted on bulk sample with a load of 10 kg. As expected, the hardness and the compressive strength increased with the addition of B_4C, while the compressive strain to failure ratio dropped.

Properties	**B_4C (wt.%)**		
	5	**10**	**15**
Ultimate compressive strength (MPa)	371	433	485
Compressive strain to failure ratio (%)	16.3	14.1	12.1
Hardness (HV_{10kg})	120	135	163

Table 2.2: the mechanical properties of consolidated Al-B_4C nanocomposites (Mohammad Sharifi, Karimzadeh et al. 2011)

Increasing the volume fraction of reinforcements can cause agglomeration problems, especially when the reinforcements are at the nanosize scale. *Kang* et al. (Kang and Chan 2004) illustrated that the Al-Al_2O_3 nanocomposites processed by cold isotropic pressing with 2% 50nm size reinforcements addition had higher yield strength than the Al-10%SiC

(13 μm) processed in the same routine, which has been shown in Figure 2.16. However, when the Al_2O_3 proportion was larger than 4%, the yield strength did not have significant increase, while only the elongation (%) dropped. The reason might be a larger volume fraction of reinforcements could generate agglomerations. As observed in their TEM images, the Al_2O_3 particles were almost evenly distributed in the Al-1vol.%Al_2O_3 nanocomposite (Figure 2.17(a)), while the Al_2O_3 clusters with 100-400 nm in diameter could be observed in the Al-4vol.%Al_2O_3 nanocomposite (Figure 2.17(b)). The agglomerations could not transfer load as efficiently as dispersed particles and this would weaken the strength and ductility of the material (Kang and Chan 2004).

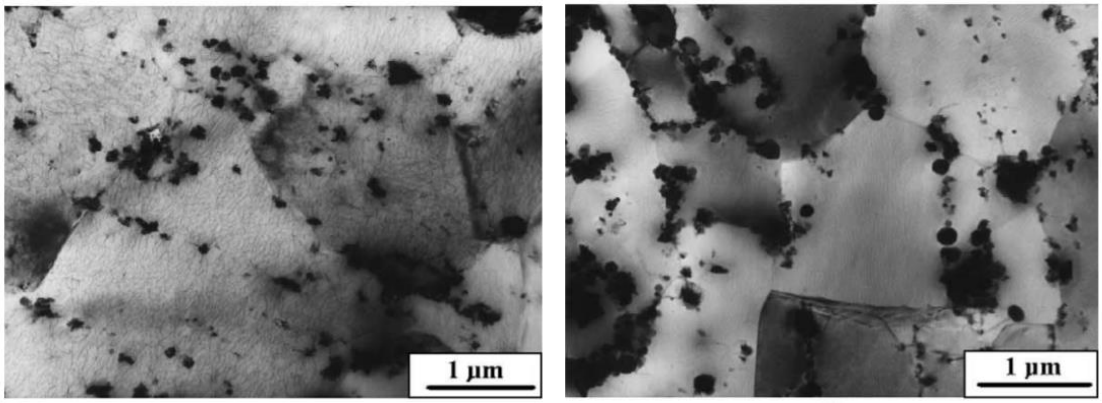

(a) (b)

Figure 2.17: TEM micrographs of Al-Al_2O_3 nanocomposites processed by wet mixing, cold isotropic pressing and sintering **(a)** 1 vol.% Al_2O_3, **(b)** 4 vol.% Al_2O_3 (Kang and Chan 2004)

2.4.4 Effects of different reinforcement particle types

Table 2.3 gives a comparison on most interested properties among different kinds of ceramic particles. It is shown that most commonly used reinforcements have very high hardness. The hardness values of the γ-Al_2O_3 (744 kg/mm^2) and AlN (1225-1230 kg/mm^2) are relative lower, less than half of the hardness for the B_4C (2800 kg/mm^2). Most ceramic

particles have a density higher than aluminium (2.7 $g \cdot cm^{-3}$), thus having trend of increasing the density of the composites except the B_4C, with a density of 2.51 $g \cdot cm^{-3}$.

	E, $GN \cdot m^{-2}$	**ρ, $g \cdot cm^{-3}$**	**C_t, 10^{-6} K^{-1}**	**σ_{UTS}, 10^3 psi**	**HV, kg/mm^2**	**Poisson's ratio**	**Ref.**
SiC	420-450	3.2	4.3	5-20, at 25℃	2500-2550	0.18-0.19	[1,2]
α-Al_2O_3	380-450	3.96	7.0	37, at 25℃	2000-2050	0.21-0.27	[2]
γ-Al_2O_3	145	3.6	-	-	744*	-	[3,4]
AlN	320	3.26-3.30	4.6	-	1225-1230	0.24	[5,6]
B_4C	448	2.51	4.5-5.5	22.5 at 980℃	2800	0.21	[2,7]
Al	68	2.7	23.6	8.6 at 25℃	-	0.35	[8]

Table 2.3: Properties of different types of composites, E means Elastic modulus, ρ is the density, C_t is the coefficient of thermal expansion, T_M is the melting point, σ_{UTS} is the tensile strength, and psi is per square inch.

Ref.: [1] (Lloyd 1994) [2](Shackelford, Han et al. 2016) [3] (Mishra, Lesher et al. 1996) [4] (Inframat Advanced Materials 2017) [5] (Smithells 1992) [6] (Chung, He et al. 2003) [7] (Li, Zhao et al. 2009) [8] (Simmons and Wang 1971)

Whether the added particles can react with matrix material in processing progress is one major concern when choosing the reinforcements type. The SiC has inert properties, but there are some works found that SiC could react with Al, generating Al_4C_3 intermetallics and Al-Si eutectic phases (Lee, Suh et al. 1997, Gu 2006, Zebarjad and Sajjadi 2007). Using milling instead of casting can process the composites in relative low temperature and avoid the formation of undesirable phases (Knowles, Jiang et al. 2014). Reaction and undesired intermetallics are also main problems in the Al-B_4C composites. According to the literature, a wide series of intermetallics, namely the AlB_2, Al_4BC, $AlB_{24}C_4$, Al_4C_3 could be obtained when processing Al-B_4C composites at different temperatures, and all of these phases have trends to lower the tensile strength of the composites (Pyzik and Beaman 1995). Usually, cryomilling, which means mechanical milling at cryogenic

temperature, is a powerful way to manufacture Al-B_4C composites with clean surfaces (Ye, He et al. 2006). In comparison, Al_2O_3 and AlN are widely applied in Al nanocomposites because they are chemically inert with Al (Chung, He et al. 2003, Prabhu, Suryanarayana et al. 2006).

2.4.5 Quantifying the distribution level of reinforcements

Yang et al. (Yang, Boselli et al. 2001) developed a method for quantifying the distribution level of the reinforcements by a finite-body tessellation. They simulated different types of inhomogeneous distributions (with 15% of atoms agglomerated) and homogeneous distributions with particles with different shapes and size distributions. After that, they used overlaying finite body tessellation to separate the particles into shells, as shown in Figure 2.18. The coefficient of variation values of several parameters, namely the cell area, local area fraction, number of near-neighbours, nearest neighbour angle, nearest neighbour distance and mean near neighbour distance, were calculated. The mean near-neighbour distance was defined as the average of the interface to interface separations with all particles that share a cell edge around each individual particle of interest. It turned out that the mean near-neighbour distances for the homogeneous and 15% inhomogeneous distributions have significant difference regardless of the shapes and particle size distributions (Yang, Boselli et al. 2001). This showed that the mean near-neighbour distance could be a powerful parameter for identifying the homogeneity quantitatively.

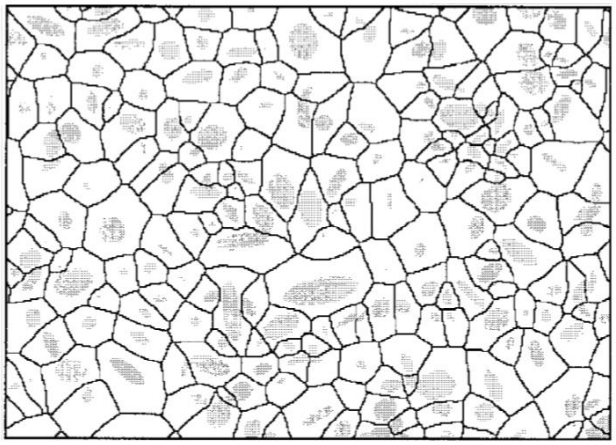

Figure 2.18: Example of simulated distribution and overlaying finite body tessellation. The grey particles are the reinforcements and the cells are the computer generated tessellations (Yang, Boselli et al. 2001)

An equation model for measuring the homogeneity of α features in β features was developed by *Hilliard et al*. (Hilliard and Cahn 1959). They selected a number of subareas A_1, A_2, A_3, *etc.*, and then measured the area of α features a_1, a_2, a_2, *etc*. in each of the selected area. The standard deviation of local area fractions of α features in the selected subareas was marked as σ_A. The average area fraction of α features in all subareas was marked as A_f, the expected number of α features in all the subareas was M_a, the expected area of α features in all the selected subareas was a, and the standard deviation of the areas of α features in all the subareas was σ_a. These parameters follow a relationship (Hilliard and Cahn 1959):

$$\left(\frac{\sigma_A}{A_f}\right)^2 = \left(\frac{1}{M_a}\right)\left[\left(\frac{\sigma_a}{a}\right)^2 + 1\right] \quad \text{-------} \quad \text{Equation 10}$$

This model has two assumptions:

- The number of α in a given area of the matrix follows a Poisson distribution since the α features are randomly distributed on the plane of polish.

- The proportions of area α in different regions of β are independent.

The value of $(\frac{\sigma_A}{A_f})^2$ should be close to $\frac{1}{M_a}$ when the distribution of reinforcements is fully homogeneous (Hilliard and Cahn 1959).

In literature, most methods for quantifying the homogeneity focus on the micro-size reinforcements. Quantifying the distribution level for the nanosize particles is still very difficult and has not been well studied. This could be due to that (1) the resolution of SEM may not be enough in distinguishing the boundaries between each nanoparticle inside the agglomerated clusters. (2) when the volume fraction of nanoparticles increases, the number of nanoparticles increases much faster than micro-size particles. Consequently, calculating the parameters, such as the nearest distances between the particles and the number of particles can be a tedious work.

2.4.6 Agglomerations and Interface bonding

The quality of the interfaces between the matrix and the reinforcement particles is crucial. A strong interface bonding allows effective load transfer from matrix to reinforcement, which improves both the strength and the stiffness (Poirier, Drew et al. 2010). However, due to the difficulty of consolidating composites, the bonding between the reinforcements and the metal matrix is quite limited. Figure 2.19 (Poirier, Drew et al. 2010) is the STEM images of the Al-10vol.%Al_2O_3 (80nm) nanocomposites. It can be seen that large numbers of cavities are visible on the interface, which leads to a mismatch between the experimental and predicted mechanical property. If the interface bonding is weak, in fracture tests it will debond, and a large number of reinforcements will be observed in the fracture surfaces (Ye, He et al. 2006).

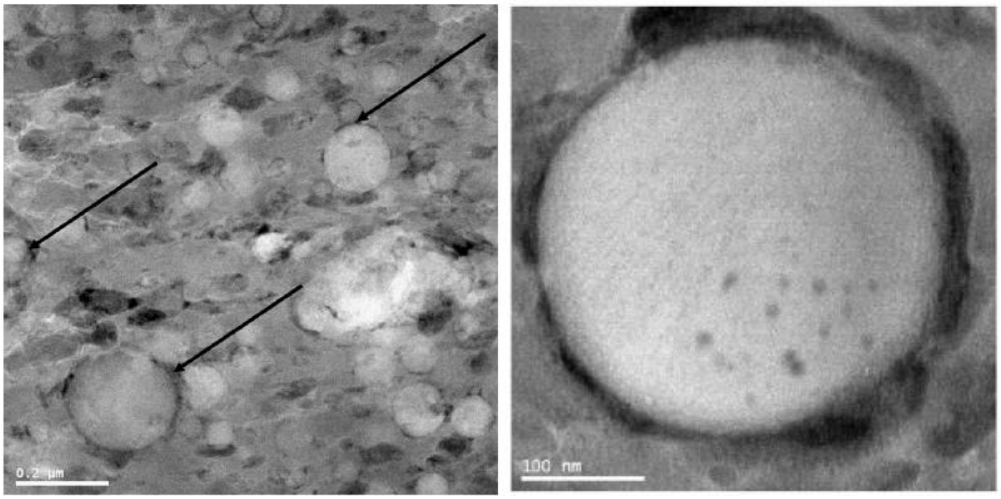

(a) (b)

Figure 2.19: (a) low and **(b)** high magnification STEM images of the cavities at the alumina/aluminium interfaces after consolidation by hot pressing of the Al-10vol.%Al_2O_3 (80nm) (Poirier, Drew et al. 2010)

2.4.7 Strengthening mechanisms

This literature focuses on strengthening mechanisms of nanocomposites processed by mechanical milling. There are two types of strengthening mechanisms typically associated with conventional metal matrix composites: (1) Indirect strengthening due to the influence of reinforcements on matrix microstructure or deformation mode, such as dislocation strengthening induced by deformation mismatch between the reinforcements and the matrix, and grain refinement effects. (2) Direct strengthening resulted from load transfer from the metal matrix to the reinforcement particles.

Orowan strengthening mechanism

Orowan strengthening comes from the resistance of closely spaced hard particles to the passing of dislocations. The enhancement of the mechanical property can be estimated by the Orowan equation (Orowan 1948, Hull and Bacon 1984, Ye, Han et al. 2005):

$$\Delta\boldsymbol{\sigma_p} = \boldsymbol{M}\frac{\mathbf{0.4}\boldsymbol{Gb}}{\boldsymbol{\pi}(\mathbf{1}-\boldsymbol{\upsilon})^{\mathbf{1/2}}}\frac{\ln(\frac{\boldsymbol{D_{p,s}}}{\boldsymbol{b}})}{\boldsymbol{\lambda_s}} \quad \text{--------} \quad \text{Equation 11}$$

where $\Delta\sigma_p$ is the particle strengthening contribution value, M is the Taylor factor, G is the shear modulus, b is the Burger vector, υ is the Poisson's ratio, λ_s is the interparticle spacing, and $D_{p,s}$ is the mean planar particle diameter which is $\sqrt{2/3}$ times the average particle radius.

When the reinforcements are of micro-size, the Orowan mechanism does not work because the particles are located intergranularly in the Al matrix (Kang and Chan 2004). In highly dispersed nanosize reinforcement particles, the Orowan strengthening can be significant. It has been reported that the dispersion of fine (~100nm) particles in a metal matrix can raise the creep resistance even for a small volume fraction (<1%), because the Orowan bowing is necessary for dislocations to bypass the particles (Zhang and Chen 2006).

Grain refinement mechanism

Grain boundaries also contribute to the strengthening of the material by impeding dislocation motions. The relationship between the tensile strength and the grain size can be described by the Hall-Petch formula (Hall 1951, Petch 1953) when the crystallite is equiaxed (Dieter and Bacon 1986):

$$\Delta\boldsymbol{\sigma_y} = \frac{\boldsymbol{K_y}}{\boldsymbol{d^x}} \quad \text{----------} \quad \text{Equation 12}$$

where $\Delta\sigma_y$ is the contribution due to grain refinement after considering the effect of grain size, K_y is a constant known as "locking parameter", which means the relative hardening contribution of grain boundaries (Dieter and Bacon 1986), d is the mean grain size, and x

is the exponent constant. This exponent was suggested as p = 0.5 by the early works of *Hall* (Hall 1951) and *Petch* (Petch 1953), related to dislocations pile up at the grain boundaries. Deviations of this value have been theoretically proposed and experimentally found in the literature. Very early works by *Mathewson* (Mathewson 1991) and *Bragg* (Bragg 1942) postulate that strength due to the crystallite size is proportional to $d^{-0.25}$ and d^{-1}, respectively.

Obviously, Equation 12 has limitations, since the strength cannot increase infinitely with decreasing crystallite sizes. The Hall-Petch relationship is based on the concept of strain within one grain being blocked by a grain boundary, leading to a grain-size dependent dislocation and stress concentration which introduces new slip systems in the second grain. At very small grain sizes, there may not be enough spaces to allow a grain to contain more than 2 dislocations, which are difficult to pile up (Whang 2011). *Nieh* et al. (Nieh and Wadsworth 1991) suggested that there was a critical grain size, and Hall-Petch was not reliable when the grain size was lower than the critical grain size d_c:

$$\boldsymbol{d_c = 3Gb/\pi(1-\upsilon)H_\upsilon} \quad \text{----------} \quad \text{Equation 13}$$

where G is the shear modulus, b is the Burgers vector, υ is the Poisson's ratio and H_υ is the material's hardness. Usually, the d_c is 5-10nm for Fe and 10-20nm for Al and Cu (Nieh and Wadsworth 1991). The schematic diagram describing the hardness or strength and the grain size is shown in Figure 2.20.

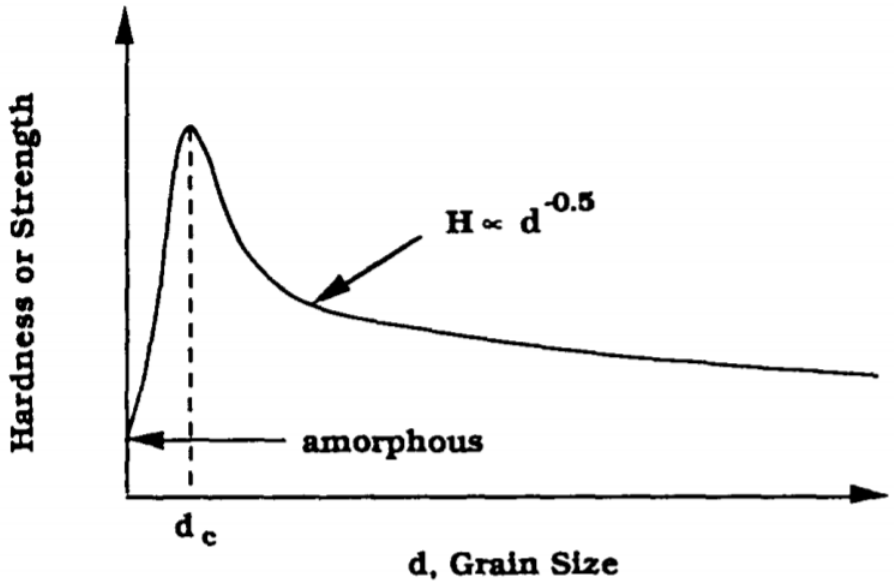

Figure 2.20: The Schematic diagram showing strength as a function of grain size. Theoretically the strength of a material should reach a maximum at a critical grain size, $\boldsymbol{d_c}$. (Nieh and Wadsworth 1991)

Dislocation Strengthening

Dislocations interacting with each other produces sessile dislocations (Dieter and Bacon 1986). The sessile dislocations can prevent the dislocation movement and an increase of stress is needed to overcome the barrier. Assuming the dislocations are randomly located, their contribution on the flow stress can be estimated by Taylor's equation (Totten and MacKenzie 2003):

$$\Delta\boldsymbol{\sigma_{w.h}} = \boldsymbol{\alpha_{w.h} M G b \rho^{0.5}} \quad \text{----------} \quad \text{Equation 14}$$

where $\Delta\sigma_{w.h}$ is the contribution to flow stress due to work hardening, M is Taylor's factor, $\alpha_{w.h}$ is a pre-factor generally ~0.2 for Al, G is the shear modulus, b is the Burgers vector, and ρ is the dislocation density.

The rule of mixtures

The load transfer models were developed on the basis that the hard, relatively undeformable reinforcements, could carry more load than the relatively soft matrix (Kamat, Hirth et al. 1989, Ali, Scudino et al. 2012, Tutcher and Sheppard 2013). This group includes the simplest and well know rule of mixtures (ROM) (Tutcher and Sheppard 2013), which is characterised for a mathematical expression which gives the homogeneous property of a heterogeneous material in terms of its properties, quantity and arrangement of its constituents. This model weights the volume average of the component properties in isolation without considering any interaction between the reinforcements and matrix.

$$\boldsymbol{\sigma = \sigma_m(1 - f) + \sigma_r f} \quad \text{----------} \quad \text{Equation 15}$$

Here, σ, σ_m, σ_r are the yield strength of the composite, the matrix and the reinforcements respectively, and *f* is the volume fraction of the reinforcements. The assumptions of this equation are that the proportion of the external load can be estimated by the volume averaging the load, and the external applied load is equal to the total volume averaged loads (Hong, Kim et al. 2003).

2.5 Processing methods: mechanical milling and extrusion

2.5.1 Introduction

Mechanical milling is a powder processing method producing materials starting from the blended elemental powder mixtures (Vicens, Chedru et al. 2002, Prabhu, Suryanarayana et al. 2006). Mechanical milling is widely used for processing amorphous alloys, nanoquasicrystalline powders, and metal ceramic composites and nanocomposites (Suryanarayana 2001, Zhang 2004), but it is metal matrix nanocomposites that are of interest. In processing, the matrix powder and the reinforcement materials as well as the

milling media are loaded into a milling pot. When the pot is moving, the powder, the milling media and the wall of the pot collide with each other to get a homogeneous distribution of reinforcement particles along with the refined microstructure (Suryanarayana 2001).

2.5.2 Influence of different milling parameters

During the milling process, when the balls slide on the surface of the pot, the powders trapped between them get a shear force. When the speed of the balls decreases, they fall down, giving an impact force on bottom powders (Calka and Nikolov 1995). During this process, mechanical milling generates strain, refines the grain size and increases the hardness of the powder (Gheisari, Javadpour et al. 2009). Several milling parameters which affect the distribution of the reinforcement and the properties of the nanocomposites are analysed.

Types of milling

The planetary miller is one of the most popular type of miller used for ceramics, chemistry, biology, material technology applications, etc. (Suryanarayana 2001). The milling process is explained in Figure 2.21. A special driving system is installed in this machine so the supporting disc and the grinding bowl can move separately around their own axes. The centrifugal force provided by the disc has the trend on adhering the balls to the surface of the pot while the opposite rotations of the balls tend to let the balls fall down. Once the ball is separate from the wall it travels freely inside the chamber and hits the opposing wall. Therefore, friction and impact effects are generated in the milling process (Suryanarayana 2001).

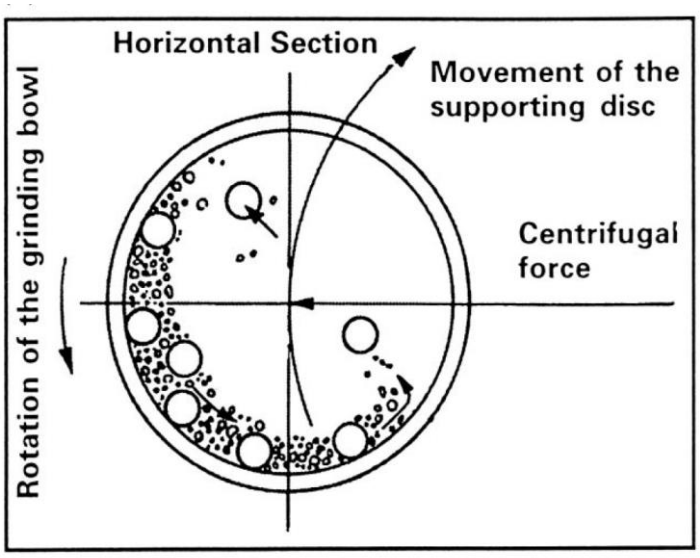

Figure 2.21: The milling process of the planetary miller (Suryanarayana 2001)

Milling time

Milling time is the most important factor in the ball milling process. During the milling process the powders are repeatedly flattened, cold welded, and fractured. Finally, a balance between rewelding and fracturing is achieved, and the crystallite size is reduced, and the microhardness of the milled powder increases first and then retains on a certain value (Zebarjad and Sajjadi 2007, Khadem, Nategh et al. 2011). It is worth mentioning that the contamination increases with the milling time, so the powders should be milled just for the required duration and not any longer (Suryanarayana 2001).

In metal matrix composites, usually a ductile metal is used as matrix and hard ceramic particles are used as reinforcements. *Fogagnolo* et al. (Fogagnolo, Velasco et al. 2003) built a model to explain the microstructure changes of ductile-brittle powders during ball milling process, as shown in Figure 2.22.

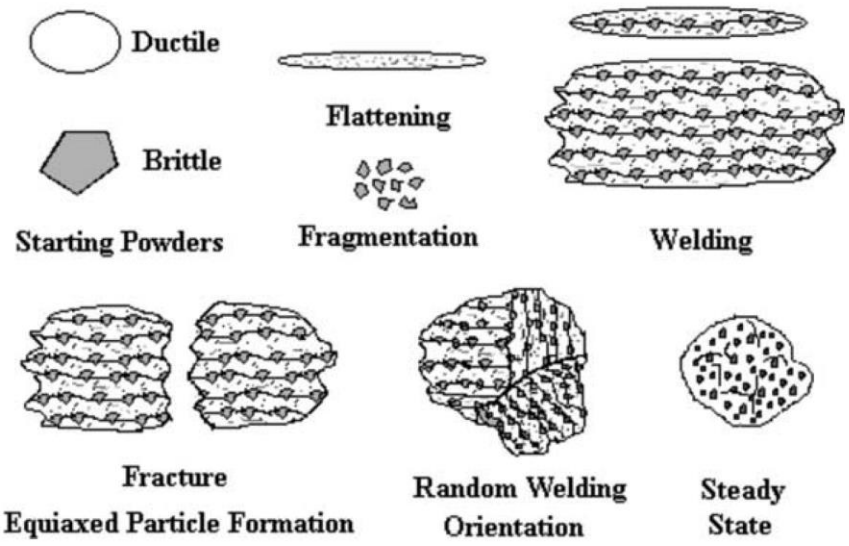

Figure 2.22: Microstructure evolution during the ball milling process (Fogagnolo, Velasco et al. 2003)

In the early stage of milling, the ductile powders are flatted by the collision of the balls, and the brittle powders are fractured. Then, the brittle pieces adhere to the surface of the ductile powder and a lamella structure is formed, as shown in Figure 2.22. After repeated fracturing and random cold welding, a steady state with homogeneous distribution of the brittle reinforcements is reached.

Milling speed

With a higher milling speed, the powder and the milling media collide more frequently per unit time. This implies less milling time is required to refine the crystallite size, get better homogeneous distribution of the reinforcements and increase the hardness (Boey, Yuan et al. 1998, Gheisari, Javadpour et al. 2009). It is worth mentioning that at low milling speed the balls may slide on the bottom of milling pots due to the gravity (Ryu, Hong et al. 1997), and at high milling speed the balls will be pinned to the inner walls of

the vial due to the centrifugal force (Suryanarayana 2001). The milling speed should be between these two values so the balls can fall down from the maximum height to get good milling results. In literature, most publications so far focus on the effect of milling time, while the investigation on the influences of milling speed is insufficient. The model in Figure 2.22 works fine when choosing proper milling speeds. However, probably it will not work when the milling speed is low and the balls cannot fracture the powder efficiently.

Ball to powder weight ratio

Higher ball to powder ratio can shorten the time needed for achieving the homogeneous structure (El-Eskandarany, Aoki et al. 1991). *El-Eskandarany* et al. (El-Eskandarany, Aoki et al. 1991) investigated the ball to powder ratio on Al-Ta alloy with ball to powder ratio from 12:1 to 324:1. According to their results, the amorphisation rate of powder processing with a ball to powder ratio 108:1 was much higher than that with a ball to powder ratio 36:1. This could be that higher ball to powder ratio transfers more energy per collision, which increases the frequency for the particles to be reacted and inter-diffused. High ball to powder ratio has the trend to generate more contamination. This is probably due to the lack of preventative wear coating on the milling media in the milling process (El-Eskandarany, Aoki et al. 1991).

Extent of filling

The sample filling in the pot should not be too high, because it is necessary for the balls and the particles to have enough space to move around freely (Suryanarayana 2001). On the contrary, the filling should not be too low, or the production per milling would be small. For a milling pot with 250ml volume, 30 to 125ml filling should be fine (FRITSCH

2017). For a milling pot with 500ml volume, 80 to 250ml filling works well (FRITSCH 2017).

Milling atmosphere

In this milling progress, the atmosphere atoms can be absorbed on fresh surfaces of the powders and then be mixed into the particles by diffusion along dislocations and grain boundaries (Ogino, Murayama et al. 1991). Therefore, milling atmosphere is a key factor for the contamination of the powder. Usually, pure argon or helium is filled in the pot to minimize this problem. Sometimes powders should be loaded or unloaded in a glovebox filled with pure inert air (Suryanarayana 2001). It has been found that nitrogen can react with metal so it cannot be used as protective air media unless one is interested in producing nitrides (Chen, Halstead et al. 1996).

Process control agents

The powder particles get cold-welded with each other, especially if they are ductile. In the milling process, the agents absorb on the surface of the powder, slowing down the cold welding and preventing the agglomeration (Suryanarayana 2001). Most of the control agents are organic compounds such as stearic acid or wax (Lee and Kwun 1996). The control agents have significant effects even if only a small proportion is added. *Ye* et al. (Ye, He et al. 2006) processed the Al5083-10%B_4C nanocomposite with cryomilling (starting powder size <40μm for Al alloy and 1-7μm for B_4C) in the condition of ball to powder ratio 32:1 and milling speed 180 rpm for 8hs. According to their research, by increasing the stearic acid from 0.2 wt% to 1.0 wt%, the powder size obtained decreased from about 50 μm to about 15 μm.

2.5.3 Quantification and modelling of mechanical milling

The modelling of ball milling using a planetary mill has been investigated by several studies (Burgio, Iasonna et al. 1991, Magini, Burgio et al. 1993). Unlike conventional metallurgical processes such as casting, mechanical milling is a dynamic process which is difficult for the mechanisms to be described using mathematical models. *Magini* et al. (Magini, Iasonna et al. 1996) claimed that assuming collision is the basic event by which energy is transferred from the mill to the powder, then the main parameters to evaluate are:

i. The kinetic energy of the ball;
ii. The fraction of the kinetic energy given to the powder during ball milling
iii. The amount of material trapped in the collisions

The energy transferred in each collision is proportional to the mass of the ball and the square of the milling speed (Burgio, Iasonna et al. 1991). A faster milling speed will also increase the number of collisions (Abdellaoui and Gaffet 1995). The maximum quantity of trapped material is proportional to the square of the radius of the ball and the density of the material (Burgio, Iasonna et al. 1991, Magini, Iasonna et al. 1996). Therefore, when the radius of the ball is fixed, powders milled with lower speed require less milling time to suffer the same amount of collisions and obtain the same energy from the mill.

2.5.4 Mechanical milling on quasicrystalline nanocomposites

Recently it has been proved that mechanical alloying could be applied on producing nanoquasicrystalline aluminium nanocomposites (Galano, Marsh et al. 2015). *Galano* et al. (Galano, Marsh et al. 2015) produced $Al_{93}Fe_3Cr_2Ti_2$/8vol.% Al_2O_3 through ball milling with a ball to powder ratio of 10 and a milling speed at 250 rpm. They successfully

fabricated bulk nanocomposite by extruding the powders at 550°C. The extruded bars had ~43% higher hardness than the unreinforced extruded $Al_{93}Fe_3Cr_2Ti_2$ alloy, but the high temperature caused the decomposition of the quasicrystals. The crystallite size of the α-Al decreases dramatically with milling time (Galano, Marsh et al. 2015). This is the first time that ball milling was conducted on Al alloys containing metastable quasicrystalline phases as matrix. The results show good prospects on processing novel aluminium quasicrystalline nanocomposites for industry use. However, the effects of quasicrystal particles on the microstructure during ball milling were still not explained, and the strengthening mechanisms of the nanoquasicrystalline aluminium nanocomposites powder need to be further developed.

2.5.5 Extrusion

For both gas atomised nanoquasicrystalline aluminium alloy and the ball milled nanocomposites, the powders need to be consolidated in order to produce bulk samples. Since extrusion was commercial available following the invention in 1886, extrusion established itself as a major industrial processing routine among all the industry methods for producing bulk aluminium alloys (Sheppard 2013). The powders could be either cold or hot compacted (Tongsri, Minay et al. 2001) or canned (Todd, Chlup et al. 2004). However, for aluminium quasicrystalline alloys processed through rapid solidification, hot compaction could potentially transform the metastable phases (Tongsri, Minay et al. 2001) or increase the ultrafine crystallite sizes (Kollo, Bradbury et al. 2011). Extrusion includes loading a billet of solid metal into a continuous length of generally uniform. By applying pressure, the billet is forced to flow through a shaped die. The value of the pressure depends on the materials softness and ductility (Sheppard 2013). During the extrusion, the

powders are subject to shear stress which causes their elongation following the extrusion direction (Vojtěch, Verner et al. 2007). The friction between the particles of metal matrix material breaks up the oxide layer, allowing metal to metal bonding between the powders, which produces a compacted bulk sample. During the extrusion, the aluminium matrix is deformed along the hard intermetallics and the ceramic particles, which remain their shapes (Vojtěch, Verner et al. 2007, Abdollahi, Alizadeh et al. 2014).

2.6 Summary

Quasicrystal is a structure that is ordered but not periodic. The lattice for a three-dimensional quasicrystal can be generated by projections from a six-dimensional periodic lattice. Quasicrystals are usually hard, and can form in Al alloys in rapid solidification process. The nanoquasicrystalline $Al_{93}Fe_3Cr_2Ti_2$ alloy contains a metastable nanosize quasicrystalline phase, and has a high thermal stability. This nanoquasicrystalline $Al_{93}Fe_3Cr_2Ti_2$ alloy has superior performance, with a yield strength of 420-520MPa at 473K and 320-350Mpa at 573K, and thus has potentials to solve the problems that conventional aluminium alloys have restrictions in elevated temperature applications. The quasicrystals in $Al_{93}Fe_3Cr_2Ti_2$ alloy could be maintained with short hours of ball milling, but will begin to decompose after long milling hours. The decomposition process during the mechanical milling is still not well explained.

Aluminium metal matrix with ceramic particles reinforced nanocomposite is another type of structure material with superior strength. The size, type, shape and volume fraction of reinforcements influence the mechanical properties of the nanocomposites. The performance of nanocomposites is dependent on the homogeneity of reinforcement particles. Mechanical milling is a powerful method to process nanocomposites with a

homogeneous distribution, and extrusion is a common method for converging the gas atomised quasicrystalline alloy powders or ball milled nanocomposite powders into bulk material.

Moreover, there has been study showing that nanoquasicrystalline aluminium nanocomposites are expected to have superior strength than both the nanoquasicrystalline aluminium alloys and aluminium nanocomposites. The microstructure evolution and the strengthening mechanisms of this new types of materials need to be further investigated.

2.7 Reference

Abdellaoui, M. and E. Gaffet (1995). "The physics of mechanical alloying in a planetary ball mill: mathematical treatment." Acta metallurgica et materialia **43**(3): 1087-1098.

Abdollahi, A., et al. (2014). "Dry sliding tribological behavior and mechanical properties of Al2024–5wt.% B_4C nanocomposite produced by mechanical milling and hot extrusion." Materials & Design **55**: 471-481.

Akdeniz, Z. and P. Vignolo (2017). "Condensate oscillations in a Penrose tiling lattice." Physica E: Low-dimensional Systems and Nanostructures **91**: 136-140.

Ali, F., et al. (2012). "Modeling the strengthening effect of Al–Cu–Fe quasicrystalline particles in Al-based metal matrix composites." Journal of Alloys and Compounds **536**: S130-S133.

Audebert, F., et al. (1999). "Laser cladding of aluminium-base quasicrystalline alloys." Scripta materialia **40**(5): 551-557.

Audebert, F., et al. (2002). "Structural characterisation and mechanical properties of nanocomposite Al-based alloys." Materials Transactions **43**(8): 2017-2025.

Boey, F., et al. (1998). "Mechanical alloying for the effective dispersion of sub-micron SiC p reinforcements in Al–Li alloy composite." Materials Science and Engineering: A **252**(2): 276-287.

Bragg, W. (1942). "A theory of the strength of metals." Nature **149**: 511-513.

Burgio, N., et al. (1991). "Mechanical alloying of the Fe− Zr system. Correlation between input energy and end products." Il nuovo cimento D **13**(4): 459-476.

Cahn, J. W., et al. (1986). "Indexing of icosahedral quasiperiodic crystals." Journal of Materials Research **1**(01): 13-26.

Calka, A. and J. Nikolov (1995). "Direct synthesis of AlN and Al-AlN composites by room temperature magneto ball milling: the effect of milling condition on formation of nanostructures." Nanostructured materials **6**(1): 409-412.

Chen, Y., et al. (1996). "Influence of milling temperature and atmosphere on the synthesis of iron nitrides by ball milling." Materials Science and Engineering: A **206**(1): 24-29.

Chung, K. H., et al. (2003). "Mechanisms of microstructure evolution during cryomilling in the presence of hard particles." Materials Science and Engineering: A **356**(1): 23-31.

Coxeter, H. S. M. (1973). Regular polytopes, Courier Corporation.

Davies, J. R. (1993). Aluminium and aluminium alloys, ASM international.

Dieter, G. E. and D. J. Bacon (1986). Mechanical metallurgy, McGraw-Hill New York.

Doel, T. and P. Bowen (1996). "Tensile properties of particulate-reinforced metal matrix composites." Composites Part A: Applied Science and Manufacturing **27**(8): 655-665.

Duneau, M. and A. Katz (1985). "Quasiperiodic patterns." Physical review letters **54**(25): 2688.

Dursun, T. and C. Soutis (2014). "Recent developments in advanced aircraft aluminium alloys." Materials & Design **56**: 862-871.

El-Eskandarany, M. S., et al. (1991). "Calorimetric characterization of the amorphization process for rod milled $Al_{50}Nb_{50}$ alloy powders." Scripta metallurgica et materialia **25**(7): 1695-1700.

Elser, V. (1985). "Indexing problems in quasicrystal diffraction." Physical Review B **32**(8): 4892.

Elser, V. (1986). "The diffraction pattern of projected structures." Acta Crystallographica Section A: Foundations of Crystallography **42**(1): 36-43.

Fogagnolo, J., et al. (2003). "Effect of mechanical alloying on the morphology, microstructure and properties of aluminium matrix composite powders." Materials Science and Engineering: A **342**(1): 131-143.

FRITSCH (2017). "Available: http://www.fritsch-international.com/sample-preparation/milling/planetary-mills/details/product/pulverisette-6-classic-line/."

Galano, M., et al. (2004). "Structural characterisation and stability of new nanoquasicrystalline Al-based alloys." Materials Science and Engineering: A **375**: 1206-1211.

Galano, M., et al. (2009). "Nanoquasicrystalline Al–Fe–Cr-based alloys. Part II. Mechanical properties." Acta Materialia **57**(17): 5120-5130.

Galano, M., et al. (2009). "Nanoquasicrystalline Al–Fe–Cr-based alloys. Part I: Phase transformations." Acta Materialia **57**(17): 5107-5119.

Galano, M., et al. (2015). "Nanoquasicrystalline Al-based matrix/γ-Al_2O_3 nanocomposites." Journal of Alloys and Compounds **643**: S99-S106.

García-Escorial, A., et al. (2015). "Microstructural transformation of quasicrystalline AlFeCrTi extruded bars upon long thermal treatments." Journal of Alloys and Compounds **643**: S199-S203.

George, R., et al. (2005). "Strengthening in carbon nanotube/aluminium (CNT/Al) composites." Scripta Materialia **53**(10): 1159-1163.

Gheisari, K., et al. (2009). "The effect of milling speed on the structural properties of mechanically alloyed Fe–45% Ni powders." Journal of Alloys and Compounds **472**(1): 416-420.

Girot, F. A., et al. (1987). "Discontinuously-reinforced aluminum matrix composites." Composites science and technology **30**(3): 155-184.

Gu, W.-l. (2006). "Bulk Al/SiC nanocomposite prepared by ball milling and hot pressing method." Transactions of Nonferrous Metals Society of China **16**: s398-s401.

Hall, E. (1951). "The deformation and ageing of mild steel: III discussion of results." Proceedings of the Physical Society. Section B **64**(9): 747.

Hassan, S. and M. Gupta (2006). "Effect of particulate size of Al_2O_3 reinforcement on microstructure and mechanical behavior of solidification processed elemental Mg." Journal of Alloys and Compounds **419**(1): 84-90.

Hesabi, Z. R., et al. (2006). "Structural evolution during mechanical milling of nanometric and micrometric Al_2O_3 reinforced Al matrix composites." Materials Science and Engineering: A **428**(1): 159-168.

Hilliard, J. E. and J. W. Cahn (1959). An evaluation of procedures in quantitative metallography. I. Volume-Fraction Analysis, General Electric Co. Research Lab., Schenectady, NY.

Hong, S.-J., et al. (2003). "Effect of clustering on the mechanical properties of SiC particulate-reinforced aluminum alloy 2024 metal matrix composites." Materials Science and Engineering: A **347**(1): 198-204.

Hosseini, N., et al. (2010). "Tribological properties of Al6061–Al_2O_3 nanocomposite prepared by milling and hot pressing." Materials & Design **31**(10): 4777-4785.

Hull, D. and D. J. Bacon (1984). Introduction to dislocations, Pergamon Press Oxford.

Inframat Advanced Materials (2017). "http://www.advancedmaterials.us/26N-0801G.htm." **2017**.

Inoue, A. (1998). "Amorphous, nanoquasicrystalline and nanocrystalline alloys in Al-based systems." Progress in materials science **43**(5): 365-520.

Inoue, A. and H. Kimura (1999). "High elevated-temperature strength of Al-based nanoquasicrystalline alloys." Nanostructured Materials **11**(2): 221-231.

Inoue, A. and H. Kimura (2000). "High-strength aluminum alloys containing nanoquasicrystalline particles." Materials Science and Engineering: A **286**(1): 1-10.

Inoue, A. and H. Kimura (2001). "Fabrications and mechanical properties of bulk amorphous, nanocrystalline, nanoquasicrystalline alloys in aluminum-based system." Journal of light metals **1**(1): 31-41.

Inoue, A., et al. (2000). "High-strength aluminum-and zirconium-based alloys containing nanoquasicrystalline particles." Materials Science and Engineering: A **294**: 727-735.

Janowski, G. and B. Pletka (1990). "The influence of interfacial structure on the mechanical properties of liquid-phase-sintered aluminum-ceramic composites." Materials Science and Engineering: A **129**(1): 65-76.

Kainer, K. U. (2006). Metal matrix composites: custom-made materials for automotive and aerospace engineering, John Wiley & Sons.

Kamat, S., et al. (1989). "Mechanical properties of particulate-reinforced aluminum-matrix composites." Acta Metallurgica **37**(9): 2395-2402.

Kang, Y.-C. and S. L.-I. Chan (2004). "Tensile properties of nanometric Al_2O_3 particulate-reinforced aluminum matrix composites." Materials chemistry and physics **85**(2): 438-443.

Kelly, A. (1985). "Composites in context." Composites Science and Technology **23**(3): 171-199.

Khadem, S., et al. (2011). "Structural and morphological evaluation of Al–5vol.% SiC nanocomposite powder produced by mechanical milling." Journal of Alloys and Compounds **509**(5): 2221-2226.

Khakbiz, M. and F. Akhlaghi (2009). "Synthesis and structural characterization of Al–B_4C nano-composite powders by mechanical alloying." Journal of Alloys and Compounds **479**(1): 334-341.

Kimura, H., et al. (2000). "Formation, microstructure and mechanical properties of Al–Fe base quasicrystalline alloys." Materials Science and Engineering: A **294**: 168-172.

Kimura, H. M., et al. (2000). "Al–Fe-based bulk quasicrystalline alloys with high elevated temperature strength." Journal of Materials Research **15**(12): 2737-2744.

Knowles, A., et al. (2014). "Microstructure and mechanical properties of 6061 Al alloy based composites with SiC nanoparticles." Journal of Alloys and Compounds **615**: S401-S405.

Knowles, A., et al. (2014). "Microstructure and mechanical properties of 6061 Al alloy based composites with SiC nanoparticles." Journal of Alloys and Compounds.

Kollo, L., et al. (2011). "Nano-silicon carbide reinforced aluminium produced by high-energy milling and hot consolidation." Materials Science and Engineering: A **528**(21): 6606-6615.

Kramer, P. and R. Neri (1984). "On periodic and non-periodic space fillings of Em obtained by projection." Acta Crystallographica Section A: Foundations of Crystallography **40**(5): 580-587.

Lee, D., et al. (1997). "Fabrication, microstructures, and tensile properties of magnesium alloy AZ91/SiCp composites produced by powder metallurgy." Materials science and technology **13**(7): 590-595.

Lee, J., et al. (1994). "The interface in Al_2O_3 particulate-reinforced aluminium alloy composite and its role on the tensile properties." Journal of materials science **29**(8): 1983-1990.

Lee, W. and S. Kwun (1996). "The effects of process control agents on mechanical alloying mechanisms in the Ti-Al system." Journal of Alloys and Compounds **240**(1-2): 193-199.

Levine, D. and P. J. Steinhardt (1986). "Quasicrystals. I. Definition and structure." Physical Review B **34**(2): 596.

Li, Y., et al. (2009). "Investigation of aluminum-based nanocomposites with ultra-high strength." Materials Science and Engineering: A **527**(1): 305-316.

Lloyd, D. (1994). "Particle reinforced aluminium and magnesium matrix composites." International Materials Reviews **39**(1): 1-23.

Ma, K., et al. (2017). "Particulate reinforced aluminum alloy matrix composites–a review on the effect of microconstituents." Rev. Adv. Mater. Sci **48**: 91-104.

Magini, M., et al. (1993). "Analysis of energy transfer in the mechanical alloying process in the collision regime." Journal of Materials Synthesis and Processing(USA) **1**(3): 135-144.

Magini, M., et al. (1996). "Ball milling: an experimental support to the energy transfer evaluated by the collision model." Scripta Materialia **34**(1): 13-19.

Manaila, R., et al. (1989). "On the transition-metal quasisublattice in icosahedral Al-Cr-Fe phases." Philosophical Magazine B **60**(5): 589-599.

Mathewson, C. H. (1991). "Discussion." Transaction TMS-AIME **60**: 451-455.

Miracle, D. (2005). "Metal matrix composites – From science to technological significance." Composites Science and Technology **65**(15-16): 2526-2540.

Mishra, R. S., et al. (1996). "High‐Pressure Sintering of Nanocrystalline γ-Al_2O_3." Journal of the American Ceramic Society **79**(11): 2989-2992.

Mohammad Sharifi, E., et al. (2011). "Fabrication and evaluation of mechanical and tribological properties of boron carbide reinforced aluminum matrix nanocomposites." Materials & Design **32**(6): 3263-3271.

Nair, S., et al. (1985). "SiC-reinforced aluminium metal matrix composites." International Metals Reviews **30**(1): 275-290.

Nieh, T. and D. Chellman (1984). "Modulus measurements in discontinuous reinforced aluminum composites." Scripta Metallurgica **18**(9): 925-928.

Nieh, T. and J. Wadsworth (1991). "Hall-Petch relation in nanocrystalline solids." Scripta Metallurgica et Materialia **25**(4): 955-958.

Niikura, A., et al. (1994). "Amorphous and quasi-crystalline phases in rapidly solidified Mg-Al-Zn alloys." Materials Science and Engineering: A **181**: 1387-1391.

Ogino, Y., et al. (1991). "Influence of milling atmosphere on amorphization of chromium and Cr-Cu powders by ball milling." Journal of the Less Common Metals **168**(2): 221-235.

Orowan, E. (1948). "Discussion in The Symposium on Internal Stresses in Metals and Alloys, Inst." Metals, London **451**.

Penrose, R. (1979). "Pentaplexity a class of non-periodic tilings of the plane." The mathematical intelligencer **2**(1): 32-37.

Petch, N. (1953). "The cleavage strength of polycrystals." J. Iron Steel Inst. **174**: 25-28.

Poirier, D., et al. (2010). "Fabrication and properties of mechanically milled alumina/aluminum nanocomposites." Materials Science and Engineering: A **527**(29): 7605-7614.

Poirier, D., et al. (2010). "Fabrication and properties of mechanically milled alumina/aluminum nanocomposites." Materials Science & Engineering A **527**(29-30): 7605-7614.

Polmear, I. and M. Couper (1988). "Design and development of an experimental wrought aluminum alloy for use at elevated temperatures." Metallurgical and Materials Transactions A **19**(4): 1027-1035.

Prabhu, B., et al. (2006). "Synthesis and characterization of high volume fraction Al–Al_2O_3 nanocomposite powders by high-energy milling." Materials Science and Engineering: A **425**(1): 192-200.

Prima, F., et al. (2004). "In situ resistometric investigation of phase transformations in rapidly solidified Al-based alloys containing dispersed nanoscale particles." Materials Science and Engineering: A **375**: 772-775.

Pyzik, A. J. and D. R. Beaman (1995). "Al‐B‐C Phase Development and Effects on Mechanical Properties of B_4C/Al‐Derived Composites." Journal of the American Ceramic Society **78**(2): 305-312.

Rao, K., et al. (1986). "Melt-spun $Al_{84}V_{16}$: a new icosahedral crystal." EPL (Europhysics Letters) **1**(12): 647.

Ryu, H. J., et al. (1997). "Mechanical alloying process of 93W-5.6 Ni-1.4 Fe tungsten heavy alloy." Journal of Materials Processing Technology **63**(1): 292-297.

Saberi, Y., et al. (2009). "On the role of nano-size SiC on lattice strain and grain size of Al/SiC nanocomposite." Journal of Alloys and Compounds **484**(1): 637-640.

Shackelford, J. F., et al. (2016). CRC materials science and engineering handbook, CRC press.

Shechtman, D., et al. (1984). "Metallic phase with long-range orientational order and no translational symmetry." Physical review letters **53**(20): 1951.

Sheppard, T. (2013). Extrusion of aluminium alloys, Springer Science & Business Media.

Simmons, G. and H. Wang (1971). "Single crystal elastic constants and calculated aggregate properties."

Smithells, C. (1992). Smithells' Metals Reference Book, Butterworth-Heinemann Ltd, London.

Suryanarayana, C. (2001). "Mechanical alloying and milling." Progress in materials science **46**(1): 1-184.

Todd, I., et al. (2004). "The influence of processing variables on the structure and mechanical properties of nano-quasicrystalline reinforced aluminium alloys." Materials Science and Engineering: A **375**: 1235-1238.

Tongsri, R., et al. (2001). "Microstructures and their stability in rapidly solidified Al-Fe-(V, Si) alloy powders." Journal of materials science **36**(8): 1845-1856.

Totten, G. E. and D. S. MacKenzie (2003). Handbook of aluminum: Vol. 1: physical metallurgy and processes, CRC Press.

Tutcher, M. and T. Sheppard (2013). "Extrusion limits of Al-5Mg-0.8Mn alloy (AA 5456)." Metals Technology.

Vicens, J., et al. (2002). "New Al–AlN composites fabricated by squeeze casting: interfacial phenomena." Composites Part A: Applied Science and Manufacturing **33**(10): 1421-1423.

Vojtěch, D., et al. (2012). "Properties of the thermally stable $Al_{95}Cr_{3.1}Fe_{1.1}Ti_{0.8}$ alloy prepared by cold-compression at ultra-high pressure and by hot-extrusion." Materials Characterization **66**: 83-92.

Vojtěch, D., et al. (2007). "Properties of thermally stable PM Al–Cr based alloy." Materials Science and Engineering: A **458**(1): 371-380.

Whang, S.-H. (2011). Nanostructured metals and alloys: Processing, microstructure, mechanical properties and applications, Elsevier.

Yamasaki, M., et al. (2007). "Inhibition of Al grain coarsening by quasicrystalline icosahedral phase in the rapidly solidified powder metallurgy Al–Fe–Ti–Cr alloy." Scripta Materialia **56**(9): 785-788.

Yang, N., et al. (2001). "Simulation and quantitative assessment of homogeneous and inhomogeneous particle distributions in particulate metal matrix composites." Journal of microscopy **201**(2): 189-200.

Ye, J., et al. (2005). "A tri-modal aluminum based composite with super-high strength." Scripta materialia **53**(5): 481-486.

Ye, J., et al. (2006). "Cryomilling for the fabrication of a particulate B_4C reinforced Al nanocomposite: Part I. Effects of process conditions on structure." Metallurgical and Materials Transactions A **37**(10): 3099-3109.

Zebarjad, S. M. and S. A. Sajjadi (2007). "Dependency of physical and mechanical properties of mechanical alloyed $Al–Al_2O_3$ composite on milling time." Materials & Design **28**(7): 2113-2120.

Zhang, D. (2004). "Processing of advanced materials using high-energy mechanical milling." Progress in materials science **49**(3): 537-560.

Zhang, Z. and D. Chen (2006). "Consideration of Orowan strengthening effect in particulate-reinforced metal matrix nanocomposites: a model for predicting their yield strength." Scripta Materialia **54**(7): 1321-1326.

3. Experimental methods

This Chapter describes the experimental methods performed in order to process and study the nanoquasicrystalline alloys powders, the ball milled quasicrystalline alloy powders and nanocomposite powders, as well as the extruded nanocomposite bar. It outlines suitable extrusion procedures to consolidate the nanocomposite powders into bulk specimens and the microstructural investigation performed after extrusion.

Two batches of nanoquasicrystalline aluminium alloy powders and five batches of nanoquasicrystalline aluminium nanocomposite powders were ball milled with different milling time and speeds. Characterisation experiments focused on the powder size, morphology, alumina distribution, microstructure, thermal stability and the mechanical properties. The nanocomposite powders with suitable milling conditions were used for extrusion. The extruded bulk nanocomposite was characterised and mechanically tested.

3.1 Fabrication

3.1.1 Materials

Gas atomised nanoquasicrystalline $Al_{93}Fe_3Cr_2Ti_2$ powders were produced in collaboration with Alpoco Ltd. The powders had already been sieved into 0-50μm size range. A stack of Retsch stainless steel sieves with 25 μm gauge size, 200mm in diameter and 50mm in height were used to further sieve the atomised powder to 25-50μm range. The sieves were placed onto a Retsch A200 automatic sieve shaker, as shown in Figure 3.1. 30ml of the atomised powder was poured onto the 25μm gauge size sieve. The stacks were sealed with a lid. The sieves were then shaken for 14 minutes with an interval time of 20 seconds. Each fraction of the powder was collected and the sieves were cleaned using a dry stiff

brush. After that, the sieves were further cleaned with ethanol to remove the adhered powders before the next sieving being conducted. Sieved powders with 25-50 μm size range were checked by scanning electron microscopy (SEM). The operation procedure for SEM will be described in section 3.2.2. If smaller particles were caught in the larger size fractions, the powders would be re-sieved for another 14 minutes using the same conditions as described above. It has been confirmed that after two sieving runs the powders consist of almost only one size fraction from 25-50 μm.

γ-Al_2O_3 powders of 99.99% purity, particle size ranging from 20nm to 50nm and specific surface area > 150 m^2/g were used (Inframat Advanced Materials 2017).

Figure 3.1: Retsch A200 automatic sieve shaker and Retsch stainless steel sieves

3.1.2 Mixing

Nanoquasicrystalline $Al_{93}Fe_3Cr_2Ti_2$ alloy powders (25-50 μm) and nanosize γ-Al_2O_3 powders (20-50 nm) were selected to produce nanocomposite powders. For all batches of

nanocomposite powders, 87.1 vol.% $Al_{93}Fe_3Cr_2Ti_2$ and 12.9 vol.% γ-Al_2O_3 were loaded in glass jars and mixed in a Turbula type T2F automatic mixer, as shown in Figure 3.2. Glass jars with volume of 60ml and 250ml were used for powder mass 10g and 40g respectively. The jars need to have more than half empty space to ensure the movement of the powders during the mixing. The mixing time was 10min, with a rotation speed of 45 rotates per minute (rpm).

Figure 3.2: Turbula type T2F automatic mixer

3.1.3 Ball milling

A Fritsch Mono Mill Pulverisette 6 Classic was used, with stainless steel milling vessels of 250ml and 500ml in volume and stainless steel milling balls of 10mm in diameter. The milling vessel was loaded and unloaded in an argon filled glovebox. For all batches of powder, an initial ball to powder ratio (BPR) of 10:1 was used.

To assess the effects of varying the milling time on the nanocomposite powders, a 10g powder charge of mixed powder with a composition of 87.1 vol.% $Al_{93}Fe_3Cr_2Ti_2$ and 12.9

vol.% γ-Al_2O_3 was milled. The vessel had a capacity of 250ml and the milling speed was 250 rpm. Milling intervals of 1 hour with pauses of 20 minutes after each hour were applied to release the heat generated in the milling process. 0.5 gram of powders was taken out from the milling vessel every hour up to 5 hours. The rest of the powder was taken out after 10 hours of milling. The vessel was placed in the glovebox whilst the powder was removed to minimise contamination of the milling atmosphere. A second charge of 10g powder, also of the same composition was processed with powders being taken out every 5 hours from 5 to 30 hours of milling. Other milling conditions, namely the powder mass, the BPR and the milling speed remained the same with the first charge.

Taking a small amount of sample every period of time to be analysed slightly increases the BPR with the milling time, although such method is of common use in ball milling processing research (Ying and Zhang 2000, Hesabi, Simchi et al. 2006, Galano, Marsh et al. 2015). The first batch and the second batch nanocomposite powders both contained samples after 5 hours and 10 hours of milling, yet with different BPRs. These powders were analysed to judge whether the BPR changes had significant effects on the powder properties.

To assess the effects of the γ-Al_2O_3 reinforcement on the nanocomposite properties, other two batches of nanoquasicrystalline $Al_{93}Fe_3Cr_2Ti_2$ alloy powder (25-50 μm) with no reinforcement addition were milled. The conditions, namely the milling time, the milling speed, the vessel capacity, the powder mass and BPR remained the same as those used for milling the nanocomposites. The first batch was with 1 to 10 hours of milling, and the second batch was with 5 to 30 hours of milling.

The nanocomposites powders with 1-10 hours of milling were named with C250_I_*t*. The nanocomposites powders with 5-30 hours of milling were named with C250_II_*t*. Here C is the abbreviation of composites, 250 is the milling speed, I and II represent the batch number, and *t* is the milling time. Similarly, the milled nanoquasicrystalline alloy powders were named with A250_I/II_*t*, where A is the abbreviation of alloy.

To assess the effects of various milling speed on the nanocomposite powder, two batches of powder were produced at 150rpm and 200rpm. The powder composition was of 87.1 vol.% $Al_{93}Fe_3Cr_2Ti_2$ and 12.9 vol.% γ-Al_2O_3, equal to the nanocomposite batches produced at 250rpm. The vessel used had a capacity of 250ml. In total, 10g powder was milled, with 0.5g of powder being taken out every 5 hours from 5 to 30 hours of milling. For these powders, C*a*_*t* was used to represent the powder. C is the abbreviation of the composites, *a* is the milling speed and *t* is the milling time. After the powder being characterised, a new batch powder milled at 250rpm up to 5 hours of milling, while at 200rpm from 5 to 30 hours of milling was produced. This batch was labelled as C250/200 batch.

Nanocomposite powders were also milled using a larger vessel with a 500ml capacity. Three batches of powder were milled: (1) the first batch, at 250 rpm from up to 5 hours of milling and at 200 rpm from 5 till 10 hours of milling. The two samples obtained are named as CL_5 and CL_10 respectively. (2) the second batch, at 250rpm up to 4 hours of milling and at 200rpm from 4 to 8 hours of milling. This sample is named as CL_8. (3) the third batch, at 250rpm up to 4 hours of milling and at 200rpm from 4 to 9 hours of milling. This sample was named as CL_9. Here the letter CL means composites processed with large volume pot. These powders were compared with the C250/200_10 powder. The

reason for choosing the 500ml pot instead of the 250ml one is to process enough powders for extrusion with a relative shorter time. The abbreviations of all the powders are shown in Table 3.1.

After each batch of milling, nanoquasicrystalline powders and nanocomposite powders were adhered on the surfaces of the vessel and the balls. To clean them, 10-20g of sand and used stainless steel balls were loaded into the vessel and milled for 5 hours, with intervals of 10 minutes and pauses of 20 minutes. Subsequently, the vessel and the balls were cleaned with ethanol.

3.1.4 Extrusion

After analysing the microstructure and mechanical properties, the powders produced with 250rpm for up to 4 hours of milling and 200rpm from 4 to 9 hours of milling in a 500ml vessel were thought to be ideal for extrusion, considering the distribution of the γ-Al_2O_3, the crystallite size, the decomposition level of the quasicrystal, and the time taken to manufacture the composite powder.

The nanocomposite powders were placed into an Al can sealed with an Al lid at both ends. A hole was drilled in the front lid of the can to let the air out during the extrusion. The aluminium can has a diameter of 50mm, a wall thickness of 5mm, and a length of 102mm. The sealed powder can was put into a furnace, preheated to 430˚C for 20min, then further heated to 445˚C for 5min, and finally heated to 460˚C for 5min. The die was preheated to 300 °C and the container was preheated to 450˚C. The extrusion experiment was performed with an extrusion ratio of 10.33, by Dr A. Hameed and Prof. M. Galano at the Materials Department of Oxford, using the extruder shown in Figure 3.3. Extrusion ratio (A_o/A_f) can also affect the total extrusion pressure; a smaller extrusion ratio results in a

lower extrusion pressure (Todd, Chlup et al. 2004). In the present study, an average maximum extrusion pressure of 1026MPa was observed at a temperature of 450°C and an extrusion ratio of 10.33:1. The extrusion was conducted at a target speed of 1mm/s and an actual average extrusion speed of 0.81mm/s.

In the current work, the CL_9 powders are chosen for extrusion. The CL_9_HT is the CL_9 powders after heat treatment but before extrusion. The E_L and E_C are used to represent the longitudinal section and the cross section of the extruded bar, as shown in Table 3.1.

Milled powder	**Batch**	**Composition**	**Milling time**	**Milling speed**
A	/	Pure $Al_{93}Fe_3Cr_2Ti_2$ (at.%)	0 hours	/
A250_I_*t*	1st		*t* hours, *t* = 1, 2, 3, 4, 5, 10	250rpm
A250_II_*t*	2nd		*t* hours, *t* = 5, 10, 15, 20, 25, 30	250rpm
C250_I_*t*	1st	$Al_{93}Fe_3Cr_2Ti_2$ and 12.9 vol.% Al_2O_3 (at.%)	*t* hours, *t* = 1, 2, 3, 4, 5, 10	250rpm
C250_II_*t*	2nd		*t* hours, *t* = 5, 10, 15, 20, 25, 30	250rpm
C200_*t*	/	$Al_{93}Fe_3Cr_2Ti_2$ and 12.9 vol.% Al_2O_3 (at.%)	*t* hours, *t* = 5, 10, 15, 20, 25, 30	200rpm
C150_*t*	/			150rpm
C250/200_*t*	/			250/200rpm
CL_*t*[1]	/	$Al_{93}Fe_3Cr_2Ti_2$ and 12.9 vol.% Al_2O_3 (at.%)	*t* hours, *t* = 5, 8, 9, 10	250/200rpm
CL_9_HT			9 hours	250/200rpm
Extruded bar		**Composition**	**Description**	
E_L	/	$Al_{93}Fe_3Cr_2Ti_2$ and 12.9 vol.% Al_2O_3 (at.%)	The longitudinal section of the extruded bar	
E_C	/		The cross section of the extruded bar	

Table 3.1: Sample denominations

Note (1): The CL batch powder was processed with a 500ml vessel. All other batches were processed with a 250ml vessel.

Figure 3.3: Extrusion Press at Materials Department in Oxford

3.2 Particle size and morphology

3.2.1 Mastersizer measurement

A Malvern Mastersizer 2000 was used to measure the powder particle size distribution with a detection range of 0.02 – 2000 μm (Malvern 2007).

Powder samples of approximately 150mg were tested 3 times to minimise the error. During the interval of each test, a 15-second ultrasonic vibration was applied to prevent the powder agglomerations. The γ-Al_2O_3 particles, with size range from 20nm to 50nm, have strong trend to agglomerate (Rozita, Brydson et al. 2010). Therefore, although the particle size is within the detection range, measurements cannot be reliably conducted.

3.2.2 Scanning Electron Microscope (SEM)

Scanning Electron Microscope (SEM) analysis of the powders was performed using a W-filament JEOL 5510 with an Oxford instruments Energy Dispersive X-ray (EDX) detector and a W-filament Zeiss EVO.

The powders were adhered onto a double-sided carbon conductive sticker attached to a 12.5mm SEM Al pin stub. Micrographs of the powders have been taken using Secondary Electron Imaging (SEI) mode to get better topographic contrast. The working distance ranges from 8 to 12mm. The working voltage and the beam current were 15kV and 100pA respectively.

EDX was also performed on the same specimens, using an Oxford instrument EDX detector attached to the JEOL 5510 SEM. The data were analysed using the Aztec software. The acceleration voltage was set to 10kV to reduce the interaction volume of the X-ray and the specimen to get more accurate results. Moreover, the working distance had to be about 20mm in order to optimise the signal received by the EDX detector.

3.2.3 Focused ion beam (FIB)

The Focused ion beam (FIB) powder samples were prepared by mounting powders in resin with conductive carbon filter using a Kemet Metapress-A mounting press, grinding it up to 4000 grit SiC paper and polishing it with a 40 nm colloidal silica solution.

A FEI FIB200 FIB was used for imaging to verify the γ-Al_2O_3 distribution level in the nanocomposites. A square well pattern at 2×10^4 pA probe current was used to mill away the surface oxide layer. The oxide layer has a thickness ranging from 400nm to 1000nm.

An imaging beam current of 100pA for 0° tilt offered the best compromise between the phase contrast, resolution and the surface degradation rate. 8000x magnification was found to give the best representation of the reinforcement distribution on a single powder particle. 15000x magnification was used to identify the γ-Al_2O_3 cluster sizes in the powder when the distribution is relative homogeneous.

3.2.4 Scanning transmission electron microscope (STEM)

Scanning transmission electron microscope (STEM) analysis was performed on a JEOL 2100 transmission electron microscope (TEM) with a LaB_6 filament, a 200kV acceleration voltage and an Oxford instruments EDX detector. In order to obtain accurate values from EDX analysis a double tile Beryllium holder was used. The EDX data were processed with the Aztec software.

The powder samples used for SEM and FIB imaging were also used for liftout sample preparation, using a Focused Ion Beam microscope (FEI FIB200 FIB). FIB was used to dig trenches and lift the specimens with 500~1000nm thickness, using an inside micromanipulator onto a Cu half grid. The specimen was then further thinned with very low beam current (100pA) to minimise the Ga contamination. The final thickness of the specimens was measured to be 80-130nm in FIB.

STEM dark field (DF) images were obtained. All the STEM images were taken by collecting the high angle scattering electrons on high annular detector. In ADF mode in STEM, the heavier the atom, the higher the intensity of the scattering, which leads to the atomic number (Z) contrast (Nellist and Pennycook 2000). The contrast of STEM DF image scales as the atomic number $Z^{1.7}$ (Voyles, Grazul et al. 2003). The γ-Al_2O_3 particles,

which contain 60 at.% of oxygen element, are suspected to have the darkest contrast. The second smallest spot size was applied for imaging. EDX was performed in the STEM mode, using an Oxford instrument EDX detector attached to the JEOL 2100 TEM, with the Aztec software. The samples were tilted in x direction for about 10° to face to the EDX detector for obtaining better X-ray counts. EDX analysis was conducted both on interest areas of the sample (mapping analysis) or on interest points of the sample (point analysis). The interest feature needs to be about 130nm or less in thickness, therefore errors were minimised by selecting larger particles for EDX analysis.

3.3 Microstructure analysis

3.3.1 X-ray Diffractograms analysis

For the powder samples, X-ray diffractograms were obtained with a Bruker D5000 θ–2θ diffractometer with a wavelength of Cu Kα 0.15418 nm at 40 kV and 40 mA. The scanning conditions of 2θ range were 20–100° with a step size of 0.02° and a scan rate of 0.003°/s. A combination of data sheets from PCPDFWIN (as shown in Appendix 1) and published papers (Swanson, Tatge et al. 1953, Galano, Audebert et al. 2009) were used for the peak indexation.

For the extruded bulk sample, X-ray diffractograms were obtained with a Rigaku θ–2θ diffractometer. The wavelength of Cu Kα radiation was 0.15418 nm at 40 kV and 15 mA, and the scanning condition of 2θ range was 10–100° with a step size of 0.02° and a scan rate of 0.05°/s.

The longitudinal section specimen was cut along the extrusion direction and the cross-section specimen was cut in the direction perpendicular to the extruded direction. This was

done to provide assessment of not only the phases, but also the texture. Both specimens were ground using 2500-grit and 4000-grit SiC papers.

Williamson-Hall analysis is a semi-quantitative measurements of crystallite size and strain by examining the broadening of the phase's XRD peaks relative to a reference specimen (Williamson and Hall 1953). The full-width half maximum (FWHM) values for peaks of a specific phase are measured in the sample of interest, as well as the reference sample which has a crystallite size larger than 500nm without internal strain. The Warren formula is used to estimate the contribution of size and strain effects to the FWHM of each peak (Suryanarayana and Norton 2013):

$$\boldsymbol{B = [B_M^2 - B_s^2]^{1/2}} \quad \text{----------} \quad \text{Equation 1}$$

where B is the broadening in full-width half maximum (FWHM) of a sample's peak due to the size and strain effects (in the unit of radians), B_M is FWHM of a peak in a sample, B_S is FWHM of a peak in a reference sample (instrumental broadening).

The values of $B\cos\theta$ and $\sin\theta$ in relation to each peak of the phase were calculated through Williamson-Hall plot (Williamson and Hall 1953, Suryanarayana and Norton 2013). Equation 2 is used to obtain average crystallite size and strain from the y-intercept and gradient of the linear best fit line respectively:

$$\boldsymbol{B\cos\theta = \frac{k\lambda}{d} + \eta\sin\theta} \quad \text{----------} \quad \text{Equation 2}$$

Where θ is the position of a peak, k is a constant, usually equals 1, λ is the wavelength of the X-ray, d is the average crystallite size and η is the strain. Equation 2 is used to obtain average crystallite size and strain from the y-intercept and gradient of the linear best fit

line respectively. A reference sample of high purity Al powder was used, annealed at 530°C for 1 h in a tube with 99.998% purity argon gas pumped through at 70 cc/min to remove any residual strains. The theoretical upper size limit of validity for this technique is around 500nm (Suryanarayana and Norton 1998), in practice it is appropriate for crystallite sizes of 10-100nm (Suryanarayana 2001, Galano, Marsh et al. 2015).

3.3.2 Transmission electron microscope (TEM)

To understand the effects of ball milling, the $Al_{93}Fe_3Cr_2Ti_2$ quasicrystalline alloy powders without milling and the mechanically milled powders were characterised using a JEOL 2100 with a LaB_6 filament TEM with an Oxford instrument EDX detector, a JEOL 3000F with a field emission gun and an JEM-ARM 200F high resolution transmission electron microscope (HRTEM).

The TEM samples were prepared using the same procedures as preparing STEM samples described in section 3.2.4 in this Chapter. For HRTEM, these liftout samples were further thinned to a 40-50nm thickness using a Zeiss NVision FIB.

For the JEOL 2100 TEM analysis, the initial objective was to identify the microstructure with bright field imaging, the crystal orientations with the diffraction patterns, and the atom composition with EDX. For EDX analysis, when ignoring the absorption and fluorescence, the atom percentages were obtained with the following equation (Williams, Carter et al. 1998):

$$\boldsymbol{C_A/C_B = k_{AB} I_A/I_B} \quad \text{----------} \quad \text{Equation 3}$$

Where C_A is the weight percents of element *A*, C_B is the weight percents of element *B*, k_{AB} is a sensitive factor (not a constant) which varies according to the TEM system and

the acceleration voltage, I_A is the measured intensity of element *A*, and I_B is the measured intensity of element *B.* This equation is for a binary system, but can be extended to higher order systems (Williams, Carter et al. 1998). The sensitive factor could be measured from samples with known standard composition. For EDX point analysis, at least 10^4 counts above backgrounds were obtained to control the total error in weight percentage within ±5% (Williams, Carter et al. 1998).

Very often the particles present in the microstructure were too small to use the smallest selected area aperture to get the diffraction patterns from a single phase. Therefore, convergent beam diffraction patterns (CBDPs) had to be taken using the second or third smallest spot sizes, which, when converged, allow diffraction patterns to be taken from microstructure features as small as ~30nm.

For the mechanical milled powders, the crystallite sizes can be even smaller (<30nm). In this situation, ring selected area diffraction patterns (SADPs) were obtained using the selected area aperture and were indexed.

Dark field (DF) images were also taken in the JEOL 2100 TEM to obtain the size of the ultrafine crystallites. In the DF mode, the aluminium crystallites corresponding to the selected spots were observed with a much better inversed contrast.

A JEOL 3000F TEM, with low spherical aberration (C_s), a field emission gun and a smaller wavelength of electron beams due to higher acceleration voltage 300kV, is able to obtain HRTEM images. Only nanoquasicrystalline $Al_{93}Fe_3Cr_2Ti_2$ powders before milling were characterised. Different from bright field (BF) imaging, samples have to be adjusted along to a zone axis, so that the atoms overlap in column, and sharp high-resolution images

could be obtained (Williams, Carter et al. 1998). In order to obtain images from the low index zone axes, a double tilt holder was used.

A JEM-ARM 200F with a cold field emission gun and an acceleration voltage 200kV was used to obtain dark field atom resolution images in STEM ADF mode to investigate the atom structure of the icosahedral quasicrystalline particles. The same as the JEOL 3000F, a double tilt holder was used for imaging in the low index zone axis. The camera length is 10cm, and the ADF angle ranges from 61.7-242.8 mrad. The Dwell-time is 6 microseconds. The imaging was conducted by Dr L. Jones at the Materials Department of Oxford university. Thirty series frames were taken to reduce the noises, the sample drifts and the scan distortion following a previous method developed by their group (Jones, Yang et al. 2015).

3.4 Thermal analysis

3.4.1 Differential scanning calorimetry (DSC) analysis

Atomised powders, ball milled powders and ground powders from the extruded bar were analysed using a TA Instruments 2010 3.4.1 differential scanning calorimetry (DSC). The machine was calibrated using the melting points of pure Indium, Zinc and Aluminium which are 156.63°C, 419.58°C and 660.45°C respectively (Lide 1993).

The powders and ground bars were placed in the Cu pans. To prevent reactions between the aluminium alloy samples and the copper DSC pans molybdenum sheets were used. Circular sections of a molybdenum sheet were stamped out. One piece was placed into bottom of the DSC pan. A sample of approximately 10mg was put onto the molybdenum disk and a second molybdenum disk was loaded on top. The copper pan was then sealed

by crimping with a hand press. A similar reference pan was also made, with two sections of molybdenum but without powder sample inside.

Samples were heated from 70℃ at different heating rates of 10℃/min, 20℃/min, 40℃/min and 80℃/min until an isothermal hold for 0.5 minute at 610℃. For each sample, after the first heated run finished, a second reheated run was conducted as reference. All tests were performed in an inert argon atmosphere. The curves obtained were then processed by subtracting the second run from the first one. The goal is to remove common fluctuations in energy across the temperature range of scan that are a product of the machine rather than the changes within the powder. Examples of heating and reheating scans of ball milled pure $Al_{93}Fe_3Cr_2Ti_2$ powders with 30 hours of milling at 250 rpm are shown in Figure 3.4.

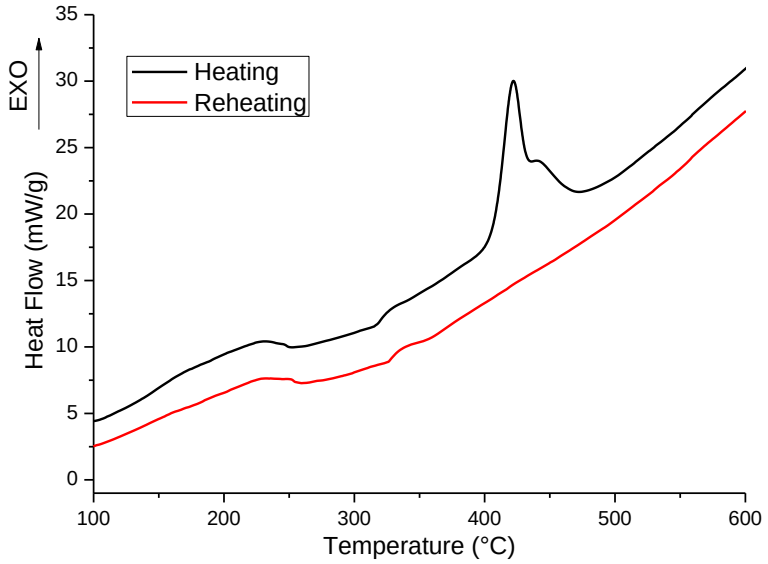

Figure 3.4: DSC curves obtained from heating and reheating of the 25-50 µm fraction of ball milled pure $Al_{93}Fe_3Cr_2Ti_2$ powder after 30 hours of milling at 250 rpm

A Kissinger (Kissinger 1956) plot was used to calculate the activation energy of a peak's transformation, using the DSC curves at heating rate of 10℃/min, 20℃/min, 40℃/min and 80℃/min. The equation for the best linear fit line is stated in Equation 4.

$$\ln\left(\frac{b}{T_p^2}\right) = \left(\frac{E_A}{R}\right)\left(\frac{1000}{T_p}\right) + C \quad \text{---------} \quad \text{Equation 4}$$

where b is the heating rate (℃/min), T_p is the peak temperature of the transformation peak (K), E_A is the activation energy (kJ/mol), R is the gas constant (8.314 J/(mol·K)) and C is the intercept on y axis. Plotting $\ln\left(\frac{b}{T_p^2}\right)$ against $\frac{1000}{T_p}$ allows the activation energy to be extracted from the gradient of the linear best fit line, $\frac{E_A}{R}$. As shown in Figure 3.4, sometimes two peaks overlap with each other. In such situations, Gaussian fits were applied to separate them (Milkereit, Kessler et al. 2009). One example for estimating the activation energy for the right peak of C250_II_10 was shown in Figure 3.5. The absolute value of the slope is the activation energy with the unit of kJ/mol.

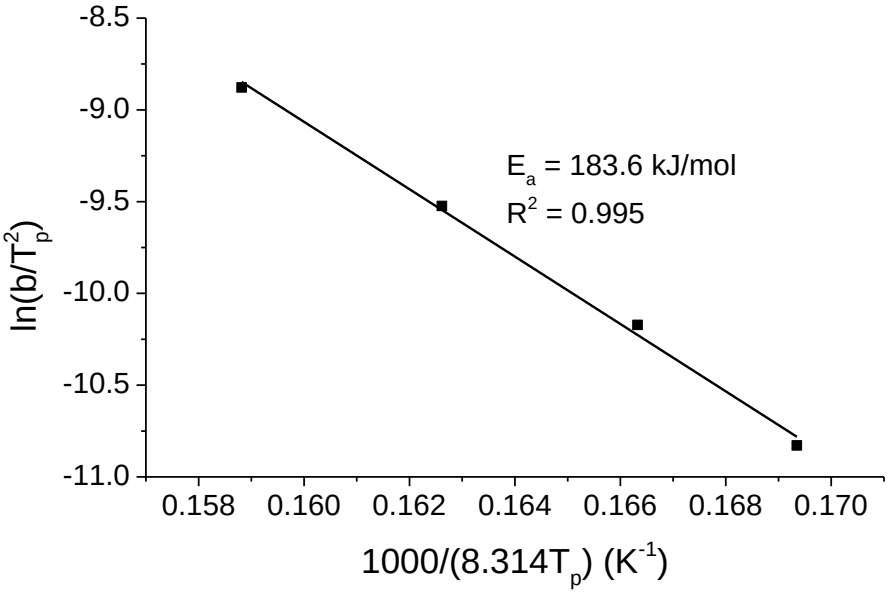

Figure 3.5: Activation energy plot for the four right exothermic peaks observed in C250_II_10 at heating rate from 10K/min to 80K/min. b is the heating rate, T_p is the peak temperature, and R is the correlation coefficient of the least squares method. E_a is the measured activation energy.

3.4.2 Heat treatment and STEM analysis

Nanoquasicrystalline $Al_{93}Fe_3Cr_2Ti_2$ alloy powders with 10 hours of milling at 250rpm (A250_I_10) had two overlapped peaks in the DSC curves. This sample was heat treated in the DSC at 40℃/min up to 405℃ (~5 °C lower than the first peak). After heating the sample was cooled down in the air without holding time. As shown in Figure 3.6, for this sample only the exothermal event relative to the peak at lower temperature (peak 1) was involved. This sample is named as A250_I_10_405. The A250_I_10 was also heated up to 410℃ (~ 12 ˚C higher than the first peak) at a heating rate of 20℃/min. A 3min isothermal time at 410˚C was applied subsequently to confirm the transformation for peak 1 had been fully finished, as shown in Figure 3.6. This sample is named as A250_I_10_410. The A250_I_10 powder was heat treated in DSC from room temperature

to 550 °C (over the end of the second exothermic peak) at 20℃/min, and a 3-min heat treatment was applied to ensure all the exothermal events have been finished. XRD, TEM, STEM and EDX analysis were conducted on these three samples.

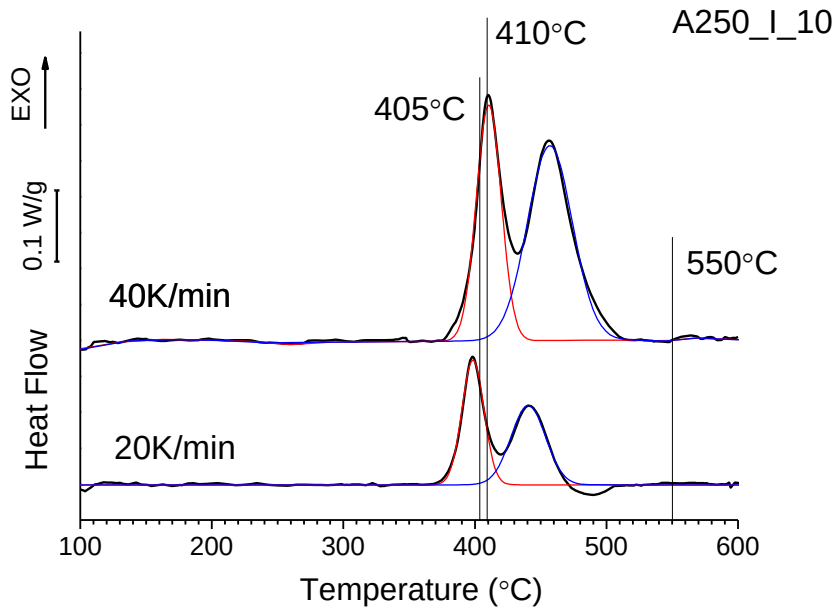

Figure 3.6: DSC runs of A250_I_10 with isothermal temperature labelled

3.5 Bulk specimens

3.5.1 Density

Three samples from the extruded bar were cut off. The surface of the bar is pure aluminium from the can, which has been grinded away. Archimedes method is applied to measure the density of the extruded bar (Spierings, Schneider et al. 2011), which is explained in Figure 3.7. First, the weight of the sample was measured in the air, as shown in Figure 3.7(a). Afterwards, the weight of the sample was measured in the water, as shown in Figure 3.7(b).

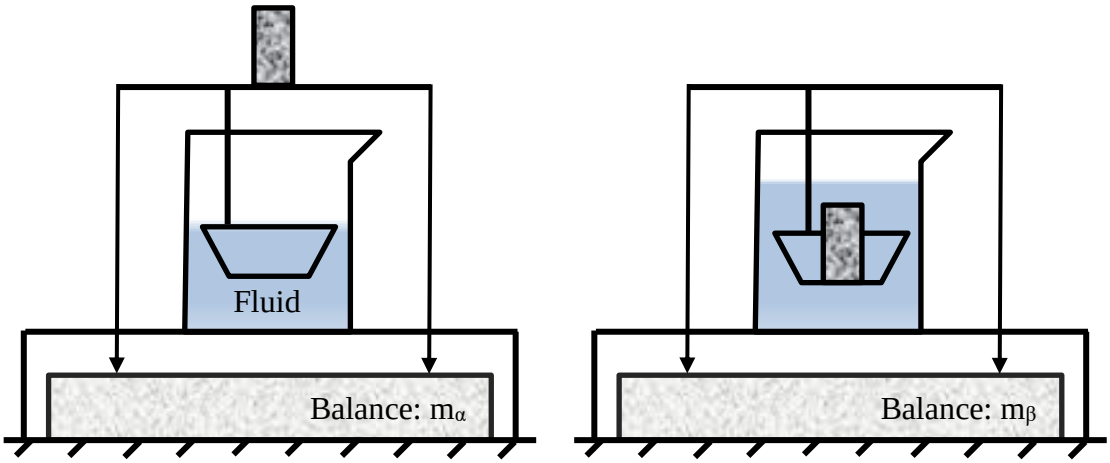

Figure 3.7: Archimedes density measurements **(a)** measurement in the air, **(b)** measurement in the fluid

The equation for measuring the density of the material is (Spierings, Schneider et al. 2011):

$$\boldsymbol{\rho_m = \frac{m_\alpha}{m_\alpha - m_\beta}\rho_f} \quad \text{----------} \quad \text{Equation 5}$$

Where ρ_m is the density of the material, ρ_f is the density of the fluid, m_α is the weight in the air, and m_β is the weight in the fluid. Here ρ_f equals to 0.9982 g/cm^3 (the water density at room temperature). Three samples were measured to minimise the error.

3.5.2 Hardness

For the powder, samples for Vickers hardness tests were prepared by mounting powders in non-conductive bakelite using a Kemet Metapress-A mounting press, grinding it up to 4000 grit SiC paper and polishing it with a 40nm colloidal silica solution. For the extruded

bar, a piece of the bar from the cross section was cut, ground and polished following the same procedures for the mounted powder sample.

Vickers hardness (HV) was measured using a Wolpert hardness microindenter with a 10-gram force load and 15s of dwelling time. Powder samples were mounted in conductive Bakelite and polished until obtaining a metallographic quality surface. Vickers hardness was measured following the recommendations in the ASTM E384-16 standard (Joseph, Penelope et al. 1979). Only powder particles with large circular surface in the mounted samples were measured with only one microindentation per powder particle. This allows meeting the recommended conditions of minimum thickness and the minimum distance from the centre of the indentation to the particle surface as 1.5 and 2.5 times of the indentation's diagonal, respectively. Bulk cylinder shape sample with 12.5mm in diameter and 1mm in height was cut from the extruded bar. This sample was also grinded with 4000 grit SiC paper and polished with 40nm colloidal silica solution.

The Vickers hardness was calculated using the average value of the two diagonals of each microindentation and applying the corresponding formula for HV (ASTM Standard 2000), as in Equation 6:

$$\mathbf{H = 1854.4\ \frac{P}{d^2}} \qquad \text{----------} \qquad \text{Equation 6}$$

Where, H is the hardness value, P is the load in gf and *d* is the average diagonal length value in μm. For each milled powder sample, 20 symmetric indentations were measured to ensure the accuracy of the Vickers hardness values.

3.5.3 Compression tests

Compression test specimens were prepared by Peter Flaxman at the University of Oxford. The cracks on the surfaces of the extruded bar were cut off with a steel saw. Next the samples were loaded and thinned down to cylinder shape with 5mm in diameter using a lathe turning. The ends were then cut off to make the cylinder 10mm in length. These ends were further ground slightly by hand with 4000 grit silicon carbide paper to ensure that the faces were parallel and smooth, preventing deformation leading to shear during the compression testing.

Tests were conducted in an Instron 5582 testing frame, with a 100kN load cell and hardened steel platens by I. Dyson at the Engineering Department at the University of Oxford. Strain was calculated from the crosshead displacement. This involves calibrating the rig at both room temperature and 250°C to see how much displacement was recorded at loads up to 25kN (more than the maximum load on the samples) when no sample was loaded, and using the data together with the crosshead displacement and the length of the sample to calculate the strain. The stress-strain curve without sample loaded was shown in Figure 3.8. Instron Bluehill 3 software was used to input a compression method. The tests were run at an initial strain rate of $1 \times 10^3\ s^{-1}$. The samples were placed in the rig between the platens. For room temperature tests, Vaseline was used for lubricating the samples to prevent the barrelling. The samples were pre-loaded with a load of 0.1kN to hold the sample in place and the strain zeroed. Tests were performed until the machine reached the limitation or until the sample fractured. The load-extension data were exported in the CSV format, and were manipulated with the OriginPro software to get the desired mechanical properties.

Compression tests were also performed at elevated temperatures, 250℃ in an Instron 3119 furnace. This furnace was placed around the compression rig. The sample was loaded before heating. A thermal stable anti-seize compounds named Rocol was used for lubrication. A thermocouple was placed against the platen, near the compression sample. As the sample was heated, the temperature increased to 250℃, and each sample was held for 15 minutes. The temperature stayed within 1℃ fluctuation range during the tests. For both tests at room and elevated temperatures, the results of the compression tests were produced from the crosshead displacement and force recorded from the load cell.

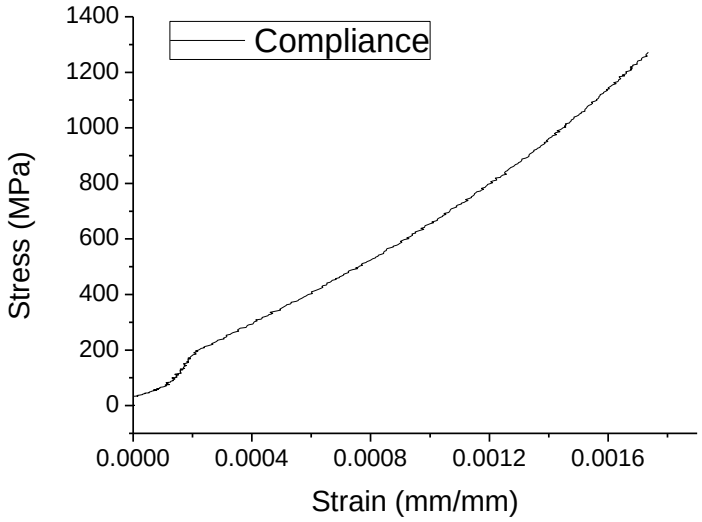

Figure 3.8: Stress-strain curve with no sample loaded at room temperature

3.6 Reference

ASTM Standard (2000). "E384, Standard test method for microindentation hardness of materials." West Conshohocken, PA: ASTM International.

Galano, M., et al. (2009). "Nanoquasicrystalline Al–Fe–Cr-based alloys. Part I: Phase transformations." Acta Materialia **57**(17): 5107-5119.

Galano, M., et al. (2015). "Nanoquasicrystalline Al-based matrix/γ-Al_2O_3 nanocomposites." Journal of Alloys and Compounds **643**: S99-S106.

Hesabi, Z. R., et al. (2006). "Structural evolution during mechanical milling of nanometric and micrometric Al_2O_3 reinforced Al matrix composites." Materials Science and Engineering: A **428**(1): 159-168.

Inframat Advanced Materials (2017). "http://www.advancedmaterials.us/26N-0801G.htm." **2017**.

Jones, L., et al. (2015). "Smart Align—a new tool for robust non-rigid registration of scanning microscope data." Advanced Structural and Chemical Imaging **1**(1): 8.

Joseph, R., et al. (1979). Metals handbook: Properties and selection, ASM International, Materials Park, OH.

Kissinger, H. E. (1956). "Variation of peak temperature with heating rate in differential thermal analysis." Journal of research of the National Bureau of Standards **57**(4): 217-221.

Lide, D. R. (1993). CRC Handbook of Chemistry and Physics: A Ready-reference Book of Chemical and Physical Data: 1993-1994, CRC press.

Malvern (2007). "http://www.malvern.com/en/support/resource-center/user-manuals/MAN0384EN.aspx."

Milkereit, B., et al. (2009). "Recording of continuous cooling precipitation diagrams of aluminium alloys." Thermochimica acta **492**(1): 73-78.

Nellist, P. and S. Pennycook (2000). "The principles and interpretation of annular dark-field Z-contrast imaging." Advances in imaging and electron physics **113**: 147-203.

Rozita, Y., et al. (2010). An investigation of commercial gamma-Al_2O_3 nanoparticles. Journal of Physics: Conference Series, IOP Publishing.

Spierings, A., et al. (2011). "Comparison of density measurement techniques for additive manufactured metallic parts." Rapid Prototyping Journal **17**(5): 380-386.

Suryanarayana, C. (2001). "Mechanical alloying and milling." Progress in materials science **46**(1): 1-184.

Suryanarayana, C. and M. G. Norton (1998). "X-ray diffraction: a practical approach." Microsc Microanal **4**: 513-515.

Suryanarayana, C. and M. G. Norton (2013). X-ray diffraction: a practical approach, Springer Science & Business Media.

Swanson, H. E., et al. (1953). "Standard X-ray diffraction powder patterns."

Todd, I., et al. (2004). "The influence of processing variables on the structure and mechanical properties of nano-quasicrystalline reinforced aluminium alloys." Materials Science and Engineering: A **375**: 1235-1238.

Voyles, P., et al. (2003). "Imaging individual atoms inside crystals with ADF-STEM." Ultramicroscopy **96**(3): 251-273.

Williams, D. B., et al. (1998). "Transmission electron microscopy: a textbook for materials science." MRS Bulletin-Materials Research Society **23**(5): 47.

Williamson, G. and W. Hall (1953). "X-ray line broadening from filed aluminium and wolfram." Acta Metallurgica **1**(1): 22-31.

Ying, D. and D. Zhang (2000). "Processing of $Cu–Al_2O_3$ metal matrix nanocomposite materials by using high energy ball milling." Materials Science and Engineering: A **286**(1): 152-156.

4. Characterisation of ball milled nanoquasicrystalline alloy and nanocomposite

In this chapter, nanoquasicrystalline $Al_{93}Fe_3Cr_2Ti_2$ alloy before ball milling was characterised. An orientation relationship between the icosahedral quasicrystal, the Al_3Ti intermetallic particles and the Al grains was found and explained. Two batches of $Al_{93}Fe_3Cr_2Ti_2/Al_2O_3$ (at.%) quasicrystalline nanocomposites and another two batches of pure $Al_{93}Fe_3Cr_2Ti_2$ (at.%) powders were fabricated with the procedures described in Chapter 3. For all the ball milled samples, (C250/A250)_(I/II)_(*t*) is used as abbreviations according to the processing conditions. The letters C and A represent the milled nanocomposite powders and the milled pure alloy powders; 250 is the milling speed with the unit of rotates per minute (rpm); I and II are the batch number, where (I) corresponds to the 1st batch with 1-10 hours of milling and (II) corresponds to the 2nd batch with 5-30 hours of milling respectively; *t* is the milling time. The codes for all the mechanical milled samples are shown in Table 5.1.

The particle size and the morphology of the milled powders with different milling time were studied through Mastersizer and scanning electron microscope (SEM). The phases were examined by X-ray diffractograms. The microstructure and the γ-Al_2O_3 distribution were characterized through transmission electron microscope (TEM), scanning transmission electron microscope (STEM) imaging and energy dispersive X-ray (EDX) mapping. The thermal stability was investigated by differential scanning calorimetry (DSC). The microhardness of the powders was tested with Wolpert microhardness indenter.

Milled powder	Batch	Composition	Milling time
A	/	Pure $Al_{93}Fe_3Cr_2Ti_2$ (at.%)	0 hours
A250_I_*t*	1st		*t* hours, *t* = 1, 2, 3, 4, 5, 10
A250_II_*t*	2nd		*t* hours, *t* = 5, 10, 15, 20, 25, 30
C250_I_*t*	1st	$Al_{93}Fe_3Cr_2Ti_2$ and 12.9 vol.% Al_2O_3 (at.%)	*t* hours, *t* = 1, 2, 3, 4, 5, 10
C250_II_*t*	2nd		*t* hours, *t* = 5, 10, 15, 20, 25, 30

Table 4.1: Codes for mechanical milled powder corresponding to different batches

4.1 Microstructure and phase components of the unmilled matrix powder

4.1.1 Phase components

The properties of the $Al_{93}Fe_3Cr_2Ti_2/Al_2O_3$ (at.%) without milling are investigated. An X-ray diffractogram of the pre-mixed powder is shown in Figure 4.1. The α-Al phase is observed with peak position at 2θ of 38.5°, 44.7°, 65.1°, 78.3° and 82.5°. The quasicrystalline phase, labelled with Cahn's notation (Cahn, Shechtman et al. 1986) as explained in section 2.2.3 in Chapter 2, is also detected at 2θ of 22.70°, 41.1°, 43.3°, 61.8° and 73.3°. For the γ-Al_2O_3, only the γ(440) peak is detected, probably due to the low volume fraction. The Al_3Ti phase is detected at 39.3°.

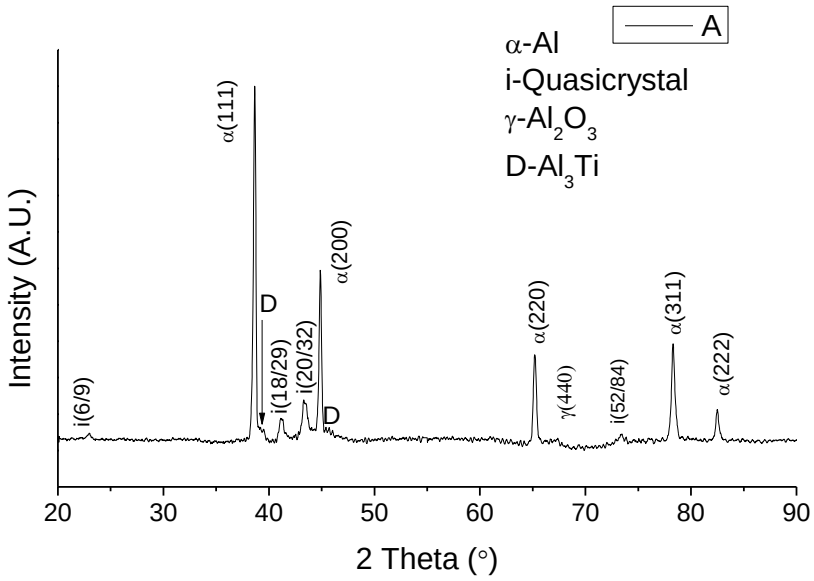

Figure 4.1: The X-ray diffractogram of the unmilled (A) powder

4.1.2 Microstructure

The microstructure of the $Al_{93}Fe_3Cr_2Ti_2$ matrix powder is shown in Figure 4.2. In general, the grain size of the A powder before milling is about 1.5μm. The equiaxed grains in the TEM bright field (BF) image, for example, grain (1) in Figure 4.2(a), should be α-Al. The grey particles, such as particle (2) locating on the grain boundary and particle (3) inside the aluminium grains should be the quasicrystals. An Al_3Ti intermetallic identified by a convergent beam diffraction patterns (CBDP) was found, as shown in area (4) in Figure 4.2(b). This phase should correspond to the Al_3Ti peak detected in the X-ray diffractograms at 39.3° (Figure 4.1). The quasicrystals tend to form clusters around the Al_3Ti phase. In Figure 4.2(c), the particles labelled with (5), (6), (7), and (8) are identified to be quasicrystals by the CBDPs from fivefold, twofold and mirror plane zone axes. These quasicrystals follow an orientation relationship with the Al_3Ti phase in the centre, which will be further investigated in section 4.1.3, 4.1.4 and 4.1.5 in this Chapter. The long band

shape phases on the grain boundaries of the Al grains, for instance, area (9) in Figure 4.2(c), are thought to be intermetallics. In Figure 4.2(d) an image with larger magnification of the grain boundary intermetallics is shown. Figure 4.2(e) shows the corresponding CBDPs of this phase. Figure 4.2(f) is a zoom in image of the right bottom diffraction pattern in Figure 4.2 (e). In literature, the diffraction pattern of the α(AlFeSi) from [110] zone axis is similar to the one in Figure 4.2(f) (Audier and Guyot 1986), which indicates they may have similar structures. However, it is unable to get CBDPs from most of these grain boundary intermetallics due to their small sizes. Therefore, it is unknown whether all these phases have the same crystallography.

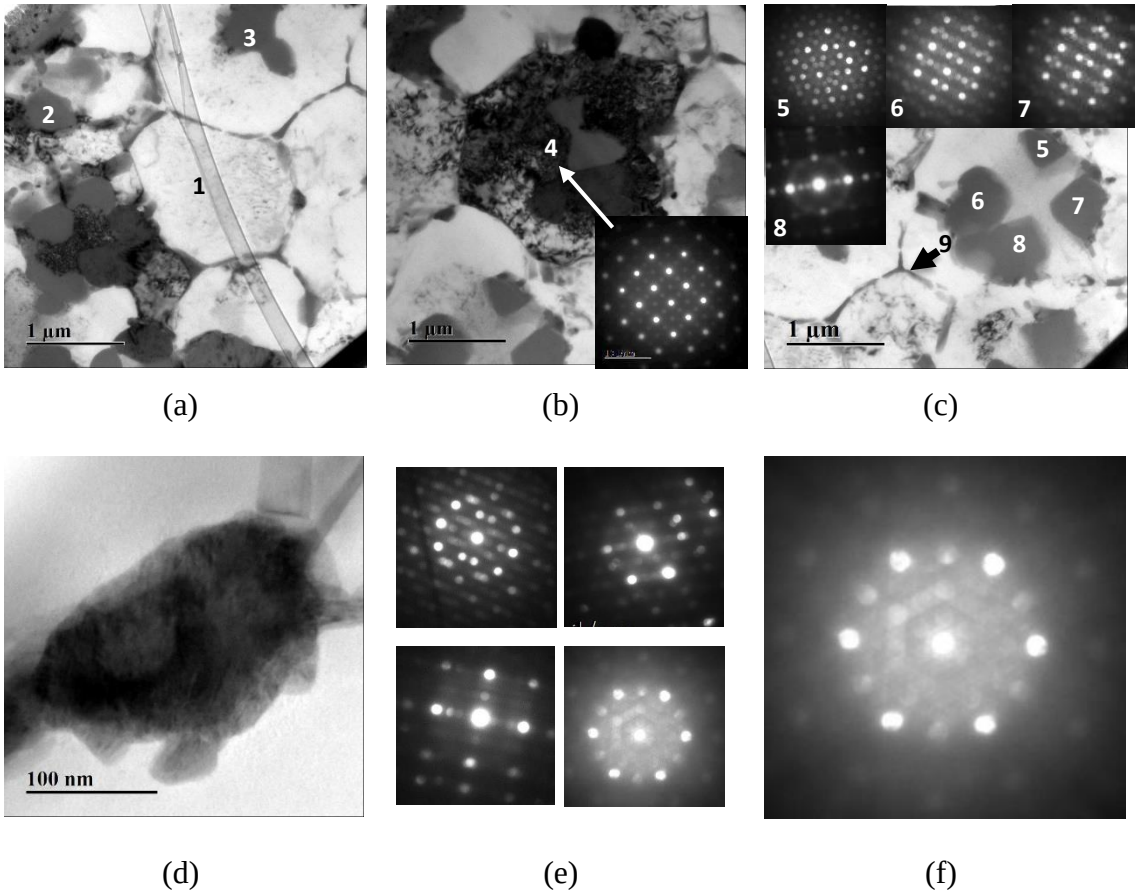

(a) (b) (c)

(d) (e) (f)

Figure 4.2: The microstructure of $Al_{93}Fe_3Cr_2Ti_2$ matrix powder **(a)** TEM BF image, **(b)** TEM BF image of Al_3Ti phase with a CBDP, **(c)** TEM BF images of four quasicrystals with corresponding CBDPs, **(d)** a zoom in image of intermetallics in position (9), **(e)** CBDPs from the grain boundary particle, **(f)** A zoom in of CBDP in (e)

The STEM dark field (DF) image was taken by collecting the high angle scattering with a high annular detector, as shown in Figure 4.3. The image in Figure 4.3(a) is from the same region in Figure 4.2(b). Before milling, four phases were observed by STEM analysis, namely the Al phase, the icosahedral phase, the Al_3Ti phase and an unidentified Al-Fe phase. The Al grain labelled as (1) contains 99.36 at.% percent of aluminium and very little amount of transition metal atoms. The quasicrystal labelled as (2) contains about 5.31 at.% of Fe, 5.48 at.% of Cr while only 2.37 at.% of Ti. The area 3, which has been confirmed by CBDP in Figure 4.2(b), should be the Al_3Ti intermetallic with theoretically

25 at.% Ti. However, the measured atom percentage of Ti element is only 3.26%, as shown in Figure 4.3(g). This is probably because the Al_3Ti phase was in the Al grains, and EDX tested the component of both the Al_3Ti phase and the Al grain. The phases surrounding the Al grain in position (4) is rich in Fe (Figure 4.3(c)), and should be Al-Fe intermetallics, identified using EDX spectrum 4 in Figure 4.3(h). The Si may come from the contamination in the raw powder, and the Ga in the spectra comes from the FIB polishing (Mayer, Giannuzzi et al. 2007).

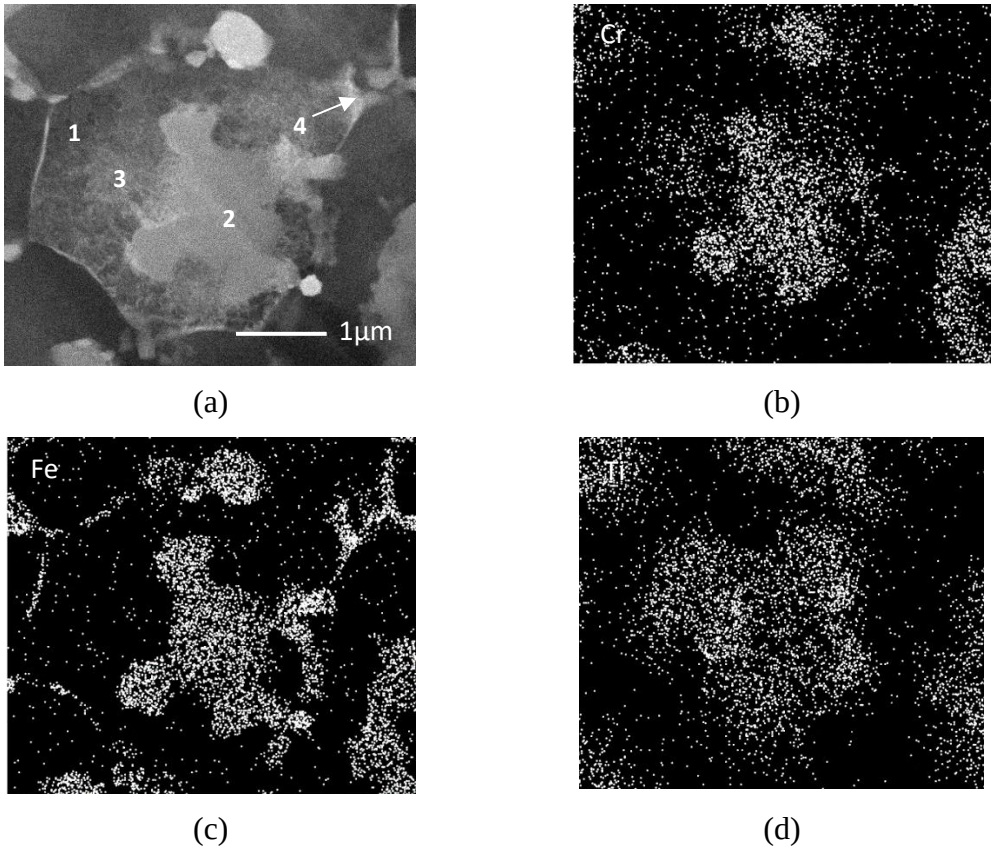

Figure 4.3: STEM DF image and EDX mappings **(a)** STEM DF image of $Al_{93}Fe_3Cr_2Ti_2$, **(b)** EDX mapping of Cr, **(c)** EDX mapping of Fe, **(d)** EDX mapping of Ti, **(e)** EDX spectrum in position 1, **(f)** EDX spectrum in position 2, **(g)** EDX spectrum in position 3, **(h)** EDX spectrum in position 4

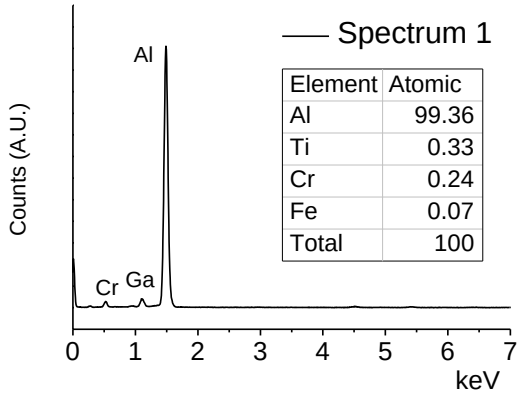

(e) EDX spectrum in position 1

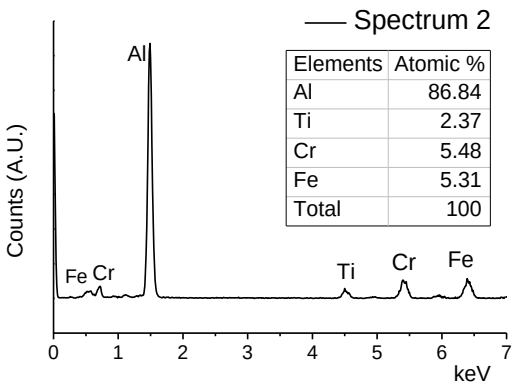

(f) EDX spectrum in position 2

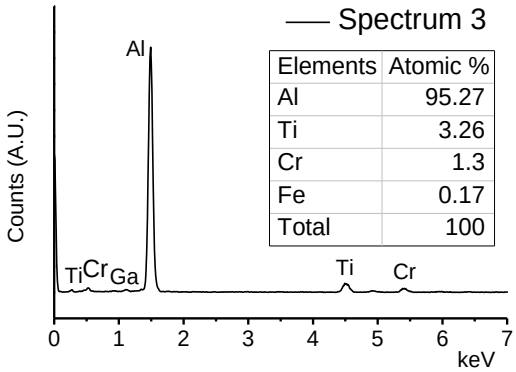

(g) EDX spectrum in position 3

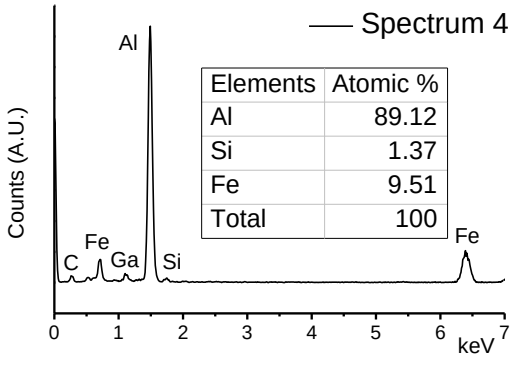

(h) EDX spectrum in position 4

Figure 4.3: STEM DF image and EDX mappings **(a)** STEM DF image of $Al_{93}Fe_3Cr_2Ti_2$, **(b)** EDX mapping of Cr, **(c)** EDX mapping of Fe, **(d)** EDX mapping of Ti, **(e)** EDX spectrum in position 1, **(f)** EDX spectrum in position 2, **(g)** EDX spectrum in position 3, **(h)** EDX spectrum in position 4

4.1.3 Orientation relationships

A large proportion of quasicrystals were found to locate near the Al_3Ti phases. Figure 4.4 is a TEM BF image from the $Al_{93}Fe_3Cr_2Ti_2$ alloy with the CBDPs. The areas with lighter contrast, for example, area (1), are Al grains. A large variety of dark particles are located in the Al matrix, for example, particle (2), (3) and (4). These particles are confirmed to be icosahedral quasicrystals by the CBDPs. One CBDP of particle (4) from a twofold [00τ]

zone axis (τ is the golden ratio which equals to $(\sqrt{5}+1)/2$)) is shown in the upper-left inset of Figure 4.4. The indexing method for the diffraction pattern of icosahedral quasicrystalline phase was illustrated in a publication of *Cahn* et al. (Cahn, Shechtman et al. 1986) and explained in section 2.2.3 in Chapter 2. Inside the dark particles, there is another kind of phase with different contrast, marked with (5), (6) and (7). These particles are confirmed to be the Al_3Ti intermetallics with the CBDPs. A CBDP of particle (7) from the [02-2] axis is shown in the bottom-right inset in Figure 4.4. From the diffraction patterns and the Crystallographic Information File (CIF) file (National Chemical Database Service 2016), the Al_3Ti phase has an cubic structure with a Pearson symbol cP4. The unit cell of the Al_3Ti phase is shown in Figure 4.5. The structure of Al_3Ti is almost the same with the FCC aluminium but the corner aluminium atoms are replaced by Ti atoms.

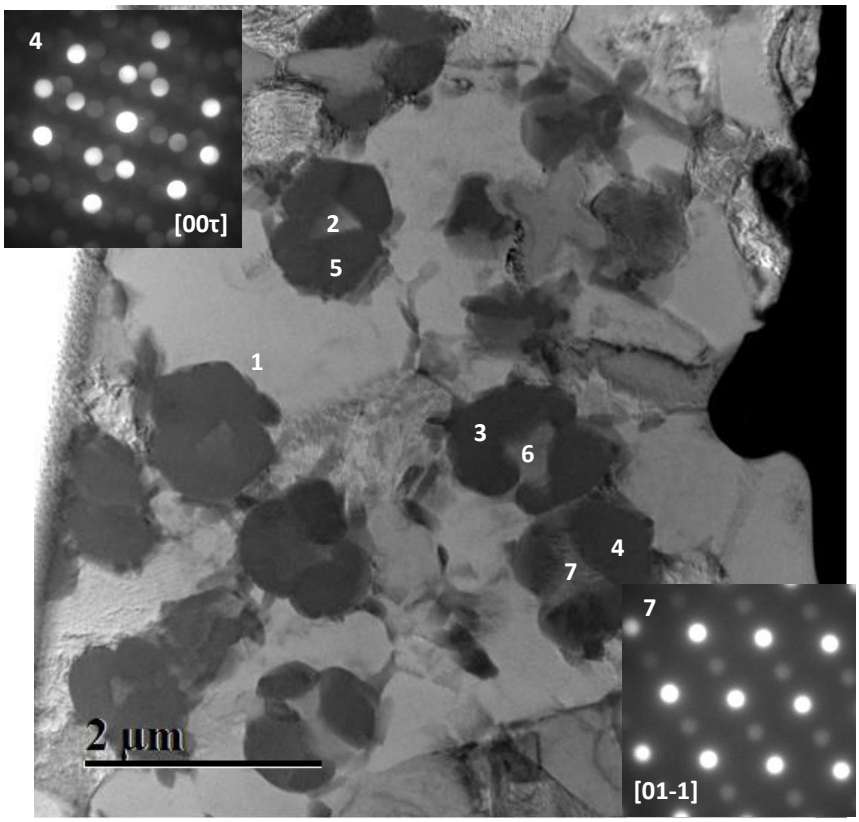

Figure 4.4: Al_3Ti intermetallics and surrounding quasicrystals identified with CBDPs in $Al_{93}Fe_3Cr_2Ti_2$ alloy powder. The upper-left inset is CBDP from particle (4) and the bottom right inset is from particle (7)

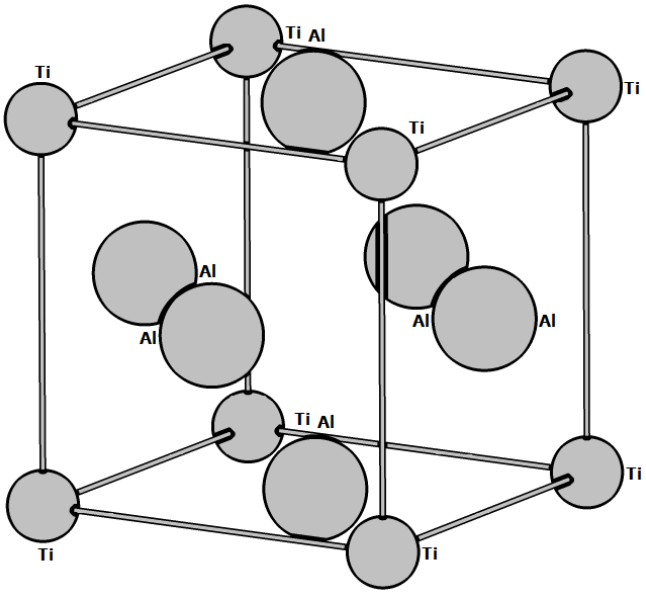

Figure 4.5: the unit cell of the Al_3Ti phase

Figure 4.6 is a zoom in TEM BF image of the $Al_{93}Fe_3Cr_2Ti_2$ alloy powder. Particle (1), (2) and (3) are an Al grain, an icosahedral quasicrystal particle and an Al_3Ti intermetallic particle respectively, identified by the CBDPs from the [2-20], [00τ] and [2-20] zone axes. All the indexings on the CBDPs of the Al_3Ti and Al phase in this work were done using the CIF provided by the National Chemical Database Service (National Chemical Database Service 2016). Since all the three diffraction patterns are taken from the same tilting angle in TEM, the [00τ], [0τ0] and the [τ00] axes of the icosahedral phase are parallel to the [2-20], [002] and [220] axes of the Al_3Ti and the Al phase.

Another TEM image was taken at the [002] zone axis of the Al_3Ti phase, as shown in Figure 4.7. Particle (1) is the Al_3Ti phase identified by a CBDP in the upper left inset in Figure 4.7. Particle (2) and (3) are the icosahedral quasicrystal phases, as shown in the diffraction patterns (2) and (3) in Figure 4.7. The [0τ0] axes of particle (2) and (3) are parallel, but the [τ00] axis of particle (2) is perpendicular to the [τ00] axis of particle (3). Nevertheless, these three twofold zone axes ([0τ0], [00τ], [τ00]) of the icosahedral quasicrystals are still parallel to the [002], [2-20] and [220] axes of Al_3Ti phase. These kinds of parallel relationships have been observed frequently (about 20 times) by the author. Although gas atomised quasicrystalline $Al_{93}Fe_3Cr_2Ti_2$ powders have been studied by a variety of researchers (Inoue 1998, Kimura, Sasamori et al. 2000), to the best of the author's knowledge, such orientation relationships have never been mentioned.

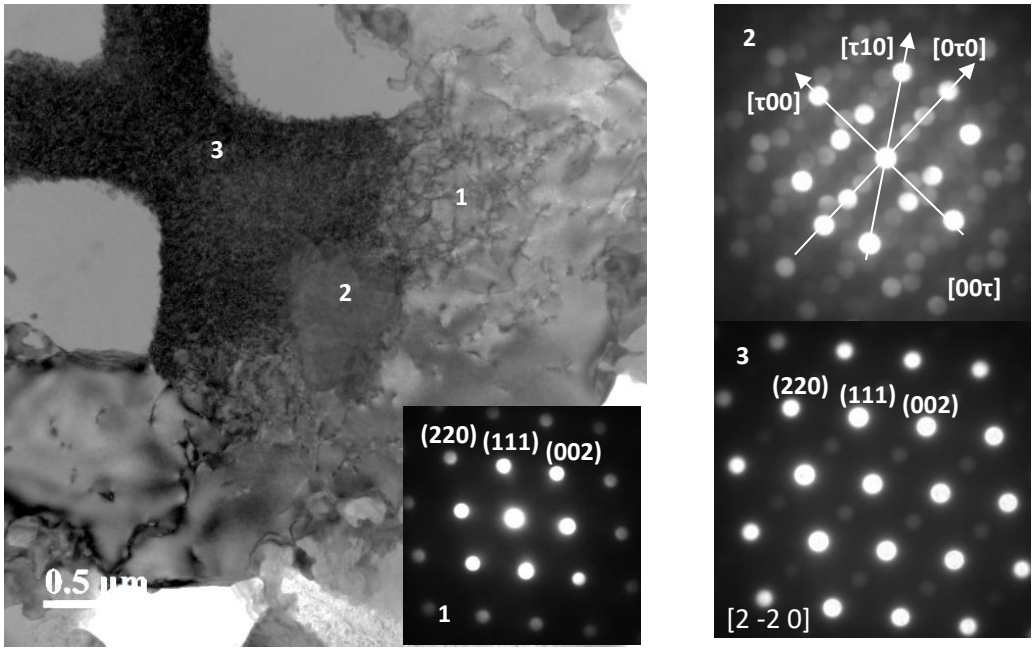

Figure 4.6: TEM BF images and CBDPs for verifying the orientation relationships between quasicrystal and Al_3Ti phase

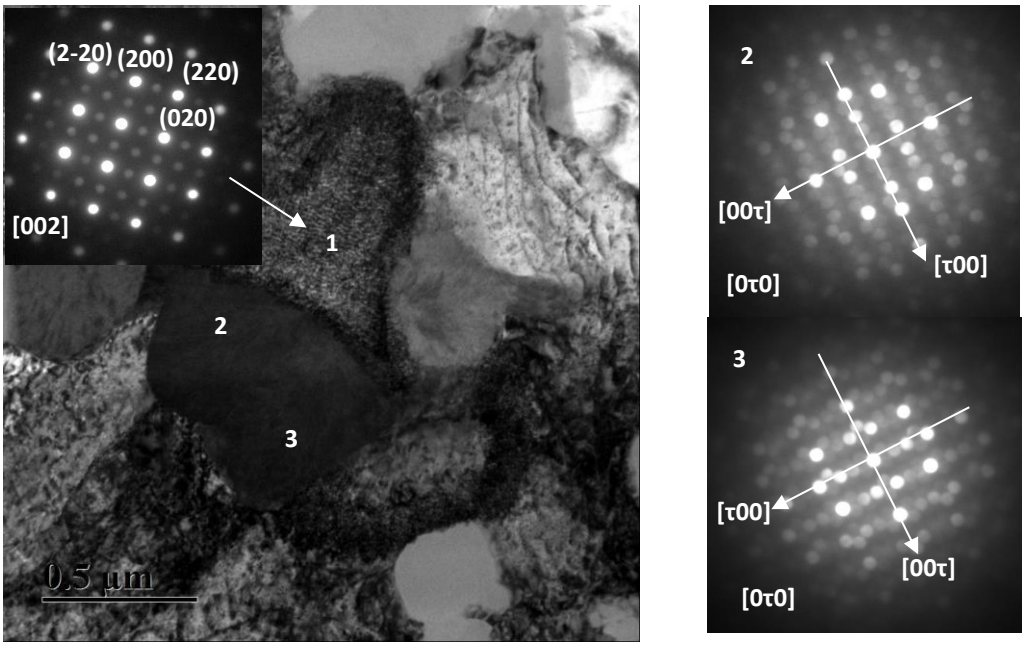

Figure 4.7: TEM BF images and CBDPs for verifying the orientation relationships between quasicrystal and Al_3Ti phase

Two CBDPs were taken on quasicrystal phase and the Al_3Ti phase in the [2-20] zone axes respectively, as shown in Figure 4.8(a) and (b). Another selected area diffraction pattern (SADP) is taken on the area containing both the quasicrystal and the Al_3Ti with the same tilt angle, as shown in Figure 4.8(c). From the overlapped diffraction points, the interplanar distances of the (200) (022) and (111) planes for the Al_3Ti phase are almost the same with the interplanar distances of the $(2+4\tau\ 0\ 0)$, $(0\ 4+6\tau\ 0)$ and $(1+2\tau\ 2+3\tau\ 0)$ planes in the quasicrystalline phase. This implicates that there should be some lattice coherency between these two phases.

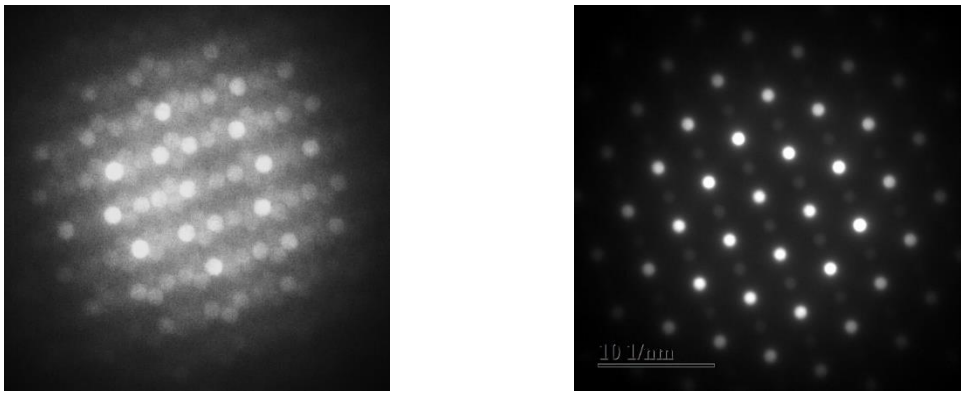

(a) (b)

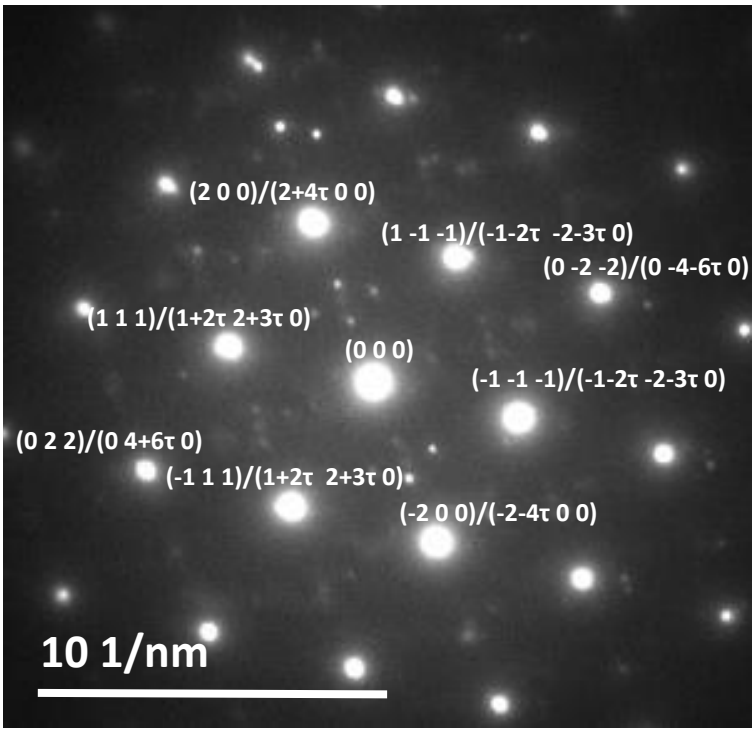

(c)

Figure 4.8: Diffraction patterns of quasicrystal and Al_3Ti phase **(a)** a twofold CBED of a quasicrystal, **(b)** a CBED of an Al_3Ti particle, **(c)** an SADP of the quasicrystal and the Al_3Ti phase

4.1.4 Atom positions

To check the lattice coherency between the Al_3Ti and the icosahedral quasicrystal, it is necessary to view their atom positions using high resolution electron microscope (HRTEM).

In both Figure 4.9 and Figure 4.10, (a) corresponds to the TEM images of the Al_3Ti phase, (b) corresponds to the HRTEM images of the Al_3Ti phase, (c) corresponds to the Fast Fourier Transform (FFT) of the HRTEM image, and (d) is the simulated atom structure of the Al_3Ti phase using the crystal maker software from the same crystallographic orientation in TEM.

As shown in both the HRTEM images (Figure 4.9(b) and Figure 4.10(b)), the atom positions of the Al_3Ti phase match well with the simulated results (Figure 4.9(d) and Figure 4.10(d)). The theoretical lattice constant of the Al_3Ti from the CIF is 0.3972 nm, while the measured lattice constant from the HRTEM images is 0.3915 nm. The FFT patterns in Figure 4.12(c) and Figure 4.13(c) are similar to the CBDPs of the phase in HRTEM image, which can be used to identify the zone axes of the HRTEM images (Williams, Carter et al. 1998).

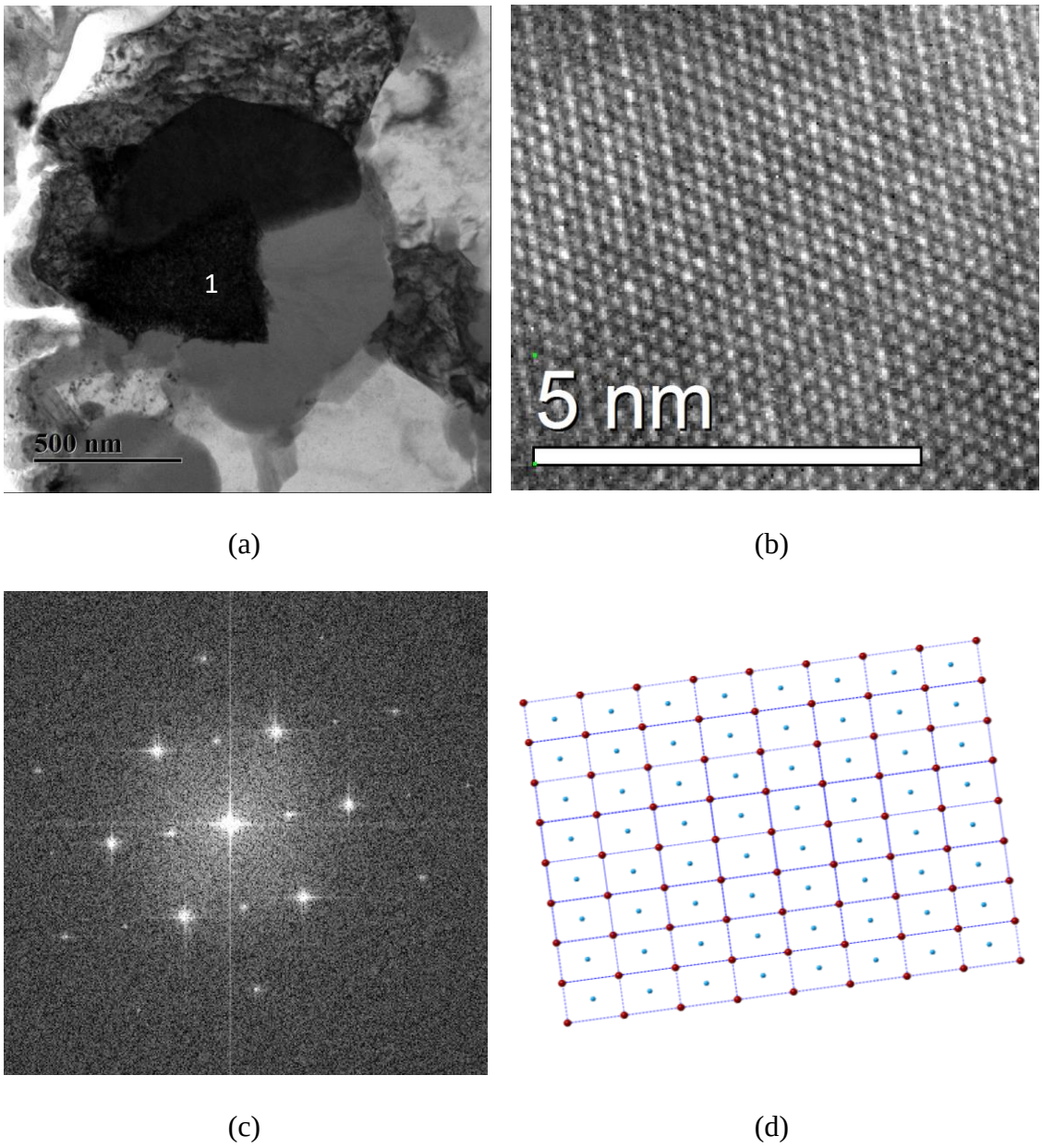

(a) (b)

(c) (d)

Figure 4.9: The Al_3Ti phase analysis from [01-1] zone axis **(a)** TEM image of the Al_3Ti phase, **(b)** HRTEM image of the Al_3Ti phase, **(c)** FFT of the image in (b), **(d)** A simulated atom structure of Al_3Ti phase

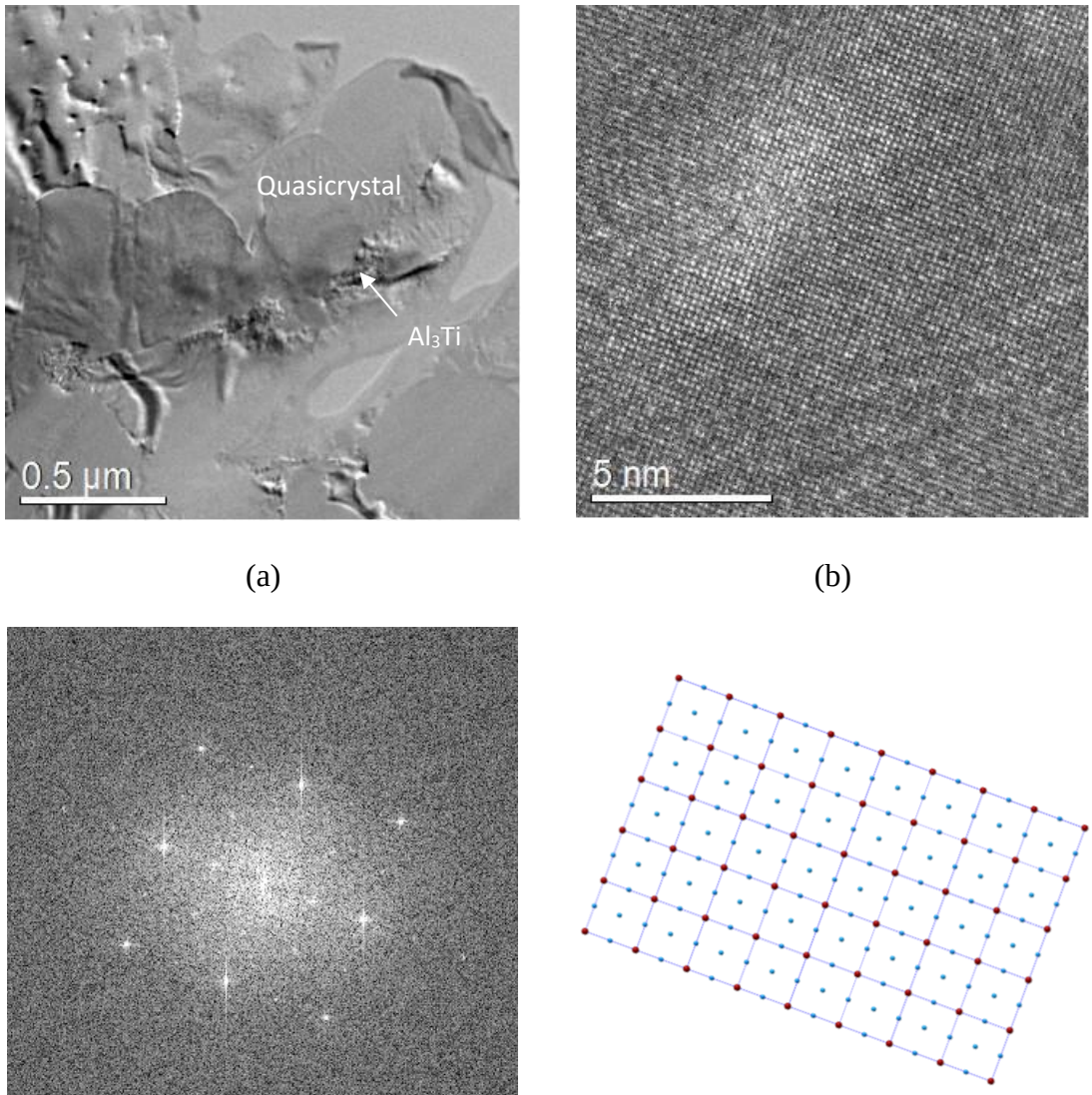

Figure 4.10: The Al_3Ti phase analysis from [001] zone axis **(a)** TEM image of the Al_3Ti phase, **(b)** HRTEM image of the Al_3Ti phase, **(c)** FFT of the image in (b), **(d)** A simulated atom structure of Al_3Ti phase

To identify the atom packings in the icosahedral phase, the annular dark field image from the fivefold zone axis of an icosahedral quasicrystal in the $Al_{93}Fe_3Cr_2Ti_2$ alloy is shown in Figure 4.11. As stated in section 3.2.4, the contrast of STEM DF image scales as the

atomic number $Z^{1.7}$ (Voyles, Grazul et al. 2003). The image in Figure 4.11 was obtained from a quasicrystalline particle of an ultra-thin sample with thickness about 30-50nm. It is noticed that in each fivefold motif the centre atom is much brighter than the other atoms. This is probably because the centres of the motifs have more atoms overlapped with each other due to the quasiperiodic structure (Elser 1985).

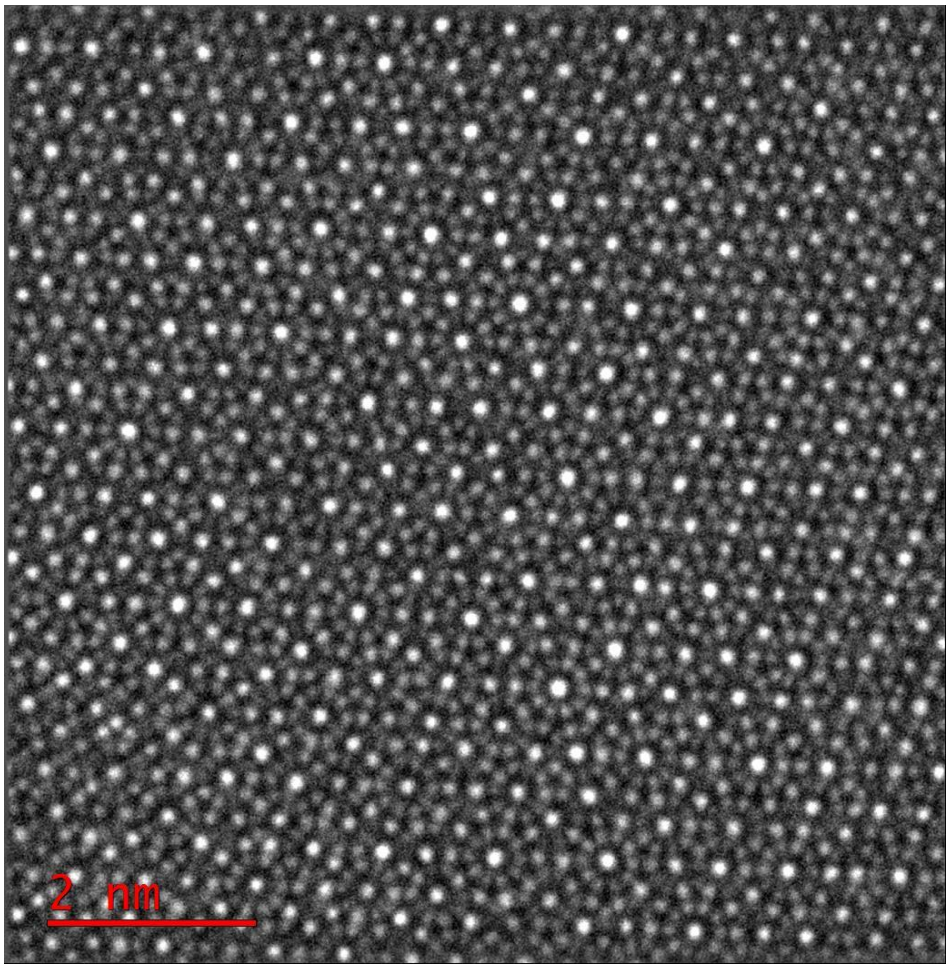

Figure 4.11: An atom resolution annular dark field image of icosahedral quasicrystal

A crystal can be packed with one type of repeated unit. For the icosahedral quasicrystals, two types of rhombohedral units with the same unit length are need to compile in three-dimensional space (Levine and Steinhardt 1986). The edge length of the rhombohedral

cells that is named as “quasilattice” constant. The quasicrystal lattice constant for the icosahedral quasicrystals in the nanoquasicrystalline $Al_{93}Fe_3Cr_2Ti_2$ alloy is 0.287nm, calculated from the STEM image in Figure 4.11. The calculation method can be found in the publications of *Elser* (Elser 1986) and *Levine* et al. (Levine and Steinhardt 1986).

When the samples are too thick, atom resolution imaging becomes difficult. To further investigate the atom position in three-dimensional space, quasiperiodic lattices with sample thickness of 10nm were simulated. The method for lattice calculation follows the work of *Elser* (Elser 1986) and explained in 2.2 in Chapter 2. Figure 4.12 and Figure 4.13 are the HRTEM images and simulated atom positions of quasicrystals from fivefold and twofold zone axes respectively. As observed, the images taken in annual dark field (ADF) mode in STEM match well with the simulated atom positions.

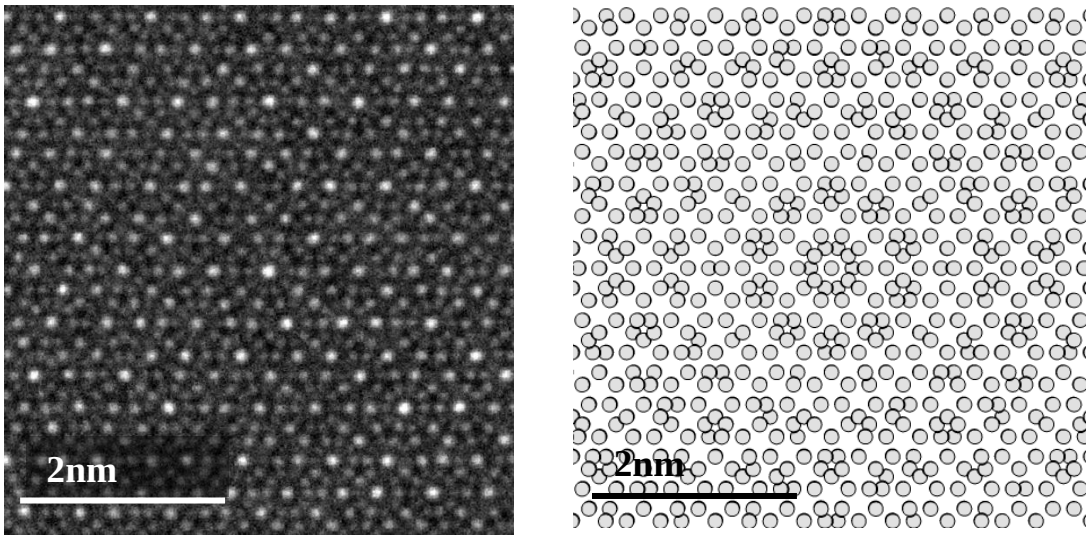

(a) (b)

Figure 4.12: (a) STEM ADF image from fivefold zone axis, **(b)** calculated atom positions from fivefold axis

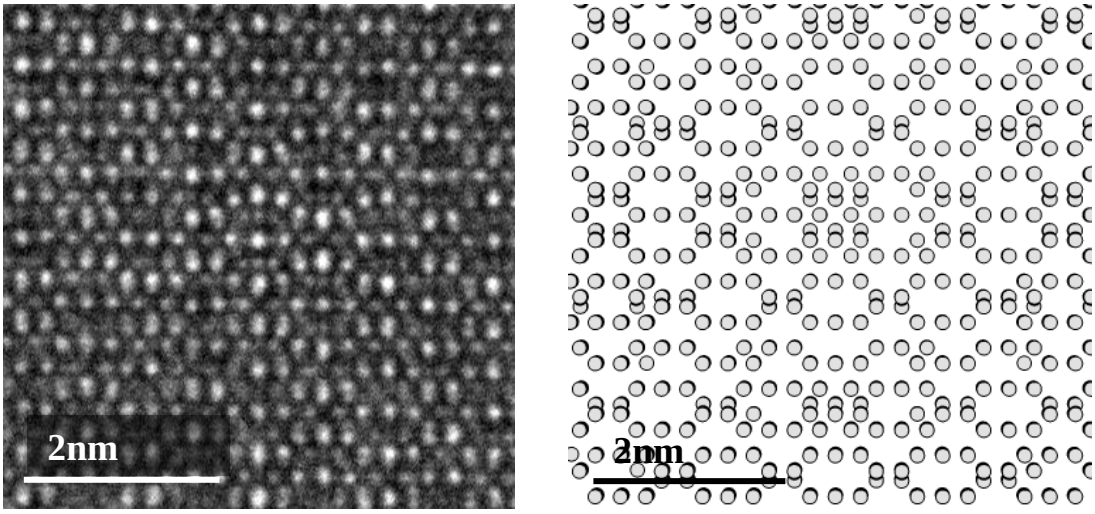

(a) (b)

Figure 4.13: (a) STEM ADF image from twofold zone axis, **(b)** calculated atom positions from twofold axis

4.1.5 Atom coherency

Figure 4.14 (a) is an HRTEM image on the bonding area between the quasicrystal and the Al_3Ti intermetallics. The crystallographic orientations were labelled with white arrows. As shown, the [00τ] and the [τ00] directions of the quasicrystal are parallel to the [220] and [2-20] directions of the Al_3Ti phase. This result matches the diffraction patterns in Figure 4.7. The angle between the [-τ01] direction in the quasicrystal and the [2-20] direction in the Al_3Ti phase is θ ($\tan\theta = 1/\tau$). The projections of two-dimensional periodic lattices on a one-dimensional plane could form a Fibonacci chain (Elser 1985), which is explained in 2.2 in Chapter 2. The atom positions in quasicrystals in one dimension could also form a Fibonacci chain (Levine and Steinhardt 1986). Therefore, if the two Fibonacci atom chains have similar short and long intervals, the Al_3Ti might have a "projection coherency" with the icosahedral quasicrystalline phase.

In Figure 4.14 (b), black and white image on the left side is the atom position in the icosahedral quasicrystals from a twofold zone axis. The coloured image on the right is the atom positions of the Al_3Ti phase from a [002] zone axis. The red and blue atoms are Ti and Al respectively, while the grey atoms are those projected from other planes. Line 1 is a connection of atoms in [-τ0-1] direction in the icosahedral quasicrystal. Line 2 and Line 3 are two lines parallel with Line 1, passing two Ti atoms labelled with (1) and (2). The atom positions on Line 1 follow a Fibonacci chain with intervals L and S. The intervals L_{ico} and S_{ico} are calculated to be 0.464nm and 0.287nm with the DF image in Figure 4.11. The Ti atoms (represented with red solid circles) sitting between Line 1 and 2 are connected by the grey dash lines. If projected onto Line 2, they also follow a Fibonacci order with intervals $L_{Al\text{-}Ti}$ and $S_{Al\text{-}Ti}$ (Levine and Steinhardt 1986). Since the lattice constant was 0.392nm for Al_3Ti, the $L_{Al\text{-}Ti}$ and $S_{Al\text{-}Ti}$ values are calculated to be 0.471nm and 0.291nm, respectively. Since $L_{Al\text{-}Ti}$ and $S_{Al\text{-}Ti}$ are only 1.5% larger than the L_{ico} and the S_{ico}, and the boundaries of the quasicrystal and the Al_3Ti phase are parallel to the [2-20] and [220] orientations with a stair shape (as shown in the white dash lines in Figure 4.11(a)), the hypothesis that the icosahedral phase has a coherency relationship with the Al_3Ti phase is reasonable. However, more HRTEM investigations are needed to verify this.

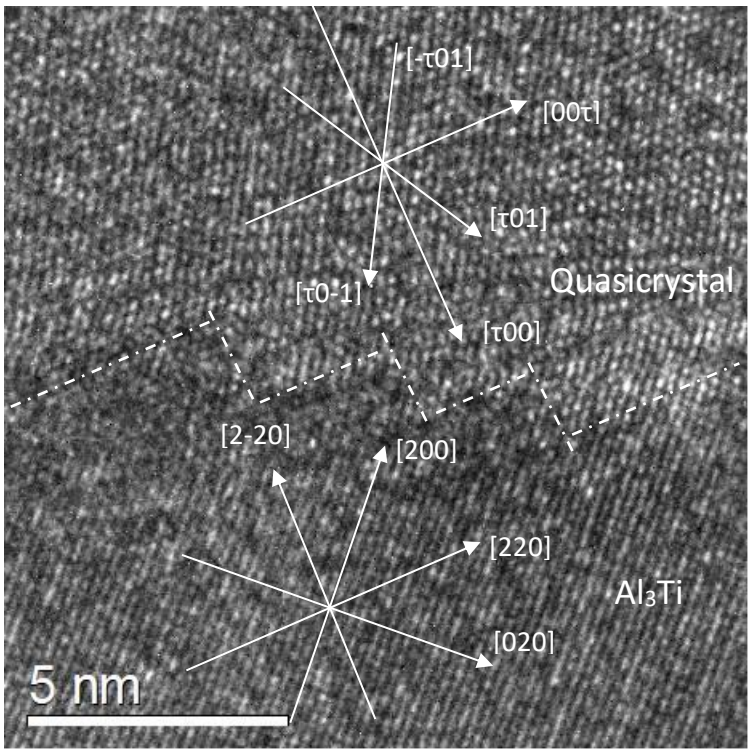

(a) HRTEM of bonding between quasicrystal and Al_3Ti phase

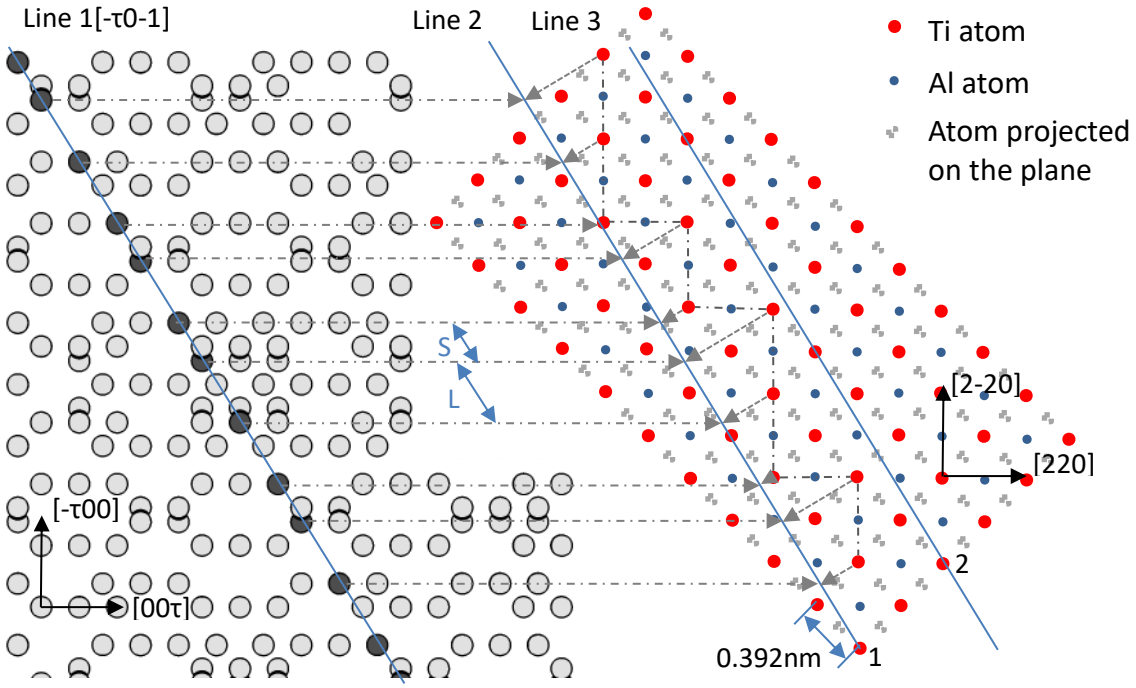

(b) the schematic diagram

Figure 4.14: the lattice disregistry between quasicrystal and Al_3Ti phase **(a)** HRTEM in the bonding area between quasicrystal and Al_3Ti phase, **(b)** the schematic diagram

4.2 Particle size and powder morphology

All the powders with different milling times show a Gaussian distribution of the volume fraction of powder particles against the logarithm of the powder particle size. Figure 4.15 plots the particle size distribution of the mechanical milled powder with different milling time. For all the samples, in the Gaussian curves, the values of the particle size corresponding to the highest and lowest position of full width half maximum (FWHM) are marked as P_{max} and P_{min} respectively, which can illustrate the particle size distribution range. The value of the particle size corresponding to the peak position of the curve is marked as P, which is also taken as the peak particle size of the powders. P_{max} and P_{min}, as well as the peak position P for A250 and C250 sample were plotted together in Figure 4.16. The particle size increasing and decreasing trends are illustrated in Table 4.2.

In Figure 4.15, it is observed that in low milling hours, some samples, for instance, C250_I_1 and C250_I_3, have small shoulders on the left side of the powder particle size distributions. The overlapping peak was decomposed using two Gaussian distributions. The small peak on the left side is in blue colour and the main peak on the right side is in red colour. For the C250_I_3 powders, the small peak has a peak particle size of 8μm, which should correspond to γ-Al_2O_3 clusters. After 10 hours of milling, the shoulder disappears, probably because the γ-Al_2O_3 particles have been distributed into the nanoquasicrystalline alloy powders. In low milling hours, the A250_I_1 also has a small peak, yet on the right side of the main peak. This is supposed to come from the agglomerations of the matrix powder, as shown in Figure 4.15.

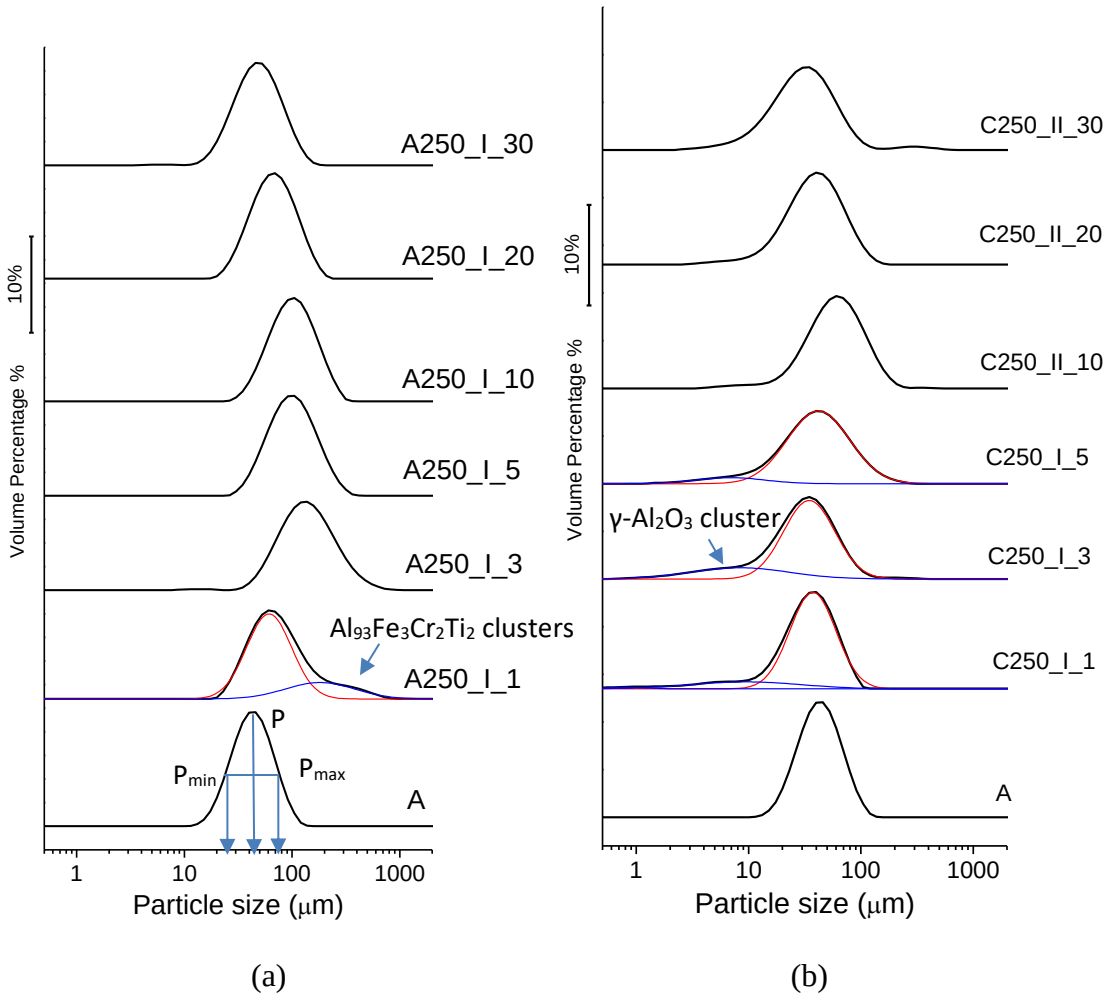

Figure 4.15: The particle size distribution plots of powders after 0, 1, 3, 5, 10, 20 and 30 hours of milling: **(a)** the A250 batch, **(b)** the C250 batch

From Figure 4.16 and Table 4.2, the particle size of the A250 batch increases during the first hours of milling, reaching the maximum value of 135μm at 3 hours of milling and then decreases gradually until 30hs, reaching the lowest value of 48 μm. The peak powder particle size of the A250_I_5 sample is similar to that of the A250_II_10 sample, probably because the latter was processed with a lower ball to powder ratio (BPR) (Suryanarayana 2001). In comparison, for the C250 batch, after 2 hours of milling the particle size decreases slightly. From 3 to 10 and from 10 to 30 hours of milling, the powder size shows

an increasing and decreasing trend respectively, as shown in Figure 4.16 (c). The largest and smallest powder sizes for the C250 batch of powder are 62 µm and 31µm, corresponding to C250_II_10 and C250_II_30 respectively, as shown in Table 4.2. The peak particle sizes of C250 powders were always smaller than those of A250 powders for all the milling times.

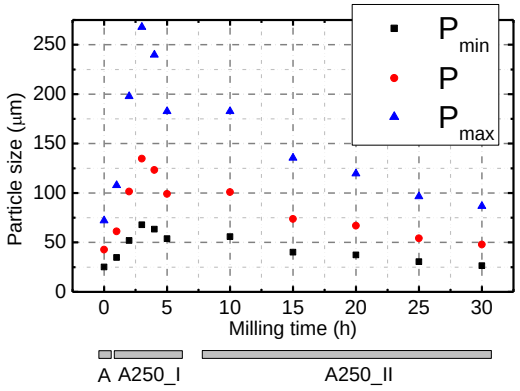

(a) the peak particle size and particle size distribution in A250

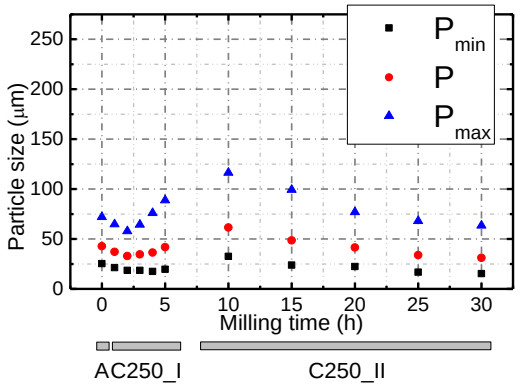

(b) the peak particle size and particle size distribution in C250

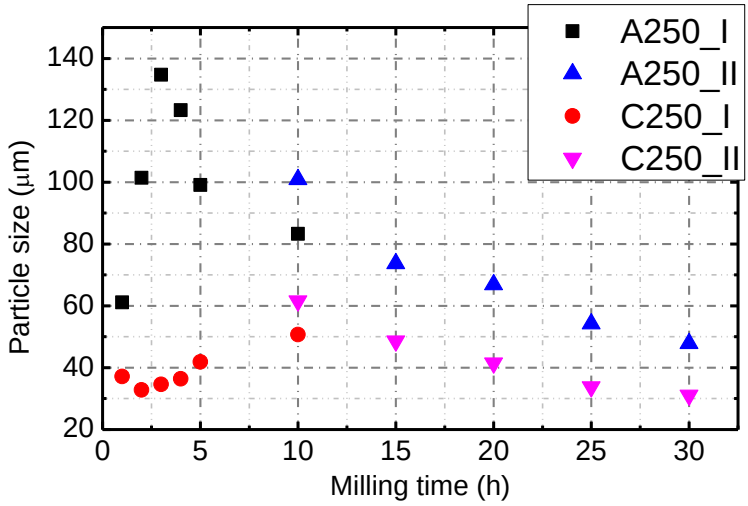

(c) The peak size comparison between the A250 and C250 batches

Figure 4.16: The particle size distribution between A and C **(a)** the peak particle size and particle size distribution in A250, **(b)** the peak particle size and particle size distribution in C250, **(c)** the peak size comparison between the A250 and C250 batches

A	A250	1h	2h	trend	3h	trend	30h
43μm	Powder size (μm)	61	101	↗	135	↘	48
	C250	1h	2h	trend	10h	trend	30h
	Powder size (μm)	37	33	↗	62	↘	31

Table 4.2: The particle sizes in different milling hours for the A250 and C250 batches of powders. Red colour: the maximum value. Blue colour: the minimum value.

The morphologies of the ball milled powders are analysed with the secondary electron images (SEI) in Figure 4.17. The powder sizes measured from SEIs match the Mastersizer results. For both the A250 batch and the C250 batch, the milled powders have a different morphology to the unmilled A powder. Figure 4.17(a1) shows that most powder particles are smooth and spherical. However, after mechanical milling the powder surfaces become very rough. The morphology of A250 is similar for powders with different milling time. The particle sizes in SEI match the measurements in Mastersizer in Figure 4.16.

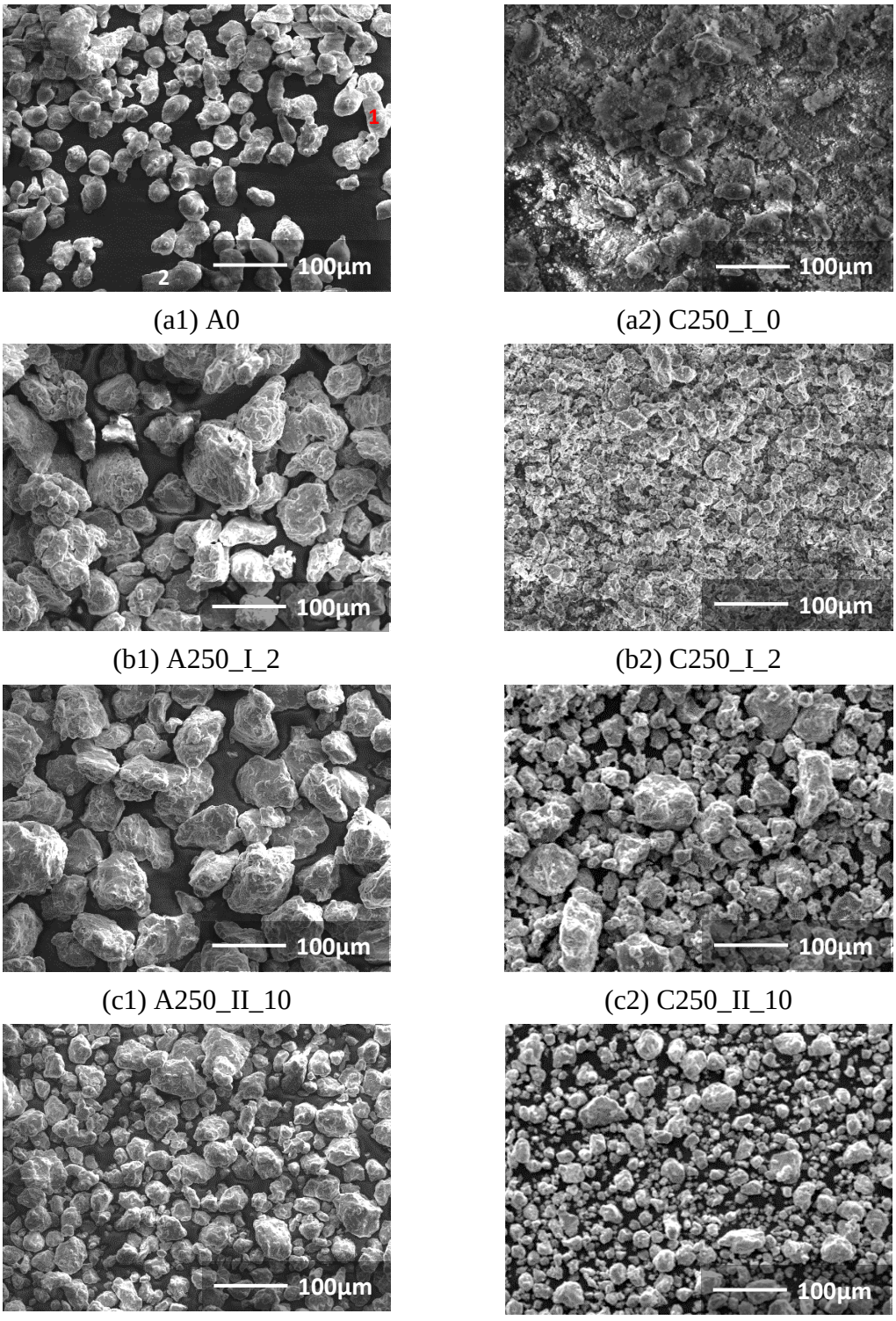

(a1) A0 (a2) C250_I_0

(b1) A250_I_2 (b2) C250_I_2

(c1) A250_II_10 (c2) C250_II_10

(d1) A250_II_30 (d2) C250_II_30

Figure 4.17: Secondary electron images (SEI) images **(a1)** A0, **(a2)** C250_I_0 (mixed composite powders), **(b1)** A250_I_2, **(b2)** C250_I_2, **(c1)** A250_II_10, **(c2)** C250_II_10, **(d1)** A250_II_30, **(d2)** C250_II_30

Figure 4.18 corresponds to the SEI and EDX analysis of the C250_I_2 and C250_II_20 samples. In Figure 4.18(a), small γ-Al_2O_3 clusters such as (1) identified using EDX (Figure 4.18(c)) are attached to the large nanoquasicrystalline powders. These nano-particles disappear after 20 hours of milling (Figure 4.18(b)), and the morphologies of the C250 powders became similar to the A250 batch powders in Figure 4.17. Figure 4.18(d) is an EDX spectrum from the matrix powder surface. The O element peak in the spectrum from position (2) could come from the oxidation of the powder surface.

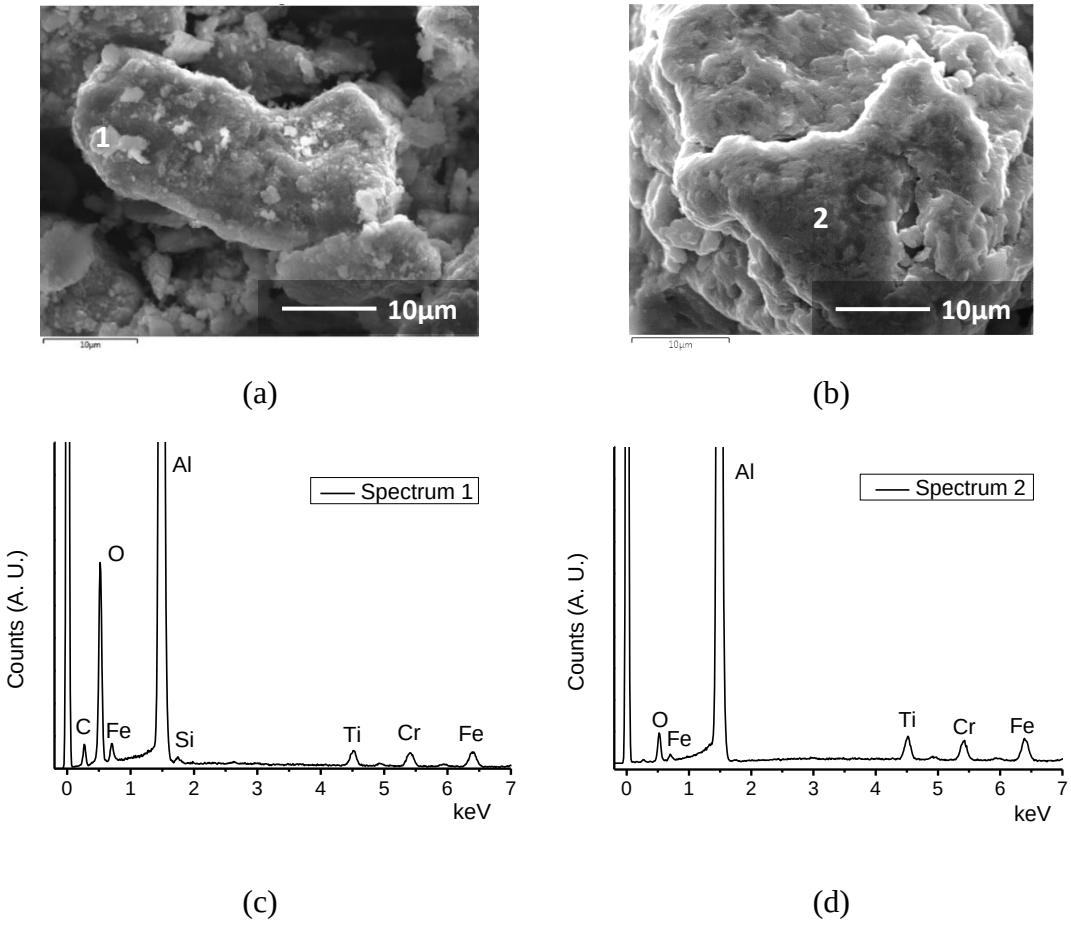

Figure 4.18: Secondary electron images (SEI) of the C250 batch with 2 and 20 hours of milling **(a)** C250_I_2, **(b)** C250_II_20, **(c)** EDX spectrum of position 1 in (a), **(d)** EDX spectrum of position 2 in (b)

4.3 Microstructure analysis

4.3.1 Phase characterisation and Al crystallite size calculation

X-ray diffractograms of A250 and C250 powders after different milling hours are shown in Figure 4.19. The α-Al phase is observed with peak position at 2θ of 38.5°, 44.7°, 65.1°, 78.3° and 82.5°. The icosahedral phase, labelled with Cahn's notation (Cahn, Shechtman et al. 1986), is also detected at 2θ of 22.7°, 41.1°, 61.0°, 43.3°, and 73.3° in all the samples except C250_II_30. Only one small peak of the γ-Al_2O_3 phase is observed in the C250 batch powders, γ(440) at 66.9°. This could be due to a combination of low volume fraction, and the nano-size particles of the γ-Al_2O_3, which produce broad and low intensity diffraction peaks, as it was observed in previous works (Galano, Marsh et al. 2015). Al_3Ti intermetallic is detected at 2θ of 39.3°. The insets in Figure 4.19(a) and Figure 4.19(b) show in details small peaks from γ-Al_2O_3 and the icosahedral phase.

For the gas atomised $Al_{93}Fe_3Cr_2Ti_2$ quasicrystalline powder, all researchers reported a microstructure with FCC-Al and the quasicrystalline phase. However, the intermetallics vary. *Todd* et al. (Todd, Chlup et al. 2004) and *Inoue* et al. (Inoue and Kimura 1999) found $Al_{23}Ti_9$ in gas atomised $Al_{93}Fe_3Cr_2Ti_2$ quasicrystalline powder. *Galano* et al. (Galano, Marsh et al. 2015) found θ-$Al_{13}(Cr,Fe)_{2\text{-}4}$ in their gas atomised $Al_{93}Fe_3Cr_2Ti_2$ quasicrystalline powder. Broadening of all peaks as increasing the milling time is observed, which indicates the refinement of the crystallite size and the increasing lattice strain (Suryanarayana and Norton 1998). Due to the broadening effects, it is difficult to judge whether the icosahedral phase remains in the C250_II_30 sample.

For both the A250 and C250 batches only samples after 10 to 30 hours of milling are used to calculate the crystallite sizes, as the Williamson-Hall method is valid within the size

range of 10-100nm (Galano, Marsh et al. 2015). The results are shown in Figure 4.20. The error bars come from when fitting the y-intercept and the slope values using the Williamson-Hall method. For both the A250 and C250 batch powders, the crystallite sizes decrease with milling time. In general, for a milling time equal or longer than 10h, the C250 batch powders have smaller crystallite sizes, as shown in Figure 4.20. The smallest crystallite sizes were 22nm and 14nm for A250 and C250 batches of powders after 30 hours of milling. The strains of A250 and C250 batch powder fluctuate randomly, but the C250_II_25 and C250_II_30 samples have much lower internal strains compared with other samples.

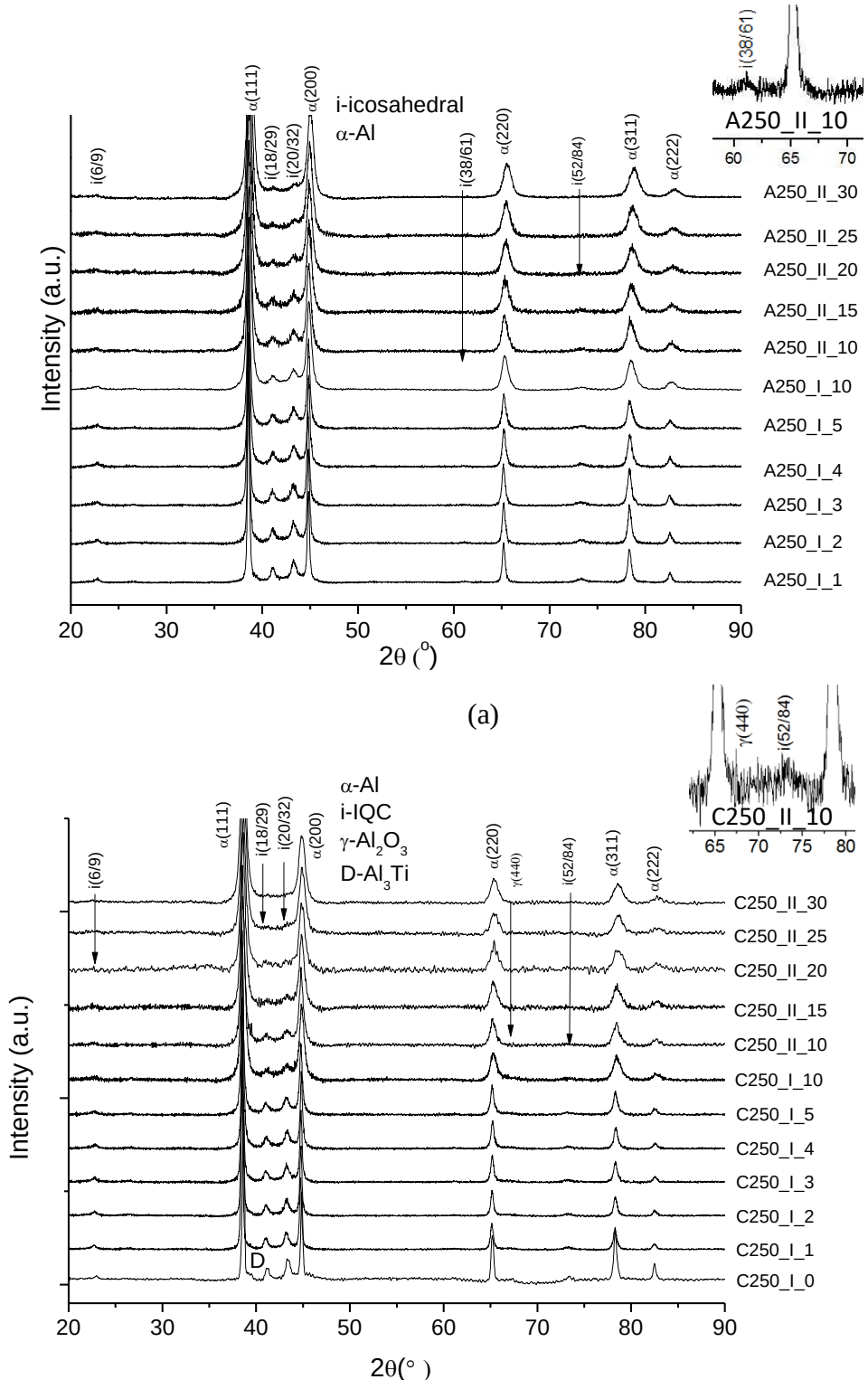

Figure 4.19: X-ray diffractograms of the ball milled **(a)** A250 powders (Inset: magnification to observe the i(38/61) peak at 61.1º.) and **(b)** C250 powders from 1 to 30h milling time (Inset: magnification to observe the γ(440) at 66.9° and the i(52/84) peak at 73.3º.)

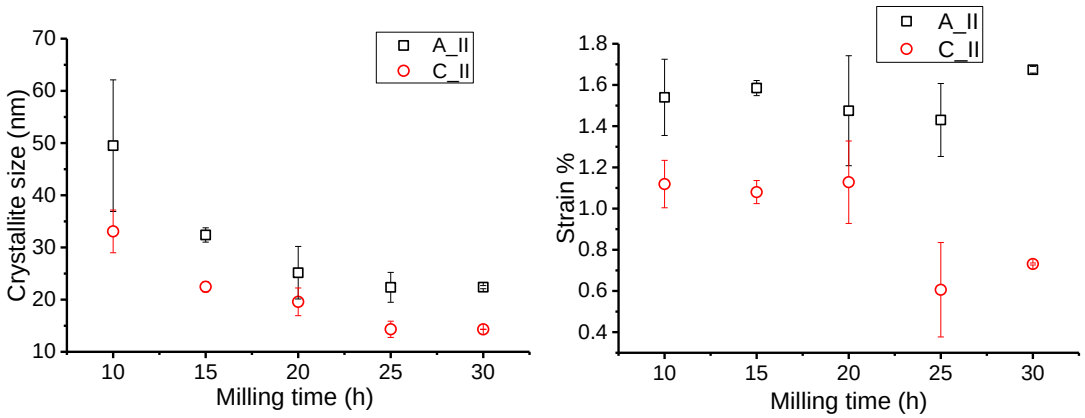

(a) (b)

Figure 4.20: (a) Al crystallite sizes and **(b)** strains against milling time for the range of 10 to 30 hours milling for both the A250_II and C250_II batches of powders

Figure 4.21 is TEM images of A250_II_5 and C250_II_5. For these two samples, the crystallites are too large for Williamson-Hall to be applied, and were calculated through TEM BF images, as shown in Figure 4.21(b). The crystallites were measured by drawing two pairs of parallel vertical and horizontal lines on each crystallite. The lengths between each pairs of lines were marked as d_1 and d_2 respectively. The average value of d_1 and d_2 was taken as the crystallite size (Galano, Marsh et al. 2015). At least 30 crystallites were measured for each sample. The crystallite size for C250_II_5 is 130±29nm. For the A250_II_5 sample, the crystallite size varies dramatically according to TEM image in Figure 4.21(a). For the crystallites sitting on the lamella shaped area, the average crystallite size is about 66±19nm, while for the crystallites sitting on the equiaxed area, the average crystallite size is about 125±31nm. The errors are the standard deviation of 30 measured Al crystallites.

The Al crystallite sizes (d) of several A250 and C250 ball milled powders were measured in TEM and compared with the ones measured with Williamson-Hall from the X-ray diffractograms as are summarized in Table 4.3. It is observed that results from both techniques are in good agreement.

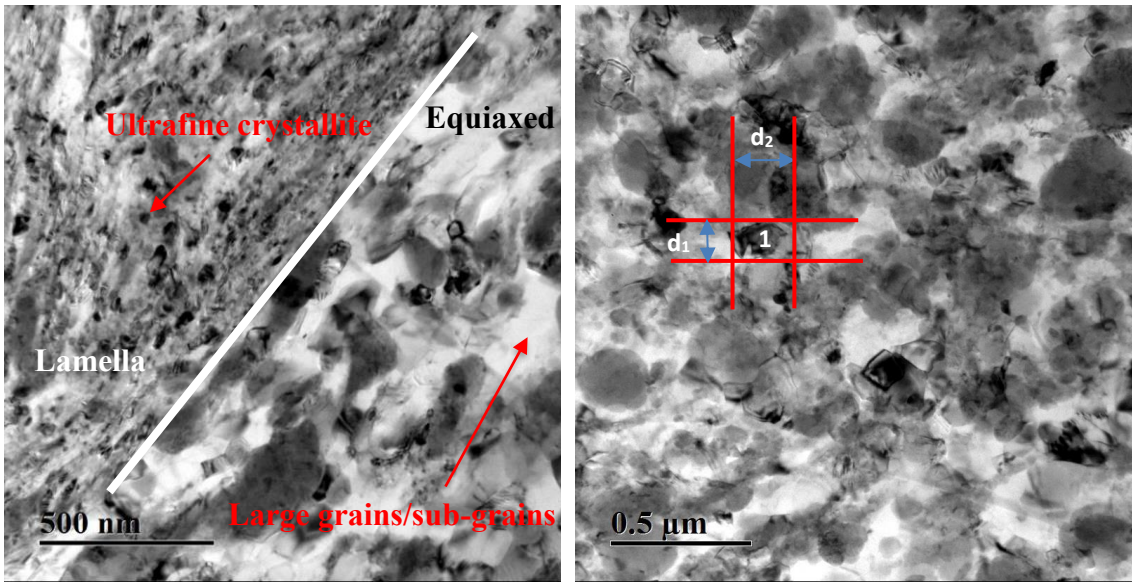

(a) (b)

Figure 4.21: Crystallite size calculation for samples with 5 hours of milling **(a)** A250_II_5, **(b)** C250_II_5

	A250_I	A250_II		C250_II		
Milling time (h)	**10**	**10**	**30**	**5**	**10**	**30**
TEM (nm)	48±12	55±14	27±4	130±29	33±7	16±3
XRD (nm)	38±9	49±13	22±2	/	33±4	14±0

Table 4.3: The crystallites size measured by TEM and Williamson-Hall from the X-ray diffractograms for A250 and C250 powders

4.3.2 Microstructure of aluminium matrix

TEM BF images of the A250 and C250 mechanically milled powders are shown in Figure 4.22. Before milling, most of the aluminium grains in Figure 4.2 have diameter larger than 1 μm. The general microstructure of A250_I_1 is shown in Figure 4.22(a). Figure 4.22(b) and (c) are TEM BF images of A250_I_1 sample with larger magnifications. Particle (1) is a quasicrystal identified by a threefold CBDP. From the diffraction patterns, particle (2) and (4) are suspected to have similar crystallography with the α(AlFeSi) phase, as discussed in section 4.1.2 in this Chapter. They may come from the Al-Fe phase sitting on the grain boundaries before mechanical milling. Particle (3) and (5) are nanosize Al crystallites, which have been confirmed by the CBDPs. One CBDP of particle (5) is shown in the inset in Figure 4.22(c). Particle (3) and (5) are trapped between the intermetallics and the quasicrystals after 1 hour of milling and their sizes are about 200nm.

After 3 hours of milling, the icosahedral particles preserved the original size as the alloy powder before milling. However, the Al crystallites presented two size distributions in different parts of the powder's microstructure. As shown in Figure 4.22(d), a quasicrystal particle labelled as (6) is identified with a twofold CBDP from the mirror plane zone axis. The Al crystallites near to the icosahedral particles (6) were drastically refined and ultrafine Al nanocrystallites were confirmed by a ring shape selected diffraction pattern (SADP) with a ~200 nm size SADP aperture, as observed in (7). These ultrafine crystallites have an average size of 21±3 nm. The four rings in SADP corresponds to the (111), (200), (220) and (311) planes of the Al matrix (National Chemical Database Service 2016). Some relative larger Al grains with 90±30 nm size can be detected in areas further away from the icosahedral particles, for example the one labelled as (8) in Figure 4.22(d).

Two subgrains generated in ball milling progress can be seen in position (9). Figure 4.22(e) is a BF image corresponding to a zoom in area labelled as (8), which shows these crystallites with sizes around 100nm contain dislocations. The microstructure of A250 powders after 5 hours of milling are already shown in Figure 4.21(a). The lamella structured area with very refined Al grains is a high deformation zone close to the icosahedral particles, which can be considered as non-deforming particles. Thus, during the impact load received by powder particles during the ball milling leads Al grains around the icosahedral particles to produce local lattice rotations associated with the introduction of geometrically necessary dislocations to avoid the formation of voids at the interfacial surface (Engler, Kong et al. 1997). *Khakbiz* et al. (Khakbiz and Akhlaghi 2009) found that the Al6061 alloy (71 μm powder produced by gas atomisation), after 4 hours of milling with 320 rpm milling speed and 20:1 BPR, had an average grain size of about 110 nm, which is similar to the largest Al crystallites size in the ball milled nanoquasicrystalline Al alloy powder after 3 or 5 hours of milling. After 10 hours of milling, the structure is heavily refined with the Al crystallite size of 48±12 nm homogenously distributed. The structure shows an orientation along the arrow direction, as shown in Figure 4.22(f). After 30 hours of milling, Al grains were refined further having a crystallite size of 27±4 nm, as shown in Figure 4.22(g). An SADP was shown in the inset of Figure 4.22(g). The four rings, from inner to outer, correspond to the (111), (200), (220) and (311) planes of α-Al matrix. Some discrete spots could be detected in the SADPs. Their interplanar distances were calculated to be 0.41 nm, 0.38 nm, 0.31 nm, 0.22 nm and 0.21 nm, which match (100) plane of Al_3Ti phase, (211) plane of $Al_{13}Fe_4$ phase, (112) plane of Al_6Fe phase, (112) plane in Al_3Ti phase and (820) plane in $Al_{13}Cr_2$ phase respectively.

Figure 4.22(h) shows a TEM BF image of the microstructure of milled nanocomposite powder, C250_II_5 sample. After 5 hours of milling, the icosahedral particles maintain the same shape and size, the γ-Al_2O_3 appears in agglomerates and localized in layers. The Al crystallites remain equiaxed with an average size of 130±29 nm, larger than the A250_II_5 with a grain size of 66±19nm and 125±31nm in lamella area and equiaxed area (as shown in Figure 4.21(a)). The insets in Figure 4.22(h) show EDX analysis on an icosahedral particle and an γ-Al_2O_3 agglomerate. Figure 4.22 (i) shows the microstructure of the C250_II_10 sample. No Al crystallite size bimodal distribution is observed C250 powder samples as were observed for the A250 powder samples. Nanosize aluminium crystallites without any orientations are detected in the C250_II_10 sample, as shown in Figure 4.22(i). For the C250_II_30 sample, the four rings in the SADP in Figure 4.22(j), from inner to outer, correspond to the (111), (200), (220), (311) planes respectively, which indicates that the small black particles are ultrafine aluminium crystallites.

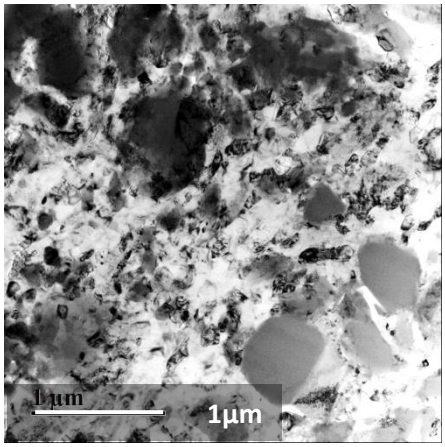

(a) A250_I_1

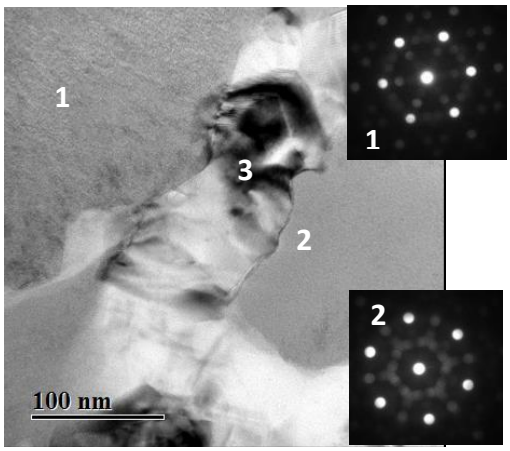

(b) A250_I_1

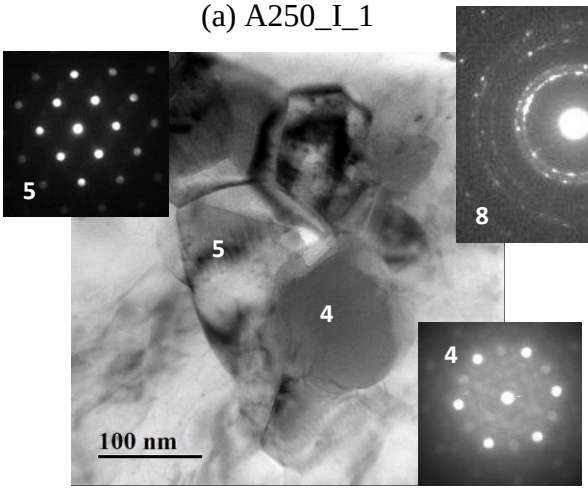

(c) A250_I_1

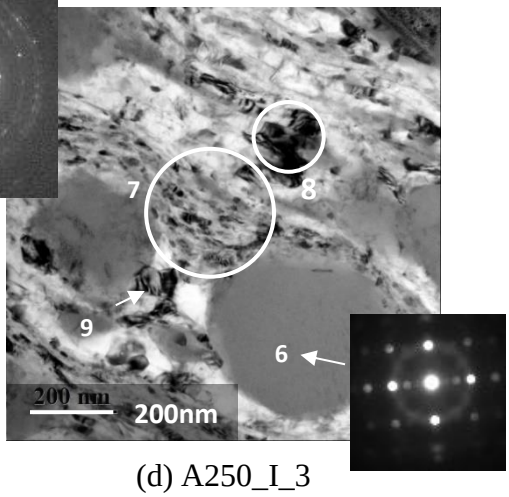

(d) A250_I_3

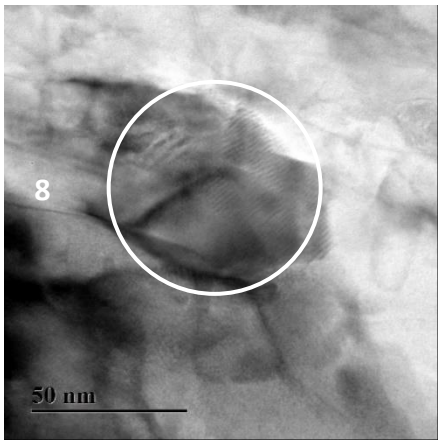

(e) a zoom in of area 8 in (d)

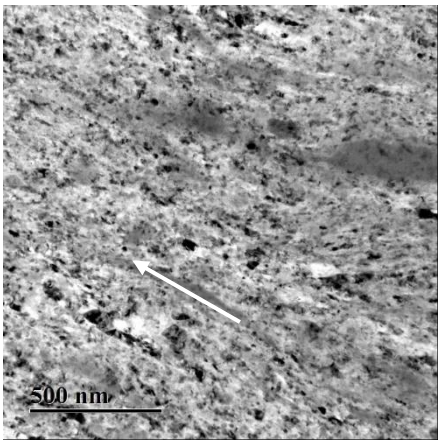

(f) A250_I_10

Figure 4.22: TEM bright field (BF) images and diffractions of A250 and C250 batch powders **(a)** A250_I_1, **(b)** A250_I_1, **(c)** A250_I_1, **(d)** A250_I_3, **(e)** a zoom in of area 8 in (d), **(f)** A250_I_10, **(g)** A250_II_30, **(h)** C250_II_5, **(i)** C250_II_10, **(j)** C250_II_30

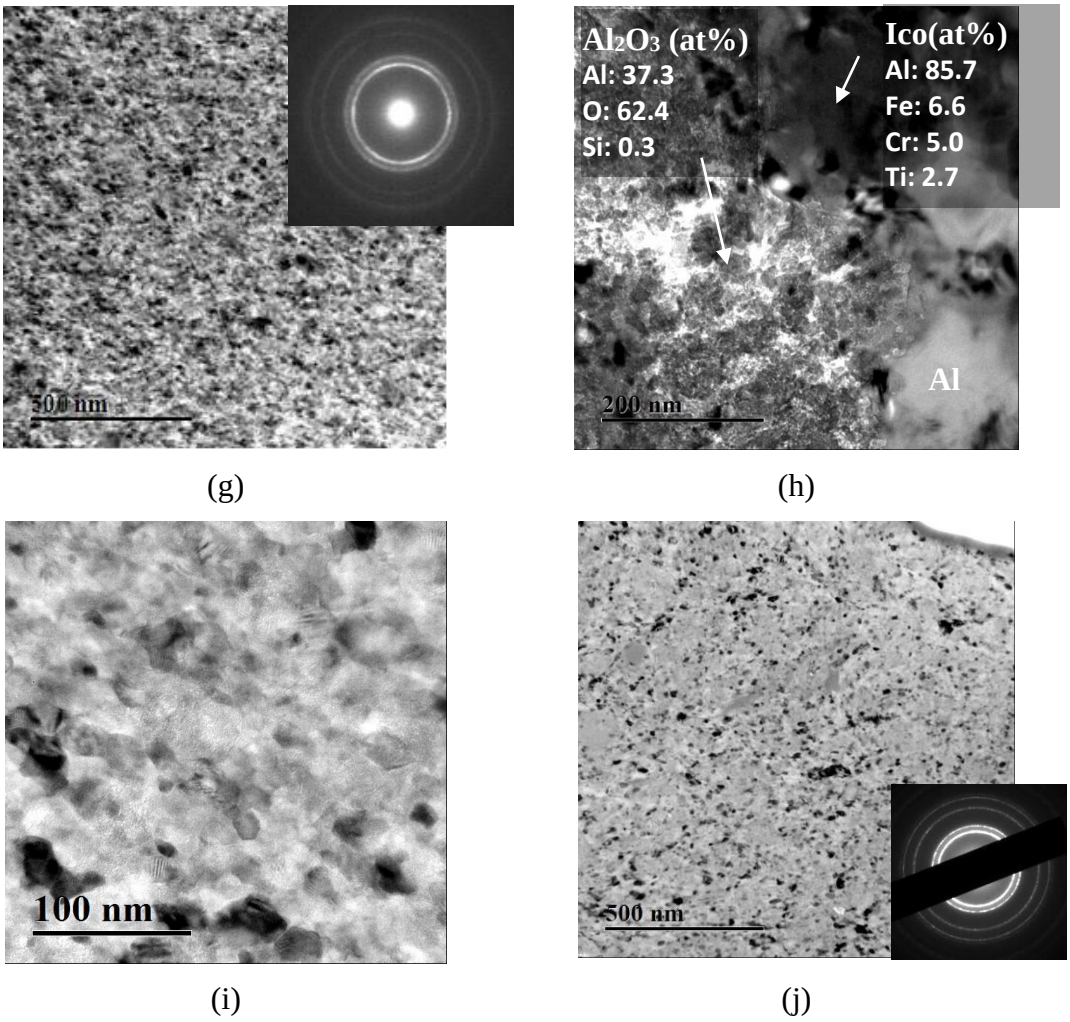

Figure 4.22: TEM bright field (BF) images and diffractions of A250 and C250 batch powders **(a)** A250_I_1, **(b)** A250_I_1, **(c)** A250_I_1, **(d)** A250_I_3, **(e)** a zoom in of area 8 in (d), **(f)** A250_I_10, **(g)** A250_II_30, **(h)** C250_II_5, **(i)** C250_II_10, **(j)** C250_II_30

4.3.3 Microstructure of quasicrystalline particles and the intermetallics

Figure 4.23 (a), (b), (c) and (d) are quasicrystals identified by convergent beam diffraction patterns (CBDPs) from fivefold, threefold, mirror, and twofold zone axes in A250 powders. It is observed after 1 hour of milling cracks which have never been detected in unmilled powders appear, for example, position (1) in Figure 4.23(a). It seems that a large quasicrystal particle is crushed into 4 pieces, labelled with (2), (3), (4) and (5). The inset

in Figure 4.23(a) is CBDP from threefold zone axis from position (3). After 5 hours of milling, there are still quasicrystals with spherical shapes, as shown in Figure 4.23(b). The inset in Figure 4.23(b) is a CBDP from threefold zone axis. After longer milling hours, several deformed and small pieces of quasicrystals were found, as shown in Figure 4.23(c) and (d). The CBDPs in Figure 4.23(c) and (d) are from the mirror plane zone axis and the twofold zone axis respectively. From milling time of 20 hours onwards, there is no quasicrystals larger than 400nm detected in TEM. For the C250 batch after 5 and 10 hours of milling, spherical quasicrystals could be detected, identified by the CBDPs from the fivefold zone axes, as shown in Figure 4.23(e) and (f). For milling time longer than 10 hours, quasicrystals could not be detected in TEM.

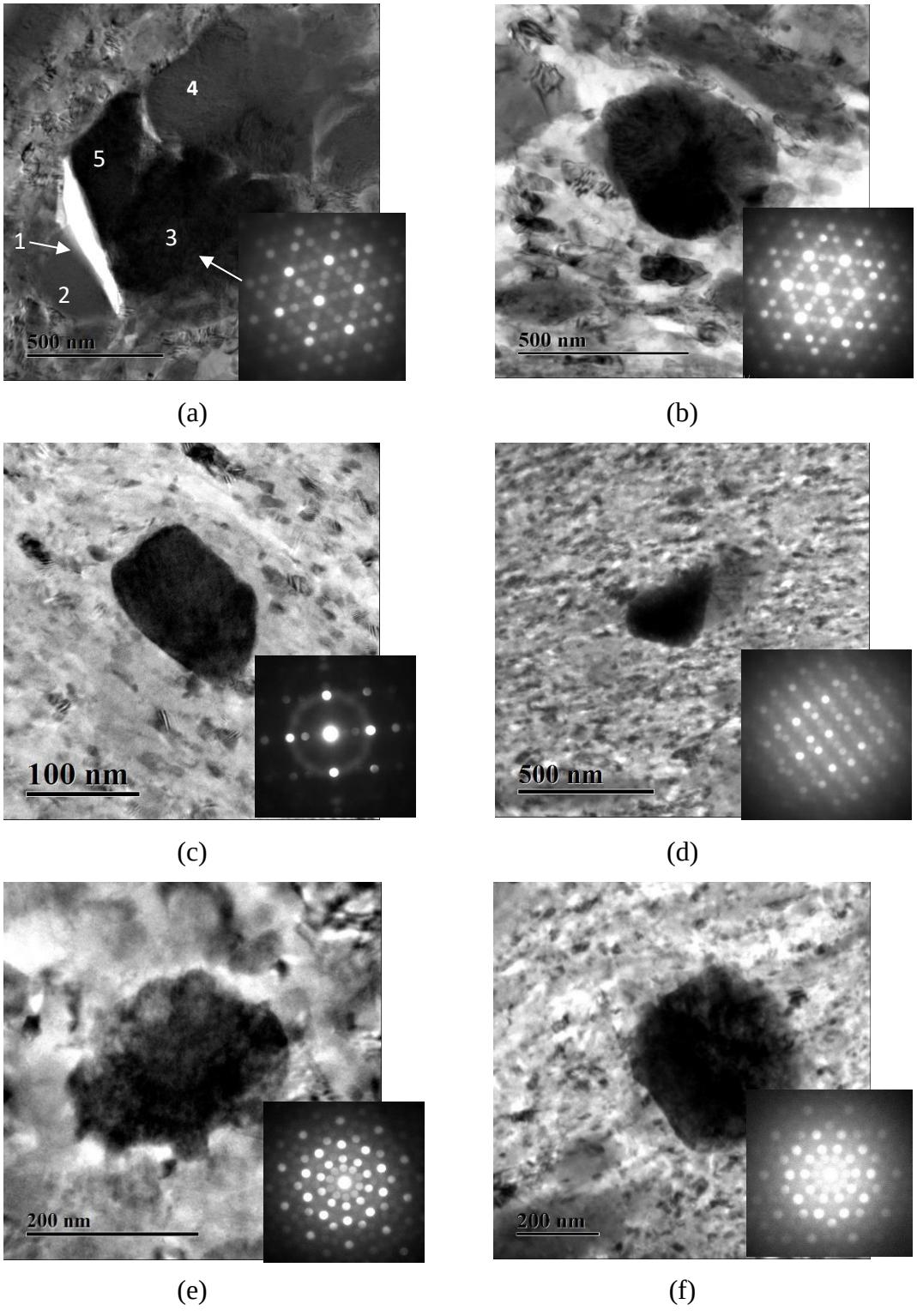

Figure 4.23: TEM BF images of quasicrystals identified by the CBDPs **(a)** A250_I_1, **(b)** A250_II_5, **(c)** A250_II_10, **(d)** A250_II_15, **(e)** C250_II_5, **(f)** C250_II_10

STEM dark field (DF) images, EDX spectra and maps from 5, 10 and 30 hours milled samples of A250 powders are shown in Figure 4.24. As stated in Chapter 3, the contrast of high angle annular dark field is based on the atomic number. Therefore, the quasicrystalline particles and the intermetallics containing high atomic number transition atoms should look brighter than the aluminium matrix, and the γ-Al_2O_3 particles should be the darkest.

Figure 4.24(a1) is an STEM DF image of A250_II_5, and Figure 4.24(a2), (a3) and (a4) are Fe, Cr and Ti EDX mappings of Figure 4.24 (a1). After 5 hours milling, the spherical particles containing Fe, Cr and Ti elements, for example, particle (1) in Figure 4.24(a1), might be the quasicrystalline particles. From the mapping data, A250_II_5 contains some Al-Fe intermetallic particles (Figure 4.24 (a1) and (a2)), marked with white circles in Figure 4.24(a1). It is difficult to judge whether these Al-Fe intermetallics come from the reactions in the milling progress, since in unmilled $Al_{93}Fe_3Cr_2Ti_2$ powder there are also Al-Fe intermetallics on the Al grain boundaries, as shown in Figure 4.3.

Figure 4.24(b1), (b2), (b3) and (b4) are the STEM DF image and the EDX mappings of A250_II_10. As shown in Figure 4.24(b1), the microstructure is highly refined. Some round shape Al-Fe based particles labelled with (2), (3) and an Al-Ti particle labelled with (4) are embedded in the Al matrix, as shown in in Figure 4.24(b1). The size of the Al-Fe based particle is around 140nm. Based on the EDX spectra, position (2) revealed an Al-Fe intermetallic particle contains 90.0 at.% of Al, 1.0 at.% of Ti, 1.3 at.% of Cr and 7.7 at.% of Fe, position (3) revealed an Al-Fe intermetallic particle contains 87.1 at.% of Al, 1.3 at.% of Ti, 2.6 at.% of Cr and 9.0 at.% of Fe, and position (4) revealed an Al-Ti

intermetallic particle contains 88.1 at.% of Al, 8.9 at.% of Ti, 1.6 at.% of Cr and 1.4 at.% of Fe.

Figure 4.24(c1) is an STEM DF image of A250_II_30 and Figure 4.24(c2) is the EDX mapping of Fe in A250_II_30. After 30 hours of milling, the structure is heavily refined and no obvious contrast is obtained from the ultrafine aluminium crystallites and intermetallics in the EDX mapping. However, some large particles containing iron and nickel are detected, labelled as (5) in Figure 4.24(c1). These contaminations should come from the stainless-steel milling media.

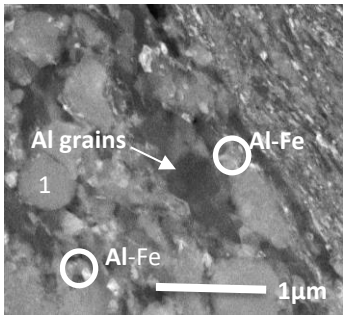

(a1) STEM image of A250_II_5

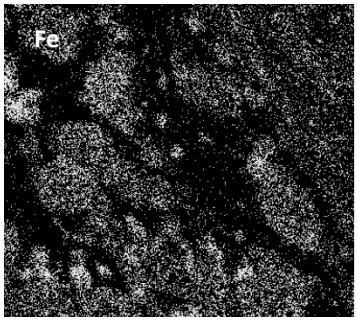

(a2) Fe EDX mapping of A250_II_5

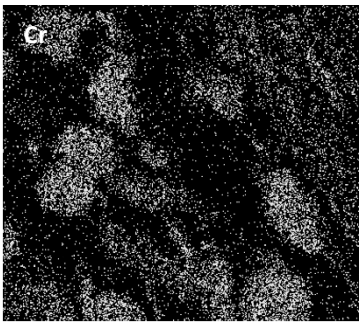

(a3) Cr EDX mapping of A250_II_5

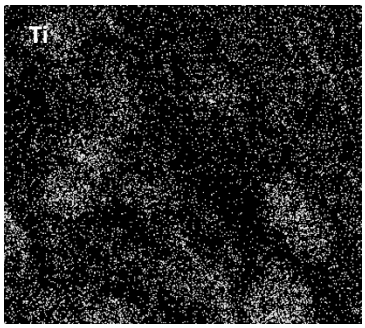

(a4) Ti EDX mapping of A250_II_5

Figure 4.24: STEM images and EDX data for A250 batch powder **(a1)** STEM image of A250_II_5, **(a2)** Fe EDX mapping of A250_II_5, **(a3)** Cr EDX mapping of A250_II_5, **(a4)** Ti EDX mapping of A250_II_5, **(b1)** STEM image of A250_I_10, **(b2)** Fe EDX mapping of A250_I_10, **(b3)** Cr EDX mapping of A250_I_10, **(b4)** Ti EDX mapping of A250_I_10, **(c1)** STEM image of A250_II_30, **(c2)** Fe EDX mapping of A250_II_30

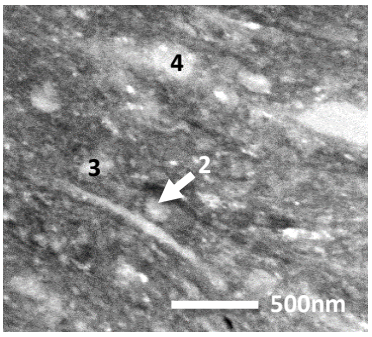

Spectrum 2
Al: 90.0 at.%
Ti: 1.0 at.%
Cr: 1.3 at.%
Fe: 7.7 at.%
Spectrum 3
Al: 87.1 at.%
Ti: 1.3 at.%
Cr: 2.6 at.%
Fe: 9.0 at.%

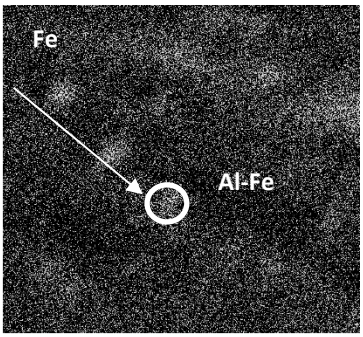

(b1) STEM image of A250_I_10 (b2) Fe EDX mapping of A250_I_10

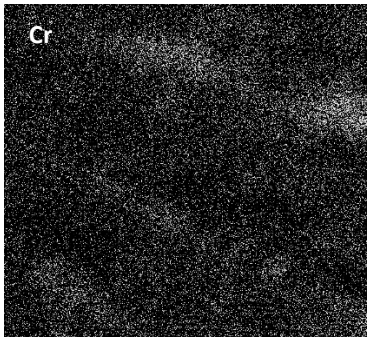

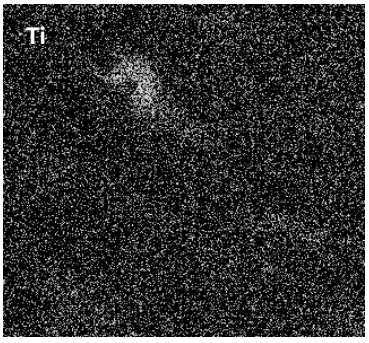

(b3) Cr EDX mapping of A250_I_10 (b4) Ti EDX mapping of A250_I_10

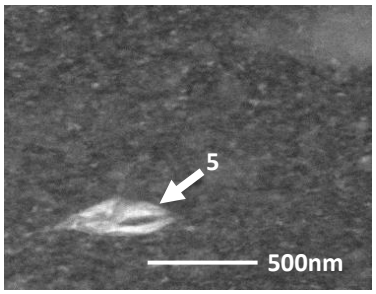

Spectrum 5
Al: 77.5 at.%
Ti: 1.4 at.%
Cr: 5.0 at.%
Fe: 14.7 at.%
Ni: 1.4 at.%

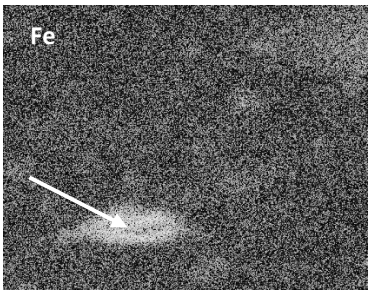

(c1) STEM image of A250_II_30 (c2) Fe EDX mapping of A250_II_30

Figure 4.24: STEM images and EDX data for A250 batch powder **(a1)** STEM image of A250_II_5, **(a2)** Fe EDX mapping of A250_II_5, **(a3)** Cr EDX mapping of A250_II_5, **(a4)** Ti EDX mapping of A250_II_5, **(b1)** STEM image of A250_I_10, **(b2)** Fe EDX mapping of A250_I_10, **(b3)** Cr EDX mapping of A250_I_10, **(b4)** Ti EDX mapping of A250_I_10, **(c1)** STEM image of A250_II_30, **(c2)** Fe EDX mapping of A250_II_30

4.3.4 Alumina distribution

The STEM images, EDX mappings and spectra for the C250 batch powers are shown in Figure 4.25. For the C250_II_5 sample, the particle labelled as (1) should be a γ-Al_2O_3 cluster, as confirmed by the EDX spectrum in Figure 4.25 (a6). The particle (2) in Figure

4.25 (a) showed a chemical composition as it is expected for the icosahedral phase, in agreement with the compositions observed by *Kimura* et al (Kimura, Sasamori et al. 2000).

After 10 hs of milling, the γ-Al_2O_3 distribution was improved and observed in small clusters and layers, as can be seen in Figure 4.25 (b1); EDX analysis from position (3) revealed the γ-Al_2O_3. After 30 hs of milling, the γ-Al_2O_3 clusters and layers disappear and are finally homogenously distributed and embedded in the nanoquasicrystalline Al alloy matrix.

In Figure 4.25(c1) can be observed the γ-Al_2O_3 particles as a dark round shape particles; an EDX composition is given for the particle marked as (4) in the same Figure 4.25(c1). The sizes of 30 γ-Al_2O_3 clusters are measured for the C250_II_10 and C250_II_30 samples. The average cluster sizes for the C250_II_10 and C250_II_30 samples are 108±29nm and 90±29nm. Compared with the C250_II_5 samples with very thick γ-Al_2O_3 bands, mechanical milling is considered to be effective in processing homogeneous nanocomposites. The mechanisms for the distribution of γ-Al_2O_3 are going to be further discussed in Chapter 5 and 7, together with other composites powders processed with different milling speeds.

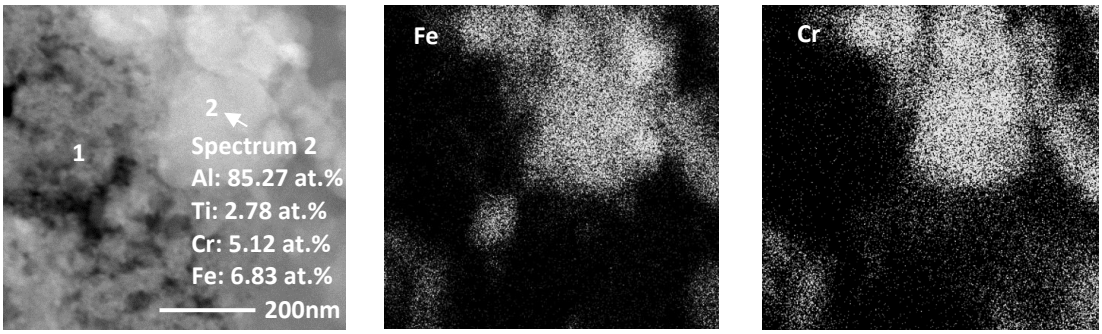

(a1) C250_II_5 (a2) C250_II_5 (a3) C250_II_5

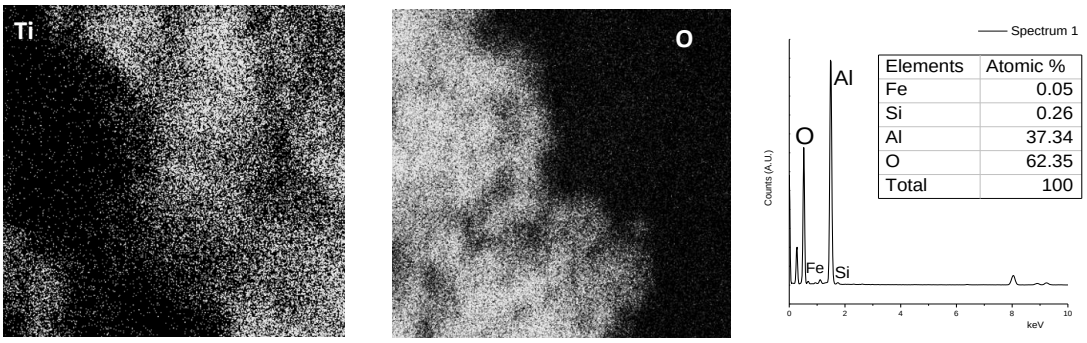

(a4) C250_II_5 (a5) C250_II_5 (a6) C250_II_5

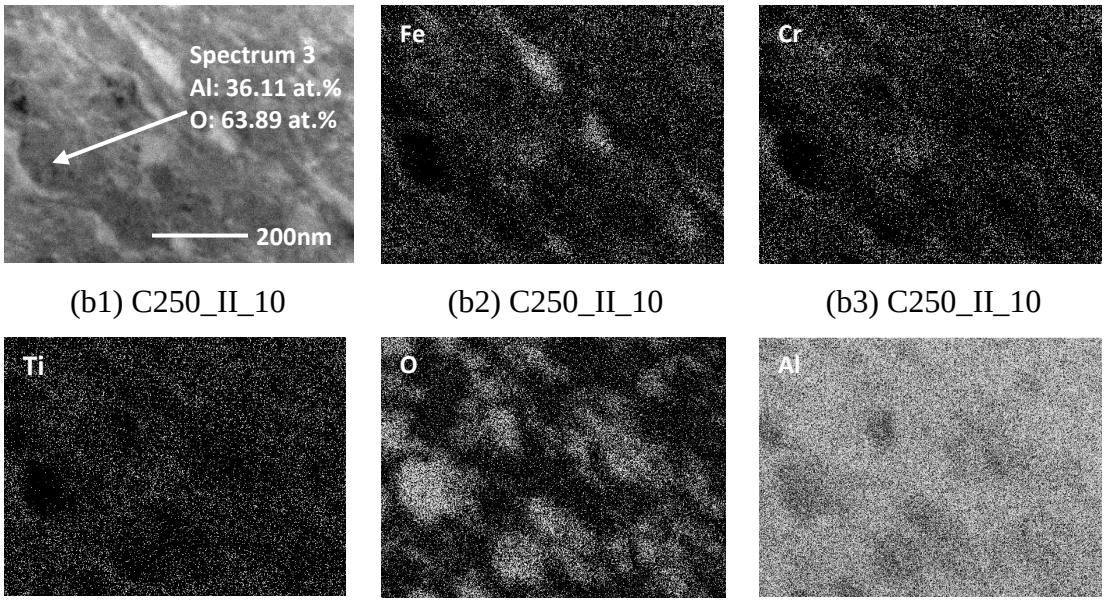

(b1) C250_II_10 (b2) C250_II_10 (b3) C250_II_10

(b4) C250_II_10 (b5) C250_II_10 (b6) C250_II_10

Figure 4.25: STEM and EDX data for C250 batch powder **(a1)** STEM image: C250_II_5, **(a2)** Fe EDX mapping, **(a3)** Cr EDX mapping, **(a4)** Ti EDX mapping, **(a5)** O EDX mapping, **(a6)** EDX spectrum in position 1, **(b1)** STEM image: C250_II_10, **(b2)** Fe EDX mapping, **(b3)** Cr EDX mapping, **(b4)** Ti EDX mapping, **(b5)** O EDX mapping, **(b6)** EDX spectrum in point 1, **(c1)** STEM image: C250_II_30, **(c2)** Fe EDX mapping, **(c3)** O EDX mapping

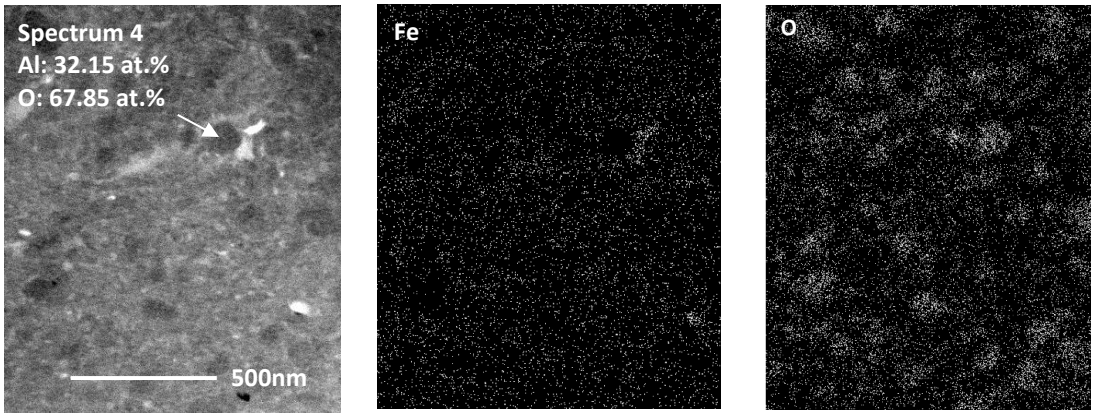

(c1) C250_II_30 (c2) C250_II_30 (c3) C250_II_30

Figure 4.25: STEM and EDX data for C250 batch powder **(a1)** STEM image: C250_II_5, **(a2)** Fe EDX mapping, **(a3)** Cr EDX mapping, **(a4)** Ti EDX mapping, **(a5)** O EDX mapping, **(a6)** EDX spectrum in position 1, **(b1)** STEM image: C250_II_10, **(b2)** Fe EDX mapping, **(b3)** Cr EDX mapping, **(b4)** Ti EDX mapping, **(b5)** O EDX mapping, **(b6)** EDX spectrum in point 1, **(c1)** STEM image: C250_II_30, **(c2)** Fe EDX mapping, **(c3)** O EDX mapping

4.4 Microstructure stability

DSC runs were conducted for each sample at 10K/min, 20K/min, 40K/min and 80K/min heating rate to investigate the decomposition temperature as well as the activation energy for the metastable phases. Figure 4.26 shows the DSC curves taken at a heating rate of 40K/min for the unmilled nanoquasicrystalline $Al_{93}Fe_3Cr_2Ti_2$ alloy powder, the ball milled nanoquasicrystalline alloy (A250) and the ball milled nanocomposite (C250) powders for different milling time. It is observed that the unmilled alloy powder (A0) shows a symmetric exothermic peak with the peak temperature at 554.4˚C. Similar DSC curve for the same nanoquasicrystalline alloy atomised powders with the same particle size range was observed by *Todd* et al (Todd, Chlup et al. 2004) with a peak temperature at 522˚C. They also observed that the peak temperature decreases as the atomised powder particle size decreases. *Audebert* et al. [3] and *Galano* et al. [21] studied the same alloy produced

by melt-spinning. *Audebert* et al, found an overlapped phase transformation with two peaks, and *Galano* et al, using also the same heating rate of 40 K/min found an asymmetric peak (peak temperature of ~510 ˚C) with a shoulder at the lower temperature side. None of them found icosahedral phase at the end of the exothermic peak. It is known that the melt-spinning technique provide higher cooling rate than the gas atomisation yielding a microstructure with higher free energy, i.e. higher phase transformation driven force (Duflos and Stohr 1982). In Figure 4.26(a) is observed that as the milling time increases, the symmetric exothermic peak of the un-milled atomised alloy powder (A0) becomes non-symmetric and at after 10 hours of milling a clear pre-peak grows at the lower temperature side. For the C250 powders in Figure 4.26 (b), the DSC exothermic peak remains quite symmetric during the first 3 hours of milling with a sustained shift to lower temperature as the milling time increases. From 4 hours of milling the exothermic peak becomes non-symmetric developing an overlapped exothermic peak at lower temperature, similar as observed for the A samples.

The use of Gaussian distribution to fit and analyse the overlapped exothermic DSC peaks is very common and provides good results as is reported in the literature, particularly for the precipitation process in Al alloys (Milkereit, Kessler et al. 2009). All the DSC curves taken at 40 K/min for A250 and C250 samples were fitted and overlapped peaks decomposed in two exothermic peaks using Gaussian distributions. The fitting curves and the calculated enthalpy values involved in each individual exothermic peak are given in Figure 4.26(a) for A250 samples and in Figure 4.26(b) for C250 samples. The fittings were done with OriginPro by maximising the R square value with all Gaussian parameters set free.

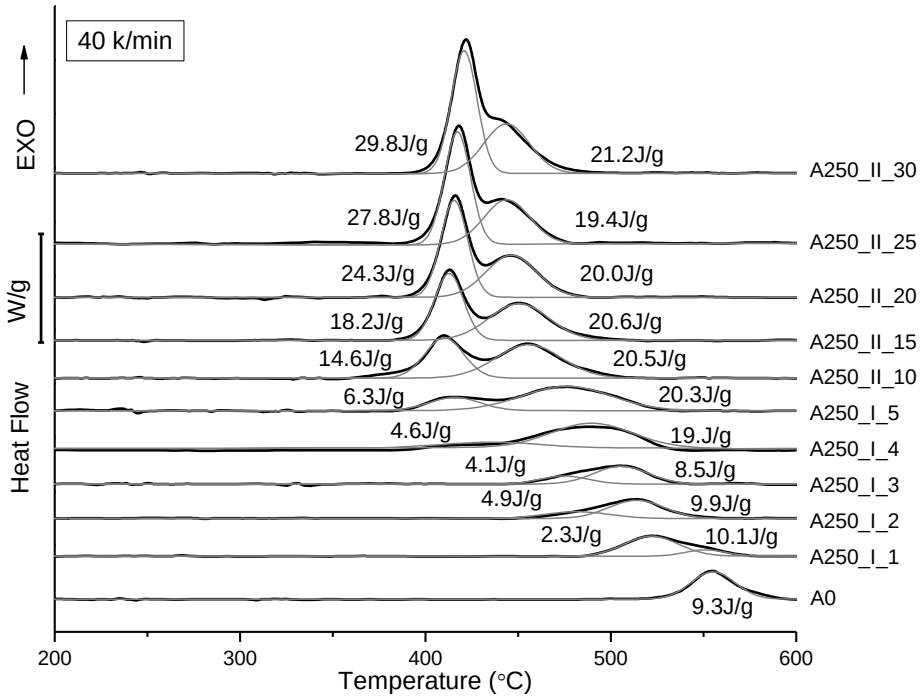

(a)

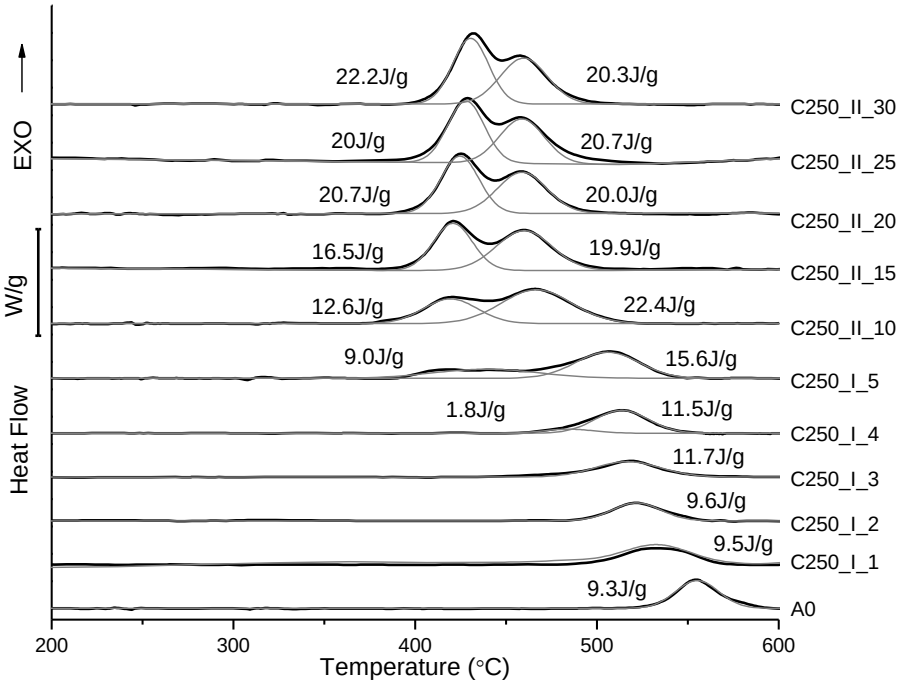

(b)

Figure 4.26: DSC curves at 40 K/min of **(a)** A250 milled powders, and **(b)** C250 milled powders. Overlapped peaks were fitting with two Gaussian distributions. Enthalpy value determined for each peak is given. A0: un-milled atomised alloy powder.

The activation energy (E_a) values for each exothermal peak were determined according to the Kissinger method (Kissinger 1956). The details for this have been explained in section 3.4.1 in Chapter 3. All the calculated activation energy values were plotted in Figure 4.27. For the as-atomised A powder (A0) the exothermic transformation consisting in a quite symmetric peak with an activation energy of E_a = 297±20 kJ/mol. There is a general tendency for both peaks also for both A250 and C250 powders in decreasing the activation energy as the milling time increases reaching a near constant value at 5/10 hours of milling as E_a = ~ 150 kJ/mol for the peak 1 and ~ 175 kJ/mol for the peak 2[1]. The C250 nanocomposite powder shows a lower decreasing rate of the E_a value during the first 5 hours of milling in comparison to the A250 alloy powders.

[1] For the DSC curves with overlapping peaks, peak 1 means the peak at lower temperatures in the DSC curve, and peak 2 means the peak at higher temperatures in the DSC curve.

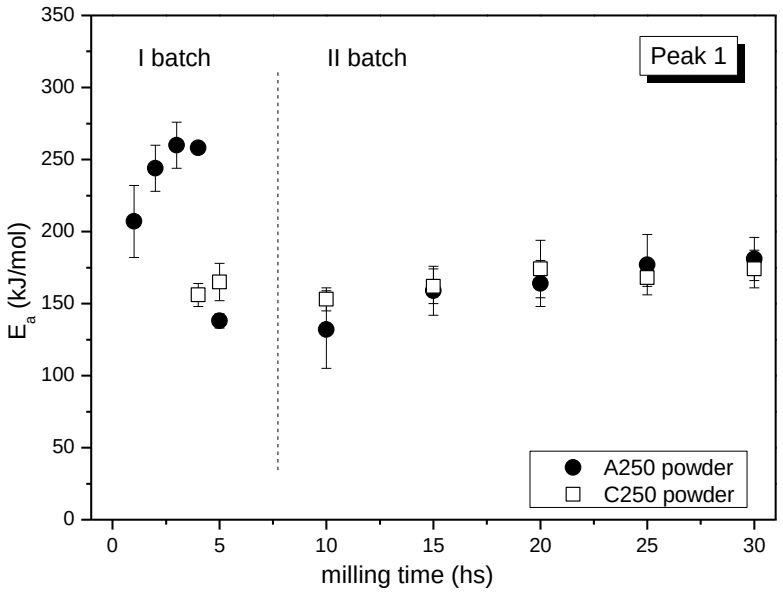

(a)

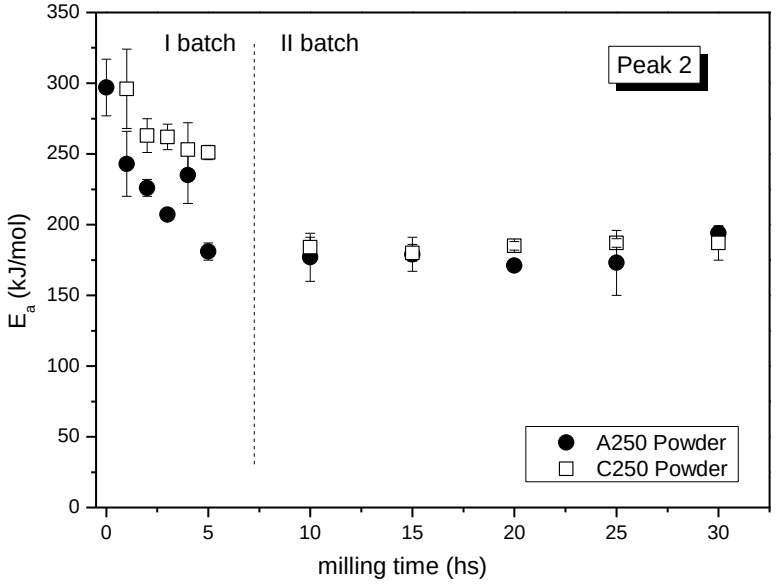

(b)

Figure 4.27: Apparent activation energy for the two exothermal peaks observed in samples of both the nanoquasicrystalline alloy powder (A250) and the nanocomposite powder (C250) against the ball milling time. **(a)** Apparent activation energy for peak 1, **(b)** Apparent activation energy for peak 2.

The A250_I_10 sample was heat treated at 405°C, 410°C and 550°C, as explained in section 3.4.2 in Chapter 3. The X-ray diffractograms of the A250_I_10, A250_I_10_405, A250_I_10_410 and A250_I_10_550 samples are shown in Figure 4.28. It is observed that Al peaks are narrower as the heat treatment temperature increases. Probably a recrystallization and coarsening process took place increasing the Al crystallite size from 48±12 nm (A250_I_10) to 176±55 nm (A250_I_10_410) and to 432±109 nm (A250_I_10_550), as measured by TEM. After the heat treatment up to 405 ˚C, the peaks corresponding to the icosahedral quasicrystalline phase show a slightly lower intensity than the sample without heat treatment (A250_I_10). Several peaks of Al_6Fe, Al_3Ti, $Al_{13}Fe_4$ and $Al_{13}Cr_2$ intermetallic phases are observed in the X-ray diffractogram, which intensity increases meanwhile the intensity of the icosahedral phase peaks decreases as the temperature of the heat treatment increases. At 550 ˚C, the presence of a small fraction of the icosahedral phase cannot be confirmed as intermetallics have several peaks in the 2θ range where should be the peaks of the icosahedral phase. All the peak positions were listed in Table 4.4.

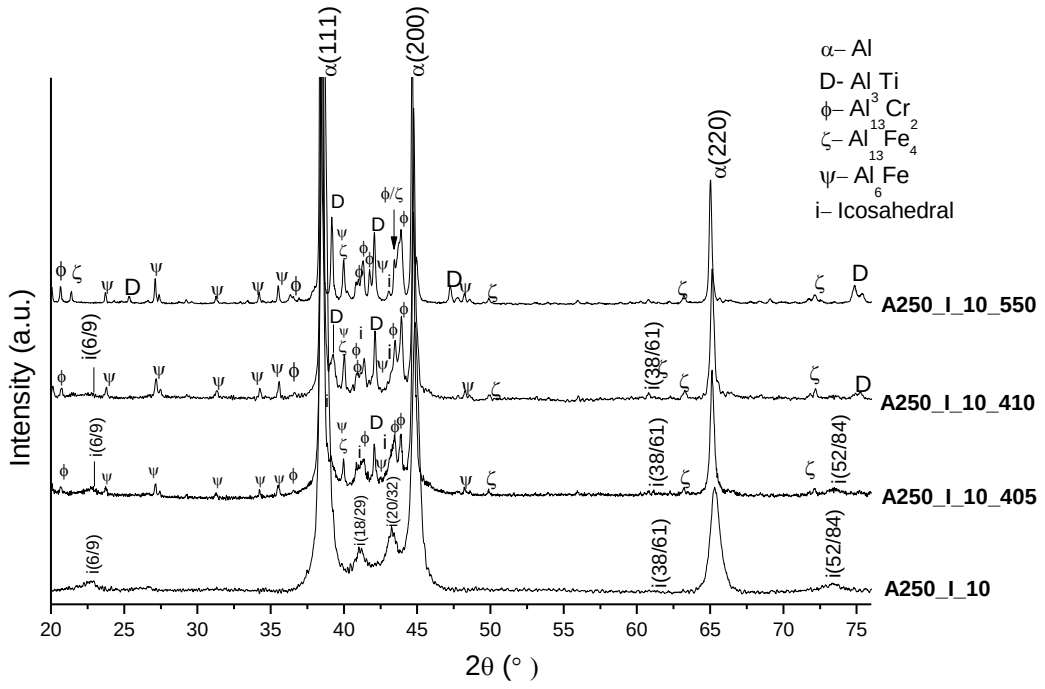

(a)

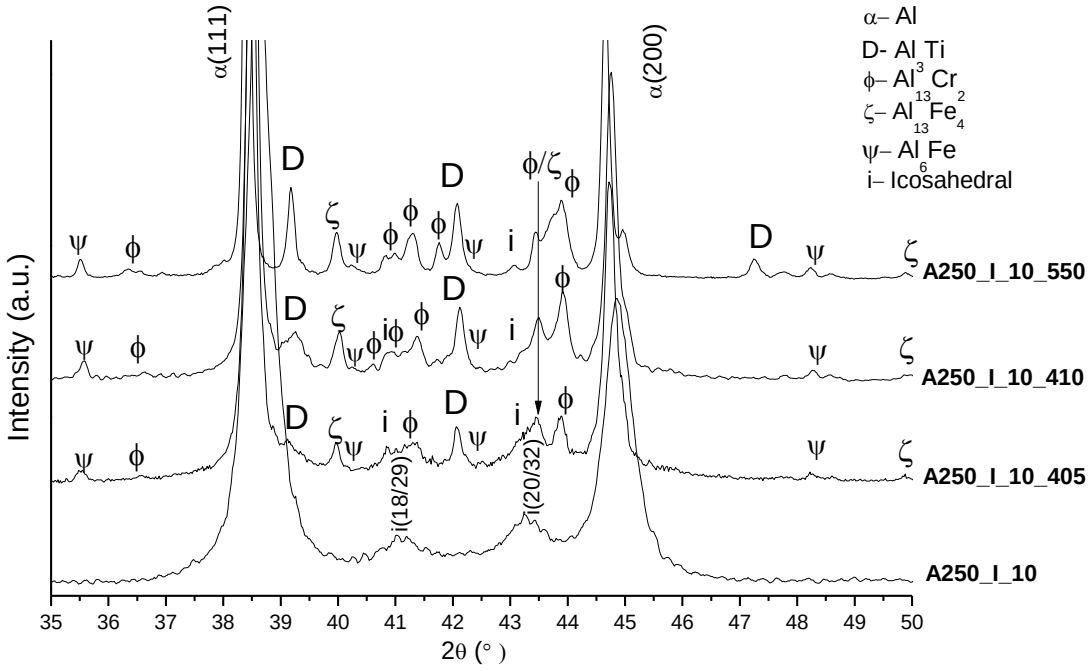

(b)

Figure 4.28: X-ray diffractograms of the as ball milled A250_I_10 sample and heat treated A250_I_10_405, A250_I_10_410 and A250_I_10_550 samples **(a)** 20-76°, **(b)** 35-50°

Sample	2θ position in XRD patterns				
	D-Al_3Ti	ϕ-$Al_{13}Cr_2$	ζ-$Al_{13}Fe_4$	ψ-Al_6Fe	i-Icosahedral
A250_I_10	/	/	/	/	22.9° 41.1° **43.3°** 61.4° 73.5°
A250_I_10_405	**39.2°** 42.1°	20.7° 36.6° 41.3° 43.4° **43.9°**	40.0° **43.4°** 50.0° 63.2° 72.2°	23.8° 27.2° 31.3° 34.2° 35.6° 40.1° **42.2°** 48.2°	22.9° 41.1° **43.3°** 61.4° 73.5°
A250_I_10_410	**39.2°** 42.1° 75.0°	20.7° 36.6° 40.6° 41.0° 41.3° 43.4° **43.9°**	40.0° **43.4°** 50.0° 63.2° 72.2°	23.8° 27.2° 31.3° 34.2° 35.6° 40.1° **42.2°** 48.2°	/
A250_I_10_550	25.4° **39.2°** 42.1° 47.2° 75.0°	20.7° 36.6° 41.0° 41.3° 43.4° **43.9°**	21.4° 40.0° **43.4°** 50.0° 63.2° 72.2°	23.8° 27.2° 31.3° 34.2° 35.6° 40.1° **42.2°** 48.2°	/

Table 4.4: Peak positions of various intermetallics in annealed sample (2θ positions corresponding to 100% intensity are in bold)

Figure 4.29(a) shows a deformed icosahedral particle in A250_I_10_410, confirmed by a fivefold CBDP in the inset. Figure 4.29(b) shows an Al_6(Fe,Cr) (at.%) near rod shape particle with a length of ~120 nm, identified with the CBDP from [001] zone axis as observed in Figure 4.29(c). The EDX spectrum, shows that the Al_6(Fe, Cr) particle also contains a small fraction of Ti in solid solution. Figure 4.29(d) is a TEM BF image of

A250_I_10_550. No quasicrystals were found in TEM. Particle (3) is suspected to be an intermetallic particle based on the EDX spectrum in the inset in Figure 4.29(d). One Al grain labelled as (4) is identified with a CBDP in the inset in Figure 4.29(d). For the A250_I_10_550 sample, the Al grains always sit between the intermetallic particles. TEM observation also shows that the Al_3Ti particles are much smaller that the Al-Fe and Al-Cr based particles, in both A250_I_10_410 and A250_I_10_550.

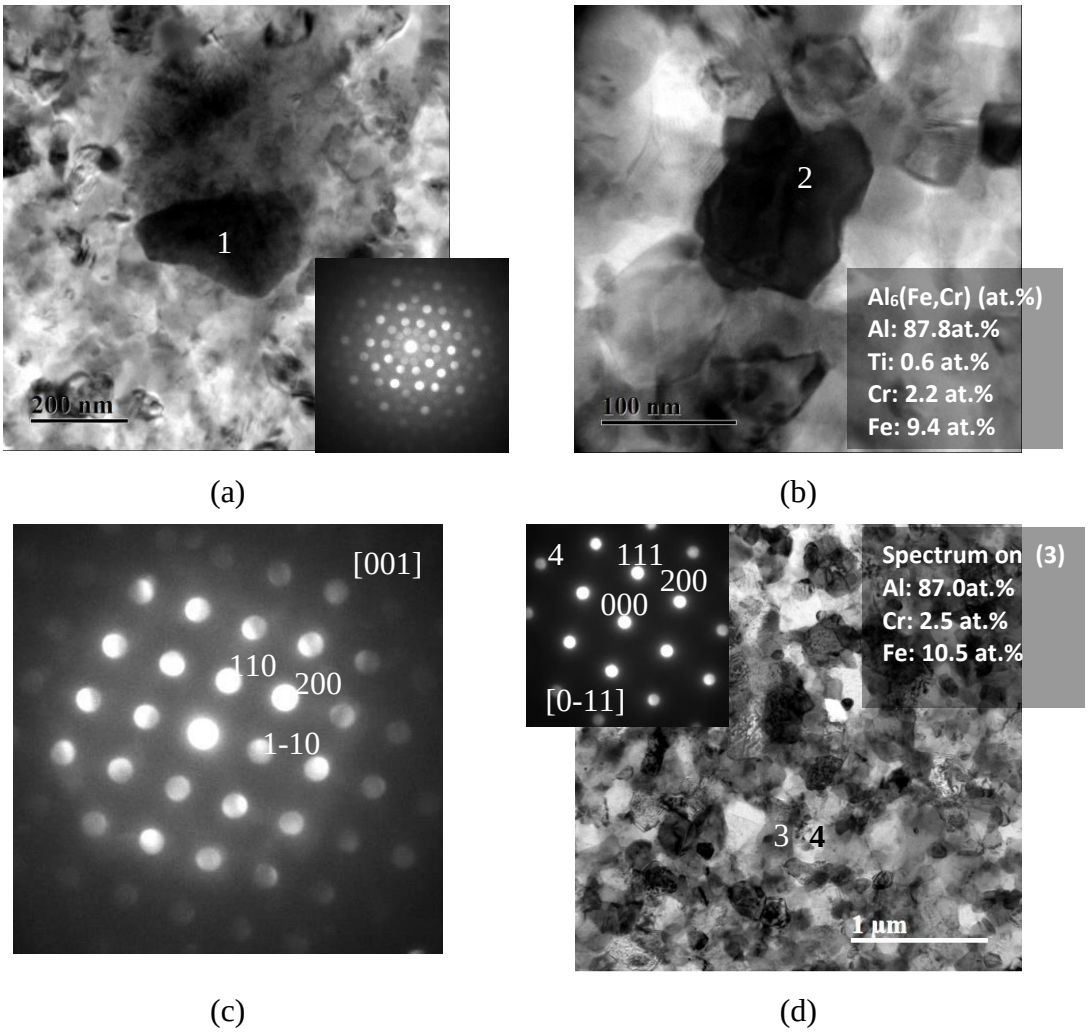

Figure 4.29: (a) The TEM BF image of A250_I_10_410, with a quasicrystal identified with a fivefold CBDP, **(b)** the Al_6(Fe, Cr) intermetallic in A250_I_10_410, **(c)** the CBDP of the Al_6(Fe, Cr) intermetallic in (b), **(d)** the TEM BF image of A250_I_10_550 with an intermetallic particle identified with EDX and an Al grain identified by a CBDP

EDX mappings were done on the A250_I_10 sample and the A250_I_10_410 sample (Figure 4.30(a) and (b)) to investigate the exothermal peaks in the DSC curves. It is observed that in the milling process the Fe, Cr and Ti could be detected in the matrix. After the DSC heat treatment, Fe, Cr and Ti precipitated into intermetallics, which matches the TEM BF image in Figure 4.29(b) and the X-ray diffractograms in Figure 4.28.

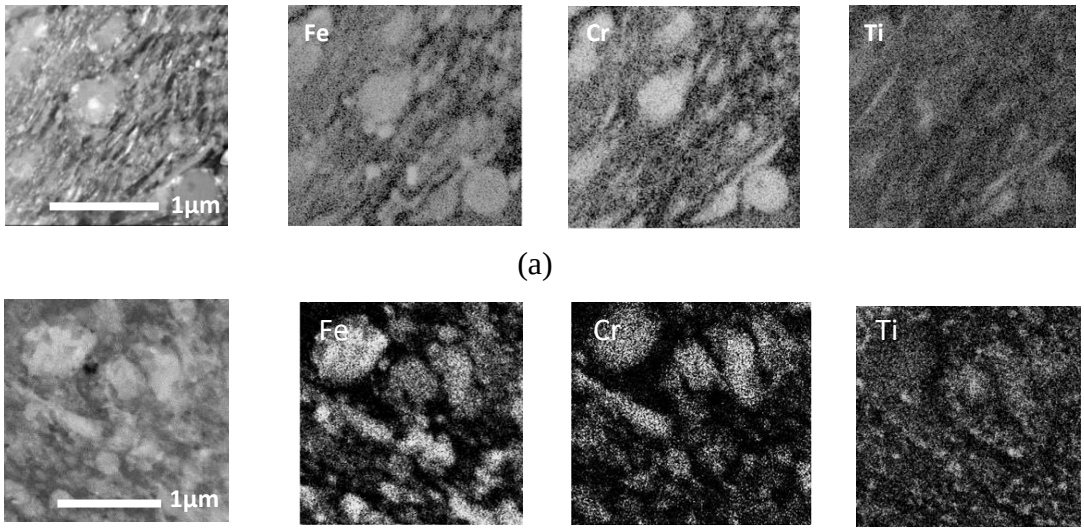

Figure 4.30: (a) STEM images and EDX maps of A250_I_10, **(a)** STEM images and EDX maps of A250_I_10_410

The solute content in the Al grain of the nanoquasicrystalline alloy milled for different milling times (5, 10 and 30 hours) and on the A250_I_10 heat treated at 410 ˚C was carefully statistically measured by EDX on thin parts of TEM samples. Areas to be measured were explored by TEM BF and in STEM mode to avoid the presence of intermetallics particles that could affect the measurements. The results are shown in Table 4.5. It is observed that the solute content dissolved in the Al grain increases as the milling time increases. The ball milling caused super saturation in the Al grains, as the equilibrium

solubility for Fe, Cr and Ti in fcc Al are 0.03 at.%, 0.01 at.% and 0.2 at.% respectively (Mehrer, Stolica et al. 1990, Zawrah and Shaw 2003). After the heat treatment at 410˚C of the A250_I_10 sample most of the solute has been segregated and precipitated as intermetallics particles as observed by comparison of X-ray diffractograms in Figure 4.28 and EDX mappings in Figure 4.30.

Sample	A0	A_II_5		A_I_10	A_II_30	A_I_10_410
Al grain size (nm)	1535±514	(Fine grains) 121±42	(Ultra-fine grains) 66±19	48±12	27±04	176±55
Al (at.%)	99.27±0.09	98.71±0.57	97.45±0.88	95.85±0.79	94.11±0.48	99.27±0.17
Ti (at.%)	0.42±0.11	0.87±0.54	1.48±0.61	1.39±0.15	1.66±0.17	0.52±0.11
Cr (at.%)	0.27±0.03	0.28±0.09	0.60±0.25	1.17±0.28	1.66±0.17	0.12±0.05
Fe (at.%)	0.04±0.03	0.14±0.06	0.47±0.47	1.59±0.41	2.57±0.21	0.09±0.02

Table 4.5: Solute content in the FCC-Al grain of the A250_II_5, A250_I_10, A250_I_30 and A250_I_10_410 samples.

4.5 Hardness of the powders

The hardness of the powders is shown in Figure 4.31. In the first 5 hours of milling the hardness of both the A250 batch and the C250 batch increases dramatically. From 10 hours onwards, the growing speed of hardness value is much slower. The A250 and C250 batches of powders reach the highest microhardness value of 515 kg/mm^2 and 638 kg/mm^2 after 25 and 30 hours of milling respectively. In general, for the same milling time the C250 batch powder has higher microhardness than the A250 batch. The hardness of the A250 batch and the C250 batch powders will be further discussed in Chapter 7.

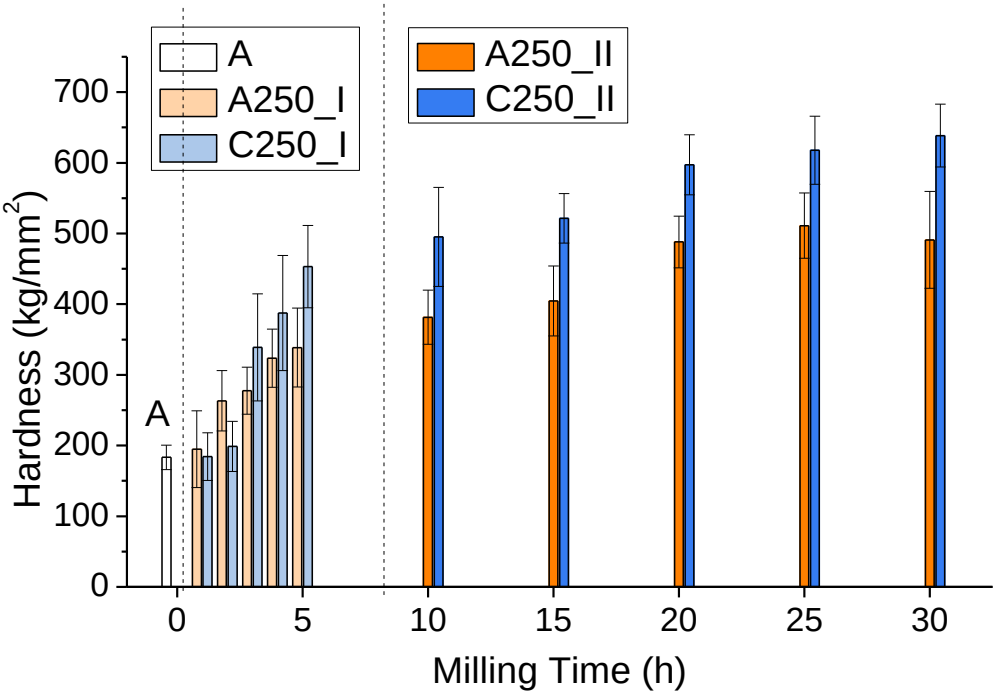

(a)

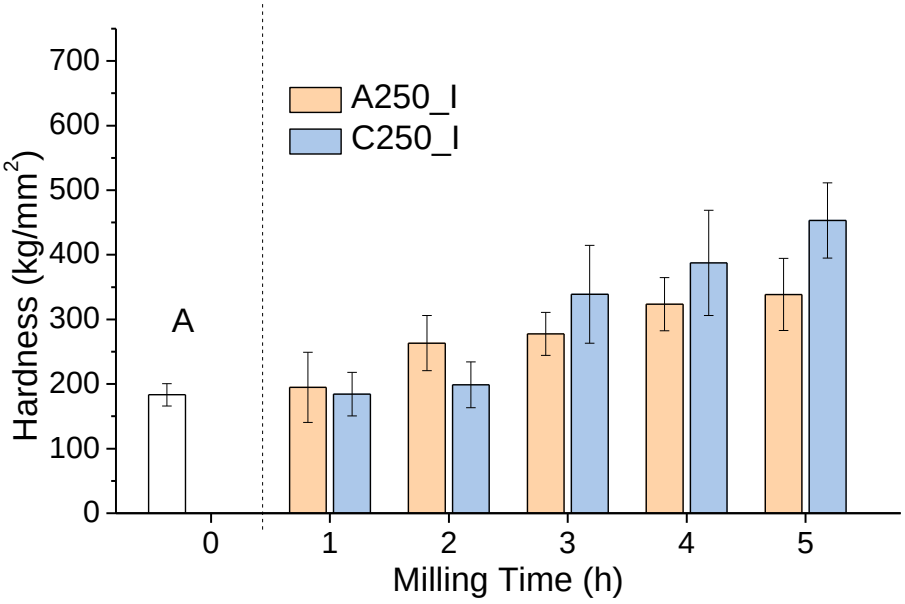

(b)

Figure 4.31: Hardness of A250 and C250 with milling time after **(a)** 0-30h **(b)** a zoom in diagram for 0-5h

4.6 The effects of ball to powder ratio

For both the pure alloy (A250 batch) and the nanocomposites (C250 batch) powders, two sub-batches were processed: the I batch with 1-10 hours of milling, and the II batch with 5-30 hours of milling. During each stop, small amount of powder (0.5g) was taken out for analysis. This will simplify the processing procedure for processing powders with different milling time, but the BPR will slightly increase with the milling time. By processing two batches, the BPR changes are controlled to a limited range to prevent affecting the powder properties significantly.

Although such methods were used by previous studies (Hesabi, Simchi et al. 2006, Galano, Marsh et al. 2015), it is necessary to verify whether such BPR changes have significant effects on the properties of the powder. For all the four batches (C250_I, C250_II, A250_I and A250_II), the initial BPR 10 is increased to 13.33 at the end of the milling, as shown in Table 4.6. As observed, both the I batch and the II batch of powders contain samples after 5 and 10 hours of milling. The samples after 10 hours of milling were divided into two groups, which are (1) the A250_I_10 and A250_II_10 samples and (2) the C250_I_10 and C250_II_10 samples. The samples corresponding to the I batch have higher BPR values than the II batch. By comparing the properties, the effects of small BPR changes on the properties of the powders are verified.

Milling time (C/A250_I batch) (h)	0 ~ 1	1 ~ 2	2 ~ 3	3 ~ 4	4 ~ 5	5 ~ 10
BPR	10	10.53	11.11	11.76	12.5	13.33
Milling time (C/A250_II batch) (h)	0 ~ 5	5 ~ 10	10 ~ 15	15 ~ 20	20 ~ 25	25 ~ 30
BPR	10	10.53	11.11	11.76	12.5	13.33

Table 4.6: The BPR ratio changes for the C250 and A250 batches of powders

Figure 4.32 is SEIs of the A250_I_10, A250_II_10, C250_I_10 and C250_II_10 samples. From the SEIs the morphologies of the A250_I_10 and A250_II_10 samples are quite similar. The C250_I_10 and C250_II_10 samples in Figure 4.32 (c) and (d) are also indistinguishable.

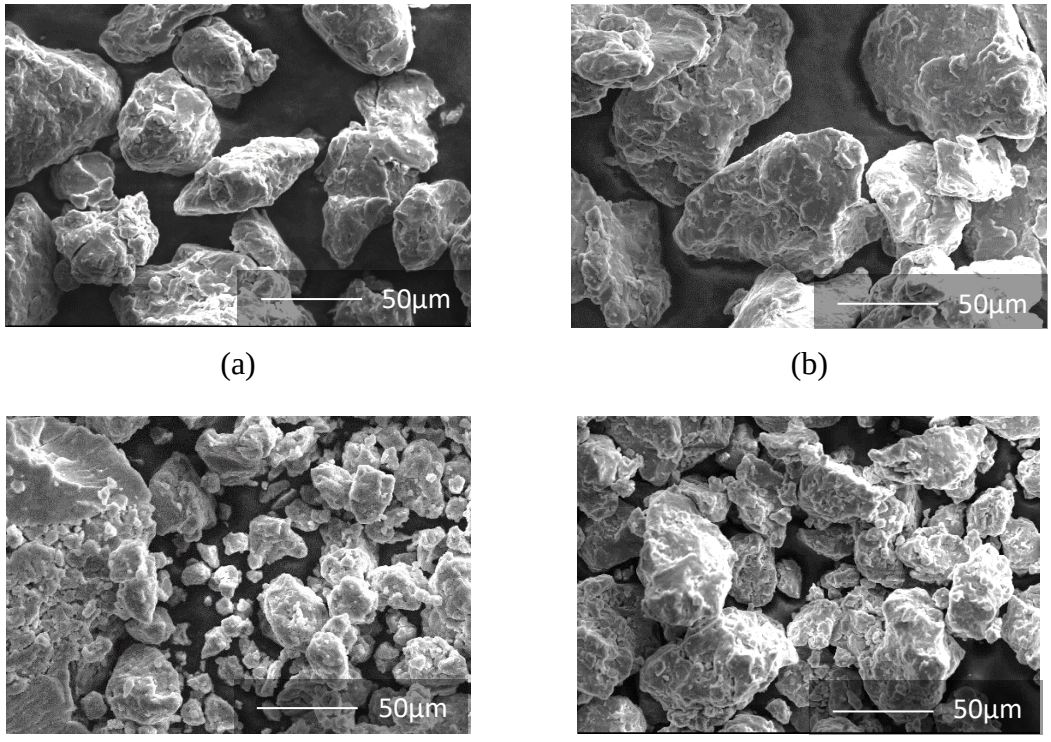

(a) (b)

(c) (d)

Figure 4.32: SEIs of the A250 and C250 batches **(a)** A250_I_10, **(b)** A250_II_10, **(c)** C250_I_10, **(d)** C250_II_10

For the phase components, the X-ray diffractograms of A250_I_10, A250_II_10, C250_I_10 and C250_II_10 powders are already provided in Figure 4.19(a) and (b). The X-ray diffractograms for samples A250_I_10 and A250_II_10 as well as for samples C250_I_10 and C250_II_10 do not show differences between them, which suggests that at the X-ray diffractogram resolution the small differences in the BPR processing condition (see Table 4.6) doesn't affect the phases present in those samples.

The crystallite sizes and the strains calculated through Williamson-Hall method were plotted in Figure 4.33. Once again, the comparisons between samples A250_I_1s0 with A250_II_10 and C250_I_10 with C250_II_10 show that measured values of the Al crystallite size are inside of the measurements error.

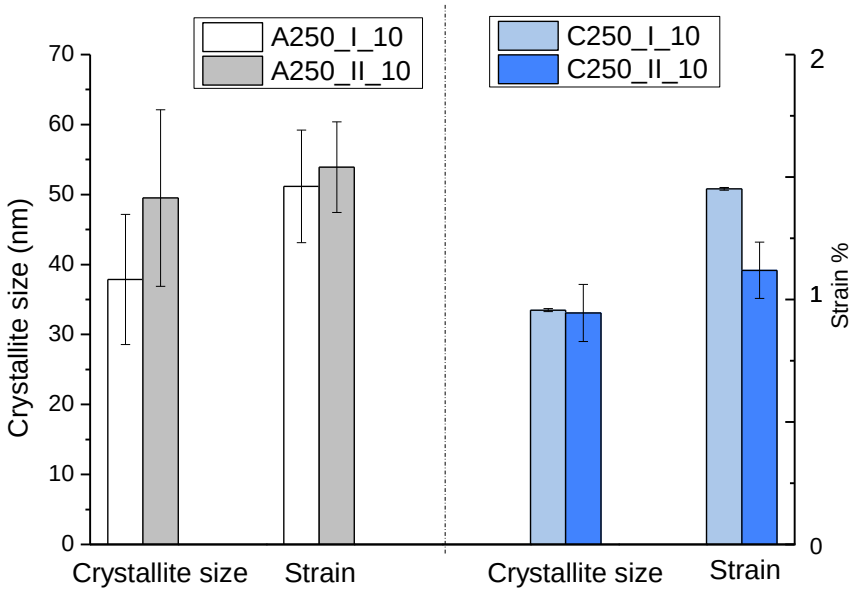

Figure 4.33: Crystallite size and strain of the A250 and C250 batches powder after 10 hours of milling

The DSC runs of the A250_I_10, A250_II_10, C250_I_10 and C250_II_10 were plotted in Figure 4.34. The temperatures and the enthalpy values corresponding to peak 1 and peak 2 are labelled. As shown, the peak temperature values and enthalpies for the A250_I_10 and A250_II_10 are similar, and the peak temperature values and enthalpies for the C250_I_10 and C250_II_10 are also indistinguishable.

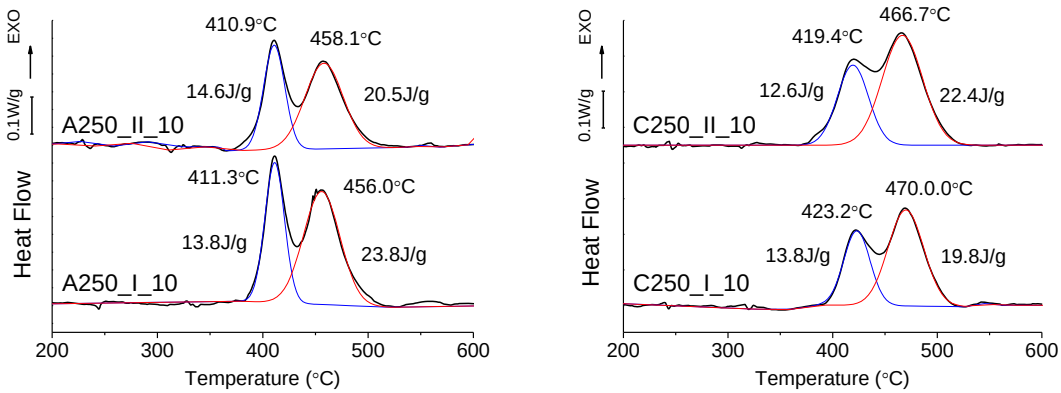

(a) (b)

Figure 4.34: DSC curves and activation energy data **(a)** DSC curves of A250_I/II_10, **(b)** DSC curves of C250_I/II_10

Table 4.7 summarises the measured numerical data including the particle sizes, the activation energy for peak 1 and peak 2 in DSC runs, and the crystallite sizes. In the literature, large ball to powder ratio is powerful in breaking and cold welding the powder (Bhattacharya, Bellon et al. 2004) and generating more collisions per unit time (Suryanarayana 2001). Therefore, a refined microstructure could be obtained in a shorter time. In the current work, the small differences in the BPR used for both batches almost do not affect much the microstructure evolution during milling under the processing condtions used.

Batch	D_p (µm)	E_a (kJ/mol)*		d_{Al} (nm)	BPR at the end of milling
		Peak 1	Peak 2		
A250_I_10	83.3	162 ± 23	188 ± 11	38 ± 9	13.3
A250_II_10	100.8	132 ± 27	177 ± 17	49 ± 13	10.5
C250_I_10	50.7	143 ± 15	185 ± 9	34 ± 0	13.3
C250_II_10	55.6	153 ± 8	184 ± 7	33 ± 4	10.5

Table 4.7: the mean value of powder particle distribution (D_p) , activation energy (E_a) , Al crystallite size (d_{Al}) and Vickers hardness (HV_{10g}) of the alloy and the composite powders

4.7 Discussion

4.7.1 Particle size changes

During mechanical milling of the nanoquasicrystalline alloy and nanocomposites, the particle sizes increase in early milling hours (Figure 4.16), because cold welding dominates in this stage (Fogagnolo, Velasco et al. 2003). The A250 batch powders have faster cold-welding rate, and reach the maximum value of 135µm after 3 hours of milling, while the C250 batch powders have minor particle size changes in this stage, as shown in Table 4.2. This is because the nanoparticles could smear on the surfaces of the matrix particles and form a network of inclusion at early milling hours, as shown in Figure 4.18(a). Under this circumstance, nanoscale brittle particles surrounding the matrix powders prevent cold welding to take place (Hesabi, Simchi et al. 2006). This outcome is inconsistent with a variety of studies (Hesabi, Simchi et al. 2006, Tousi, Rad et al. 2009, El-Kady and Fathy 2014). The particle sizes of the A250 and C250 batches decrease after 3 hours and 10 hours of milling respectively. This indicates a shift from cold-welding dominating stage to a fracturing dominating stage (Benjamin and Volin 1974).

For the same milling time, the A250 batch has higher particle size than the C250 batch powders. Apart from the reinforcement particles preventing the cold welding, the presence

of hard particles in the nanocomposites powder also results in an increase in local deformation near the reinforcement particles (Hesabi, Simchi et al. 2006, Tousi, Rad et al. 2009). This causes an increase in the hardness of the matrix powder and a decrease in the weldability (Tousi, Rad et al. 2009).

Hesabi et al. (Hesabi, Simchi et al. 2006) milled pure aluminium powder with the same milling speed (250rpm) and initial ball to powder ratio (10:1). In their work, flake shaped aluminium particles were observed after 8 hours of milling. However, no flake particles were found in the milled A250 and C250 powders, as shown in Figure 4.17. The possible explanation is the nanoquasicrystalline alloy has higher hardness (183 HV_{25g}) and lower plasticity (Young's Modulus 81GPa) (Todd, Chlup et al. 2004) than the pure Al (with a hardness of 35-50HV_{100g} and Young's modulus of 67GPa) (Davis 1998). Due to the higher Young's modulus and higher hardness, the quasicrystalline aluminium alloy matrix powders are more difficult to deform.

4.7.2 The effects of ball milling on crystallite sizes

The ball milling refines the crystallite size efficiently. As shown in Figure 4.22(a), Al grains with ~100nm can be found after only 1 hours of milling. After 3 hours of milling, some ultra-fine Al crystallites with diameter about 21±3nm were found near the quasicrystal particles, as shown in position (8) in Figure 4.22(d). This is known as the particle stimulated nucleation. When the matrix alloy contains non-deformable secondary particles, the flow of matrix encounters the particles, leading to the rotation of matrix subgrains in the vicinity of the particles (Ashby 1966). In the current work, the position (9) in Figure 4.22 is suspected to be two subgrains near the quasicrystal particles. Dislocations are generated near the particles. These deformation areas are preferable sites

for the nucleation of recrystallization, which is also known as particle stimulated nucleation (Humphreys 1977). Typically, particle stimulated nucleation requires a critical particle size larger than 1μm (Humphreys 1977, Guo, Liu et al. 2014, Parande, Manakari et al. 2017). In the current study, quasicrystalline particles have diameters from ~0.4μm to 1.0μm, less than the critical particle size. This is because the quasicrystalline matrix contains a high volume fraction (45%) of particles (Inoue and Kimura 1999). These particles are very close to each other, and form joint deformation zones (Humphreys 1977). The joint zone will have a large effective radius of curvature compared to the particle radius and therefore the critical particle size will be reduced (Humphreys 1977).

From Figure 4.20 (a), the C250 batch powders have lower crystallite sizes than the A250 batch from 10 to 30 hours of milling for the same milling time. For the γ-Al_2O_3, the particle size is only about 20~50nm. The nanoparticles are unlikely to refine the crystallite size with particle stimulated nucleation (Parande, Manakari et al. 2017). Instead, the grain refinement by adding ceramic nanoparticles is related to the high dislocation generating speed (Chung, He et al. 2003, Hesabi, Simchi et al. 2006, Poirier, Drew et al. 2010). Since γ-Al_2O_3 is a hard and non-deformable phase, it will hinder the movement of dislocations in the material (Chung, He et al. 2003). When the dislocation meets the particles, it has to bow around them, which causes faster dislocation accumulation rate compared with the materials without ceramic reinforcement particles (Dieter and Bacon 1986). The faster dislocation generating speed leads to the transformation to low-angle and high-angle grain boundaries in a lower time (Chung, He et al. 2003).

The crystallite sizes of the A250_II_5 and C250_II_5 samples are measured in TEM. The A250_II_5 sample has different microstructures, as shown in Figure 4.21. The ultra-fine

grain area and the fine grain area have grain sizes of 121±42nm and 66±19nm respectively. Both of them are lower than the grain size of C250_II_5 (130nm). As discussed in 4.7.1, in early milling hours the γ-Al_2O_3 in C250 batch smeared on the surfaces of the matrix powder. These adhered γ-Al_2O_3 particles cannot help refining the microstructure but prevent the cold welding of the matrix powder. After 10 hours of milling, γ-Al_2O_3 particles are milled into the powder. From this stage onwards, not only the milling media and the quasicrystals, but also the nanosize γ-Al_2O_3 particles help the generation of the dislocations. Compared with the γ-Al_2O_3, the quasicrystalline particles are more effective in early milling hours, since they are already located in the matrix before the ball milling.

4.7.3 The effects of ball milling on metastable phases

The ball milling process produces plastic deformation, defects such as vacancies and dislocations, and cracks in the microstructure of alloy powders and also breaks γ-Al_2O_3 agglomerates (Zhang 2004). The microstructure of the nanoquasicrystalline alloy powder consists of nanoquasicrystalline icosahedral particles embedded in an FCC-Al matrix. The Al matrix can absorb a large amount of plastic deformation; however, the quasicrystalline particles have a limited plastic deformation capacity. Moreover, the Al-Fe-Cr-Ti quasicrystal is a hard phase but thermodynamically metastable. Thus, during the ball milling process the alloy's microstructure is affected by absorbing the mechanical energy and increasing its free energy, whereas the quasicrystals trend to use the extra energy as a driven force to transform in more stable intermetallic phases.

In nanocomposite C250 samples, as discussed in the section 4.7.1, the nanosize γ-Al_2O_3 particles interfere in the welding and fracturing process of the alloy powder, which can affect the alloy's microstructure evolution with the milling time differently to the pure

alloy powder (A250).

The DSC analysis of different powder samples provides information about the stability of the milling powders allowing understanding how the milling process affected the microstructure of the alloy and the nanocomposite mixed powders. Figure 4.35 summarises the characteristic temperatures (onset and peak temperatures) and the specific enthalpies determined for each exothermic event observed in DSC runs at 40 K/min shown in Figure 4.26.

The results of heat treatments on the A250_I_10 sample (Figure 4.28, Figure 4.29 and Table 4.5) show that the first peak involves Al grain coarsening and intermetallics precipitation, whereas the second peak involves mostly quasicrystals decomposition, which leads to further intermetallic precipitation. Considering that the unmilled as-atomised alloy powder (A0) only develops one exothermic peak mainly related to the quasicrystal transformation, this suggests that during the first hours of milling some quasicrystals are partially dissolved in the Al matrix providing the solute required for the intermetallic precipitation observed in the first peak.

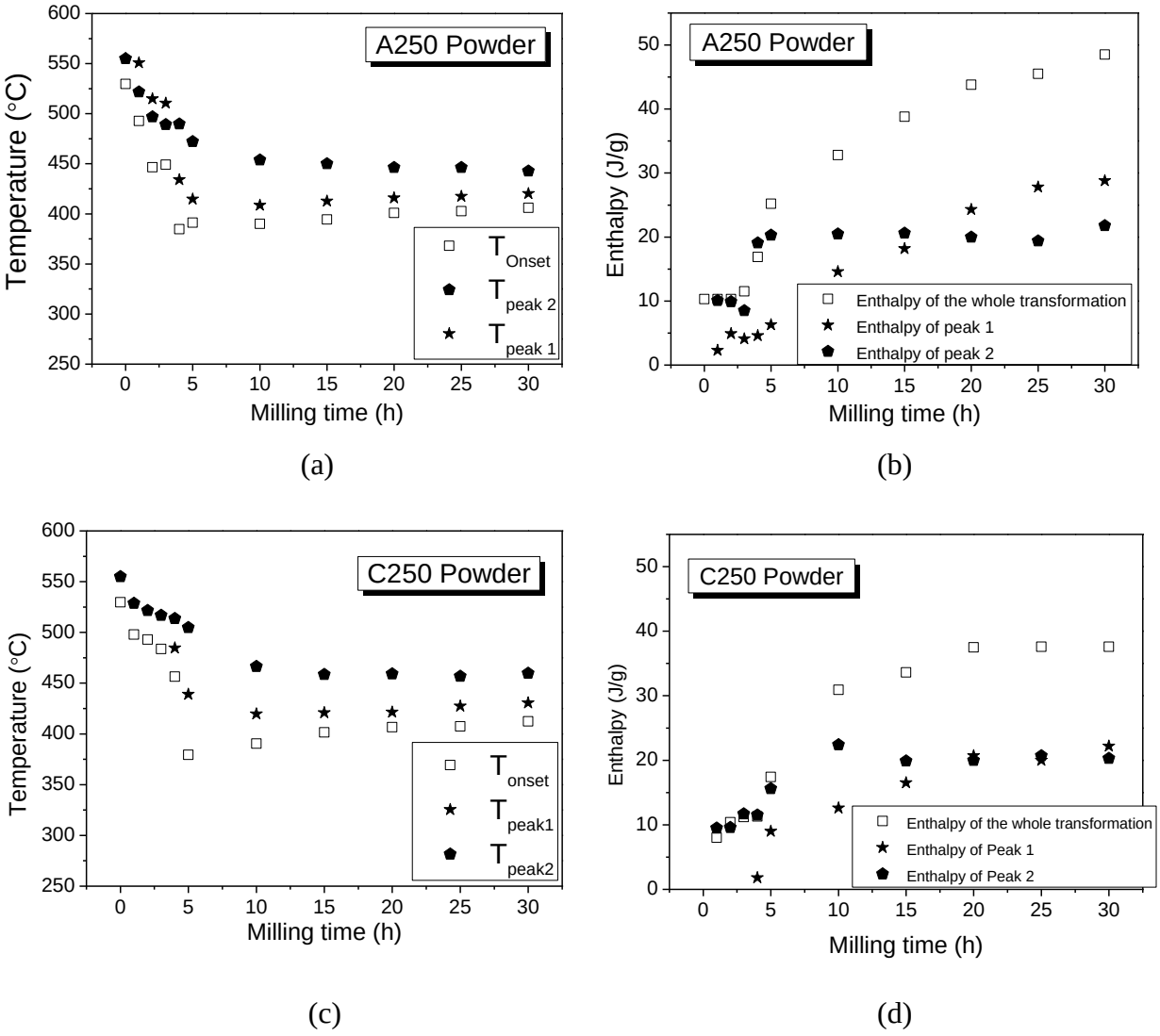

Figure 4.35: Phase transformation temperatures and enthalpies released at 40 K/min of A250 and C250 milled powder samples against the milling time. (a) Onset and peak temperatures for A250 powders; (b) specific enthalpies for phase transformation events for A250 powders; (c) Onset and peak temperatures for C250 powders; (d) specific enthalpies for phase transformation events for C250 powders.

Figure 4.35(a) shows the onset and the peak temperatures for both exothermic peaks observed in the DSC curves obtained for A250 powder samples against the milling time. There is clearly observed two main steps of the microstructure evolution during the ball milling process. During the first 5 hs of milling the onset and the maximum peak temperatures decrease rapidly and then from 5 hs onward those temperatures remain with not much change. The apparent activation energy determined for the both exothermic transformations (peaks 1 and 2) also shows a rapid decrease up to 5 hs of milling and them a more stable second step (Figure 4.27). Figure 4.35(b) that shows the specific enthalpies determined for the whole exothermic event and for both component peaks against the milling time also suggests there is a change in the microstructure evolution at ~5 hs of milling.

Considering the small plastic deformation capacity that the quasicrystals have, it is expected that during the first hours of milling the quasicrystalline particles absorb the mechanical energy by plastic deformation and accumulation of defects. This increases its free energy, which contributes to reduce the phase transformation temperatures (Figure 4.35(a)) and slightly increase the enthalpy release (Figure 4.35(b)). When the quasicrystalline particles are not able to absorb further deformation the milling process leads to increase the fracturing and dissolving of quasicrystals in the FCC-Al matrix, which would take place from 5 hs of milling onwards. Thus, when quasicrystals reached the maximum possible deformation the only possibility to absorb the mechanical energy is by increasing the surface/volume ratio by cracking, which slightly increases the free energy and facilitates the quasicrystal transformation by dissolving in the Al matrix. This is revealed in Figure 4.35(a) and (b) where after 5 hs of milling is observed a slightly

decrease of the transformation temperature (maximum temperature of peak 2) against the milling time and a near constant specific enthalpy released from 5 hs of milling onwards. Then, the volume fraction of quasicrystals in the powder decreases with the milling time. This can be estimated by the enthalpy ratio between the enthalpy involved in the peak 2 over the total enthalpy released in the whole exothermic event. Considering that *Inoue* et al. (Inoue and Kimura 1999) and *Audebert* et al. (Audebert, Prima et al. 2002) estimated 45 vol.% and 42 vol.% of quasicrystals in the $Al_{93}Fe_3Cr_2Ti_2$ alloy obtained by gas atomisation and melt-spinning respectively, after 30 hs of milling the $Al_{93}Fe_3Cr_2Ti_2$ alloy powder (A) contained ~19 vol.% of quasicrystalline particles.

The apparent activation energy determined for the transformation involved in the peak 2, which comprises mainly the quasicrystal transformation in the unmilled as-atomised alloy powder is 297$\pm$20 kJ/mol (Figure 4.27(b)). This value is higher than those found in the literature for other Al-based icosahedral quasicrystals transformation, such as 115 kJ/mol for an Al-8.5Fe-1.3V-1.7Si (wt.%) alloy (Sun, Zheng et al. 2017), 193$\pm$5 kJ/mol for $A1_{94}Cr_3Fe_3$ (at %) alloy (Ziani, Michot et al. 1995), ~147 kJ/mol for $Al_{86}Cr_{14}$ (at.%) alloy and ~140 kJ/mol for $Al_{86}Fe_{14}$ (at.%) alloy (Lawther, Dunlap et al. 1989). It is difficult to confirm which the controlling mechanism for the Al-Fe-Cr-Ti quasicrystal phase transformation is; but considering the activation energy for lattice diffusion of Fe, Cr, and Ti in the FCC-Al (~260 kJ/mol) (Du, Chang et al. 2003), and even in the icosahedral quasicrystalline structure (~250 kJ/mol) measured in Al-Cu-Fe and Al-Pd-Mn systems (Zumkley, Mehrer et al. 1996), it is reasonable to suggest the lattice diffusion of the transition metals in the FCC-Al is the most probable controlling mechanism in the unmilled gas-atomised alloy powders. As the ball milling process introduces dislocations,

vacancies and cracks it is expected that other diffusion mechanisms are activated, which can reduce the activation energy for the quasicrystalline phase transformation. Thus, in Figure 4.27 is observed that the activation energy for the peak 2 decreases to ~175 kJ/mol after 5 hours of milling and remain practically constant up to 30 hours of milling. The activation energy for dislocation diffusion of Fe and Cr in aluminium are only ~58 kJ/mol and 65 kJ/mol respectively (Hirano, Agarwala et al. 1962, Agarwala, Murarka et al. 1964). During the first 5 hours of milling, the density of defects in the FCC-Al is continually increasing, which facilitates the transition metal diffusion leading to the Al self-diffusion, ~143 kJ/mol (Lundy and Murdock 1962), become the controlling mechanism for the quasicrystal transformation. The enthalpy of the peak 2 increases with milling time, as shown in Figure 4.35. This could be due to that ball milling kept generating defects in the powder. The increase in enthalpy could be related to the release the lattice strain, rearrangement of dislocations and annihilation of dislocations (Zhou, Liao et al. 2003).

4.7.4 Precipitation of supersaturated solid solutions

Mechanical milling increases the solute content of Fe, Cr and Ti in the Al grains, as shown in Table 4.5. As the equilibrium solubility for Fe, Cr and Ti in fcc Al are 0.03 at.%, 0.01 at.% and 0.2 at.% respectively (Mehrer, Stolica et al. 1990, Zawrah and Shaw 2003), mechanical milling caused supersaturation in the Al grains. These supersaturates precipitated in the heat treatment and form Al_6Fe, $Al_{13}Fe_4$, $Al_{13}Cr_2$ and Al_3Ti intermetallics, as shown in the X-ray diffractograms in Figure 4.28, and the solute content in the Al grains dropped dramatically, as shown in Table 4.5. Precipitations in the heat-treated Al samples with Fe, Cr and Ti supersaturations were also observed by *Zawrah* et

al. (Zawrah and Shaw 2003) and *Shaw* et al. (Shaw, Luo et al. 2003). The available data for the diffusion of Al, Fe, Cr and Ti in aluminium are listed in Table 4.8.

The activation energy values for the precipitation in the A250_I batch powders after 1 to 4 hours range from 207 kJ/mol to 260 kJ/mol, as shown in Figure 4.27. These values are close to some activation energy values found in the literature, such as the precipitation of $Al_{13}Fe_4$ (194-201 kJ/mol) from Al-(5-12wt.%)Fe mechanical milled alloy (Niu, Froyen et al. 1994), the precipitation of Al_6Fe (192 kJ/mol) from Al-Fe-4wt.%Mn (Fe ≤ 6wt%) mechanical milled alloy (Froyen, Delaey et al. 1995), and the precipitation of Al_6Fe (203 kJ/mol), $Al_{13}Cr_2$ (228 kJ/mol), $Al_{13}Fe_4$ (228 kJ/mol), and Al_3Ti (192 kJ/mol) from $Al_{93}Fe_3Cr_2Ti_2$ (at%) mechanical milled alloy (Shaw, Luo et al. 2003). From Table 4.8, the diffusion of Fe, Cr and Ti has similar activation energy values with the precipitation of intermetallics for the A250_I batch powders, which indicates the precipitation may be controlled by diffusion.

For samples after 5 to 30 hours of milling, the activation energy is ~150 kJ/mol. The heat-treated powder A250_I_10 has an activation energy value 162±23 kJ/mol for peak 1. These values are also close to some values found in the literature, such as the precipitation of Al_6Fe (161 kJ/mol) from supersaturated Al-Fe (Fe ≤ 25wt%) powder processed with mechanical alloying (Froyen, Delaey et al. 1995), and the formation of Al_3Ti (147 kJ/mol) in Ti-75%Al powder (Zhang, Lu et al. 2000).

Identifying the mechanism for the precipitation of intermetallics is difficult. The diffusion circuit, such as the dislocations and the grain boundaries, can increase the diffusion speed and lower the activation energy values for diffusion (Mehrer 2007). One reasonable hypothesis is from 5 hours of milling the precipitation is limited by the diffusion of Fe in

Al grain boundaries, due to that (i) The precipitation of A250_I_10 is very close to the grain boundary diffusion of Fe in polycrystalline aluminium instead of lattice diffusion in single crystal Al, as shown in Table 4.8 (Froyen, Delaey et al. 1995); (2) the precipitated intermetallics mainly locate on the grain boundaries while there is hardly any intermetallics found inside the Al grains in TEM (Shaw, Luo et al. 2003).

As shown in Figure 4.35, the enthalpy increases with milling time. This could because the solute contents in the matrix increase simultaneously with the milling time, as shown in Table 4.5. A higher solute content lead to a higher amount of precipitations, which increases the enthalpy values (Zurob, Hutchinson et al. 2002).

In the literature, the Al_6Fe, $Al_{13}Cr_2$, $Al_{13}Fe_4$ and Al_3Ti have different onset temperatures and activation energies for precipitation (Shaw, Luo et al. 2003). For example, *Froyen* et al. (Froyen, Delaey et al. 1995) suggested that the Al_6Fe phase should precipitate prior to the $Al_{13}Fe_4$ phase, since the former had a simpler structure (orthorhombic) and a much smaller unit cell than the $Al_{13}Fe_4$ (monoclinic). In the current work, there is one exothermal peak for the precipitation process. This could be due to that he DSC equipment used in the current study has low sensitivity.

Diffusion in single crystal	D_0 (m^2/s)	Q (kJ/mol)
Ti (Du, Chang et al. 2003)	0.112	260
Cr (Du, Chang et al. 2003)	0.675	261.9
Cr (Du, Chang et al. 2003)	10	282
Cr (Peterson and Rothman 1970)	5	243.6
Fe (Hood 1970)	91	258.6
Fe (Alexander and Slifkin 1970)	0.0135	192.5
Al (Lundy and Murdock 1962)	0.171	142.8
Diffusion in polycrystals	**D_0 (m^2/s)**	**Q (kJ/mol)**
Cr (Du, Chang et al. 2003)	80	255.3
Cr (Du, Chang et al. 2003)	6.4	261.0
Fe (Mantl, Petry et al. 1983)	1.1	221.6
Fe (Beke, Gödény et al. 1987)	0.0053	183.4
Fe (Du, Chang et al. 2003)	0.77	220.9
Fe (Sørensen and Trumpy 1973)	0.000012	134.9
Diffusion through dislocations	**D_0 (m^2/s)**	**Q (kJ/mol)**
Cr (Agarwala, Murarka et al. 1964)	0.301	64.7
Fe (Hirano, Agarwala et al. 1962)	0.0041	58.4

Table 4.8: Diffusion coefficient (**D_0**) and activation energy (**Q**) of Ti, Cr, Fe and Al in aluminium

4.8 Conclusions

The unmilled nanoquasicrystalline alloy powders contain Al_3Ti particles and the quasicrystal particles in the Al matrix. The [0τ0], [00τ] and [τ00] zone axes of quasicrystalline particles is parallel to the [002], [2-20] and [220] zone axes of the Al_3Ti and Al phases respectively.

The nanoquasicrystalline $Al_{93}Fe_3Cr_2Ti_2$ alloy based nanocomposite powders containing 12.9 vol% γ-Al_2O_3 (50nm) (the C250 batch) have been produced by mechanical milling. The pure $Al_{93}Fe_3Cr_2Ti_2$ alloy powders (the A250 batch) were also fabricated under the same milling conditions for comparison.

For both the A250 and C250 batches of powders, the particle size increases first and decreases afterwards. The largest and smallest powder sizes for the A250 batch powders

are 134.7μm and 47.9μm after 3 and 30 hours respectively. In comparison, the C250 batch powders reach the largest particle size 61.5 μm after 10 hours of milling and the smallest particle size 31.1μm after 30 hours of milling. For the same milling time, the A250 batch powder has small particle sizes than the C250 batch. This could because the brittle reinforcement particles prevent the cold welding of the matrix powder at early milling hours.

For the C250 batch powder, after 5 hours of milling large γ-Al_2O_3 clusters were embedded in the matrix. After 10 hours of milling, the γ-Al_2O_3 distributes in the matrix discontinuously, but agglomerations still exist. After 30 hours of milling the γ-Al_2O_3 clusters have an average size of 90±29nm.

For the A250 batch powders, there are three main phases, the α-Al, the icosahedral quasicrystals and the Al_3Ti intermetallic. For the C250 batch powders, apart from these three phases, γ-Al_2O_3 could be detected in the XRD diffractograms. The crystallite sizes of both A250 and C250 powders decrease with milling time. The lowest crystallite sizes for A250 and C250 powders were 22nm and 14nm, obtained after 25 hours of milling. The icosahedral quasicrystals with 400~1000nm in diameter could generate particle stimulated nucleation in ball milling process. The quasicrystalline particles have small plastic deformation capacity and break during the milling. The nanosize γ-Al_2O_3 particles tend to refine the grains by inhibition the movement of dislocations, which accelerates the dislocation accumulation speed. The accumulated dislocations could be transferred into high-angle and low-angle grain boundaries.

Two peaks occur in the DSC runs after 1 hours of milling for the A250 batch and after 4 hours of milling for the C250 batch. The peak 1 (at lower temperature) involves the

precipitation of the intermetallics, including the Al_6Fe, the $Al_{13}Fe_4$, the $Al_{13}Cr_2$ and the Al_3Ti. The precipitation is suspected to be controlled by diffusion. The peak 2 (at higher temperature) mainly involves the decomposition of the quasicrystalline phase. Before milling, the lattice diffusion is probably the controlling mechanism for decomposition of the quasicrystals. During ball milling, diffusion through grain boundaries and dislocations is involved, which decrease the activation energy of quasicrystalline phase from 297±20 kJ/mol to ~175 kJ/mol after ball milling.

The microhardness of both A250 batch powders and C250 batch powders increases with milling time. The C250 batch powders have higher microhardness values than the A250 batch for the same milling time. The maximum hardness values for the A250 and C250 batch powders are 515±46 kg/mm^2 and 638±44 kg/mm^2, obtained after 25 and 30 hours of milling respectively.

4.9 References

Agarwala, R., et al. (1964). "Diffusion of chromium in aluminium." Acta Metallurgica **12**(8): 871-874.

Alexander, W. and L. Slifkin (1970). "Diffusion of solutes in aluminum and dilute aluminum alloys." Physical Review B **1**(8): 3274.

Ashby, M. (1966). "Work hardening of dispersion-hardened crystals." Philosophical Magazine **14**(132): 1157-1178.

Audebert, F., et al. (2002). "Structural characterisation and mechanical properties of nanocomposite Al-based alloys." Materials Transactions **43**(8): 2017-2025.

Audier, M. and P. Guyot (1986). "Al4Mn quasicrystal atomic structure, diffraction data and Penrose tiling." Philosophical Magazine B **53**(1): L43-L51.

Beke, D., et al. (1987). "On the diffusion of 59Fe into aluminium and Al Mn solid solutions." Philosophical Magazine A **55**(4): 425-443.

Benjamin, J. and T. Volin (1974). "The mechanism of mechanical alloying." Metallurgical Transactions **5**(8): 1929-1934.

Bhattacharya, P., et al. (2004). "Nanocrystalline TiAl powders synthesized by high-energy ball milling: effects of milling parameters on yield and contamination." Journal of Alloys and Compounds **368**(1): 187-196.

Cahn, J. W., et al. (1986). "Indexing of icosahedral quasiperiodic crystals." Journal of Materials Research **1**(01): 13-26.

Chung, K. H., et al. (2003). "Mechanisms of microstructure evolution during cryomilling in the presence of hard particles." Materials Science and Engineering: A **356**(1): 23-31.

Davis, J. R. (1998). Metals handbook, ASM international.

Dieter, G. E. and D. J. Bacon (1986). Mechanical metallurgy, McGraw-Hill New York.

Du, Y., et al. (2003). "Diffusion coefficients of some solutes in fcc and liquid Al: critical evaluation and correlation." Materials Science and Engineering: A **363**(1): 140-151.

Duflos, F. and J.-F. Stohr (1982). "Comparison of the quench rates attained in gas-atomized powders and melt-spun ribbons of Co-and Ni-base superalloys: influence on resulting microstructures." Journal of materials science **17**(12): 3641-3652.

El-Kady, O. and A. Fathy (2014). "Effect of SiC particle size on the physical and mechanical properties of extruded Al matrix nanocomposites." Materials & Design (1980-2015) **54**: 348-353.

Elser, V. (1985). "Indexing problems in quasicrystal diffraction." Physical Review B **32**(8): 4892.

Elser, V. (1986). "The diffraction pattern of projected structures." Acta Crystallographica Section A: Foundations of Crystallography **42**(1): 36-43.

Engler, O., et al. (1997). "Influence of particle stimulated nucleation on the recrystallization textures in cold deformed Al-alloys Part I—Experimental observations." Scripta Materialia **37**(11): 1665-1674.

Fogagnolo, J., et al. (2003). "Effect of mechanical alloying on the morphology, microstructure and properties of aluminium matrix composite powders." Materials Science and Engineering: A **342**(1): 131-143.

Froyen, L., et al. (1995). "Synthesizing aluminum alloys by double mechanical alloying." JOM Journal of the Minerals, Metals and Materials Society **47**(3): 16-19.

Galano, M., et al. (2015). "Nanoquasicrystalline Al-based matrix/γ-Al_2O_3 nanocomposites." Journal of Alloys and Compounds **643**: S99-S106.

Guo, J., et al. (2014). "Effects of nano-Al_2O_3 particle addition on grain structure evolution and mechanical behaviour of friction-stir-processed Al." Materials Science and Engineering: A **602**: 143-149.

Hesabi, Z. R., et al. (2006). "Structural evolution during mechanical milling of nanometric and micrometric Al_2O_3 reinforced Al matrix composites." Materials Science and Engineering: A **428**(1): 159-168.

Hirano, K.-i., et al. (1962). "Diffusion of iron, nickel and cobalt in aluminum." Acta Metallurgica **10**(9): 857-863.

Hood, G. (1970). "The diffusion of iron in aluminium." Philosophical Magazine **21**(170): 305-328.

Humphreys, F. (1977). "The nucleation of recrystallization at second phase particles in deformed aluminium." Acta Metallurgica **25**(11): 1323-1344.

Inoue, A. (1998). "Amorphous, nanoquasicrystalline and nanocrystalline alloys in Al-based systems." Progress in materials science **43**(5): 365-520.

Inoue, A. and H. Kimura (1999). "High elevated-temperature strength of Al-based nanoquasicrystalline alloys." Nanostructured Materials **11**(2): 221-231.

Khakbiz, M. and F. Akhlaghi (2009). "Synthesis and structural characterization of Al–B< sub> 4</sub> C nano-composite powders by mechanical alloying." Journal of Alloys and Compounds **479**(1): 334-341.

Kimura, H. M., et al. (2000). "Al–Fe-based bulk quasicrystalline alloys with high elevated temperature strength." Journal of Materials Research **15**(12): 2737-2744.

Kissinger, H. E. (1956). "Variation of peak temperature with heating rate in differential thermal analysis." Journal of research of the National Bureau of Standards **57**(4): 217-221.

Lawther, D. W., et al. (1989). "Structure and stability of rapidly quenched $Al_{86}Cr_{14-x}Fe_x$ alloys." Journal of materials science **24**(9): 3076-3080.

Levine, D. and P. J. Steinhardt (1986). "Quasicrystals. I. Definition and structure." Physical Review B **34**(2): 596.

Lundy, T. and J. Murdock (1962). "Diffusion of Al^{26} and Mn^{54} in Aluminum." Journal of Applied Physics **33**(5): 1671-1673.

Mantl, S., et al. (1983). "Diffusion of iron in aluminum studied by Mössbauer spectroscopy." Physical Review B **27**(9): 5313.

Mayer, J., et al. (2007). "TEM sample preparation and FIB-induced damage." MRS bulletin **32**(05): 400-407.

Mehrer, H. (2007). Diffusion in solids: fundamentals, methods, materials, diffusion-controlled processes, Springer Science & Business Media.

Mehrer, H., et al. (1990). Diffusion in Solid Metals and Alloys, Numerical Data and Functional Relationships in Science and Technology, vol. 26, Springer-Verlag, Berlin.

Milkereit, B., et al. (2009). "Recording of continuous cooling precipitation diagrams of aluminium alloys." Thermochimica acta **492**(1): 73-78.

National Chemical Database Service (2016). "http://cds.rsc.org/."

Niu, X., et al. (1994). "Effect of Fe content on the mechanical alloying and mechanical properties of Al-Fe alloys." Journal of materials science **29**(14): 3724-3732.

Parande, G., et al. (2017). "Enhancing the tensile and ignition response of monolithic magnesium by reinforcing with silica nanoparticulates." Journal of Materials Research: 1-10.

Peterson, N. and S. Rothman (1970). "Impurity diffusion in aluminum." Physical Review B **1**(8): 3264.

Poirier, D., et al. (2010). "Fabrication and properties of mechanically milled alumina/aluminum nanocomposites." Materials Science & Engineering A **527**(29-30): 7605-7614.

Shaw, L., et al. (2003). "Thermal stability of nanostructured $Al_{93}Fe_3Cr_2Ti_2$ alloys prepared via mechanical alloying." Acta Materialia **51**(9): 2647-2663.

Sørensen, K. and G. Trumpy (1973). "Dynamical Properties of Fe 57 Dissolved in Al Observed by Mössbauer Effect." Physical Review B **7**(5): 1791.

Sun, S.-B., et al. (2017). "Selective Laser Melting of an Al–Fe–V–Si Alloy: Microstructural Evolution and Thermal Stability." Journal of Materials Science & Technology **33**(4): 389-396.

Suryanarayana, C. (2001). "Mechanical alloying and milling." Progress in materials science **46**(1): 1-184.

Suryanarayana, C. and M. G. Norton (1998). "X-ray diffraction: a practical approach." Microsc Microanal **4**: 513-515.

Todd, I., et al. (2004). "The influence of processing variables on the structure and mechanical properties of nano-quasicrystalline reinforced aluminium alloys." Materials Science and Engineering: A **375**: 1235-1238.

Tousi, S. R., et al. (2009). "Production of Al–20 wt.% Al_2O_3 composite powder using high energy milling." Powder Technology **192**(3): 346-351.

Voyles, P., et al. (2003). "Imaging individual atoms inside crystals with ADF-STEM." Ultramicroscopy **96**(3): 251-273.

Williams, D. B., et al. (1998). "Transmission electron microscopy: a textbook for materials science." MRS Bulletin-Materials Research Society **23**(5): 47.

Zawrah, M. and L. Shaw (2003). "Microstructure and hardness of nanostructured Al–Fe–Cr–Ti alloys through mechanical alloying." Materials Science and Engineering: A **355**(1): 37-49.

Zhang, D. (2004). "Processing of advanced materials using high-energy mechanical milling." Progress in materials science **49**(3): 537-560.

Zhang, F., et al. (2000). "Study of thermal stability of mechanically alloyed Ti–75% Al powders." Journal of Alloys and Compounds **297**(1): 211-218.

Zhou, F., et al. (2003). "Microstructural evolution during recovery and recrystallization of a nanocrystalline Al-Mg alloy prepared by cryogenic ball milling." Acta Materialia **51**(10): 2777-2791.

Ziani, A., et al. (1995). "Transformation of the quasicrystalline phase Al-Cr-Fe induced by rapid solidification." Journal of materials science **30**(11): 2921-2929.

Zumkley, T., et al. (1996). "Diffusion of ^{54}Mn and ^{59}Fe in icosahedral Al-Pd-Mn single quasicrystals." Physical Review B **54**(10): R6815-6818.

Zurob, H., et al. (2002). "Modeling recrystallization of microalloyed austenite: effect of coupling recovery, precipitation and recrystallization." Acta Materialia **50**(12): 3077-3094.

5. The effects of ball milling speeds

In this Chapter, quasicrystalline $Al_{93}Fe_3Cr_2Ti_2$ (at.%)/12.9vol.% γ-Al_2O_3 nanocomposites processed with different milling speeds were investigated. The processing routines were described in Chapter 3. The data for the A250_II and C250_II batch powders with 250 rpm milling speed, which have been analysed in Chapter 4, will also be used in this Chapter for comparisons. The $Al_{93}Fe_3Cr_2Ti_2$ powder sample before milling is referred as A. The abbreviation and the processing conditions were listed in Table 5.1.

Powder batch	Composition	Milling speed (rpm)	Milling time (h)
A	$Al_{93}Fe_3Cr_2Ti_2$ alloy	0	0
A250_II_*t*		250	*t* hours, *t* = 5, 10, 15, 20, 25, 30
C150_*t*	$Al_{93}Fe_3Cr_2Ti_2/Al_2O_3$ nanocomposites	150	
C200_*t*		200	
C250/200_*t*		250 in first 5 hours, and 200 afterwards	
C250_II_*t*		250	

Table 5.1: Table summarising the milling conditions for each powder batch. (*t* is the milling time)

All the powders processed were investigated with the Mastersizer and the scanning electron microscope (SEM) to measure the particle sizes and characterise the morphologies. The γ-Al_2O_3 distribution was analysed with focused ion beam (FIB) imaging and scanning transmission electron microscope (STEM) dark field (DF) imaging. The phases within the processed powders were examined with X-ray diffractograms, diffraction patterns in transmission electron microscope (TEM) and energy dispersive X-ray (EDX) mappings in STEM mode. Differential scanning calorimetry (DSC) was used to determine the phase

stability of the ball milled powders. The microhardness values of the powders were also measured.

The objectives for this chapter are to investigate effects of milling speed on the properties of the nanocomposites and find the suitable milling conditions for process nanocomposites with homogeneous distribution of γ-Al_2O_3 particles while maintaining the quasicrystalline phase for extrusion.

5.1 Particle size and morphology

Figure 5.1 shows the particle size distributions of all the mechanically milled powders. All the powders (unmilled and milled) with different milling time and speeds showed a Gaussian distribution of the volume fraction of powder particles against the logarithm of the powder particle sizes. Each curve showed in Figure 5.1 is an average from three Mastersizer measurements. The differences between the three measurements are minor. It is observed that for some of the C200_5, C200_10 and all the C150 samples, the curves contain small shoulders on the left of the powder particle size distributions. For all these samples, Gaussian fits are applied to separate the overlapping peaks. The peak particle sizes of the small shoulders are less than 10μm, which should correspond to the γ-Al_2O_3 agglomerations, as discussed in section 4.2 in Chapter 4. Gaussian fits were applied for separating the overlapping peaks. The blue curves on the left correspond to the γ-Al_2O_3 clusters, and the red curves on the right side correspond to the nanoquasicrystalline $Al_{93}Fe_3Cr_2Ti_2$ powders. For the powder samples with higher milling speed or higher milling time, the small red peaks disappear, probably because the γ-Al_2O_3 particles have been milled into the matrix. For the C150 batch powders after 10 hours of milling the distribution curves shift to the left side. From 10 hours milling onwards, there are no

obvious changes with increasing milling time. For the C200, the C250/200 and the C250_II batches, the curves shift to the right side at first and then shift to the left side, which indicates the fluctuations of the particle sizes.

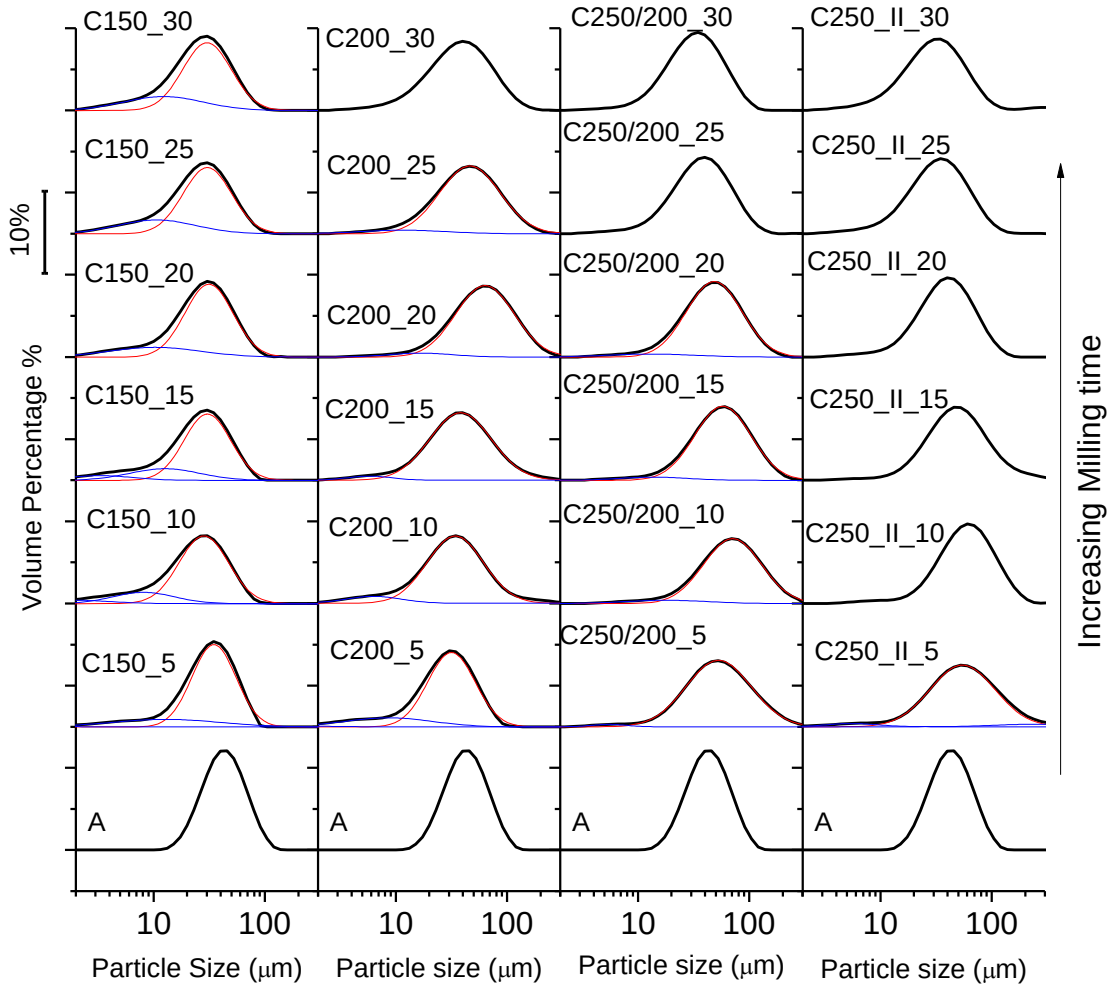

Figure 5.1: The particle size distribution for the C150, the C200, the C250/200 and the C250_II powders

The full width half maximum (FWHM) of each curve is measured. The same as section 4.2 in Chapter 4, the particle sizes corresponding to the peak position, the lowest and the highest position in FWHM are marked as P, P_{min} and P_{max} respectively. The peak position

P is used to represent the peak particle size. The P_{min} and the P_{max}, combined with each other, are used to illustrate the particle size distribution range. From Figure 5.2, the particle sizes of the C150 batch powder decrease slightly in 10 hours of milling and then reach to a plateau. For the C200, the C250/200 and the C250_II batches of powders, the particle sizes first increase and then decrease. This indicates that before milling the powders are relative ductile and tend to be cold welded with each other. After the work hardening and the welding, they become brittle and are fractured into smaller pieces. For all the powder samples processed, those with higher peak particle sizes also have higher particle size distribution ranges (P_{max}-P_{min}).

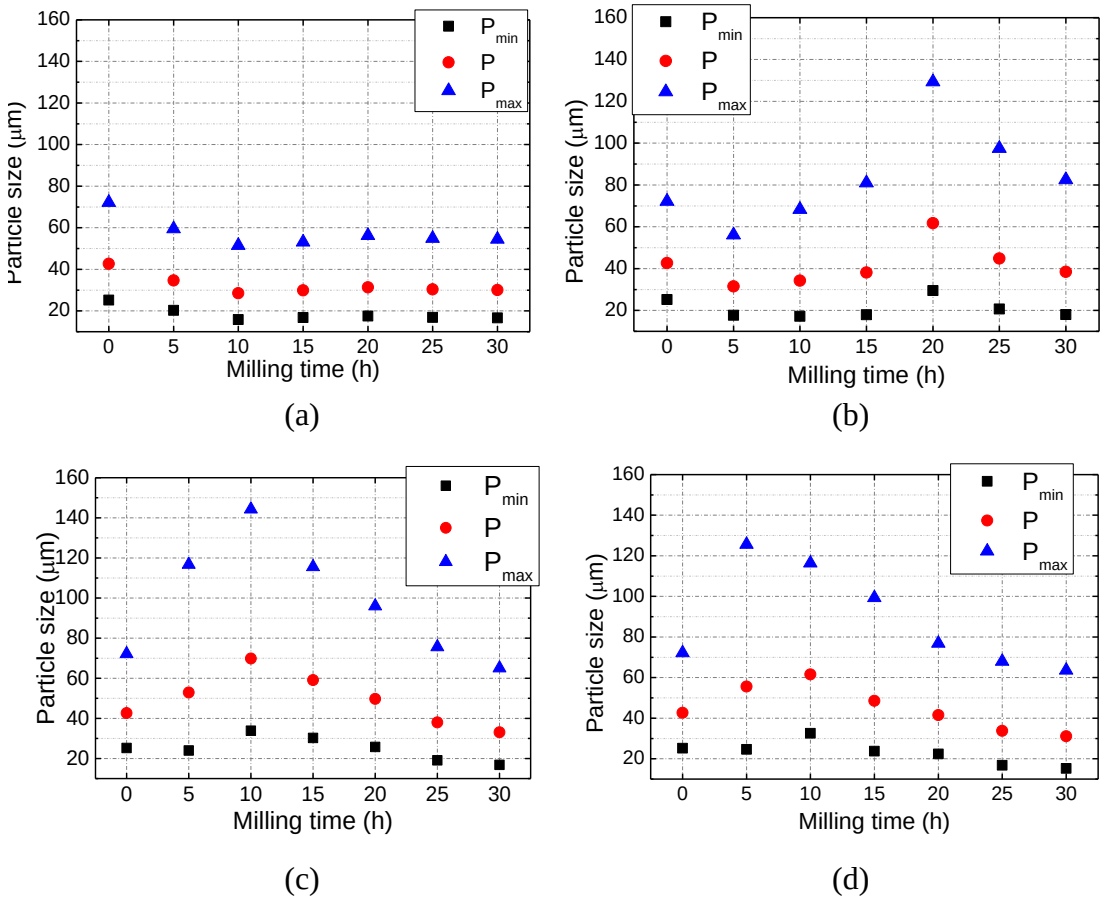

Figure 5.2: Particle sizes changing plots for **(a)** C150, **(b)** C200, **(c)** C250/200 and **(d)** C250_II powders. The P_{min} (lowest point in FWHM), P (peak position), P_{max} (highest point in FWHM) values are plotted together against the milling time.

The peak particle sizes (P) of all the mechanically milled powders are plotted together in Figure 5.3. The C150 batch powders have the lowest particle sizes among all. The particle sizes of the C200 batch reach the maximum after 20 hours of milling, while the particle sizes of the C250/200 and C250_II batches reach the maximum value after 10 hours of milling. C250/200_5 and C250_5 powers were processed with the same milling conditions. Therefore, they also have similar particle sizes. However, from 10 to 30 hours of milling, C250/200 powders with 200rpm milling speed during this period have larger particle sizes than the C250_II batch powders.

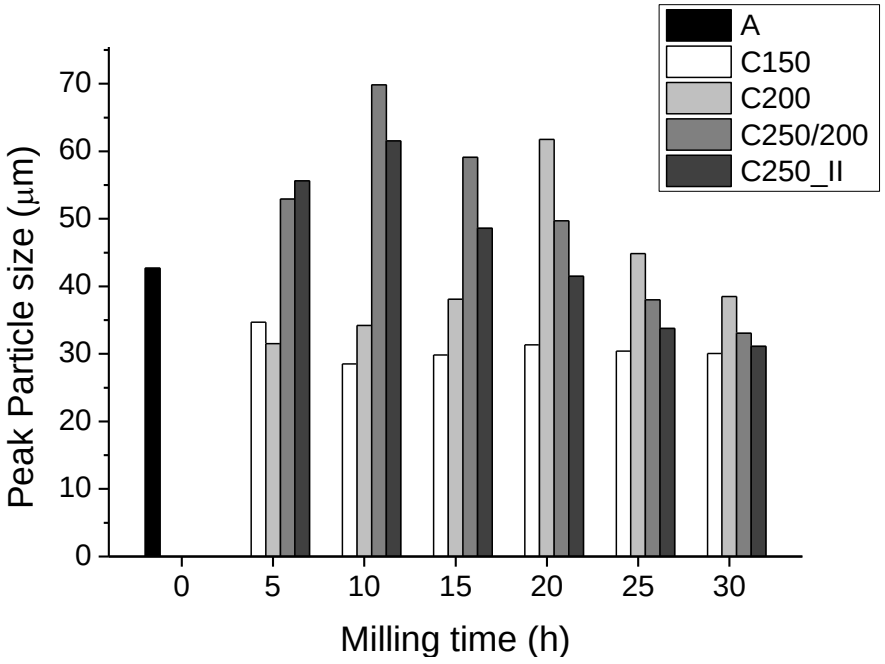

Figure 5.3: the average particle size of the A, the C150, the C200, the C250/200, and the C250_II batches of powder

The particle morphologies of all batches of powders are shown from Figure 5.4 to Figure 5.7. In Figure 5.4, C150 powders have no obvious morphology evolution. For the matrix powders, there is no significant particle morphology and particle size change from 5 to 30

hours of milling. Figure 5.4 (e) is a zoom in SEM image of C150_5. As discussed in section 4.2 in Chapter 4, in low milling hours there are usually some γ-Al_2O_3 clusters smearing on the surfaces of the $Al_{93}Fe_3Cr_2Ti_2$ particles (verified using EDX). Therefore, the small white particles adhered on the powder, labelled as (1) and (2), are suspected to be the γ-Al_2O_3 clusters.

Figure 5.5 is the SEM images of C200 powders. The particle sizes match the size distributions measured with Mastersizer in Figure 5.1. In the SEM images of C200_20, some large particles, for example, the one labelled as (1) were observed. These large particles are suspected to come from the cold welding of the powder during the ball milling, as they were less frequently observed in the C200_5 powders.

Figure 5.6 and Figure 5.7 are the SEM images of C250/200 and C250_II. The morphology changes of the C250/200 and C250_II powders are not obvious in SEM. The only notable change with milling time seems to be the particle size. For example, the C250/200_10 particles shown in Figure 5.6 (b) are larger than the C250/200_30 particles in Figure 5.6 (f). The C250_II_10 particles shown in Figure 5.7 (b) are larger than Figure 5.7 (f). For the C250/200 and the C250_II batches of powder, even after only 5 hours of milling, there are very few γ−Al_2O_3 clusters detected on the powder surface.

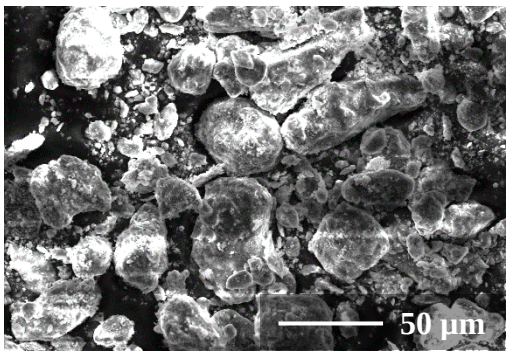

(a) C150_5

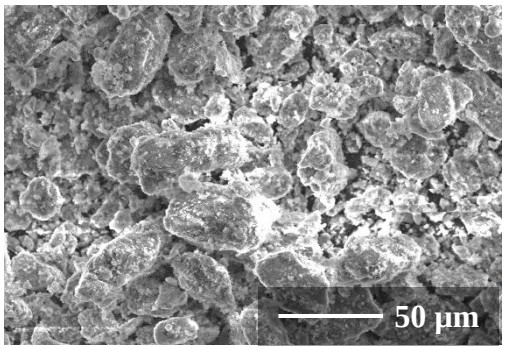

(b) C150_10

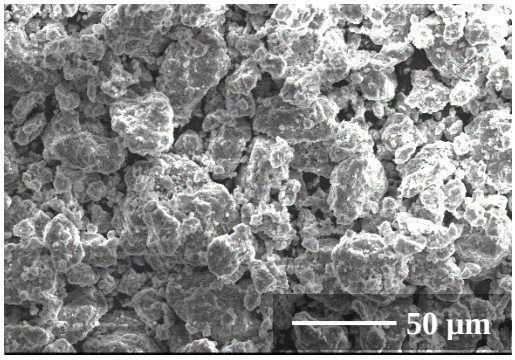

(c) C150_20

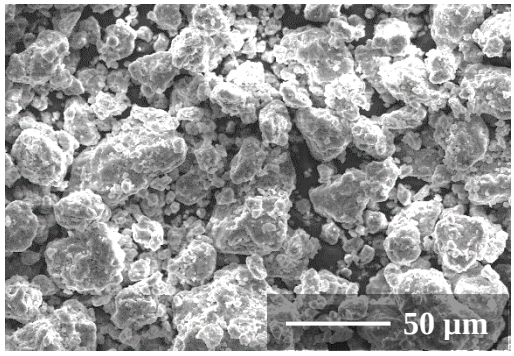

(d) C150_30

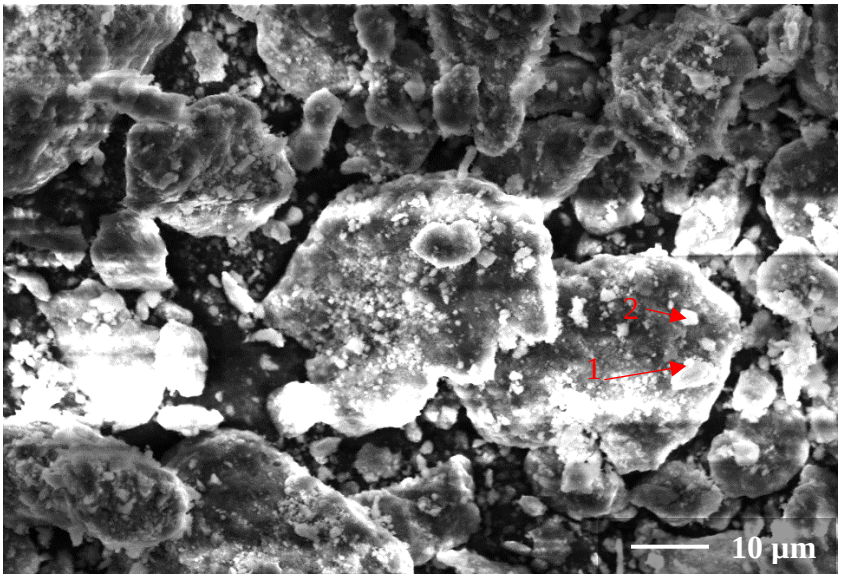

(e) C150_5 with a larger magnification

Figure 5.4: SEM images of the C150 batches of powder from 5 to 30 hours of milling **(a)** C150_5, **(b)** C150_10, **(c)** C150_20, **(d)** C150_30, **(e)** C150_5 with a larger magnification

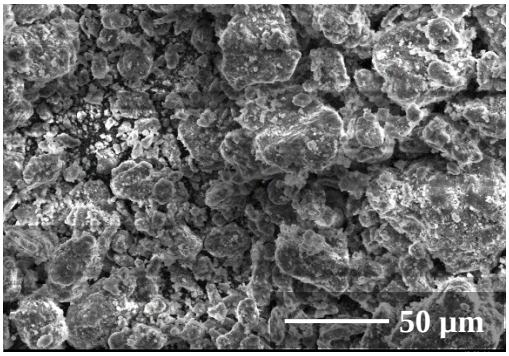

(a) C200_5

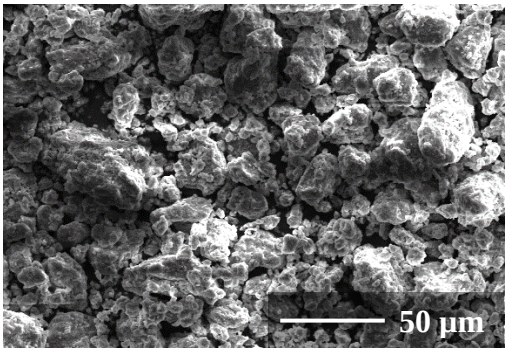

(b) C200_10

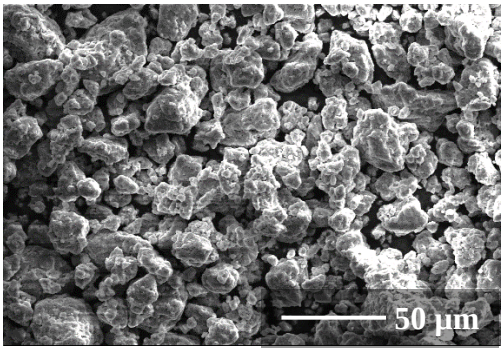

(c) C200_15

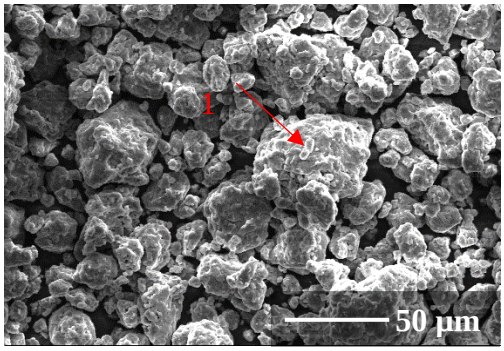

(d) C200_20

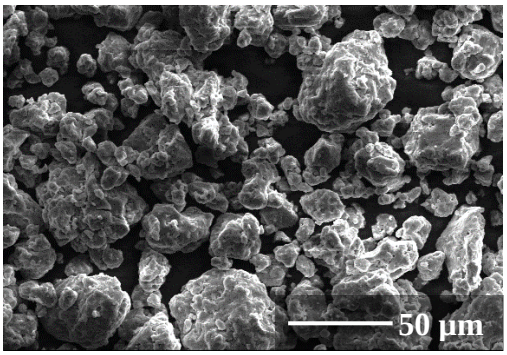

(e) C200_25

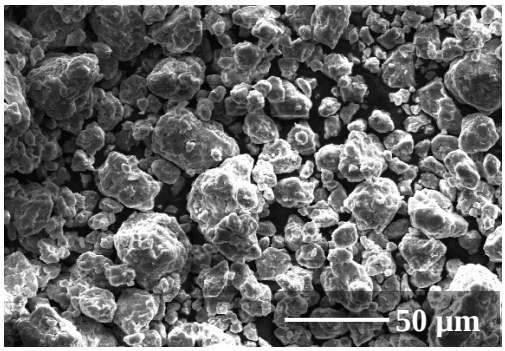

(f) C200_30

Figure 5.5: SEM images of the C200 batches of powder from 5 to 30 hours of milling **(a)** C200_5, **(b)** C200_10, **(c)** C200_15, **(d)** C200_20, **(e)** C200_25, **(f)** C200_30

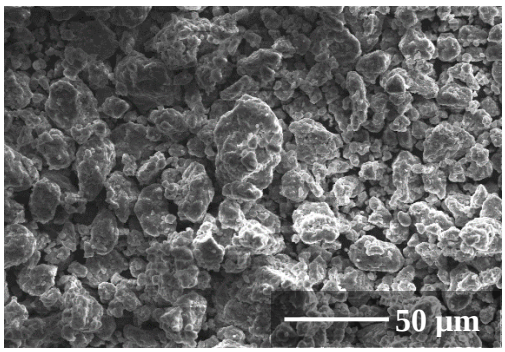

(a) C250/200_5

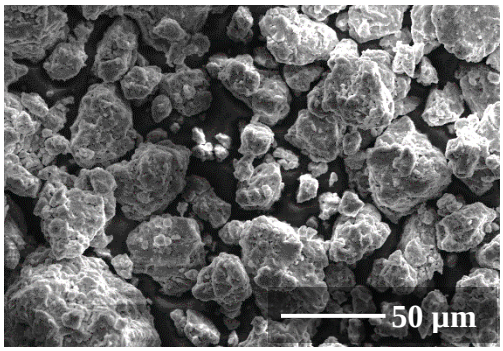

(b) C250/200_10

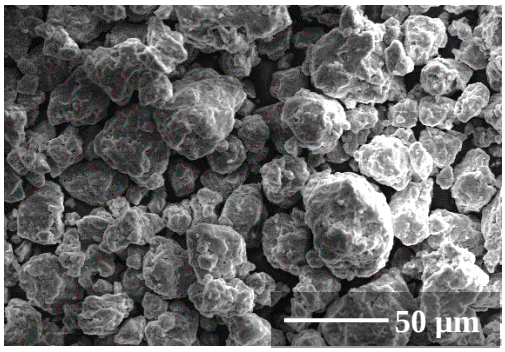

(c) C250/200_15

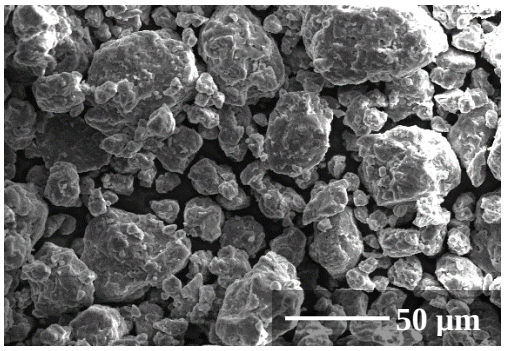

(d) C250/200_20

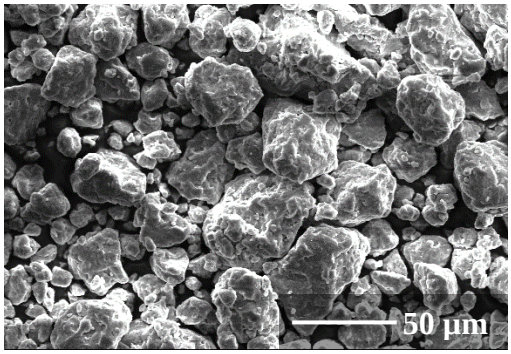

(e) C250/200_25

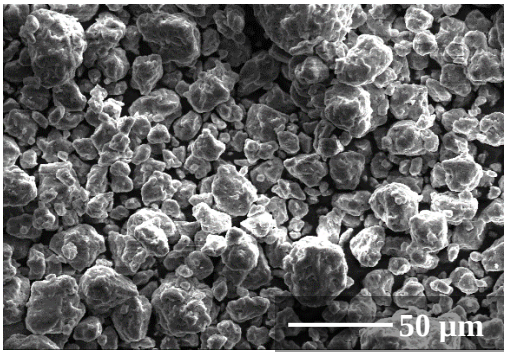

(f) C250/200_30

Figure 5.6: SEM images of the C250/200 batches of powder from 5 to 30 hours of milling **(a)** C250/200_5, **(b)** C250/200_10, **(c)** C250/200_15, **(d)** C250/200_20, **(e)** C250/200_25, **(f)** C250/200_30

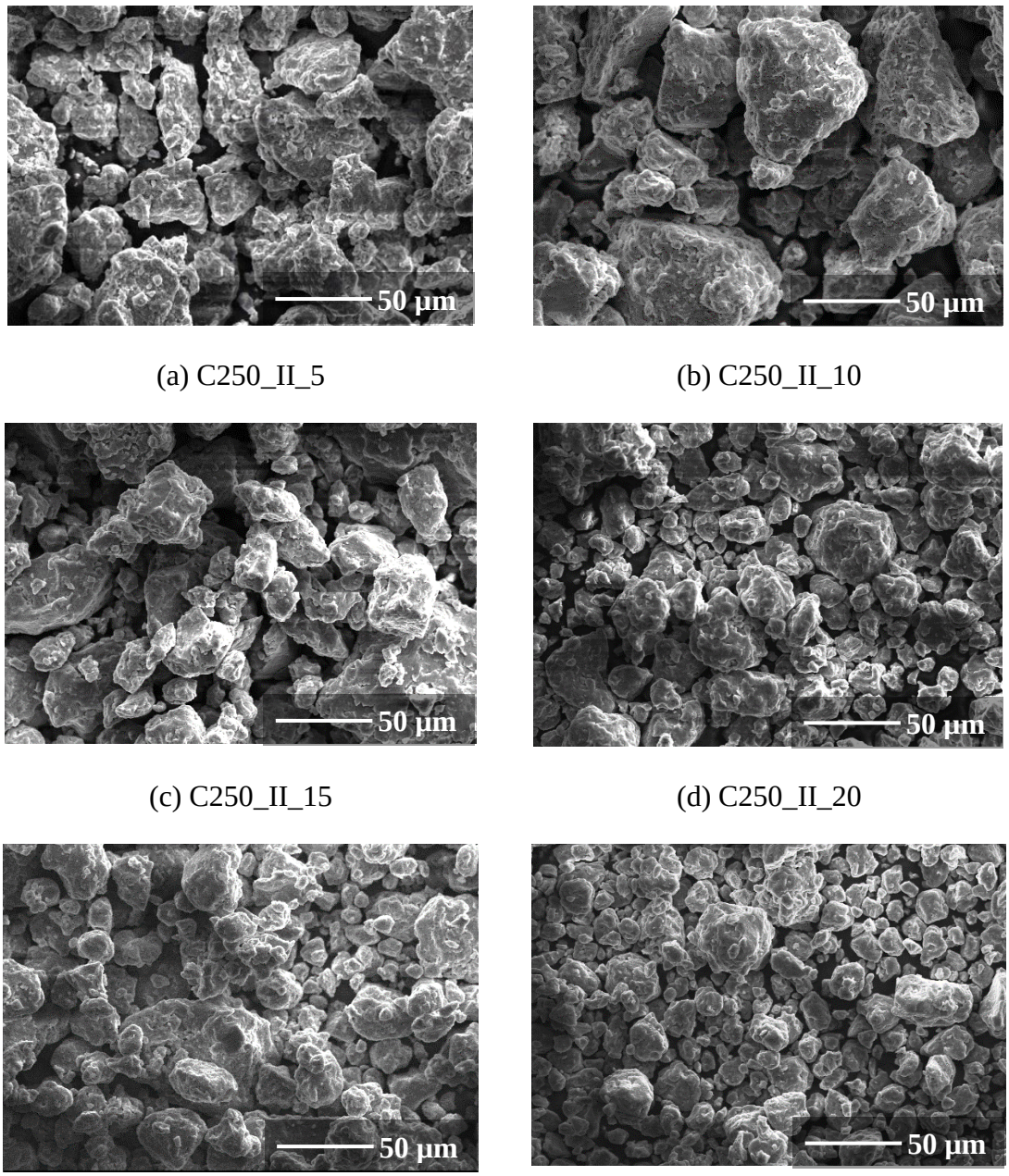

(a) C250_II_5 (b) C250_II_10

(c) C250_II_15 (d) C250_II_20

(e) C250_II_25 (f) C250_II_30

Figure 5.7: SEM images of the C250_II batches of powder from 5 to 30 hours of milling **(a)** C250_II_5, **(b)** C250_II_10, **(c)** C250_II_15, **(d)** C250_II_20, **(e)** C250_II_25, **(f)** C250_II_30

5.2 Alumina distribution

FIB imaging of cross-sectioned mechanically milled powder is used to analyse the distribution of γ-Al_2O_3. Figure 5.8 is C150 powders. As observed, after 5 and 10 hours of milling (Figure 5.8(a) and (b)), γ-Al_2O_3 particles could be hardly observed inside the matrix powders. After 20 hours of milling, γ-Al_2O_3 bands can be found inside the powder particles, but mainly near the boundaries of the powders, as shown in Figure 5.8(c). The distribution of γ-Al_2O_3 is still not homogeneous even after 30 hours of milling, as shown in Figure 5.8(d). For C200 powders in Figure 5.9, after 5 hours of milling the γ-Al_2O_3 is coated outside the matrix (Figure 5.9(a)) and after 10 hours of milling the γ-Al_2O_3 distributes in lamella shape in the matrix (Figure 5.9(b)). After 15 hours of milling the distribution homogeneity increases dramatically, as shown in Figure 5.9(c). For the C200_20 sample, as shown in Figure 5.9(d), the γ-Al_2O_3 bands still exist, with directions marked by an arrow. After 25 and 30 hours of milling, the distribution homogeneity is relative good, as shown in Figure 5.9(e) and Figure 5.9(f) respectively. The γ-Al_2O_3 distribution in the C250/200 batch and C250_II batch powders follow a similar trend. As shown in Figure 5.10 and Figure 5.11, after 5 hours of milling, the γ-Al_2O_3 is of a band shape. In the C250_II_10 sample, the γ-Al_2O_3 is distributed in the nanoquasicrystalline matrix forming thin bands with higher homogeneity than in the C200_10 (compare Figure 5.9(b) with Figure 5.11(c)). After 20 and 15 hours of milling for the C250/200 and C250_II batches respectively, the γ-Al_2O_3 particles seem quite homogeneously distributed (Figure 5.10(d) and Figure 5.11(d)) when compared with the C200_20 sample (Figure 5.9(d)). Some large γ-Al_2O_3 clusters still exist even after 30 hours of milling, as marked with the red arrows in Figure 5.10(f) and Figure 5.11(f).

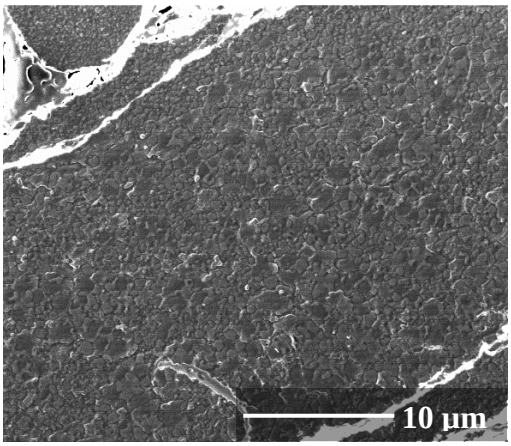

(a) C150_5

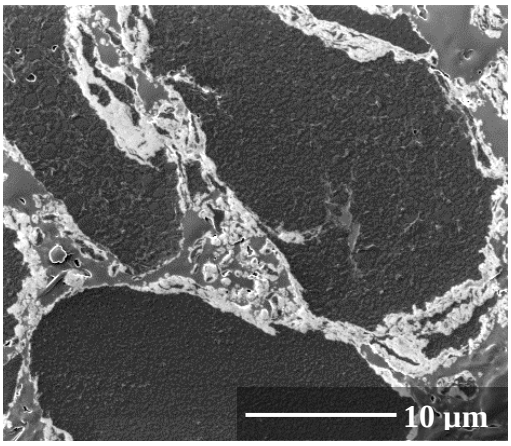

(b) C150_10

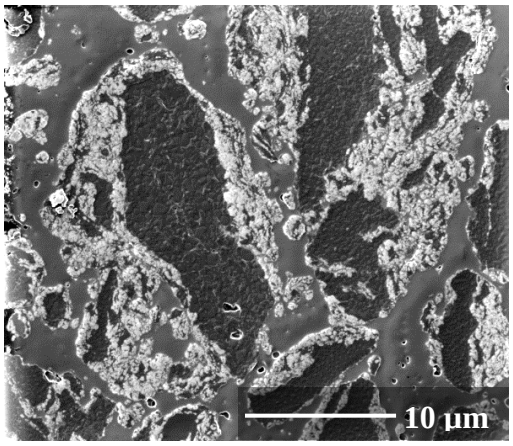

(c) C150_20

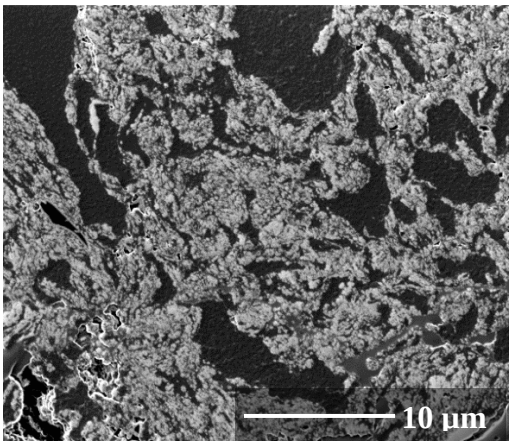

(d) C150_30

Figure 5.8: FIB images of the C150 batches of powder from 5 to 30 hours of milling **(a)** C150_5, **(b)** C150_10, **(c)** C150_20, **(d)** C150_30

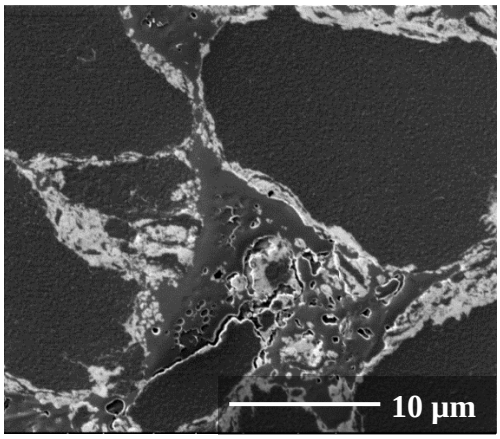

(a) C200_5

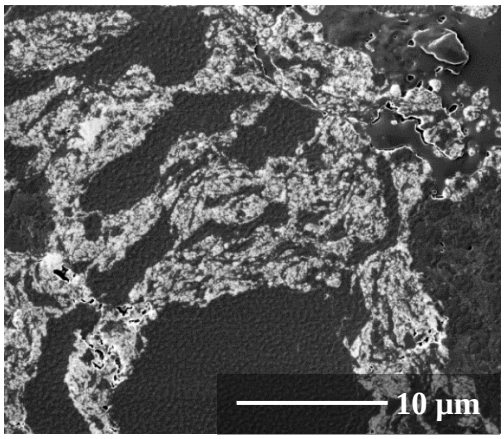

(b) C200_10

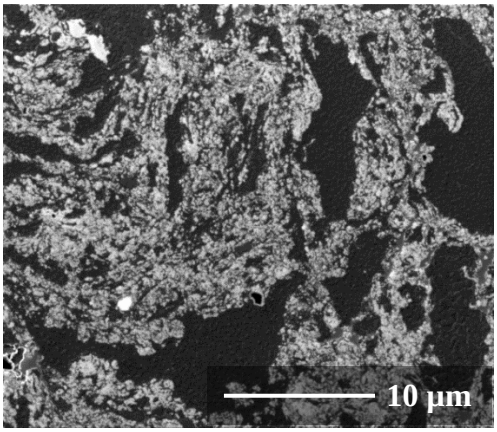

(c) C200_15

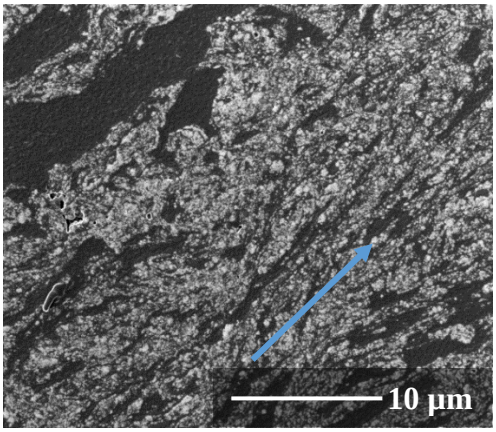

(d) C200_20

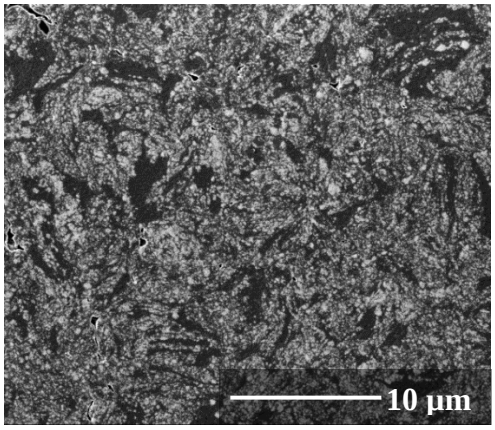

(e) C200_25

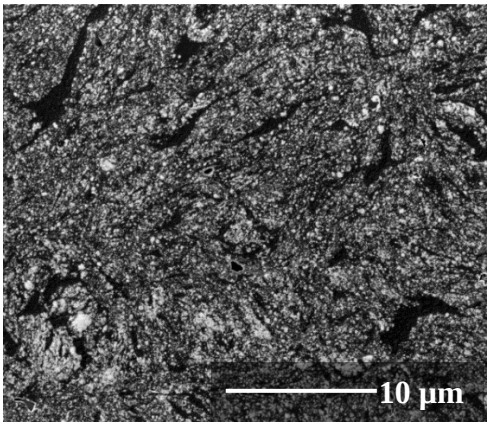

(f) C200_30

Figure 5.9: FIB images of the C200 batches of powder from 5 to 30 hours of milling **(a)** C200_5, **(b)** C200_10, **(c)** C200_15, **(d)** C200_20, **(e)** C200_25, **(f)** C200_30

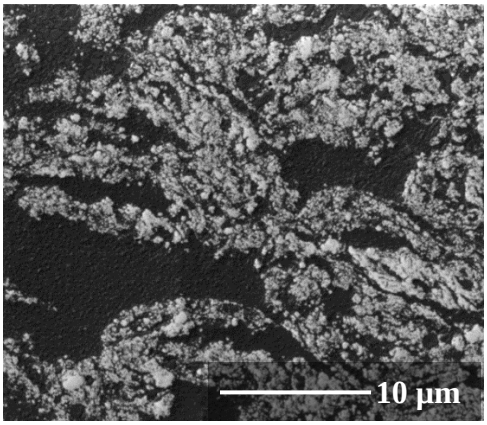

(a) C250/200_5

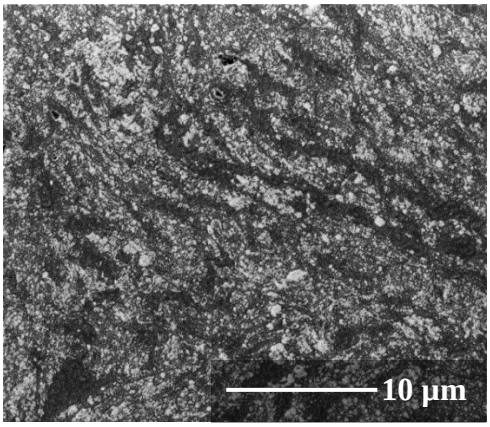

(b) C250/200_10

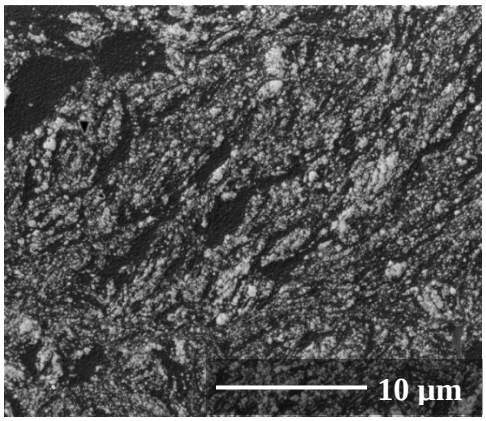

(c) C250/200_15

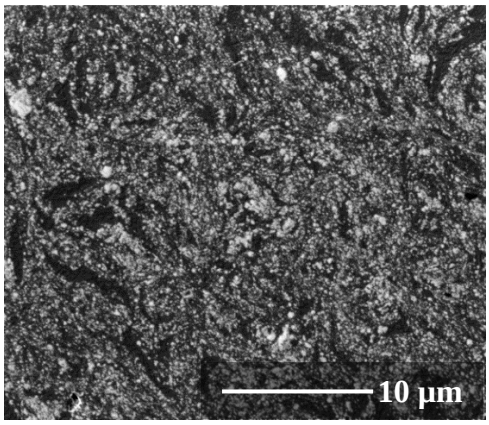

(d) C250/200_20

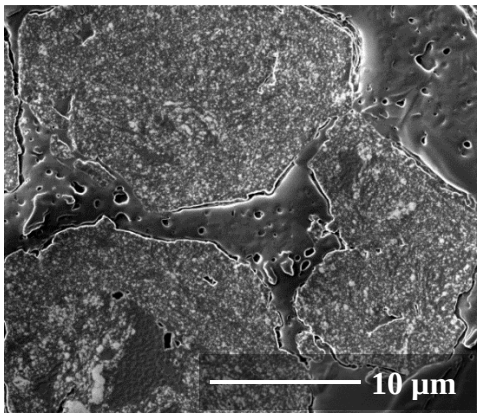

(e) C250/200_25

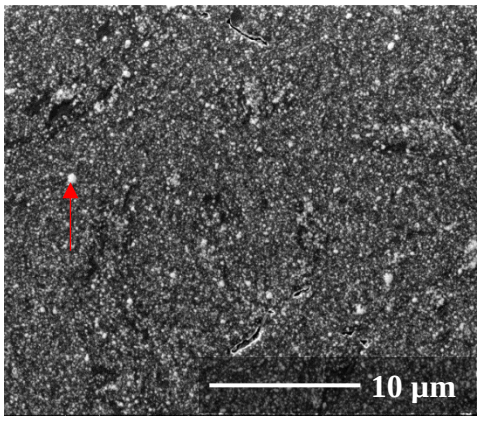

(f) C250/200_30

Figure 5.10: FIB images of the C250/200 batches of powder from 5 to 30 hours of milling **(a)** C250/200_5, **(b)** C250/200_10, **(c)** C250/200_15, **(d)** C250/200_20, **(e)** C250/200_25, **(f)** C250/200_30

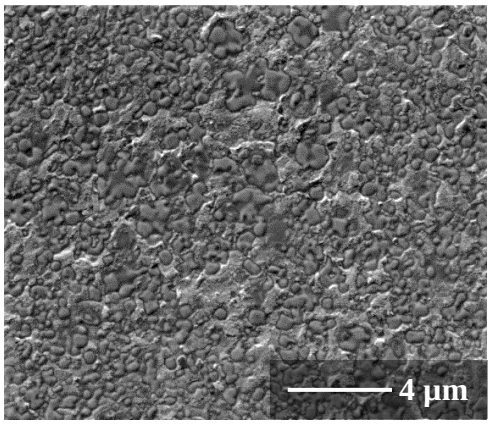

(a) C250_I_1

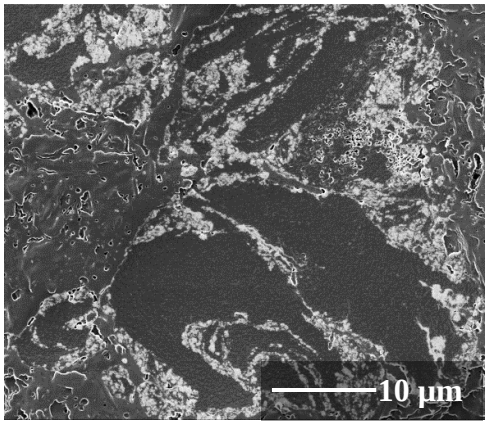

(b) C250_II_5

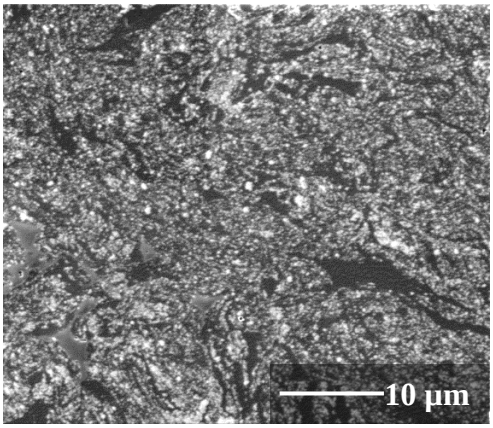

(c) C250_II_10

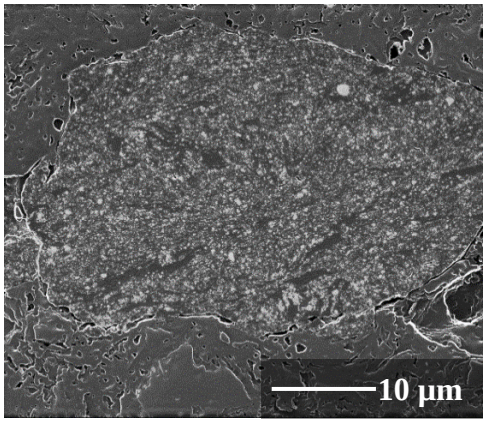

(d) C250_II_15

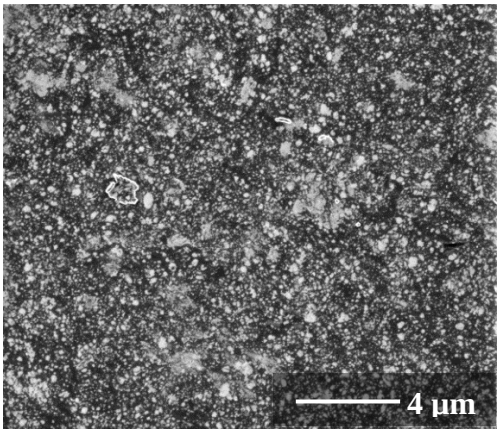

(e) C250_II_20

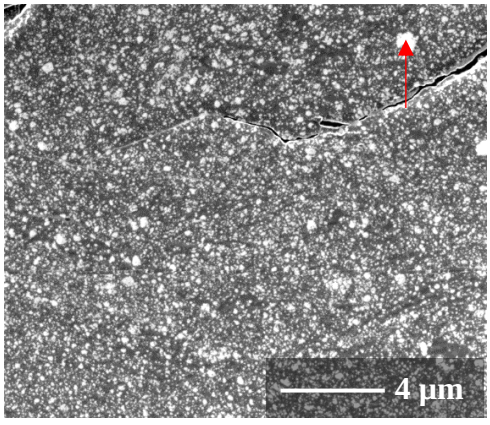

(f) C250_II_30

Figure 5.11: FIB images of the C250_II batches of powder from 5 to 30 hours of milling **(a)** C250_I_1, **(b)** C250_II_5, **(c)** C250_II_10, **(d)** C250_II_15, **(e)** C250_II_20, **(f)** C250_II_30

The low resolution of FIB makes it difficult to identify the shape and the size of the γ-Al_2O_3 particles and clusters. To solve this issue, STEM DF imaging and EDX mapping for the C150, the C200, the C250/200 and the C250 samples with various milling time are shown from Figure 5.12 to Figure 5.15. EDX mappings and EDX spectra were used for identifying the γ-Al_2O_3.

The STEM imaging and the EDX mapping also have limitations: only very small sample with size around 15μm × 6μm can be made in FIB from one powder particle, and the small size sample cannot represent the general feature of the powder when the microstructure is not homogeneous. Therefore, only samples with high milling hours and relative good homogeneity were characterised with STEM.

Figure 5.12 is a STEM image of C150_25. The particle labelled as (1) in Figure 5.12(a) with 63.9at.% O and 36.1at.% Al should be a γ-Al_2O_3 cluster. The EDX mapping of oxygen element was shown in Figure 5.12(b). This γ-Al_2O_3 cluster is still very large with about 500nm in diameter.

Figure 5.13, Figure 5.14 and Figure 5.15 are the STEM analysis of the nanocomposites. For each STEM DF image, an EDX mapping of O element is provided on the right side. The regions rich in O element were verified to be γ-Al_2O_3 clusters with EDX spectra. The proportions of O and Al elements in these areas were ~60% and ~40%. For C200 powders, from Figure 5.13(a1) after 10 hours of milling, the γ-Al_2O_3 band can be detected in the sample, labelled as (1). After 20 hours of milling, areas with very large γ-Al_2O_3 agglomerations are still observed, as shown in Figure 5.13(b1) and (b2). After 30 hours of milling, most of the γ-Al_2O_3 clusters have relative smaller sizes, ranging from 100nm to 500nm, as shown in Figure 5.13(c1) and (c2). For the C250/200 and C250_II batches, the

γ-Al_2O_3 distribution is already very good after 10 hours milling, as shown in Figure 5.14(a1), (a2) and Figure 5.15(a1), (a2) respectively. From 10 to 30 hours of milling the distribution level has no obvious changes, as shown in Figure 5.14 (b1), (b2), (c1), (c2) and Figure 5.15(b1), (b2), (c1), (c2).

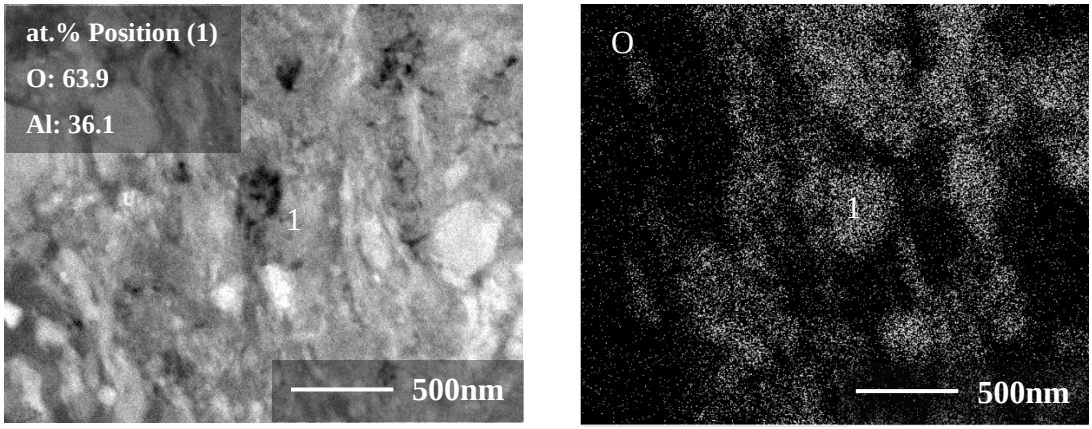

(a) C150_25 (b) EDX mapping of C150_25

Figure 5.12: STEM DF imaging and EDX mapping of C150 powders **(a)** the C150_25 sample **(b)** EDX mapping of O element of C150_25

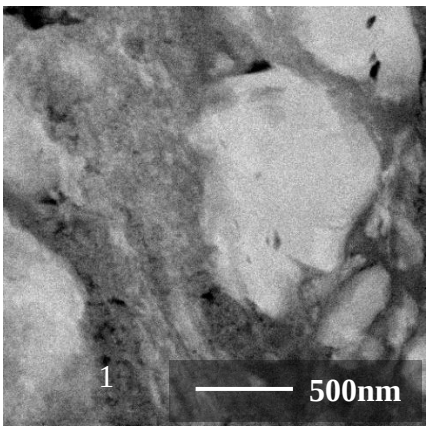

(a1) C200_10

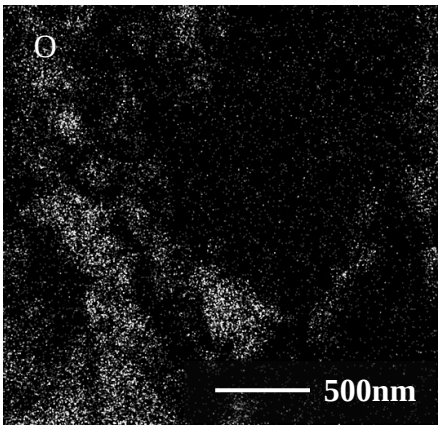

(a2) EDX mapping of C200_10

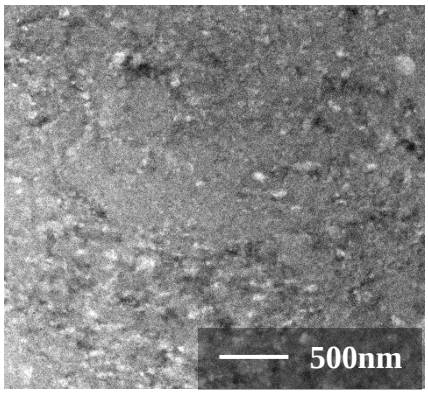

(b1) C200_20

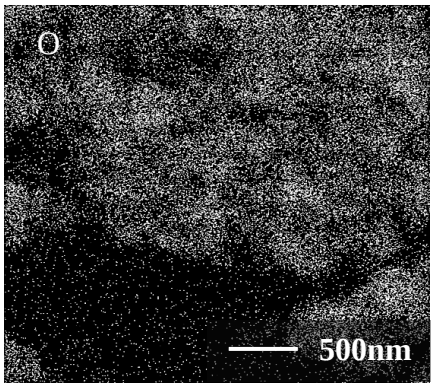

(b2) EDX mapping of C200_20

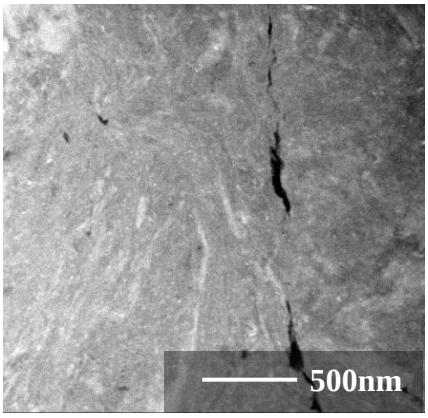

(c1) C200_30

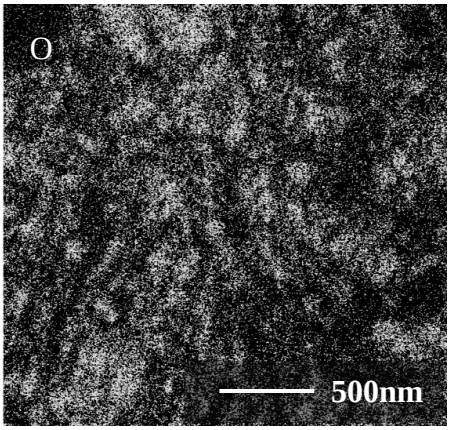

(c2) EDX mapping of C200_30

Figure 5.13: STEM DF imaging and EDX mapping of C200 batch powder **(a1)** C200_10, **(a2)** EDX mapping of O element of C200_10, **(b1)** C200_20, **(b2)** EDX mappings of O element of C200_20, **(c1)** C200_30, **(c2)** EDX mappings of O element of C200_30

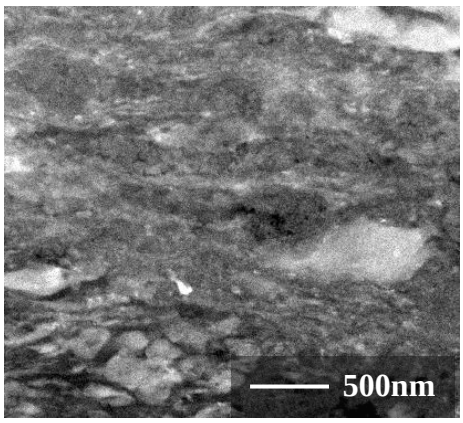

(a1) C250/200_10

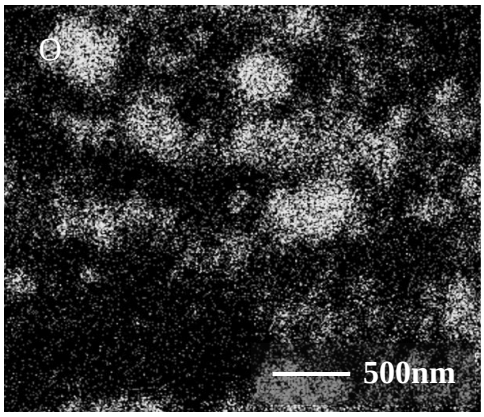

(a2) EDX mapping of C250/200_10

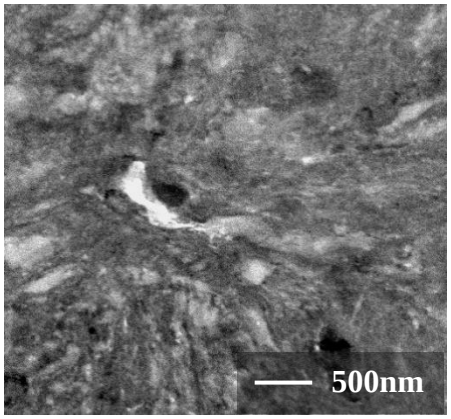

(b1) C250/200_20

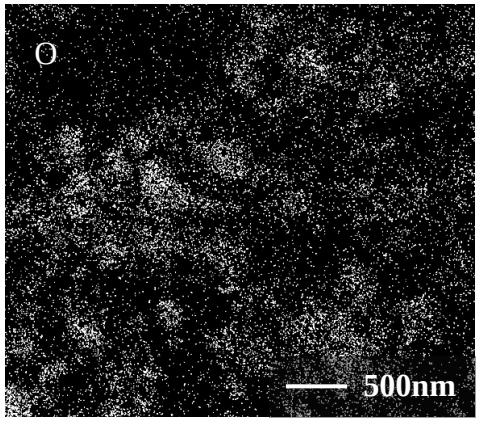

(b2) EDX mapping of C250/200_20

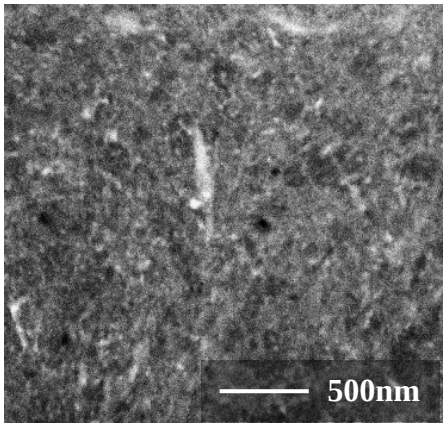

(c1) C250/200_30

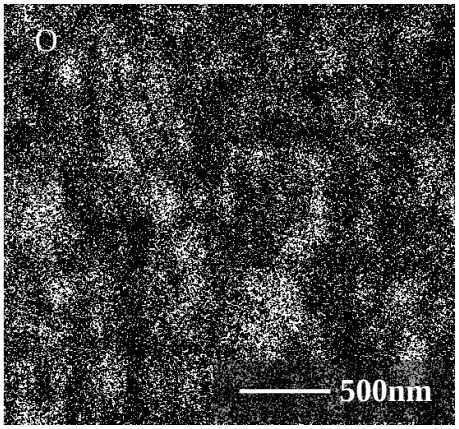

(c2) EDX mapping of C250/200_30

Figure 5.14: STEM DF imaging and EDX mapping of C250/200 batch powder **(a1)** C250/200_10, **(a2)** EDX mapping of O element of C250/200_10, **(b1)** C250/200_20, **(b2)** EDX mappings of O element of C250/200_20, **(c1)** C250/200_30, **(c2)** EDX mappings of O element of C250/200_30

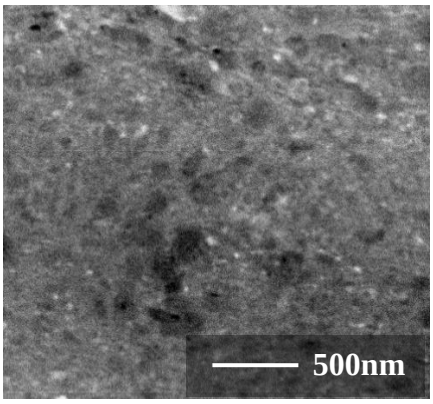

(a1) C250_II_10

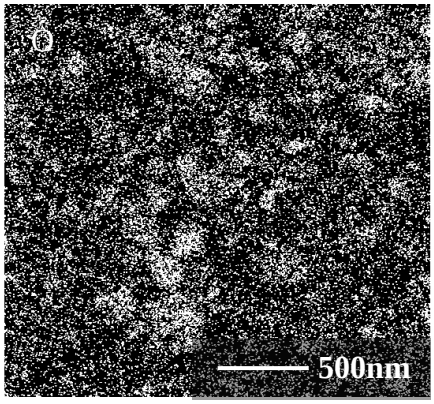

(a2) EDX mapping of C250_II_10

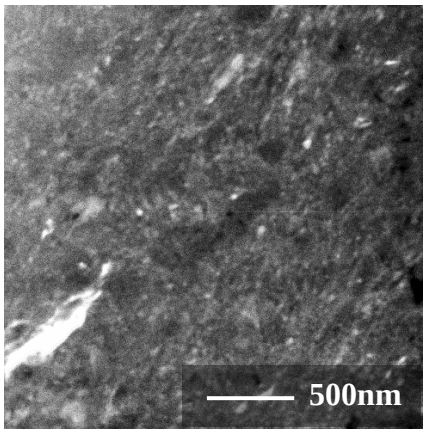

(b1) C250_II_20

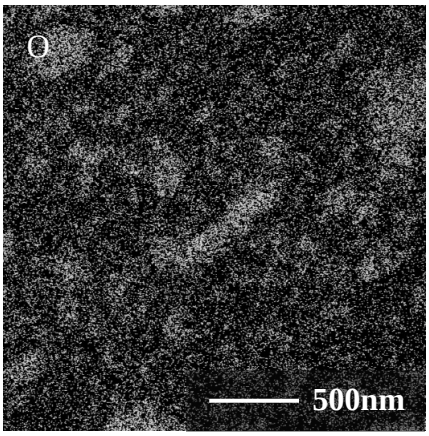

(b2) EDX mapping of C250_II_20

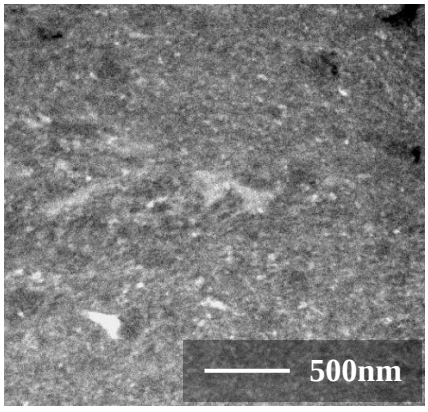

(c1) C250_II_30

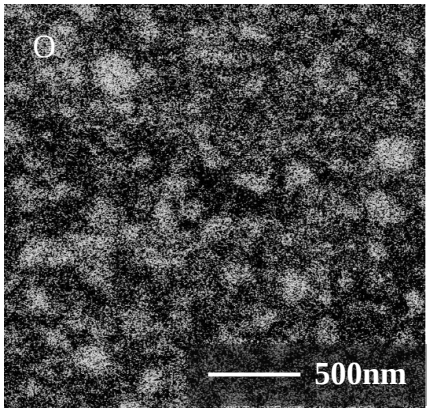

(c2) EDX mapping of C250_II_30

Figure 5.15: STEM DF imaging and EDX mapping of C250_II batch powder **(a1)** C250_II_10, **(a2)** EDX mapping of O element of C250_II_10, **(b1)** C250_II_20, **(b2)** EDX mappings of O element of C250_II_20, **(c1)** C250_II_30, **(c2)** EDX mappings of O element of C250_II_30

The same method for measuring the crystallite sizes (explained in section 4.3.1 in Chapter 4) was used for measuring the γ-Al_2O_3 cluster size. Two pairs of parallel lines were drawn around each γ-Al_2O_3 cluster in the STEM images, and the distance between each of them was measured. The average value of the two measured distances was taken as the γ-Al_2O_3 cluster size. At least 20 clusters or particles were measured to ensure the accuracy.

The γ-Al_2O_3 sizes corresponding to C200, C250/200, and C250_II powders after 10, 20 and 30 hours of milling are shown in Figure 5.16. For the C200_10 powder, the γ-Al_2O_3 distributes in band shape and the small STEM sample cannot represent the general feature of the sample. Therefore, the γ-Al_2O_3 cluster size was not provided for C200_10. As shown in Figure 5.16, the γ-Al_2O_3 cluster sizes decrease with the milling speeds. For the C200 batch and the C250/200 batch, the cluster sizes decrease with milling time. The C250_II batch have no significant changes in γ-Al_2O_3 cluster sizes during the milling from 10 to 30 hours. The γ-Al_2O_3 cluster sizes of the C200, C250/200 and C250_II batches of powders reach smallest values after 30 hours of milling, which are 273±97nm, 101±45nm and 90±29nm respectively.

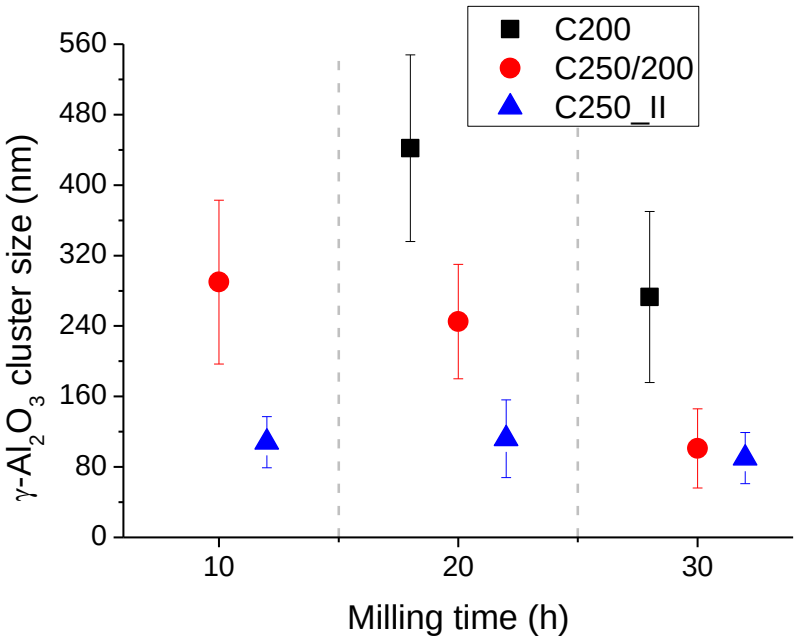

Figure 5.16: The γ-Al_2O_3 cluster sizes of the mechanically milled powder.

5.3 Phase and microstructure analysis

5.3.1 Phase characterisation

The X-ray diffractograms of the C150, C200, C250/200 and C250_II batches mechanically milled powders are shown in Figure 5.17, Figure 5.18, Figure 5.19 and Figure 5.20. For each batch, powders milled for 0 to 30 hours are plotted in one diagram to identify whether phase transformation occurs during the milling. C_0 corresponds to the composite powder without milling. The diffractograms show that there are four major phases in all the powder batches: (1) the α-Al phase observed with peak positions at 2θ of 38.5°, 44.7°, 65.1°, 78.3° and 82.5°.(2) the quasicrystalline phase detected at 2θ of 22.70°, 41.1°, 43.3°, and 73.3°, labelled following Cahn's notation (Cahn, Shechtman et al. 1986, Galano, Audebert et al. 2009) (3) the γ-Al_2O_3, with only γ(440) peak observed at 66.3°. (4) Al_3Ti phase is observed at 39.3°. The insets in these images highlight the γ(440) at 66.3° and i(52/84) at 77.3°. The

i(38/61) peak at 2θ position 61.0° of the quasicrystalline phase and other peaks corresponding to the γ-Al_2O_3 are not observed, probably because of the low volume fraction.

For C150 powders, no apparent changes are observed in the relative intensity of the icosahedral quasicrystalline phase peaks after ball milling. For the C200, the C250/200 and the C250_II batches, the quasicrystalline peak intensities drop gradually with increasing milling time. For the C250_II_30 sample, the peaks corresponding to the icosahedral phases could hardly be seen. In section 4.1.2 in Chapter 4, Al-Fe intermetallics are observed in the unmilled powder using TEM. These phases were not detected with X-ray diffractograms, probably due to the low volume fraction.

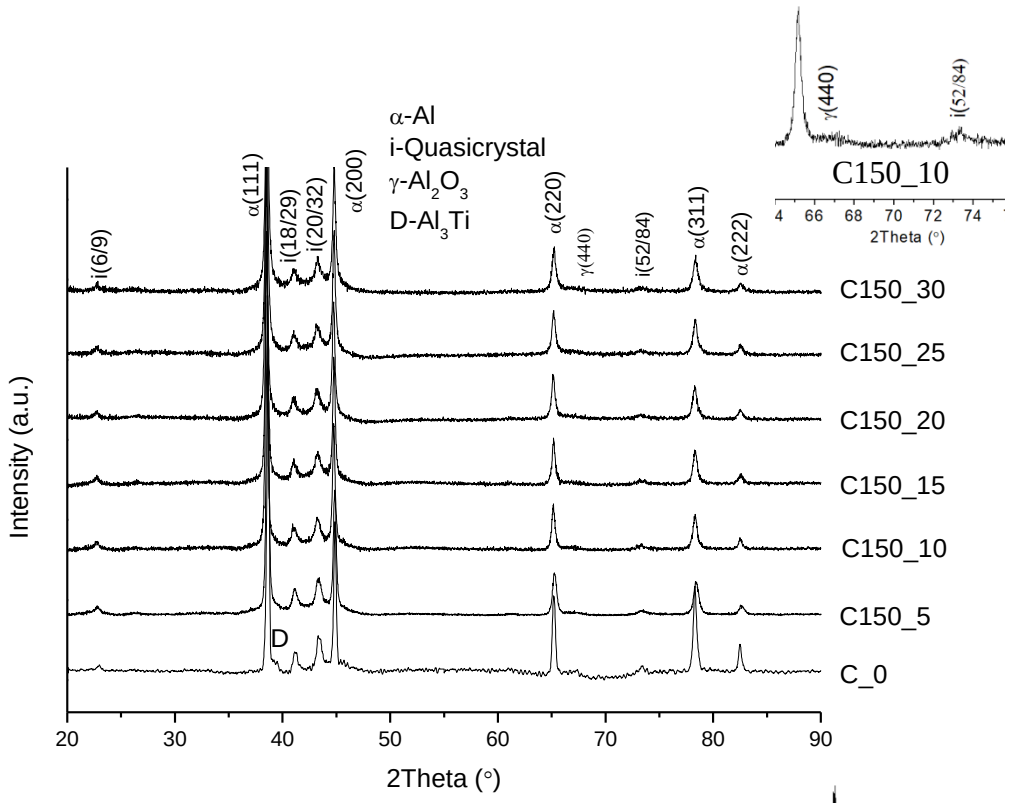

Figure 5.17: X-ray diffractograms of C150 powders

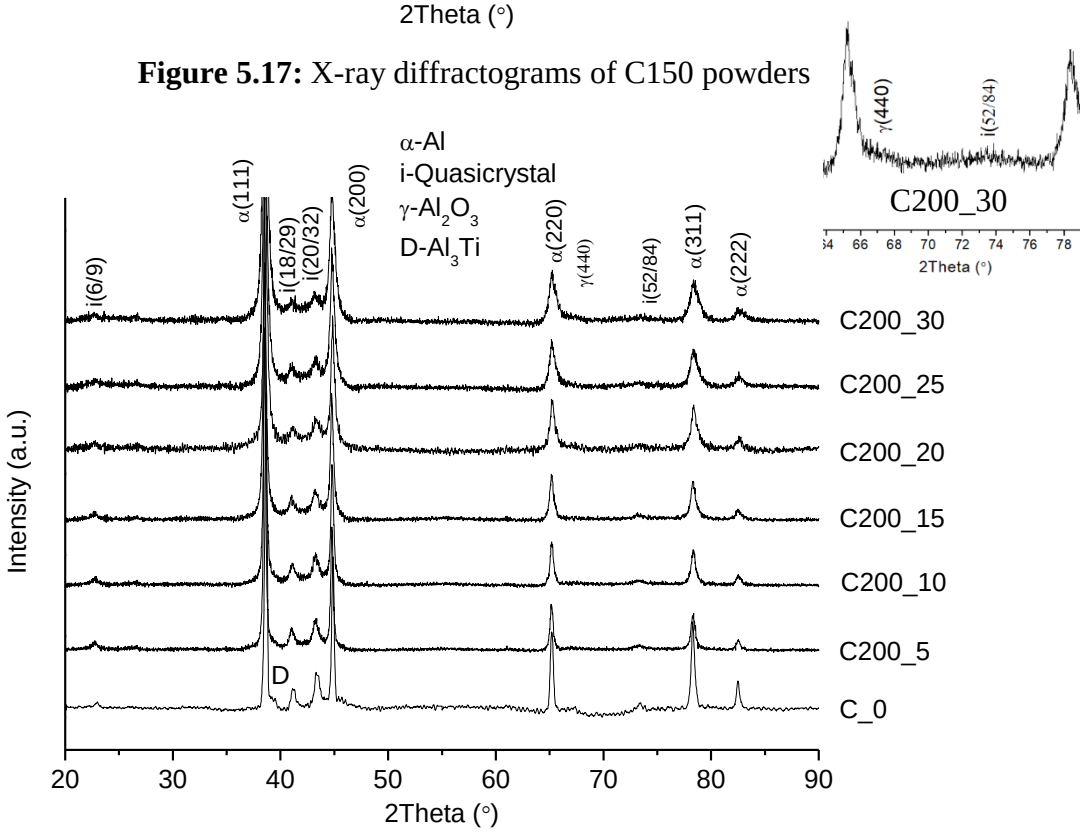

Figure 5.18: X-ray diffractograms of C150 powders

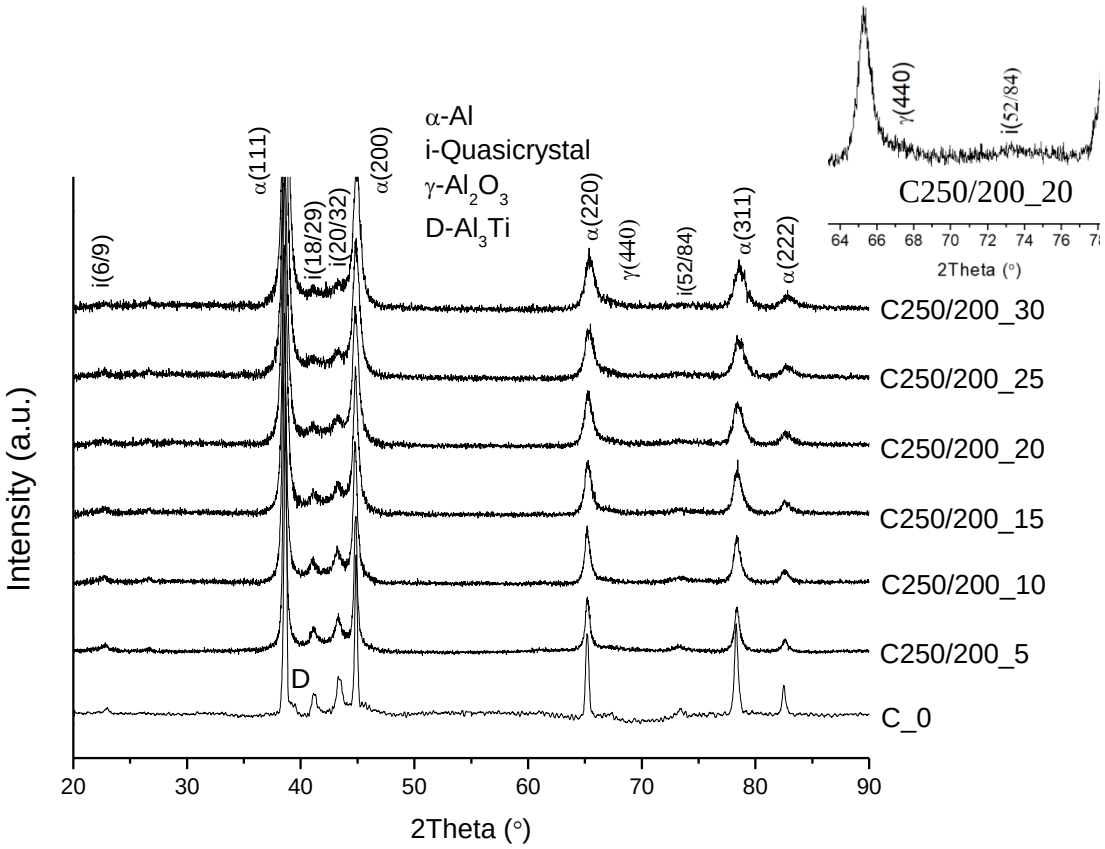

Figure 5.19: X-ray diffractograms of C250/200 powders

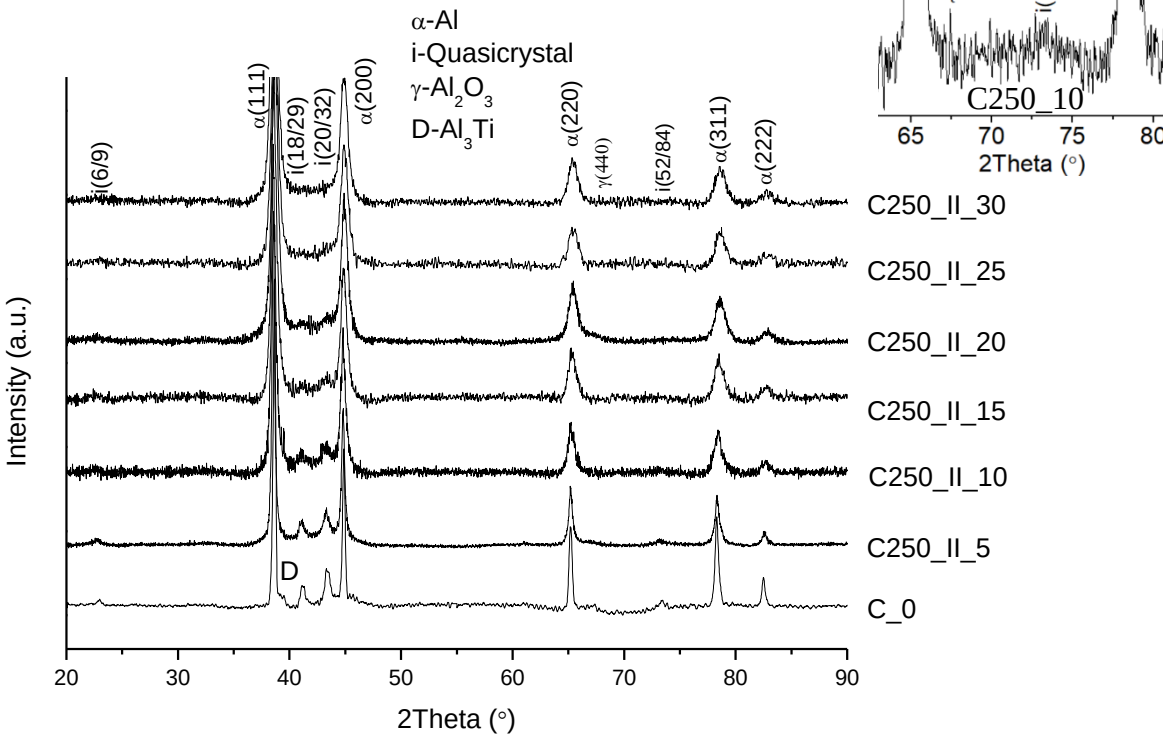

Figure 5.20: X-ray diffractograms of C250 powders

5.3.2 Crystallite sizes

The average Al crystallite sizes and the strain values of the ball milled powders were estimated through the Williamson-Hall method (Williamson and Hall 1953) and summarised in Figure 5.21. Only powder samples of the C200 batch with milling time equal or higher than 20 hours, and samples of the C250/200 and C250_II batches with milling time equal or higher than 10 hours were used in this estimation, since Williamson-Hall plot produces large errors when the Al crystallite sizes are larger than 100 nm (Galano, Marsh et al. 2015). The Al crystallite sizes of the C250/200_5 and C250_II_5 samples were also measured using TEM, following the method described in section 4.3.1 in Chapter 4.

For all the milled powders, the crystallite sizes decrease with milling time. In Figure 5.21 (a), for the same milling time, samples produced at higher milling speed have a smaller average Al crystallite size. The C200, C250/200, C250_II batches reach their lowest crystallite size values of 30nm, 20nm, and 14nm after 30 hours, 30hours, and 25 hours of milling, respectively. The strain values of all milled powder batches do not show a clear trend. Most of the values lay between 1.0% and 1.5%. The C250_II_25 and C250_II_30 samples have lower strains than other samples, 0.61% and 0.73% respectively. In the literature, most nanocomposites processed with ball milling have strain values round 1% (Fogagnolo, Robert et al. 2006, Poirier, Drew et al. 2010).

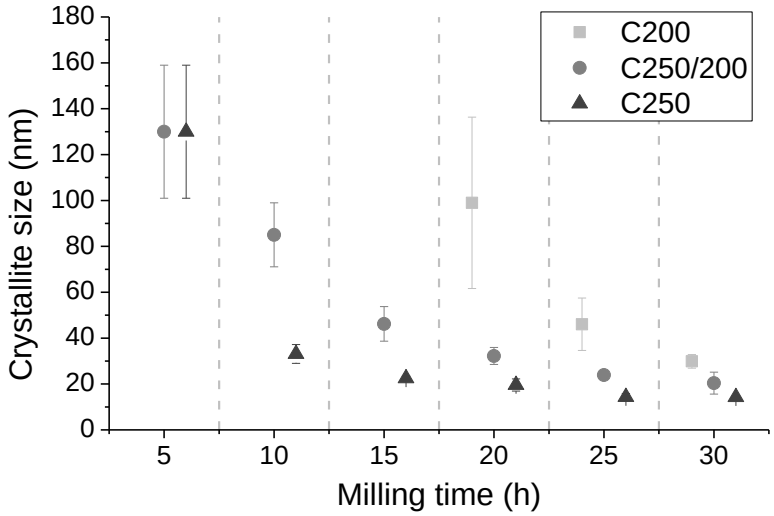

(a)

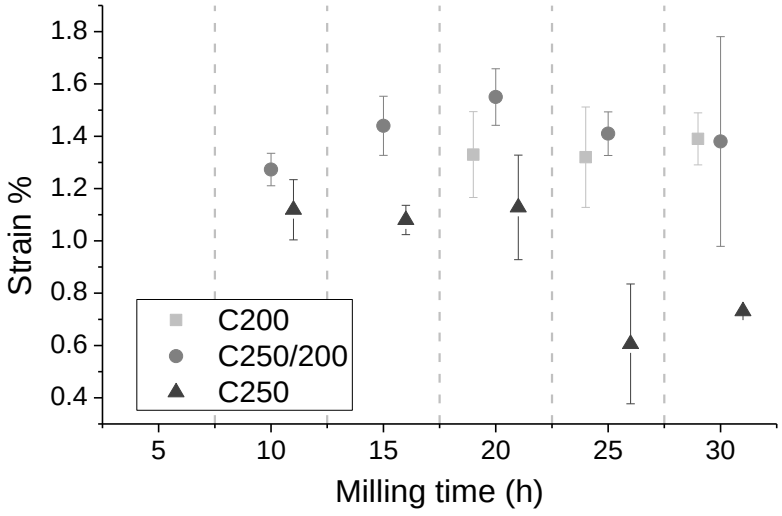

(b)

Figure 5.21: (a) Crystallite sizes and **(b)** strains of C200, C250/200, and C250_II batches powder

5.3.3 Microstructure evolution

For C150 powders the microstructure is not homogeneous. The C150_25 sample is analysed in Figure 5.22 using TEM BF imaging, STEM imaging, EDX mappings and EDX spectra. The approximate composition of transition atoms (Figure 5.22(g)) of particle (1) in Figure 5.22(a) is very close to the composition of quasicrystals in the $Al_{93}Fe_3Cr_2Ti_2$ alloy system as quoted in literature (Kimura, Sasamori et al. 2000). This indicates that such phase has a high possibility to be a quasicrystal. Particles (2) and (3) in Figure 5.22(a) should be an Al grain and a γ-Al_2O_3 cluster, verified using the EDX spectra in Figure 5.22(g). The Al grain labelled with (2) has a diameter of about 300nm. Since the unmilled A powder has an average Al grain size of 1.5 μm, there is grain refinement during the milling. The size of the γ-Al_2O_3 cluster labelled with (3) is larger than 500nm. Moreover, the large cracks in the sample which were never found in the unmilled powders were detected. Some Al-Fe intermetallics were detected through the EDX mapping near the particle (1), as highlighted in Figure 5.22(c).

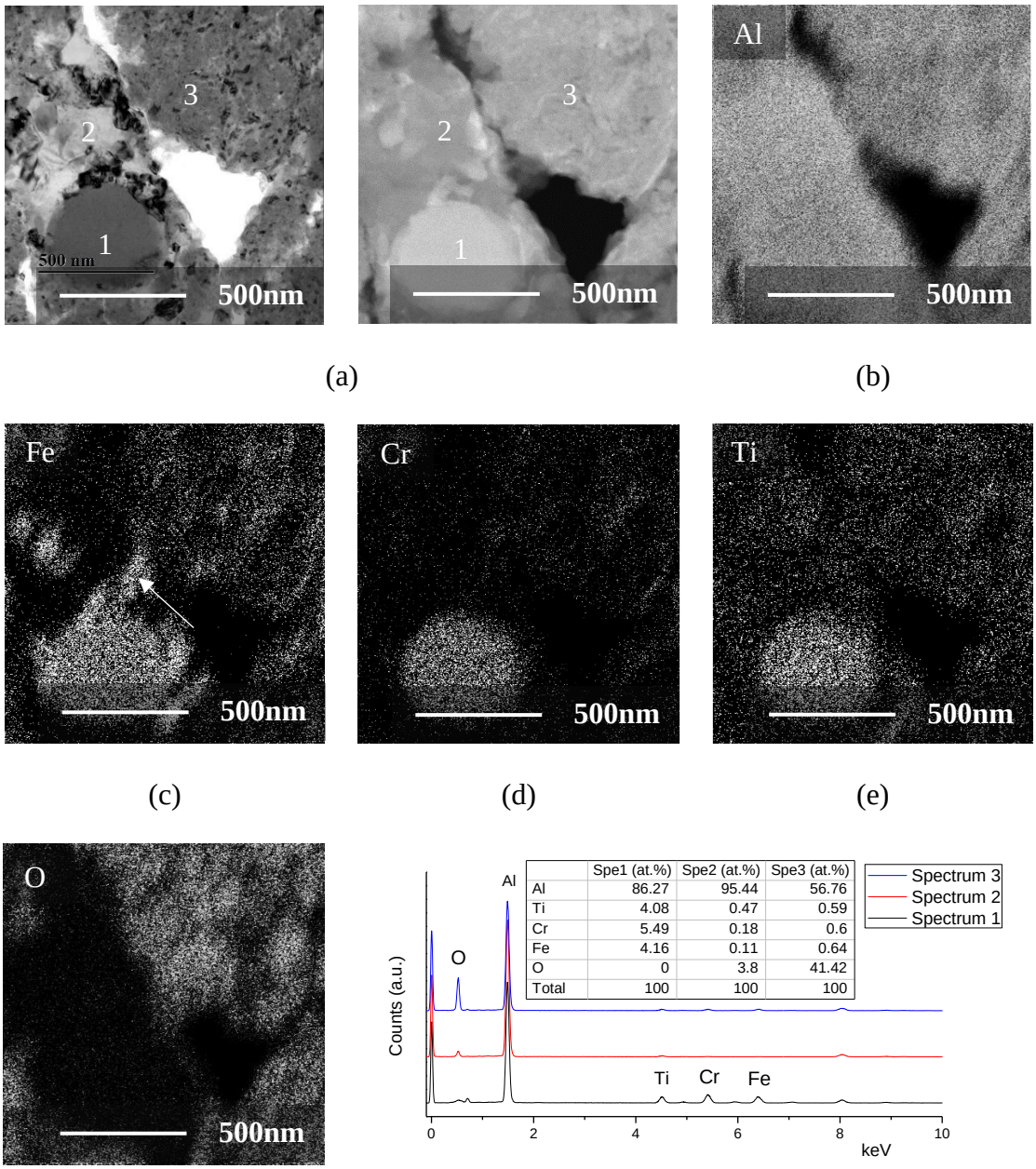

Figure 5.22: TEM, STEM images and EDX data from the C150_25 sample. **(a)** TEM BF image (left) and STEM DF image (right), **(b)** EDX mapping: Al element, **(c)** EDX mapping: Fe element, **(d)** EDX mapping: Cr element, **(e)** EDX mapping: Ti element, **(f)** EDX mapping: O element, **(g)** EDX spectra of the particles 1, 2 and 3

For the C200_10 sample, as observed in Figure 5.23(a), after 10 hours of milling, a number of spherical particles (suspected to be quasicrystals) still exist in the sample. The equiaxed shaped grains are proven to be Al, for example, particle (1) which has been identified by a CBDP in the inset of Figure 5.23(b). Figure 5.23(c) shows a TEM BF image taken from the same area with the STEM image shown in Figure 5.13(a1). Area 2 corresponds to a γ-Al_2O_3 band based on the EDX mappings in Figure 5.13(a2). Particle (3) and (4) in this image are quasicrystals as identified with the CBDPs from a mirror zone axis (the inset in Figure 5.23(c)) and a threefold zone axis (Figure 5.23(d)). The two quasicrystals are adjacent, yet with different orientations. A selected area diffraction pattern (SADP) is obtained within a circle area (5) by the selected area aperture, as shown in Figure 5.23(e). The rings match well with the aluminium indexing (National Chemical Database Service 2016), which means the tiny black particles in circle area (5) are suspected to be the Al crystallites. No discrete spots were found. After obtaining the SADP, the TEM objective aperture is adjusted to select a few diffraction spots sitting on the rings in area (6) in Figure 5.23(e). Turning back into the imaging mode, a TEM DF image is obtained in Figure 5.23(f). The benefit for DF imaging is that it offers a better contrast for the Al crystallites. The white crystallites marked with red arrows in Figure 5.23(f) correspond to those marked with blues arrows in Figure 5.23(c). The crystallites here are smaller than the ones detected in Figure 5.23(a) and (b). The C200_30 sample is also characterised by TEM. As shown in Figure 5.24(a), no large quasicrystalline particles can be observed. Small Al crystallites could still be detected in the sample, which were verified through the SADP in the inset of Figure 5.24(a) and dark field image in Figure 5.24(b).

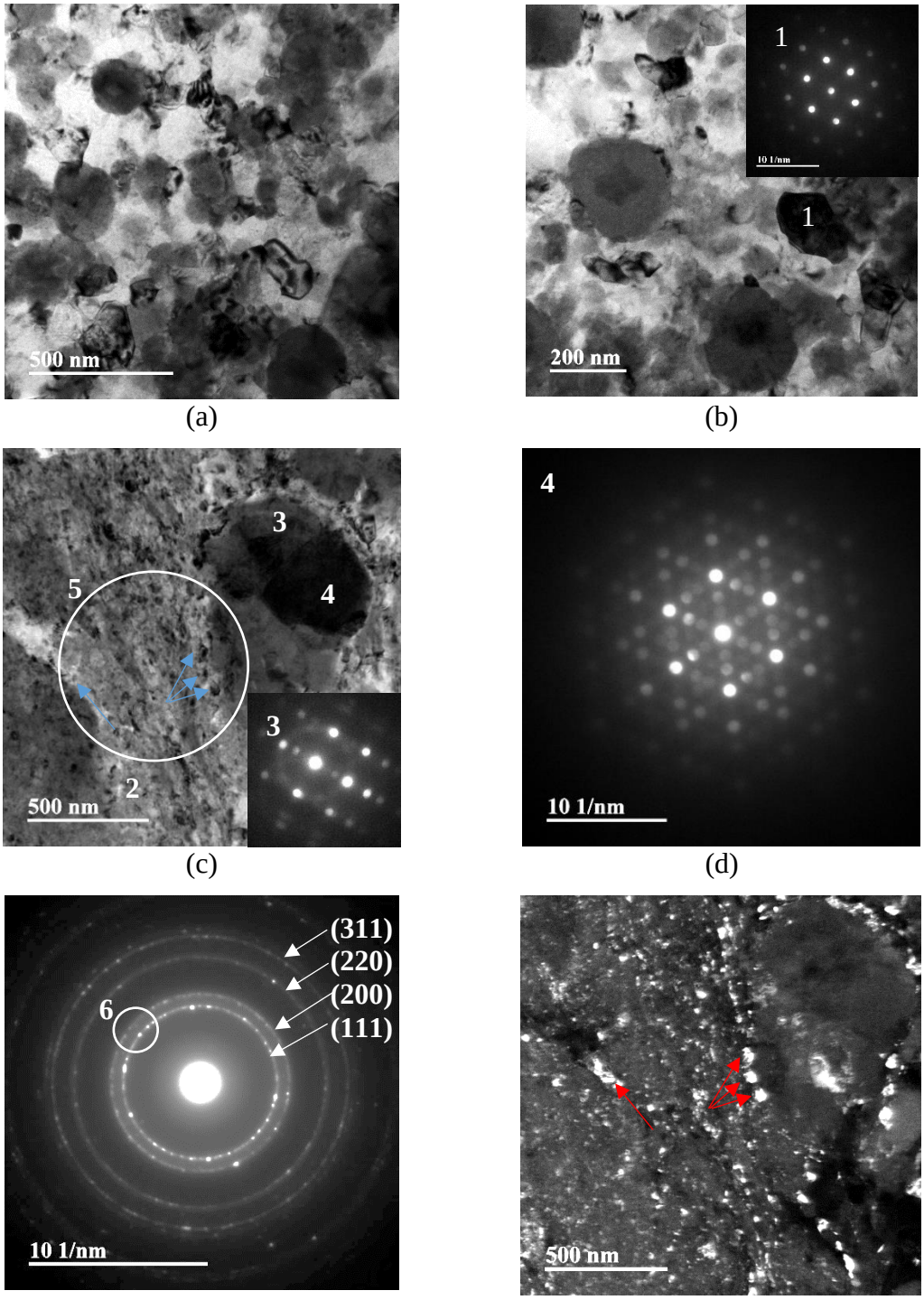

Figure 5.23: TEM characterisation of the C200_10 sample **(a)** TEM BF image, **(b)** TEM BF image and CBDP from particle (1), **(c)** TEM BF image and CBDP from particle 3, **(d)** CBDP from particle (4) showing in (c), **(e)** SADP from area (5) showing in (c), **(f)** DF image from the same area showing in (c)

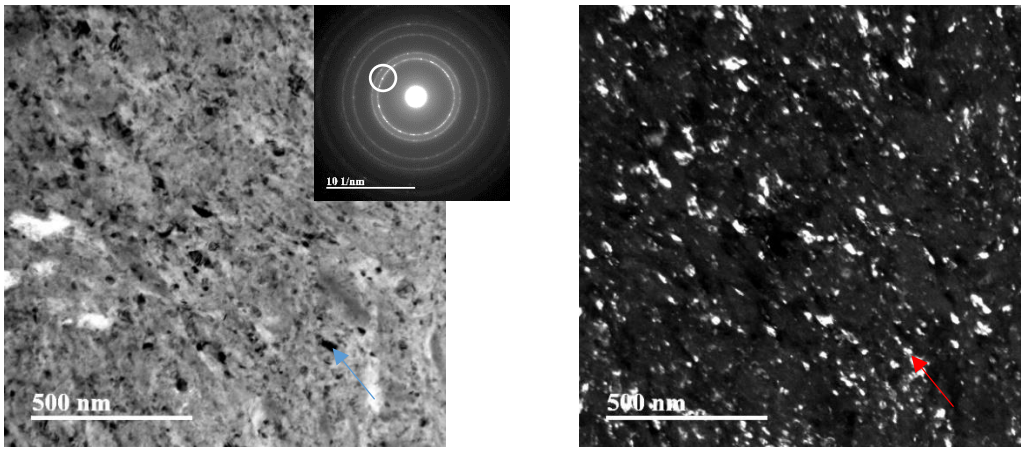

(a) (b)

Figure 5.24: (a) TEM BF image and diffraction pattern of C200_30, **(b)** TEM DF image of C200_30

For the C250/200_10 sample, ultra-fine crystallites are also detected by TEM, as shown in Figure 5.25. Figure 5.25(a) is a TEM BF image of C250/200_10, and the SADP from area (1) is shown in Figure 5.25(b). The rings in the SADP match well with the aluminium indexing (111), (200), (220) and (311) respectively. Particles (2) and (3) shown in Figure 5.25(c) are quasicrystals with the same orientations as proven by the CBDPs in the insets. The composition of particle (3) was also identified by EDX spectra in Figure 5.25(e). Particle (4) was also a quasicrystal identified with a CBDP in Figure 5.25(d), but with a different orientation of particle (2). Compared with the C200_10 sample, quasicrystals are much more difficult to find in C250/200_10. Area 5 corresponds to the γ-Al_2O_3 cluster, confirmed by the EDX spectrum in Figure 5.25(f). Figure 5.26(a) is the TEM image of C250/200_30. This sample has a rather similar microstructure with that of C200_30. The crystallites marked with blue arrows in Figure 5.26(a) can be clearly seen in the DF image in Figure 5.26(b).

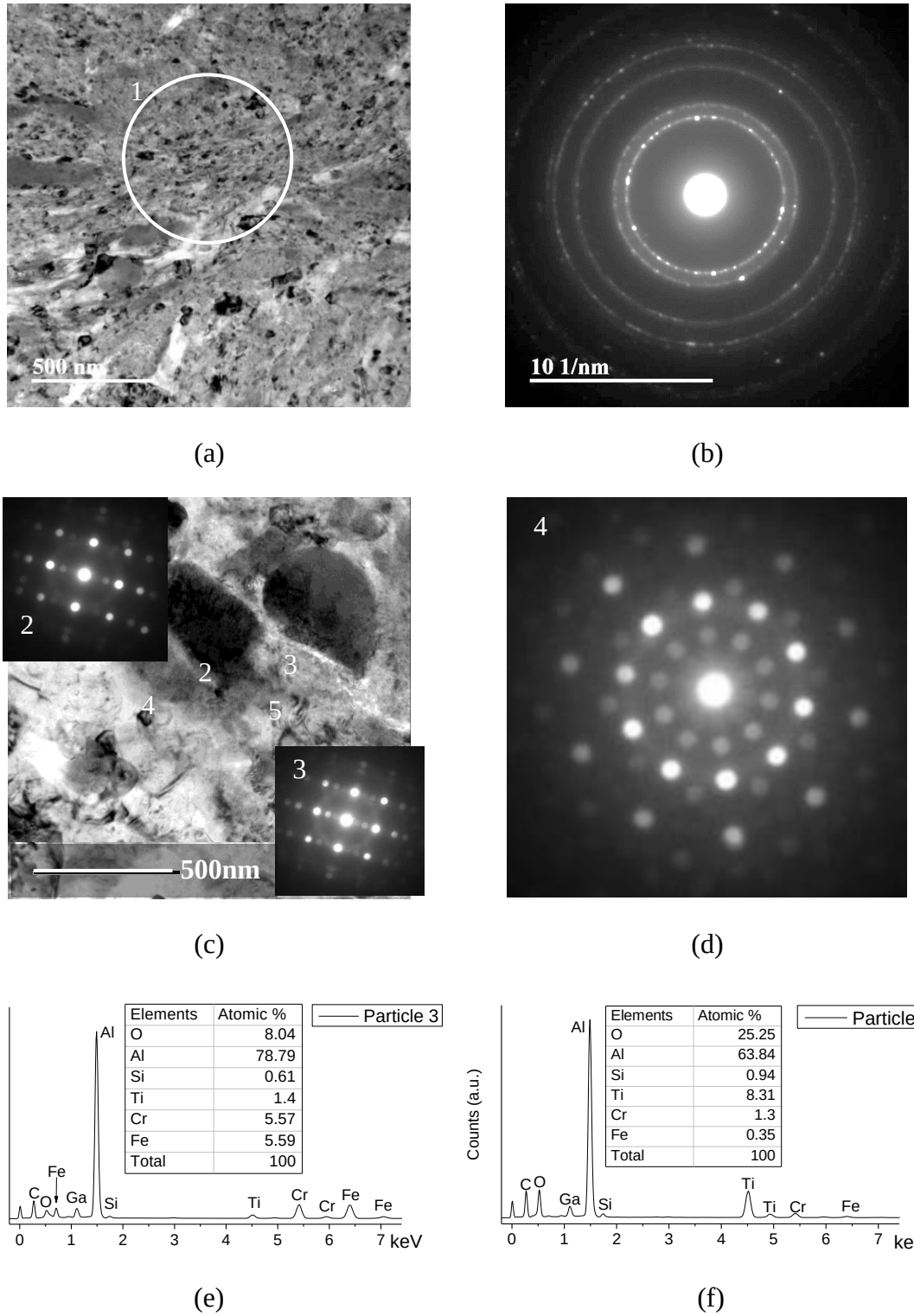

Figure 5.25: **(a)** TEM BF image of C250/200_10, **(b)** an SADP of particle 1 showing in (a), **(c)** TEM BF image of C250/200_10 together with CBDPs of particles (2) and (3), **(d)** CBDP of particle 4 showing in (c), **(e)** EDX spectrum of particle 3 showing in (c), **(f)** EDX spectrum of particle 5 showing in (c)

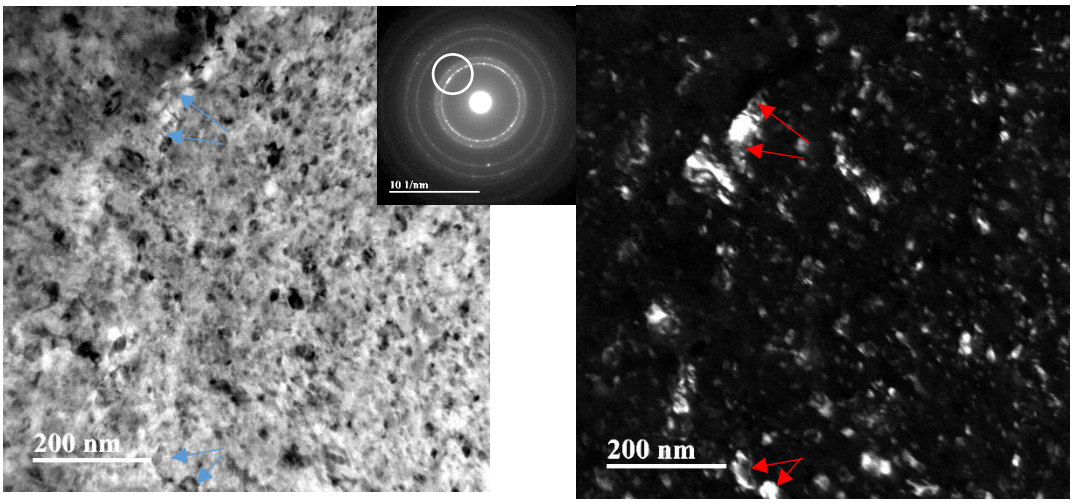

(a) (b)

Figure 5.26: (a) TEM BF images, diffraction patterns of C250/200_30 **(b)** TEM DF image of C250/200_30

The C250_II powders have been studied in detail in Chapter 4. Therefore, only a TEM BF image and a STEM DF image of the C250_10 sample are shown in Figure 5.27(a) and (b) respectively. Particle (1) and (2) in Figure 5.27(b) are γ-Al_2O_3 cluster and the Al matrix respectively, identified by the EDX spectra in Figure 5.27(c).

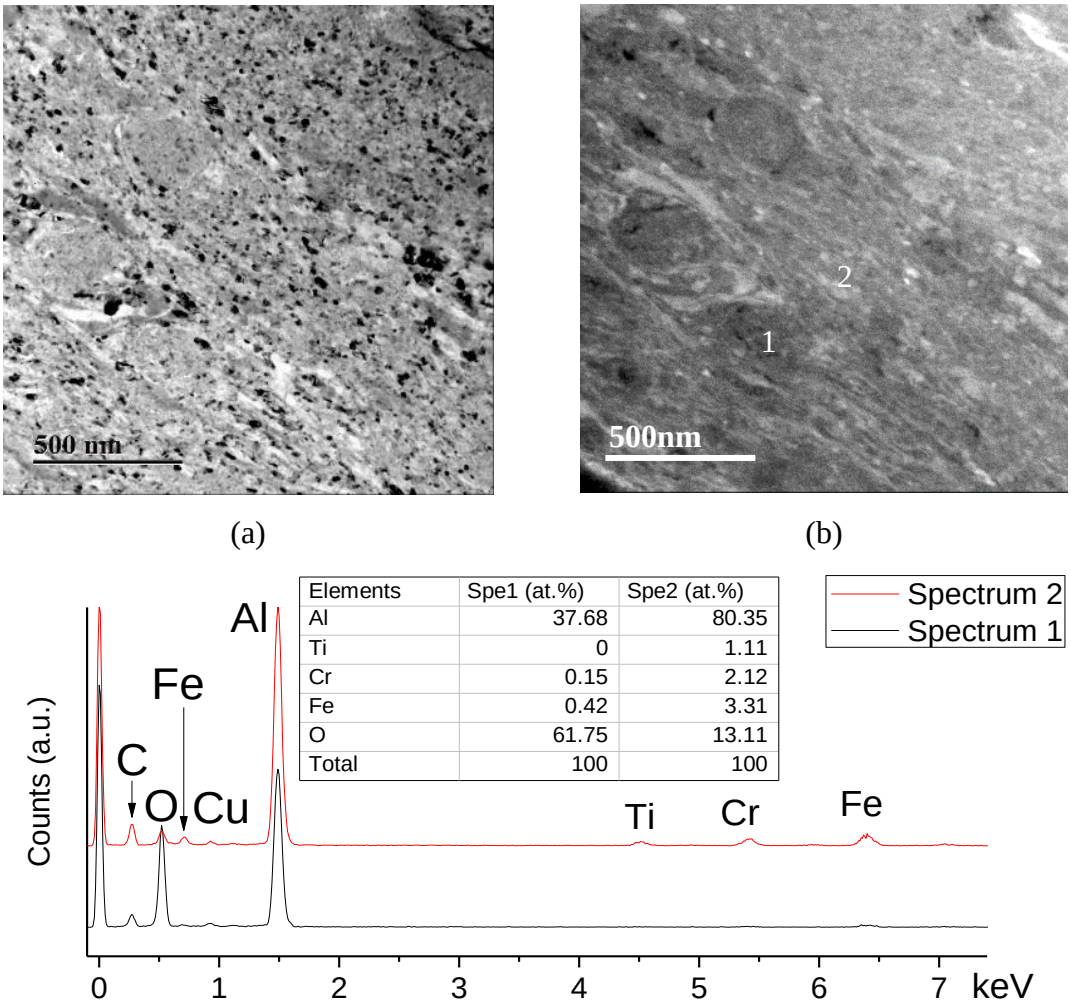

Figure 5.27: (a) TEM BF image, **(b)** STEM DF image and **(c)** EDX spectra of C250_II_10

5.4 Thermal stability of the nanocomposites

Thermal analysis was performed on each mechanically milled powder using DSC runs at different heating rate, namely 10K/min, 20K/min, 40K/min and 80K/min. The DSC analysis highlights the reactions within the powders with increasing temperature. The DSC

scans for the C150, C200, C250/200 and C250_II batches of powders are shown from Figure 5.28 to Figure 5.31.

For the C150 batch shown in Figure 5.28, before milling, the onset temperature for the alloy powder starts at approximately 530℃, and the peak temperature is about 555℃. The onset of this peak shifts to lower temperatures as the milling time increases. After 20 hours of milling the onset temperature drops to 481℃, and the peak temperature is about 515℃. Based on the X-ray diffractograms in Figure 5.17 and the EDX mapping in STEM mode in Figure 5.22, this exothermal peak should be related to the decomposition of the quasicrystal, which is the major metastable phase in the powder. After 25 and 30hs of milling, the exothermal peak becomes unsymmetrical. In literature, unsymmetrical peak is very common in the DSC curves, and usually indicates there might be multiple exothermal events and the peaks overlap with each other (Fujieda and Uchida 1991, Giancola, De Sena et al. 1997). Gaussian fits are applied to separate the overlapping peaks, following the same methods explained in section 4.4 in Chapter 4. For the curves with overlapping peaks in all the images including Figure 5.28, Figure 5.29, Figure 5.30 and Figure 5.31, the peak at lower temperature is named as peak 1, and the peak at higher temperature is named as peak 2.

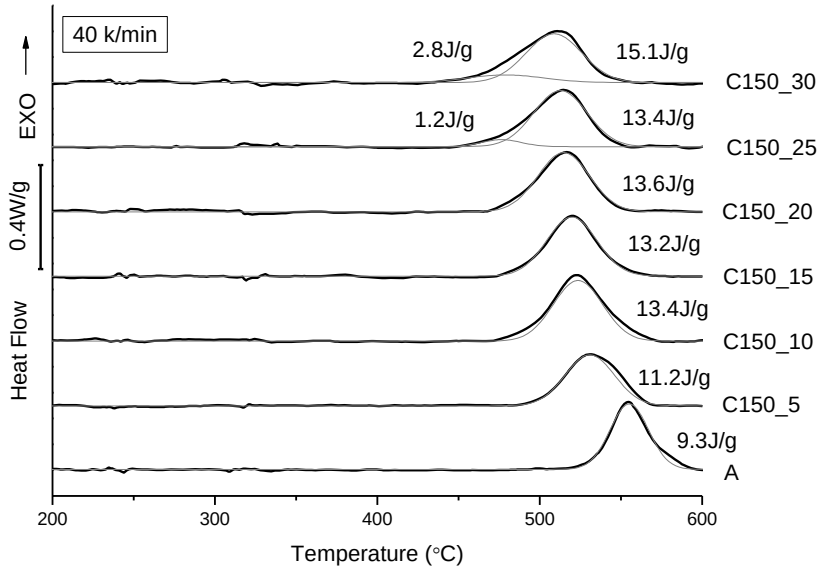

Figure 5.28: DSC heating runs at 40K/min of C150 batches powder. Energy data from an empty pan and the fluctuating baseline have been subtracted from each curve. The sample references are written on the right side of each curve

For the C200 batch powder after 5 hours of milling there is only one exothermal peak, which should correspond to the decomposition of the quasicrystalline phase. After 10 hours of milling another peak on the left side appears, as shown in Figure 5.29. Based on the discussions in section 4.7.3 in Chapter 5, the first peak (peak 1) involves Al grain coarsening and intermetallics precipitation, whereas the second peak (peak 2) involves mostly quasicrystals decomposition. The decomposition temperature corresponding to the right peak drops with milling time. For the C250/200 and C250_II batches of powder two peaks appear after 5 hours of milling. The peak 2 shifts to left side until 15 hours of milling, and then tends to stay stable, as shown in Figure 5.30 and Figure 5.31.

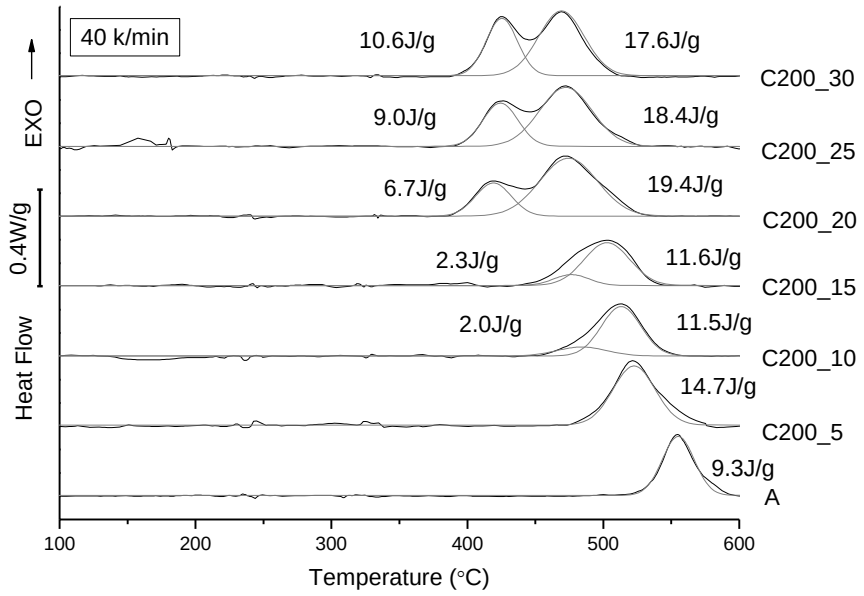

Figure 5.29: DSC heating runs at 40K/min of C200 batches powder. Energy data from an empty pan and the fluctuating baseline have been subtracted from each curve. The sample references are written on the right of each curve

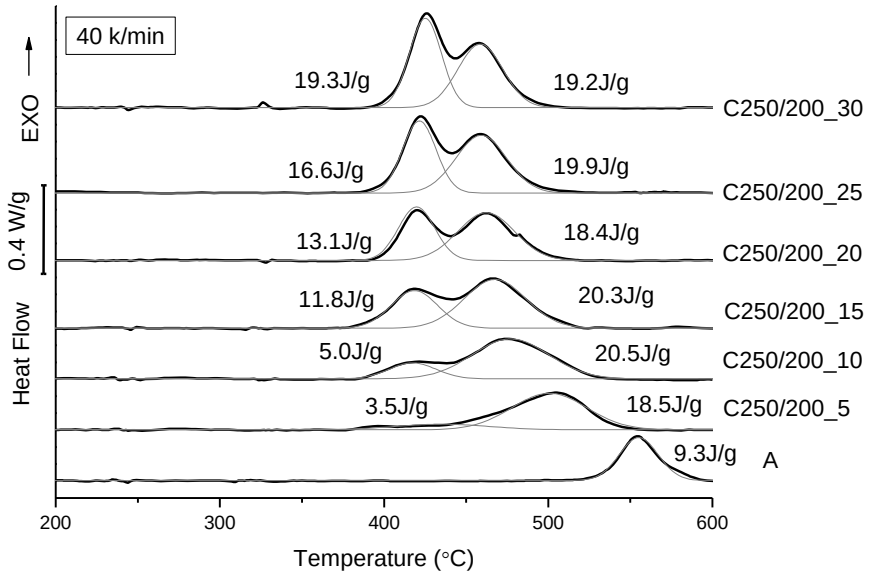

Figure 5.30: DSC heating runs at 40K/min of C250/200 batches powder. Energy data from an empty pan and the fluctuating baseline have been subtracted from each curve. The sample references are written on the right of each curve

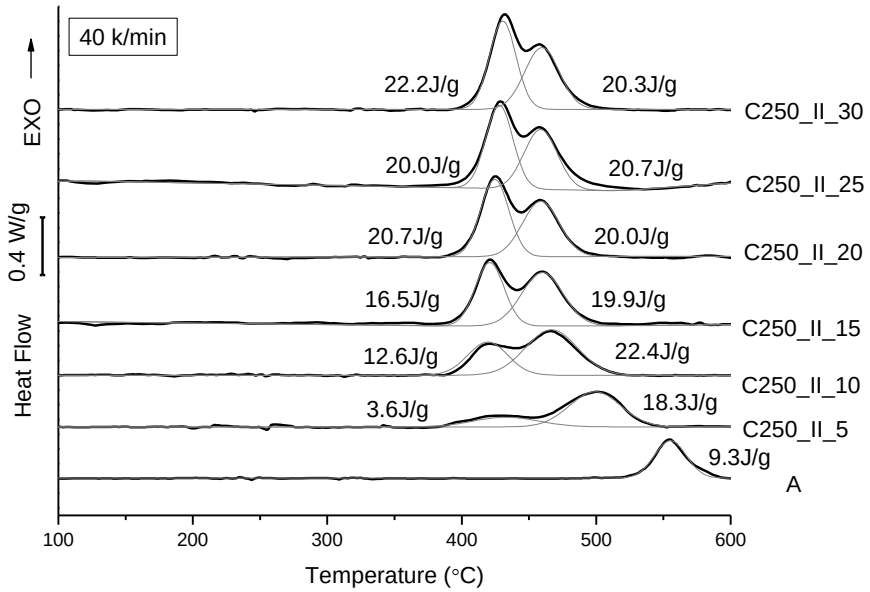

Figure 5.31: DSC heating runs at 40K/min of C250_II batches powder. Energy data from an empty pan and the fluctuating baseline have been subtracted from each curve. The sample references are written on the right of each curve

The peak temperature values corresponding to peak 2 are plotted together, as shown in Figure 5.32. For the C200 batch, the C250/200 batch and the C250_II batch powders, the peak temperature values decrease faster at first, and then reach a plateau. The higher the milling speed, the faster the dropping. For the C150 batch powders, the peak temperature drops from 555℃ to 508℃ after 30 hours of milling. For the C250_II batch powders, the peak temperature decreases from 555℃ to 454℃ after 30 hours of milling.

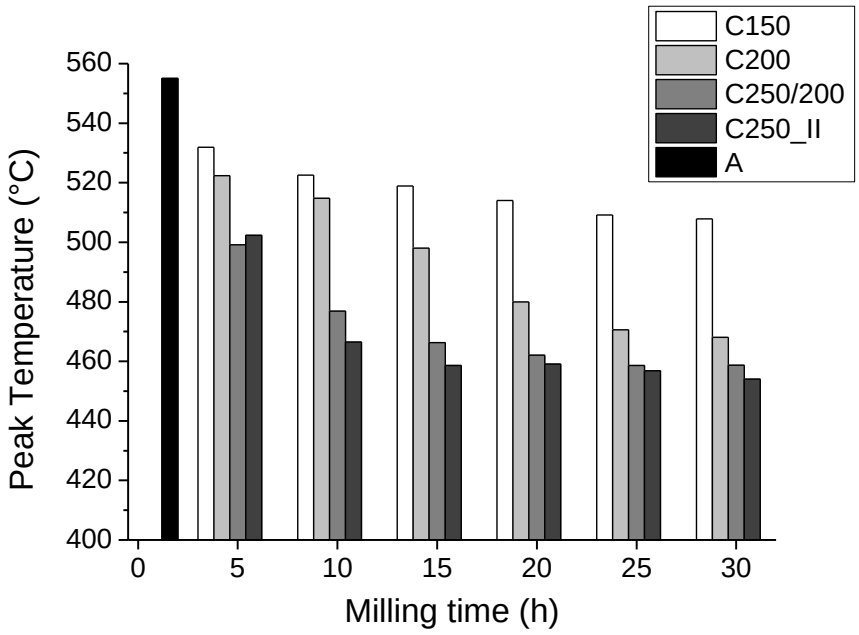

Figure 5.32: the temperature values corresponding to the right peak for C150, C200, C250/200 and C250_II batches of powders

The activation energy values of all the samples are calculated with Kissinger plot (Kissinger 1956) by conducting DSC runs with heating rates of 10K/min, 20K/min, 40K/min, and 80K/min, as explained in section 3.4.1 in Chapter 3. Figure 5.33 shows the activation energy values corresponding to peak 1 of all the samples. The average activation energy values seem to increase with milling time and milling speeds, but are ~150kJ/mol.

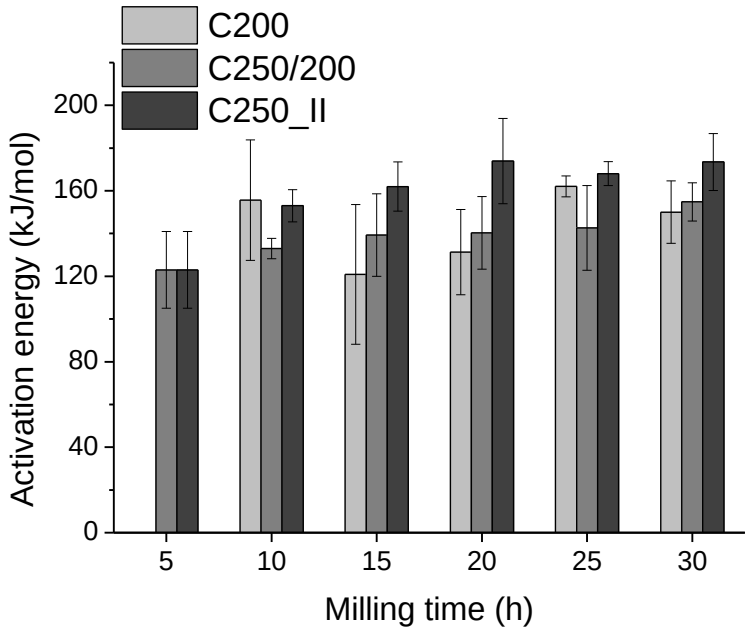

Figure 5.33: Activation energy values of peak 1 in DSC scans for C150, C200, C250/200 and C250_II batches of powders, calculated by the Kissinger analysis

The activation energy values corresponding to peak 2 are plotted in Figure 5.34. The C150 batch maintains the highest activation energy value at ~250 kJ/mol until 30 hours of milling. The activation energy values of the C200 batch decrease from 0 to 20 hours of milling, and become stable at a value of ~180 kJ/mol. The activation energy values of the C250/200 and the C250_II batches decrease to 180 kJ/mol after only 10 hours of milling, much faster than the C200 batch.

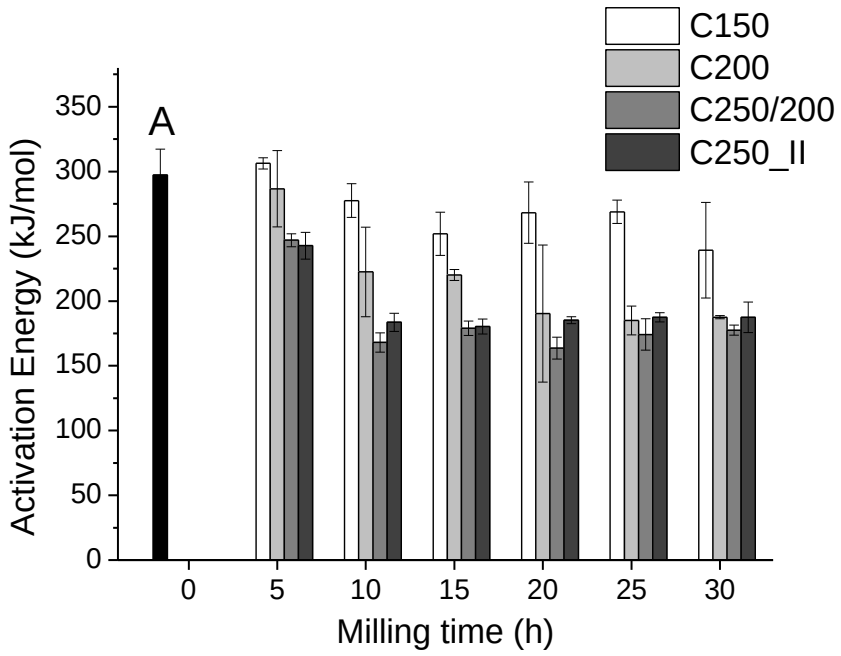

Figure 5.34: Activation energy values of peak 2 in the DSC scans for C150, C200, C250/200 and C250_II powders, calculated with the Kissinger analysis

5.5 The hardness of the ball milled powder

The Vickers hardness for the ball milled powders is shown in Figure 5.35. Before milling, the Vickers hardness of the powder is 134±10kg/mm^2 (Marsh 2013). For the C150 batch the hardness increases slightly with the milling time, reaching a hardness of 297±103kg/mm^2 after 30 hours of milling. The hardness values of all the nanocomposite samples (C batches) increase with milling time and milling speed. For the C200 batch, the increasing trend for the average microhardness has two stages. First it increases almost linearly from 134±10kg/mm^2 to 365±61kg/mm^2 after 10 hours of milling. From 10 hours of milling onwards the microhardness still increases, yet at a relative lower speed. The maximum microhardness for the C200 batch is 513±68kg/mm^2 after 30 hours of milling. For the C250/200 and C250_II batches, the microhardness increasing trends are similar to

the C200 batch. However, the increasing speed is faster from 0 to 5 hours, and then slows down. The maximum microhardness values of the C250/200 and C250_II batches are obtained after 30 hours of milling, which are 566 ± 46kg/mm^2 and 638 ± 44kg/mm^2 respectively.

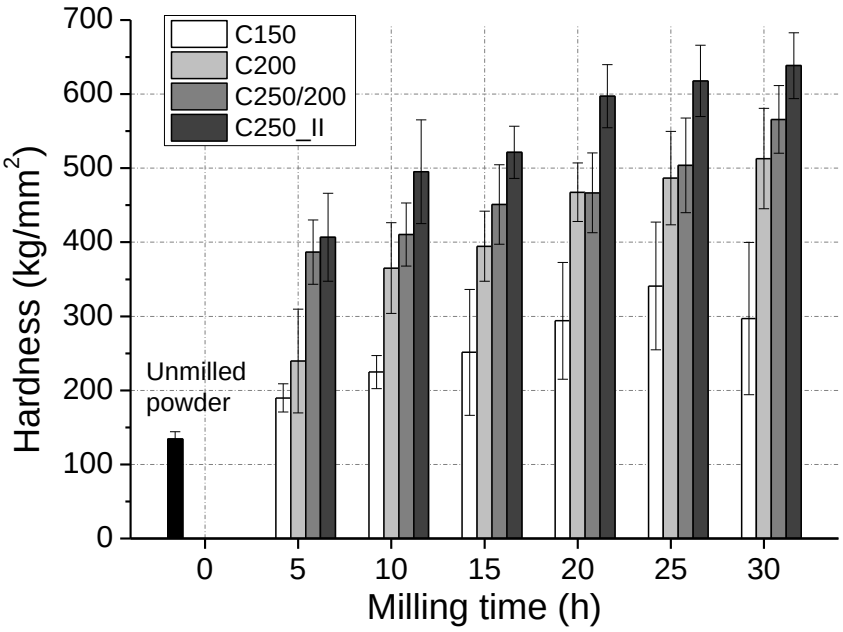

Figure 5.35: The microhardness values of the unmilled, C150, C200, C250/200 and C250 powders

5.6 Discussion

5.6.1 The effects of milling speeds on particle sizes and morphologies

The particle sizes of the C150 batch powder have a different behaviour with the C200, C250/200 and C250_II batches. For the C150 batch, the peak powder particle size distribution decreases from 43μm to 29μm after 10 hours of milling. From 10 hours of milling onwards, the particle sizes are relative stable. For the C200, C250/200 and C250_II batches, the particle sizes increase and decrease during the milling, which indicates a cold-welding dominated and fracturing dominated process respectively (Hesabi, Simchi et al. 2006). The C200 batch reaches the maximum particle size 62μm after 20 hours of milling, while the C250/200 and the C250_II batches powders reach the maximum particle sizes at 70μm and 62μm respectively after a shorter milling time, 10 hours.

It is accepted that ball milling brings collisions to the powder. It have been modelled that the impact energy the balls transferred to the powders was in proportional to the square of the milling speed (Burgio, Iasonna et al. 1991), and the frequency of collisions was in proportional to the milling speed (Abdellaoui and Gaffet 1995). Considering the insignificant particle size changes in the C150 batch, probably the low impact energy caused by the low milling speed failed to cold weld the powders efficiently. The conclusion is supported by a variety of researchers, where in their study minor cold welding is found when milling the powders at low speed. (Boey, Yuan et al. 1998, Munkhbayar, Nine et al. 2013). In the literature, sometimes the milling speed of 150rpm in a planetary ball mill is used for the purpose of mixing the powders instead of milling the powders (Rahimian, Parvin et al. 2011).

When the milling speed is equal or higher than 200rpm, the impact energy is enough for cold-welding and fracturing to occur, as there are particle sizes fluctuations in C200, C250/200 and C250_II batches of powders. Compared with 250rpm, the frequency of cold welding for the C200 batch should be lower due to the low milling speed. Therefore, the time required for the C200 batch powder to reach the maximum particle size is longer. The C200 batch powder particle size decreases from 20 to 30 hours of milling. *Boey* et al. (Boey, Yuan et al. 1998) processed Al-Li/SiC_p composite powder with 150rpm and 200rpm using a Fritsch Pulverisette planetary milling. In their work, using a 150rpm milling speed has minor effects on the particle sizes. When the milling speed was increased to 200rpm, the particle sizes increased from 40μm to 50μm after 2 hours of milling, and decreased to 8μm after 8 hours of milling.

5.6.2 Quantitative methods for estimating the distribution level

A variety of methods such as field method, inner-particle spacing and tessellation, have been developed for quantifying the spatial distribution of discrete secondary phase on two-dimensional sections, as discussed in section 2.4.5 in Chapter 2 (Yang, Boselli et al. 2001). In the current work, field method is used.

Field method

One way for quantifying the distribution level is to calculate the standard deviations of the local area fraction of reinforcements in different areas in the matrix (Pishko, McKimpson et al. 1979, McKimpson, Niemi et al. 1990). First, a number of squares in the sample were selected. Provided the number of squares is sufficient, the mean value of $A_{f\text{-}s}$ [1] would be an

[1] the volume fraction of the reinforcements in each of the selected area

estimation of the average volume fraction of the reinforcements, and the variance of $A_{f\text{-}s}$ could be used for measuring the non-uniformity (Van Hille, Bengtsson et al. 1989). A model for measuring the homogeneity of α features in β features was developed by *Hilliard et al*. (Hilliard and Cahn 1959). First, a few subareas were selected and the area of α features in each of the selected subarea was measured. An equation model was built up:

$$\left(\frac{\sigma_A}{A_f}\right)^2 = \left(\frac{1}{M_a}\right)\left[\left(\frac{\sigma_a}{a}\right)^2 + 1\right] \quad \text{-------} \quad \text{Equation 1}$$

Where σ_A is the standard deviation of local area fraction of α features, A_f is the average area fraction of α features in all subareas, M_a is the expected number of α features in all the subareas, a is the expected area of α features in all the selected subareas, and σ_a is the standard deviation of the area of α features in each of the selected subarea.[2] The details of this methods are explained in section 2.4.5 in Chapter 2.

This model has been used widely for measuring the distribution homogeneity in composite materials (Exner 1972, Pezzotti 1993). In the ideal homogeneous composites, σ_a should equal to 0 (a condition which is impossible to achieve in a random section of even the most regular structure), and $\left(\frac{\sigma_A}{A_f}\right)^2 M_a$ should converge to 1 (Hilliard and Cahn 1959). For inhomogeneous composites, as σ_A grows larger, $\left(\frac{\sigma_A}{A_f}\right)^2 M_a$ is also larger (Rigaut, Lantuéjoul et al. 1987). However, this model has restrictions for nanocomposites. First, the nanosize particles are extremely easy to form agglomerations (Poirier, Drew et al. 2010). Under these circumstances, SEM and FIB imaging techniques are very difficult to identify the shapes of the nanoparticles. As a consequence, calculating M_a would be a problem.

[2] The difference between σ_A and σ_a might be confusing. The former is the standard deviation of volume fractions, and the latter is the standard deviation of the area.

Furthermore, a large variety of data need to be collected for an accurate homogeneity estimation (Van Hille, Bengtsson et al. 1989).

In current work, for the sake of simplicity, M_a is assumed to follow:

$$\boldsymbol{M_a \pi d^2/(4A) = A_f} \quad \text{----------} \quad \text{Equation 2}$$

where $\boldsymbol{d}$ is the diameter of the γ-Al_2O_3, assumed to be a constant value (40nm) in this work, and $\boldsymbol{A}$ is the selected area.

In the current work, 48 subareas are selected. The $(\frac{\sigma_A}{A_f})^2 M_a$ and A_f values are calculated with a MATLAB package coded by the author. The results for C150, C200, C250/200 and C250_II powders are shown in Figure 5.36. The inhomogeneity in Figure 5.36 represents the $(\frac{\sigma_A}{A_f})^2 M_a$ value. For a reinforcement evenly distributed composite, inhomogeneity should be close to 1. It is found that the volume fraction of γ-Al_2O_3 is about 30%, different from the theoretical value 12.9 vol.%. This is because the volume fractions were calculated with the FIB images. In FIB, the surfaces are milled away by the ions, and the milling speed is in proportion to the density (Mulders, De Winter et al. 2007). Since γ-Al_2O_3 particles have a higher density (3.60g/cm^3) (Inframat Advanced Materials 2017) than nanoquasicrystalline $Al_{93}Fe_3Cr_2Ti_2$ powders (2.88g/cm^3) (Rounthwaite 2012), they are less likely to be milled away by FIB.

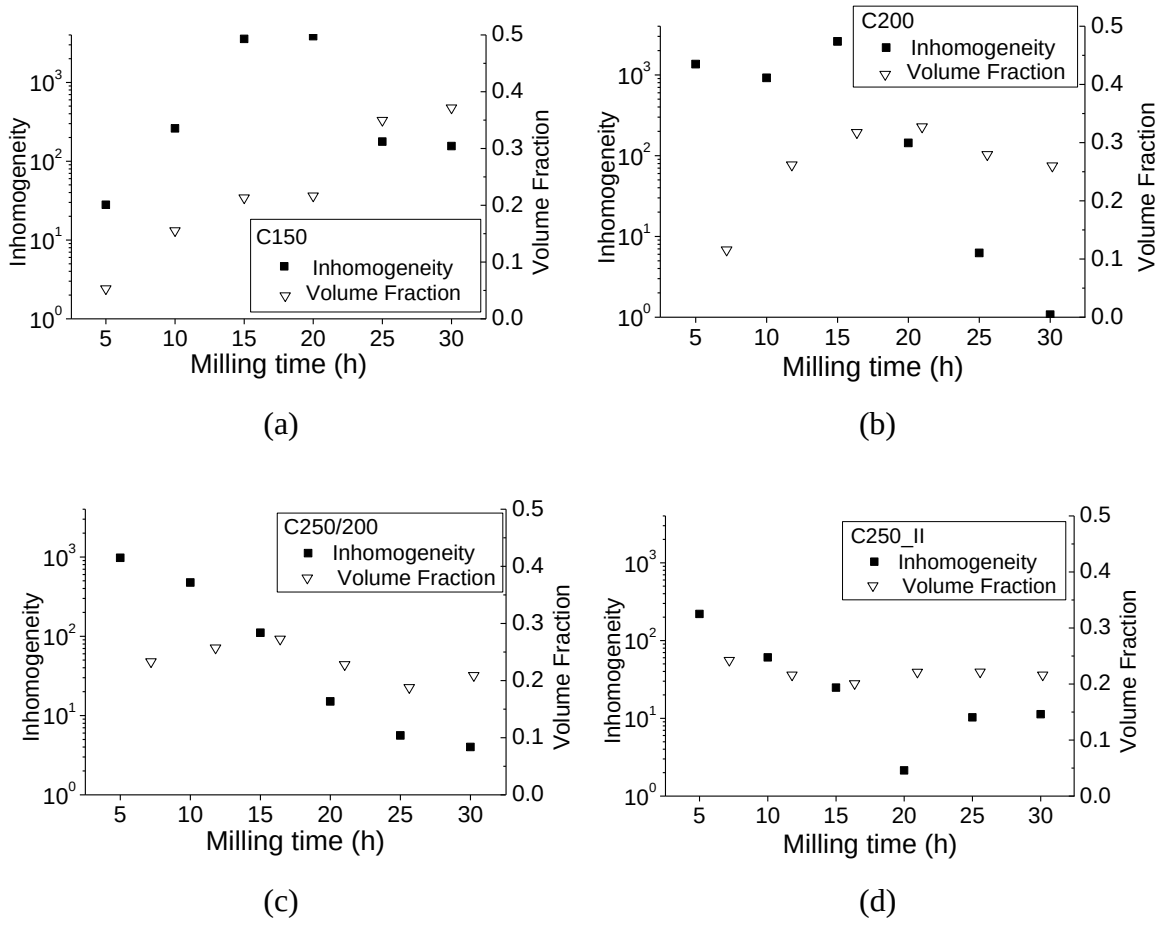

Figure 5.36: The inhomogeneity level and reinforcement volume fraction against the milling time **(a)** C150 batch, **(b)** C200 batch, **(c)** C250/200 batch, **(d)** C250_II batch. The inhomogeneity is the $(\frac{\sigma_A}{A_f})^2 \boldsymbol{M_a}$ value.

The proportion of the γ-Al_2O_3 occupied region

The model from *Hilliard* et al.'s study is efficient for quantifying homogeneity of the composites. However, the physical meaning of $(\frac{\sigma_A}{A_f})^2 M_a$ is ambiguous. For example, if a sample has $(\frac{\sigma_A}{A_f})^2 M_a$ values equals to 500, it is difficult to know the microstructure and the reinforcement distribution of the sample intuitively. *Van* et al. (Van Hille, Bengtsson et al. 1989) measured the homogeneity from the standard deviation of the microhardness values. They argued that a sample with reinforcement particles unevenly distributed should have

higher standard deviation in microhardness, since parts of the matrix are unreinforced by the reinforcements. However, ball milling is a very complex processing routine, and whether the standard deviation of microhardness is only because of the uneven distribution of the reinforcements is not clear.

In our work, a new term called the particle-free region is defined. Assuming that in an ideal situation the γ-Al_2O_3 particles are distributed in the matrix fully homogeneously and all the particles have the same distances to the nearest neighbours, as sketched in Figure 5.37. Assuming the γ-Al_2O_3 particles are spherical, and the fraction of the γ-Al_2O_3 in the powder is equal to 12.9%. Then:

$$\mathbf{n\pi d^2/(4A) = 12.9\%} \qquad \text{----------} \qquad \text{Equation 3}$$

where n is the number of the γ-Al_2O_3 particles in an area of A, and *d* is the diameter of the γ-Al_2O_3, assumed to be 40nm in this work. Thus, the distance between the γ-Al_2O_3 particles could be presented as:

$$\mathbf{l = \sqrt{A/n} = \sqrt{\pi d^2/(0.129\times 4)}} \qquad \text{---------} \qquad \text{Equation 4}$$

where l is the distance between the particles, and is calculated to be 100 nm based on Equation 4.

If the γ-Al_2O_3 distribution is inhomogeneous, clusters should form in certain places and there should be less γ-Al_2O_3 particles in other areas. In this work, if an area larger than 100*100nm^2 contains no γ-Al_2O_3 particles, then this region is defined as the particle-free region.

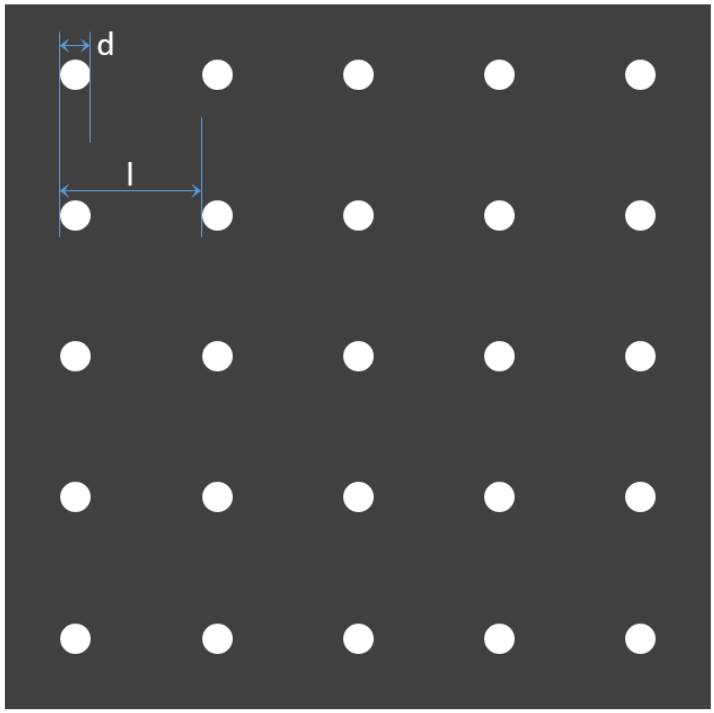

Figure 5.37: Composites with full homogeneous distribution of reinforcement particle

An FIB image of the C200_20 is shown as an example in Figure 5.38. The irregular black areas labelled as (1) and (2) respectively in Figure 5.38 are two examples of the particle-free regions. Any region which does not belong to the particle free region is defined as the particle-occupied region in this work.

The fraction of particle-occupied regions is defined as:

$$\mathbf{r} = \mathbf{1} - \frac{A_{free}}{A_{total}} \qquad \text{----------} \qquad \text{Equation 5}$$

where A_{free} and A_{total} are the area of the particle-free regions and the area in total respectively.

The particle free region has an irregular shape, with an area cannot be calculated with conventional methods. Such regions can be approximated using a Monte Carlo simulation

(Robert 2004, Obaid, Alasadi et al. 2016). The idea is to surround the irregular shape by a regular shape. Then a number of random points are generated in the surrounded regular area. The irregular area can be calculated with the following equation (Obaid, Alasadi et al. 2016):

$$\boldsymbol{A_{irr} = \left(\frac{K}{N}\right) * A_{reg}} \quad \text{---------} \quad \text{Equation 6}$$

Where A_{irr} is the area of irregular shape, *K* is the number of points locating in the irregular area, *N* is the total number of points generated and A_{reg} is the area of regular area which can be easily calculated.

Monte Carlo requires a large number of simulations to reduce the variance (Robert 2004). In this work, we use regular pattern sampling for variance reduction (Byrn 1980). Figure 5.38 provides an example illustrating how the area of the particle free region was measured. First, the FIB image is split with a 10 × 8 square shape mesh grids. These grids are drawn with thicker lines, which are also named as main grids in this work. Each main grid is divided into 10 sub-grids with thinner lines. According to the scale bar, the length of each main grid and sub-grid are approximate 2000nm and 100nm respectively. Therefore, if a segment of a sub-grid does not go through the γ particles, it is reasonable to consider that such segment belongs to a particle-free region. The segments with such properties will be named as the particle-free segments. The number ratio of the particle-free segments to the sum of all the segments in this image is measured. This ratio can be roughly taken as the ratio $\frac{A_{free}}{A_{total}}$ in Equation 5. The range of $\frac{A_{free}}{A_{total}}$ is between 0 and 1.

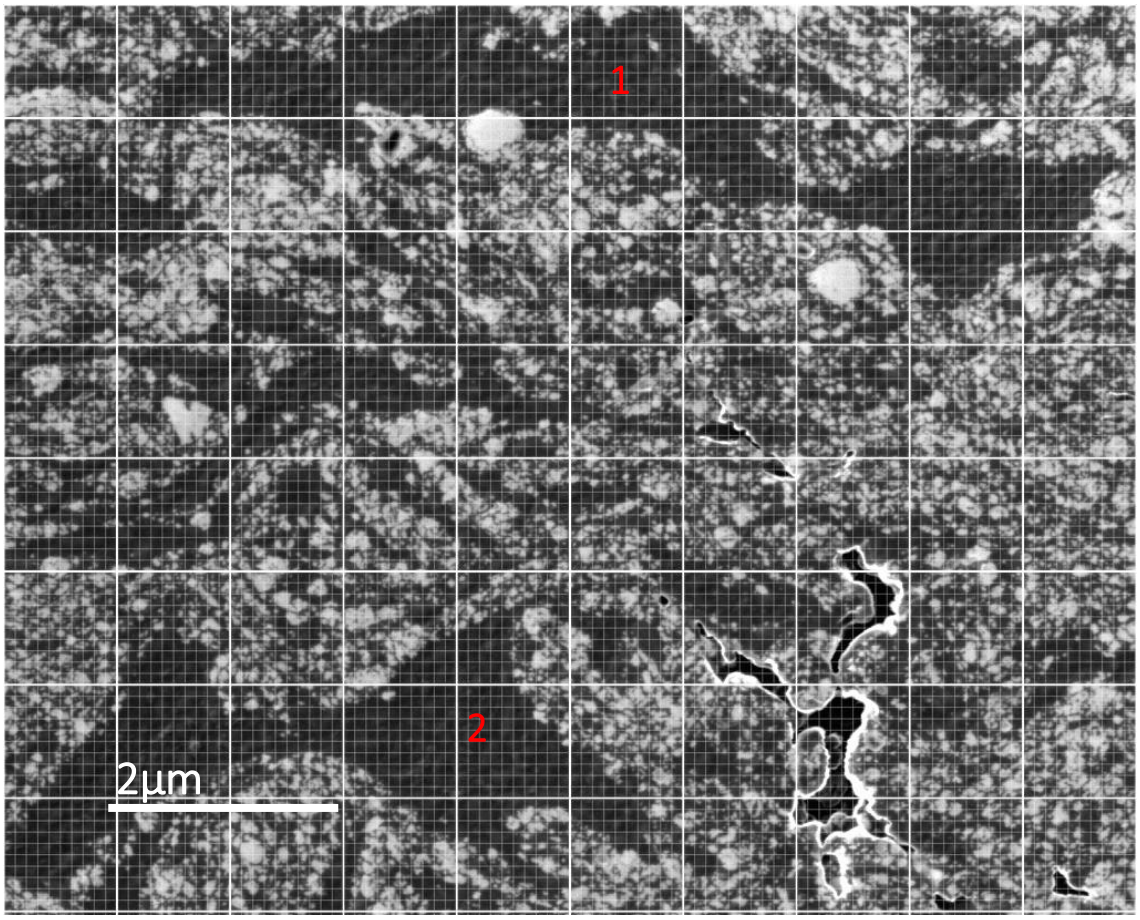

Figure 5.38: The FIB image of C200_20 sample with grid meshes

The fraction of particle-occupied regions for all batches of powders is plotted in Figure 5.39. The C150 and C200 powders have 68% and 91% region being occupied by γ-Al_2O_3 particles after 30 hours of milling. For the C250/200 and C250_II batches, homogeneous structures with almost no particle free regions in the FIB image were obtained after 25 and 20 hours of milling respectively.

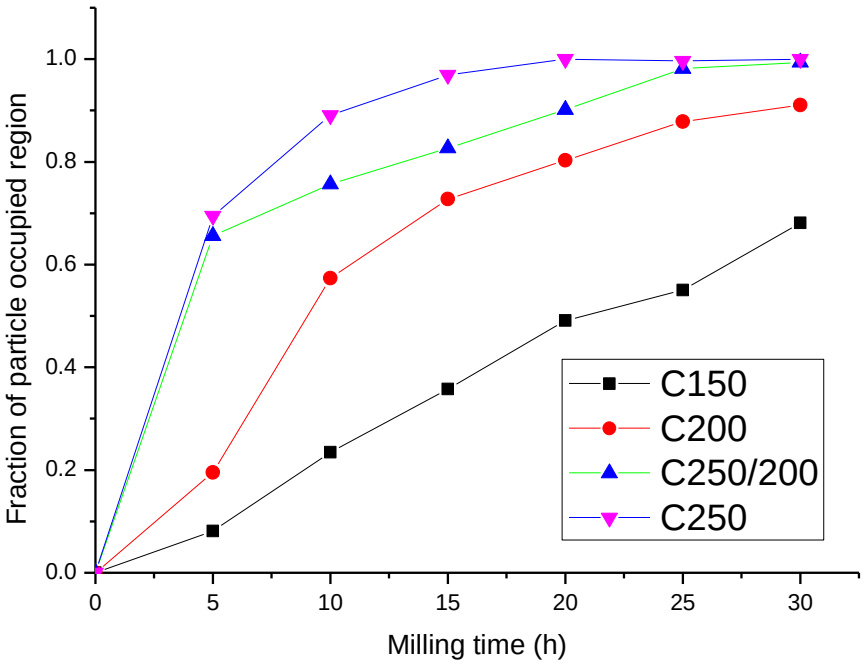

Figure 5.39: Homogeneity level of the ball milled powders

5.6.3 The effects of milling speeds on reinforcement distribution

Mechanical milling can provide a more homogeneous mix than that can be achieved via conventional blending (Ye, He et al. 2006). From Figure 5.36(a), the inhomogeneity of C150_5 is very low. However, this state is "unstable", since the γ-Al_2O_3 particles have not been milled into the powders. From 5 to 30 hours of milling, the volume fraction of the γ-Al_2O_3 increases from 0% to 36% percent.

Conventionally, the reinforcements were milled into the matrix through cold-welding and fracturing mechanisms (Fogagnolo, Velasco et al. 2003). However, as explained in section 5.6.1 in this Chapter, milling at 150 rpm cannot cold weld the powders effectively. As the volume fraction of γ-Al_2O_3 increases quite fast with milling time, it is expected that the reinforcement particles were milled into the matrix powders following a different

mechanism. This part is going to be further discussed in Chapter 7. From Figure 5.8(d), Figure 5.36(a) and Figure 5.39, the C150 batch does not have a homogeneous γ-Al_2O_3 distribution even after 30 hours of milling.

For the C200 batches, the inhomogeneity values from 5-15 hours of milling are high, as shown in Figure 5.36(b). Meanwhile, the volume fraction of homogeneous γ-Al_2O_3 increases up to 32%. As the particle size values show an increasing trend in Figure 5.2, the reinforcement particles should be milled into the powder particles through cold-welding. For the C250/200 and C250 batches, the volume fraction of γ-Al_2O_3 is nearly 30% after 5 hours of milling. This could be due to that when milling at 250rpm, the impact energy is effective in welding the powders, and the γ-Al_2O_3 particles are already blended into the matrix after 5 hours of milling. For further milling, through random fracturing and cold welding, the γ-Al_2O_3 clusters and large particle free regions are broken into small pieces, and the homogeneity improves simultaneously (Fogagnolo, Velasco et al. 2003).

The milling speed has dramatic effects on the homogeneity. When the powders are trapped in the milling media, they have possibilities to change their original shapes. The changes mean being deformed, cold welded, or fractured, depending on the milling stages and the properties of the powder (Fogagnolo, Velasco et al. 2003, Zhang 2004). However, since ball milling is a stochastic processing routine (Zhang 2004), the collisions between the milling media and the powder may also have insufficient impact energy by chance. Then the powders also have possibilities to remain the original shapes. As stated in section 5.6.1, with a higher milling speed, the impact energy and the frequency of collisions are increased, and thus powders are cold-welded and fractured in a higher rate, which improved the reinforcement distributions.

5.6.4 The effects of milling speeds on the microstructure

It has been discussed in section 4.7.3 in Chapter 4 that ball milling can fracture the quasicrystals. This was observed in Figure 5.23(c) and Figure 5.25(c), where quasicrystalline particles were broken into pieces with different orientations, identified with the CBDPs. Breaking micro-sized hard particles requires energy to break the atom bonding, and is more difficult than breaking the clusters of nano-size particles (Zhang 2004). This implies at higher milling speeds, quasicrystals are more likely to be fractured. For the C150 batch powder, large quasicrystal particles can be observed even after 25 hours of milling, as shown in Figure 5.12 (a). For the C250_II batch powder, the quasicrystalline phase peaks dropped dramatically with milling time in the X-ray diffractograms, as shown in Figure 5.20.

Apart from breaking the quasicrystals, ball milling can generate severe deformations and accumulations of dislocations in the matrix (Ye, Lee et al. 2006), since the quasicrystals, the γ-Al_2O_3 and the Al grains have different Young's modulus (Chou, Nieh et al. 1991, Rounthwaite 2012), as discussed in 4.7.2. At a certain level, the crystal disintegrates into subgrains which are initially separated by low-angle grain boundaries. During further milling, deformation occurs randomly, and the orientation of the subgrains becomes random (Fecht, Hellstern et al. 1990, Kamrani, Simchi et al. 2007). The powders processed with higher millings speed have lower grain sizes, probably because higher impact energy generate more severe deformations, and the dislocation accumulation speed is faster (Chung, He et al. 2003).

5.6.5 The effects of milling speed on microhardness

Hardness increases with the milling time and milling speed, as shown in Figure 5.35. As stated earlier, ball milling generates a high degree of deformation and reduces the grain size to nanometre, as shown in Figure 5.21. *Sharifi* et al. (Sharifi, Karimzadeh et al. 2011) observed increase in microhardness in Al-10wt.%B_4C nanocomposites with increasing milling time. *Poirier* et al. (Poirier, Drew et al. 2010) milled pure Al and Al/10vol.Al_2O_3 nanocomposite powder and found the increase in hardness is mainly due to the grain refinement and the direct strengthening from load transfer between the reinforcement particles and the matrix. Therefore, with a higher milling speed or longer milling time, the powders processed have better γ-Al_2O_3 distribution (as shown in Figure 5.36 and Figure 5.39) and finer grain sizes (as shown in Figure 5.21), and thus have higher microhardness. The mechanisms for the increase of hardness is going to be further discussed in Chapter 7.

5.6.6 Powders Suitable for extrusion

Four factors determining whether the composite powders are suitable for extrusion are discussed:

(1) The milling time

When the 250ml milling vessel is used, the technical data suggest to use 50 balls with 10 mm in diameter each time (Fritsch 2016). From measurement, each ball weights about 4 grams. If the initial BPR remains 10:1, the ideal condition for powder processing is to use 200g balls with 20g powder per milling. For extrusion, approximate 400g powder is needed. Therefore, if one batch need to be mechanically milled for 30 hours before extrusion, 600 hours (30 × 20) are required to process enough powders. Powders with 10

hours of milling would be much better, since only 200 hours (approximately 10 days) are required.

(2) The γ-Al_2O_3 distribution level

When the reinforcements are homogeneously distributed, decreasing reinforcement size from microscale to nanoscale leads to an increase in strength and ductility (Kang and Chan 2004).

It is assumed that the C150 batch powders are not suitable for extrusion, due to the poor γ-Al_2O_3 distribution even after 30 hours of milling. For the C200 batch, it requires at least 20 hours to reach a relative homogeneous structure, as shown in Figure 5.9. In comparison, for the C250/200 and the C250_II batches, although the particle-free region disappears after 25 and 20 hours of milling, the reinforcement distributions are already quite good after 10 hours of milling, as shown in Figure 5.10 and Figure 5.11.

(3) The decomposition of the quasicrystal

As discussed in section 4.7.3 in Chapter 4, the quasicrystals will decompose during the milling, and the volume fraction of quasicrystals can be estimated by the enthalpy ratio between the enthalpy involved in the peak 2 over the total enthalpy released in the whole exothermic event. In the current work, the C250/200_10 and C250_II_10 samples have 36vol.% and 29vol.% of quasicrystals respectively. Compared with the unmilled powder (45vol.% of quasicrystals) (Inoue and Kimura 1999), less than half of the quasicrystals were decomposed. The C200_10 sample has ~38vol.% of quasicrystal, higher than the C250/200_10 and C250_II_10 samples. In the DSC curves with heating rate at 40K/min, the onset temperatures for the quasicrystal decomposition peak are 425℃ and 428℃ for

the C250_II_10 and C250/200_10 respectively, as shown in Figure 5.31 and Figure 5.30. The onset temperature for the quasicrystalline phase decomposition of C200_10 is 472℃ (Figure 5.29), much higher than those of the C250_II_10 and C250/200_10 samples.

(4) The crystallite sizes and the microhardness

The crystallite size of the C200_10 sample is too large for Williamson-Hall equation to be applied. Considering the C200_20 sample has an average crystallite size of 99 ± 37nm, and the crystallite sizes decrease with milling time, the C200_10 should have a crystallite size larger than 100nm. The C250/200_10 has a crystallite size and microhardness value of 85 ± 14nm and 410 ± 43kg/mm^2 respectively. The C250_II_10 has a crystallite size and microhardness value of 33 ± 4nm and 495 ± 70kg/mm^2 respectively.

In general, higher milling speeds and milling time have the advantages of achieving better γ-Al_2O_3 distribution, finer crystallite size and higher microhardness in a shorter time, but at a cost of decomposing the quasicrystalline phases. When choosing powders for extrusion these factors need to be balanced. C250/200_10 powders might be a suitable one, considering the factors discussed above.

5.7 Conclusions

The quasicrystalline $Al_{93}Fe_3Cr_2Ti_2$ alloy based nanocomposites powders with 12.9 vol% γ-Al_2O_3 (20 - 50nm) addition have been produced by mechanical milling with milling speeds from 150rpm to 250rpm.

The low milling speed transfers insufficient energy, which makes it difficult for the powders to be cold welded together. As a consequence, the particle sizes of C150 powders have no obvious changes during the ball milling from 5 to 30 hours. The γ-Al_2O_3 distribution in C150 batch powder is not homogeneous, even after 30 hours of milling. In contrast, for the nanocomposites produced with 200rpm or higher milling speed, the γ-Al_2O_3 particles are distributed evenly in the matrix through repeated fracturing and cold welding. For C250/200 and C250 powders, after 25 hours and 20 hours of milling respectively, γ-Al_2O_3 is homogeneously distributed, and the matrix powders almost contain no γ-Al_2O_3 free regions. The γ-Al_2O_3 cluster sizes decrease with milling time and speeds. The smallest average γ-Al_2O_3 cluster sizes for the C200, C250/200 and C250 batches powders are 273±97nm, 101±45nm and 90±29nm, achieved after 30 hours of milling. The quasicrystal particles are fractured during the milling.

A higher milling speed will increase the impact energy and the frequency of collisions of the milling media. This leads to a faster crystallite sizes refinement rate. The smallest crystallite sizes for the C200, C250/200 and C250_II batches of powders are 30nm, 20nm and 14nm, obtained after 30, 30 and 20 hours of milling respectively.

The microhardness increases with milling time and speeds. The addition of 12.9 vol% γ-Al_2O_3 (20-50nm) particles to the nanoquasicrystalline $Al_{93}Fe_3Cr_2Ti_2$ alloy powders processed with a ball to powder ratio of 10, at 250 rpm after 30 hours of milling allows

obtaining a homogeneous nanocomposite powder with 4.8 times higher Vickers hardness (638 kg/mm^2) than that of the nanoquasicrystalline Al alloy matrix (132 kg/mm^2).

5.8 Reference

Abdellaoui, M. and E. Gaffet (1995). "The physics of mechanical alloying in a planetary ball mill: mathematical treatment." Acta metallurgica et materialia **43**(3): 1087-1098.

Boey, F., et al. (1998). "Mechanical alloying for the effective dispersion of sub-micron SiC p reinforcements in Al–Li alloy composite." Materials Science and Engineering: A **252**(2): 276-287.

Burgio, N., et al. (1991). "Mechanical alloying of the Fe− Zr system. Correlation between input energy and end products." Il nuovo cimento D **13**(4): 459-476.

Byrn, N. (1980). "Monte Carlo variance reduction."

Cahn, J. W., et al. (1986). "Indexing of icosahedral quasiperiodic crystals." Journal of Materials Research **1**(01): 13-26.

Chou, T., et al. (1991). "Microstructures and mechanical properties of thin films of aluminum oxide." Scripta metallurgica et materialia **25**(10): 2203-2208.

Chung, K. H., et al. (2003). "Mechanisms of microstructure evolution during cryomilling in the presence of hard particles." Materials Science and Engineering: A **356**(1): 23-31.

Exner, H. (1972). "Analysis of grain-and particle-size distributions in metallic materials." International metallurgical reviews **17**(1): 25-42.

Fecht, H., et al. (1990). "Nanocrystalline metals prepared by high-energy ball milling." Metallurgical and Materials Transactions A **21**(9): 2333-2337.

Fogagnolo, J., et al. (2006). "Mechanically alloyed AlN particle-reinforced Al-6061 matrix composites: Powder processing, consolidation and mechanical strength and hardness of the as-extruded materials." Materials Science and Engineering: A **426**(1): 85-94.

Fogagnolo, J., et al. (2003). "Effect of mechanical alloying on the morphology, microstructure and properties of aluminium matrix composite powders." Materials Science and Engineering: A **342**(1): 131-143.

Fritsch (2016). "Handbook on grinding bowls and grinding balls."

Fujieda, S. and R. Uchida (1991). "Simplex optimized decomposition of overlapped model peaks in DSC curves." Analytical sciences **7**(Supple): 701-704.

Galano, M., et al. (2009). "Nanoquasicrystalline Al–Fe–Cr-based alloys. Part I: Phase transformations." Acta Materialia **57**(17): 5107-5119.

Galano, M., et al. (2015). "Nanoquasicrystalline Al-based matrix/γ-Al_2O_3 nanocomposites." Journal of Alloys and Compounds **643**: S99-S106.

Giancola, C., et al. (1997). "DSC studies on bovine serum albumin denaturation effects of ionic strength and SDS concentration." International journal of biological macromolecules **20**(3): 193-204.

Hesabi, Z. R., et al. (2006). "Structural evolution during mechanical milling of nanometric and micrometric Al_2O_3 reinforced Al matrix composites." Materials Science and Engineering: A **428**(1): 159-168.

Hilliard, J. E. and J. W. Cahn (1959). An evaluation of procedures in quantitative metallography. I. Volume-Fraction Analysis, General Electric Co. Research Lab., Schenectady, NY.

Inframat Advanced Materials (2017). "http://www.advancedmaterials.us/26N-0801G.htm." **2017**.

Inoue, A. and H. Kimura (1999). "High elevated-temperature strength of Al-based nanoquasicrystalline alloys." Nanostructured Materials **11**(2): 221-231.

Kamrani, S., et al. (2007). "Effect of reinforcement volume fraction on mechanical alloying of Al–SiC nanocomposite powders." Powder Metallurgy **50**(3): 276-282.

Kang, Y.-C. and S. L.-I. Chan (2004). "Tensile properties of nanometric Al_2O_3 particulate-reinforced aluminum matrix composites." Materials chemistry and physics **85**(2): 438-443.

Kimura, H. M., et al. (2000). "Al–Fe-based bulk quasicrystalline alloys with high elevated temperature strength." Journal of Materials Research **15**(12): 2737-2744.

Kissinger, H. E. (1956). "Variation of peak temperature with heating rate in differential thermal analysis." Journal of research of the National Bureau of Standards **57**(4): 217-221.

Marsh, A. (2013). Processing of quasicrystalline aluminium matrix nanocomposites. Materials Science. University of Oxford, University of Oxford. **Part 2:** 116.

McKimpson, M., et al. (1990). "Quantitative microscopy of SiC-reinforced aluminum composites fabricated from mechanically alloyed powders." Structural applications of mechanical alloying: 203-211.

Mulders, J., et al. (2007). "Measurements and calculations of FIB milling yield of bulk metals." Microelectronic engineering **84**(5): 1540-1543.

Munkhbayar, B., et al. (2013). "Influence of dry and wet ball milling on dispersion characteristics of the multi-walled carbon nanotubes in aqueous solution with and without surfactant." Powder Technology **234**: 132-140.

National Chemical Database Service (2016). "http://cds.rsc.org/."

Obaid, T., et al. (2016). "A New Method to Calculate an Irregular Area of a Lake using Image Processing Techniques."

Pezzotti, G. (1993). "On the actual contribution of crack deflection in toughening platelet-reinforced brittle-matrix composites." Acta metallurgica et materialia **41**(6): 1825-1839.

Pishko, R., et al. (1979). "The effect of steelmaking on the hydrogen attack of carbon steel." Metallurgical and Materials Transactions A **10**(7): 887-894.

Poirier, D., et al. (2010). "Fabrication and properties of mechanically milled alumina/aluminum nanocomposites." Materials Science & Engineering A **527**(29-30): 7605-7614.

Rahimian, M., et al. (2011). "The effect of production parameters on microstructure and wear resistance of powder metallurgy Al–Al_2O_3 composite." Materials & Design **32**(2): 1031-1038.

Rigaut, J., et al. (1987). "Relationship between variance of area density and quadrat area–Interpretation by fractal and random models." Acta Stereologica **6**(1): 107-113.

Robert, C. P. (2004). Monte carlo methods, Wiley Online Library.

Rounthwaite, N. (2012). "Development of bulk nanoquasicrystalline alloys for high strength elevated temperature applications." PhD thesis, University of Oxford.

Sharifi, E. M., et al. (2011). "Fabrication and evaluation of mechanical and tribological properties of boron carbide reinforced aluminum matrix nanocomposites." Materials & Design **32**(6): 3263-3271.

Van Hille, D., et al. (1989). "Quantitative metallographic study of fibre morphology in a short alumina fibre reinforced aluminium alloy matrix." Composites science and technology **35**(2): 195-206.

Williamson, G. and W. Hall (1953). "X-ray line broadening from filed aluminium and wolfram." Acta Metallurgica **1**(1): 22-31.

Yang, N., et al. (2001). "Simulation and quantitative assessment of homogeneous and inhomogeneous particle distributions in particulate metal matrix composites." Journal of microscopy **201**(2): 189-200.

Ye, J., et al. (2006). "Cryomilling for the fabrication of a particulate B_4C reinforced Al nanocomposite: Part I. Effects of process conditions on structure." Metallurgical and Materials Transactions A **37**(10): 3099-3109.

Ye, J., et al. (2006). "Cryomilling for the fabrication of a particulate B_4C reinforced Al nanocomposite: Part II. Mechanisms for microstructural evolution." Metallurgical and Materials Transactions A **37**(10): 3111-3117.

Zhang, D. (2004). "Processing of advanced materials using high-energy mechanical milling." Progress in materials science **49**(3): 537-560.

6. Processing and characterisation of the extruded bar

In this Chapter, the powders processed with 500ml milling pot were characterised. The powders were compared with the C250/200_10 powder to find the suitable milling conditions for producing powders for extrusion with a larger pot. This chapter also analyses the microstructure, phase components and the mechanical properties of extruded bar fabricated from the consolidation of the powder.

6.1 Characterisation of powders produced for extrusion

Four batches of $Al_{93}Fe_3Cr_2Ti_2/\gamma\text{-}Al_2O_3$ nanocomposite powders were produced by ball milling using the processing routine described in section 3.1.3 in Chapter 3. CL_*t* was used to represent the ball milled powders, where the letter CL means composite powders processed with large milling pot, and *t* represents the milling time. The abbreviations of the powders were listed with the milling conditions in Table 6.1.

Abbreviation	**Milling speed**	**Pot volume**	**Powder mass**
CL_5	250rpm for 5 hours	500ml	40g
CL_8	250rpm for 4 hours and 200rpm for 4 hours	500ml	40g
CL_9	250rpm for 4 hours and 200rpm for 5 hours	500ml	40g
CL_10	250rpm for 5 hours and 200rpm for 5 hours	500ml	40g
C250/200_10	250rpm for 5 hours and 200rpm for 5 hours	250ml	10g

Table 6.1: Abbreviations for the powder processed in the 500ml milling pot

For each batch of powders, the powder sizes, $\gamma\text{-}Al_2O_3$ distribution, phase components, crystallite sizes, thermal stability and hardness were analysed using the Mastersizer, focused ion beam (FIB), X-ray diffractograms, differential scanning calorimetry (DSC) and Vickers hardness microindenter respectively.

6.1.1 Particle sizes

For all the milled powders, the volume fraction and the particle sizes were plotted in Figure 6.1 and Figure 6.2. All the curves follow the Gaussian distribution in log-linear plot. The full width half maximums (FWHMs) of each Gaussian peak were calculated. The particle sizes corresponding to the minimum, maximum point in FWHM and the peak values in the curve are marked as P_{min}, P_{max} and P respectively, as shown in Figure 6.1. The P values are taken as the peak particle sizes. These values were plotted together in Figure 6.2. As shown, CL_5, CL_9 and C250/200_10 powders have similar peak particle sizes and the particle size distributions. Even though both the C250/200_10 and the CL_10 powder have the same milling speed (250rpm up to 5 hours of milling and 200rpm for the rest 5 hours), the particle size of CL_10 powder is smaller. This indicates the volume of the vessel has an effect on the size of the powders.

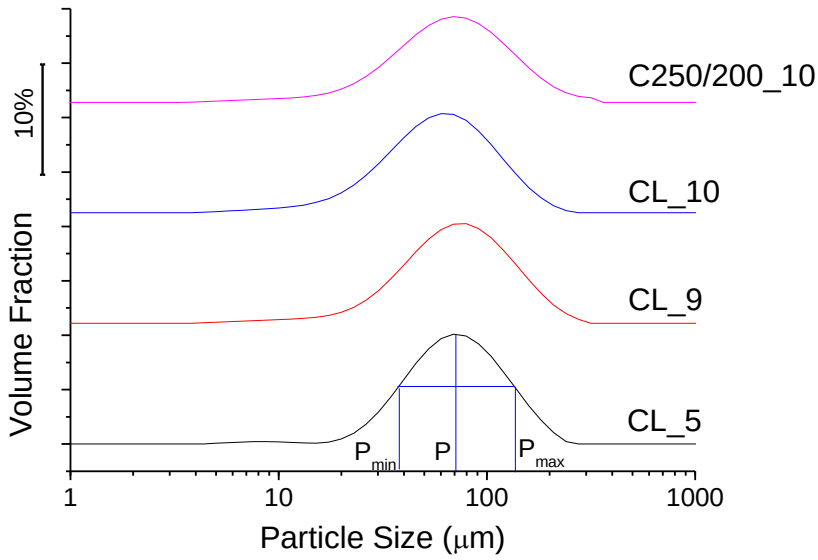

Figure 6.1: The particle size distribution of the powders processed with large milling pot

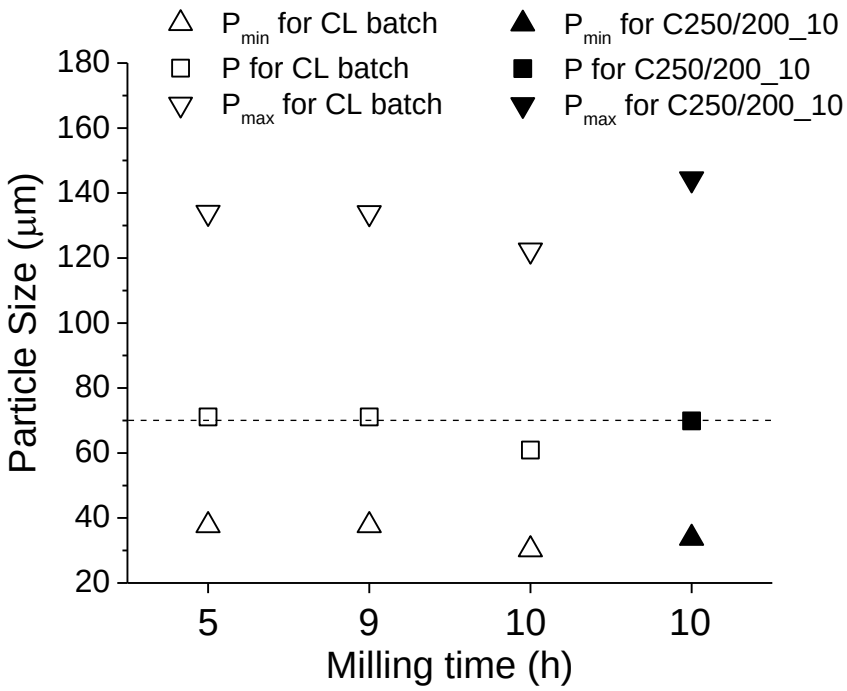

Figure 6.2: the P_{max}, P, P_{min} values of the CL batch powder

6.1.2 Alumina distribution

The FIB images of the C250/200_10, CL_8, CL_9 and CL_10 powders are shown in Figure 6.3. The white particles are γ-Al_2O_3 particles distributed in the aluminium matrix (Galano, Marsh et al. 2015). As expected, powders with longer milling time have better γ-Al_2O_3 distributions. The CL_5 in Figure 6.3(b) has the most inhomogeneous γ-Al_2O_3 distribution, and large γ-Al_2O_3 free regions could be found. For the CL_8, CL_9 and C250/200_10 batches of powders in Figure 6.3(c), (d) and (e), γ-Al_2O_3 particles distribute in a lamella structure. Some black areas with no γ-Al_2O_3 could be seen. The CL_10 batch powder has the most homogeneous γ-Al_2O_3 distribution among all, since γ-Al_2O_3 particles spread evenly in the matrix and there are seldom γ-Al_2O_3 free areas in the matrix. Since

the γ-Al_2O_3 distribution of CL_5 is not homogeneous enough, it is not going to be further investigated in this Chapter.

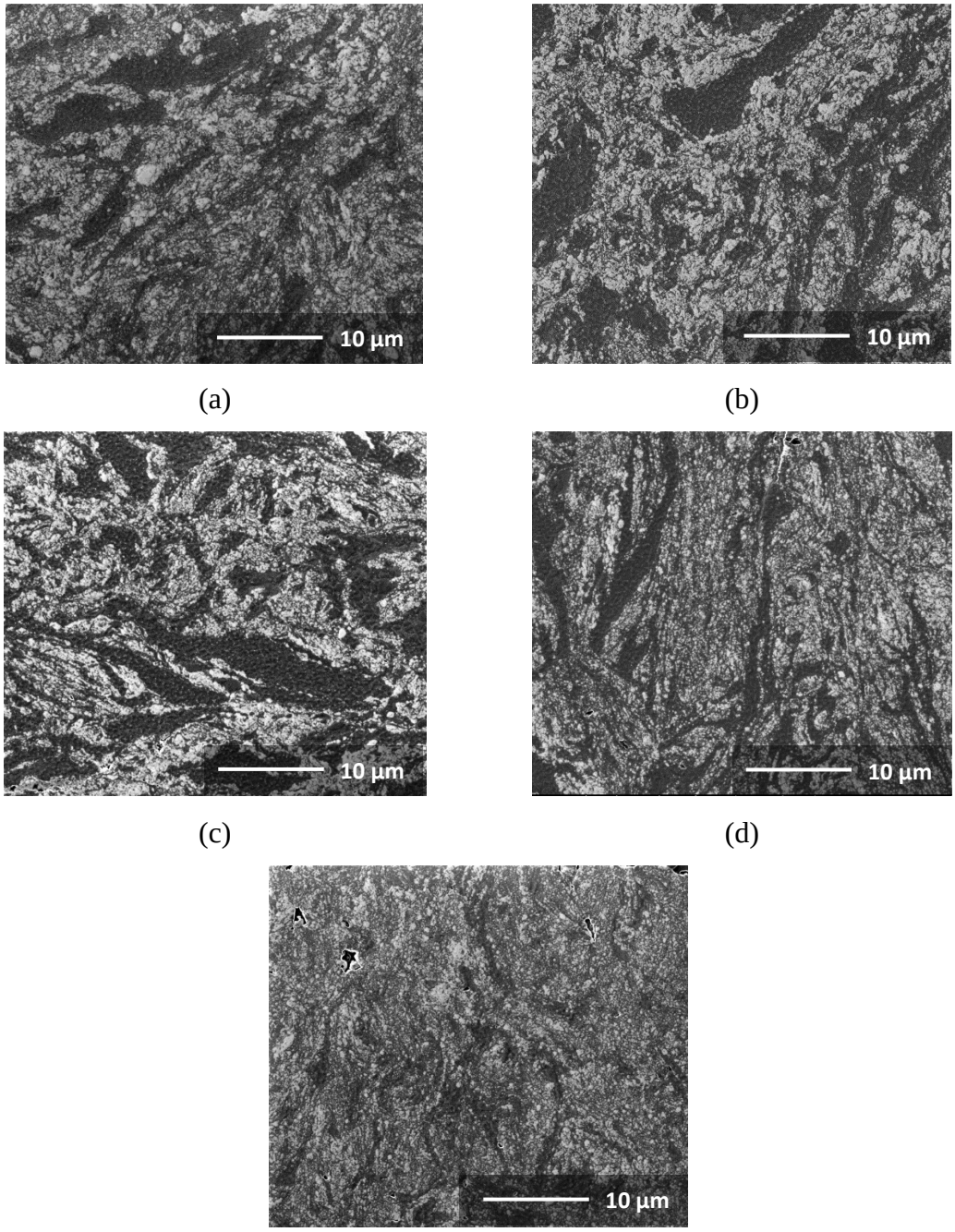

(a) (b)

(c) (d)

(e)

Figure 6.3: FIB images of CL batch powders and C250/200_10 powders **(a)** C250/200_10, **(b)** CL_5, **(c)** CL_8, **(d)** CL_9, **(e)** CL_10

6.1.3 Phase components and crystallite sizes

X-ray diffractograms for the CL_8, CL_9 and CL_10 batches of powders are displayed to compare with the C250/200 powders in Figure 6.4(a). Figure 6.4(b) shows the enlarged central section of the X-ray diffractograms with 2θ ranging from 35° to 50°. All the phases present in the powders were indexed as follow: α-Al peaks were identified by indexing the reflections corresponding to the (111), (200), (220), (311) and (222) planes in the 2θ = 20°-90° range at 38.5° (full intensity), 44.7°, 65.2°, 78.3° and 82.5° (Swanson, Tatge et al. 1953). The icosahedral phase was identified at 2θ ~ 22.9°, 41.3°, 43.5° and 73.5° (Audebert, Prima et al. 2002, Galano, Audebert et al. 2009). In the case of γ-Al_2O_3 phase, only γ(440) peak was detected. This is probably because the apparatus is not sensitive enough to identify the low volume fraction of γ-Al_2O_3. The Al_3Ti phase was detected at 39.0°.

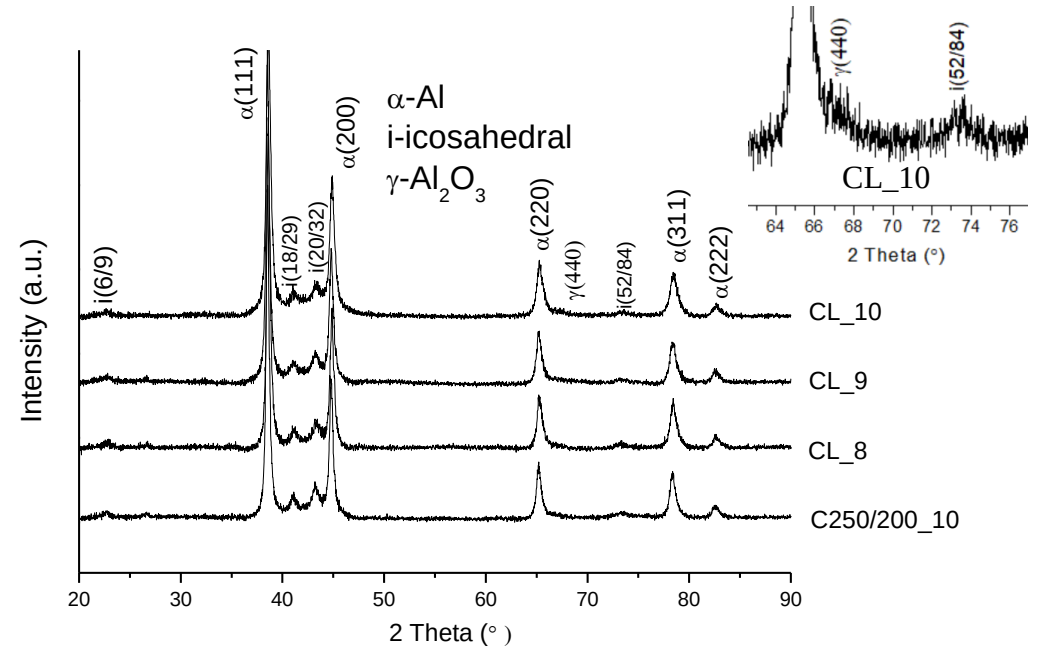

(a)

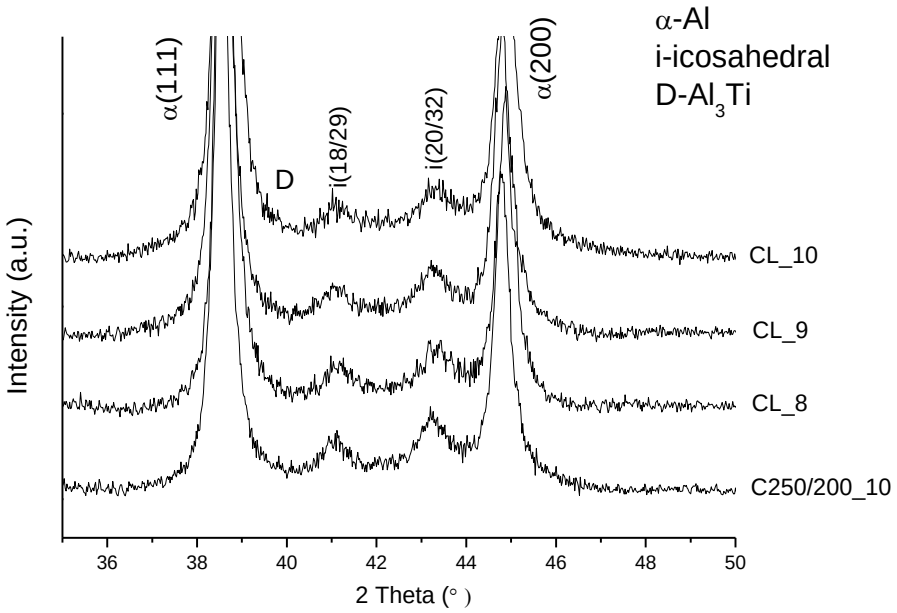

(b)

Figure 6.4: The X-ray diffractograms for the C250/200_10, CL_8, CL_9 and CL_10 batches of powder **(a)** overall view from 20° to 90°, **(b)** magnified view from 35° to 50°. The inset in (a) highlights the γ(440) and i(52/84) peaks

In this work, the X-ray diffractograms for the four batches of powder have no significant differences. This indicates the powders processed in these milling conditions have similar phases. The average Al crystallite sizes and strain values were calculated with the Williamson-Hall (Williamson and Hall 1953), as described in section 3.3.1 in Chapter 3. These values were plotted against the milling time, as shown in Figure 6.5. There is a clear crystallite size decreasing trend in crystallite size for the CL batch powders from 8 to 10 hours. The CL_8 sample has similar crystallite size with the C250/200_10 powders. For the strains, all the samples are between 1% to 1.5%, and the differences among them are neglectable.

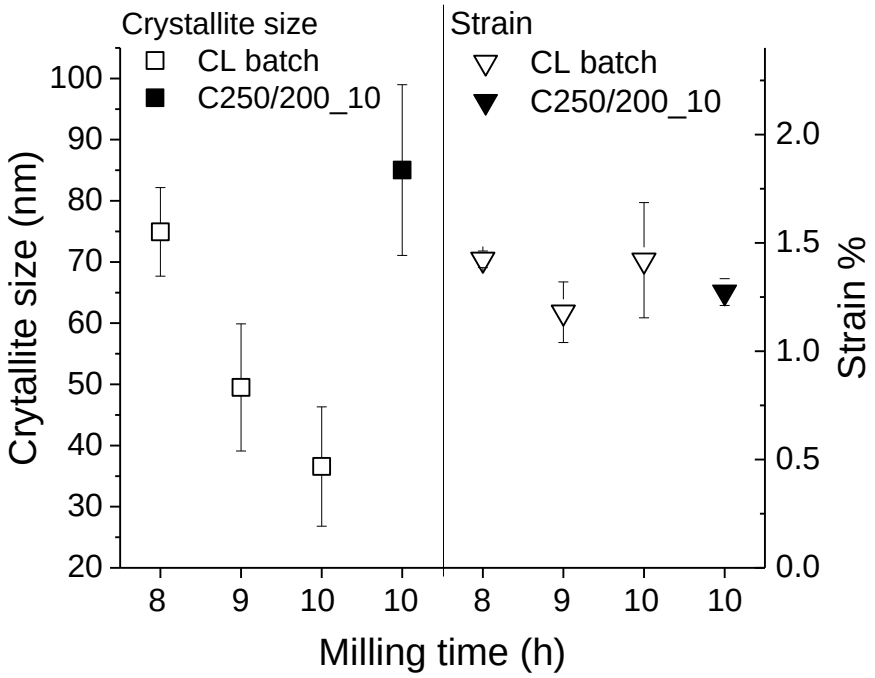

Figure 6.5: Al crystallite average sizes and strains against the milling time for the CL batch powders and C250/200_10 powders

6.1.4 Thermal stability

Thermal analysis of the CL batch powders was performed by DSC at a heating rate of 40 K/min. This was done to check the transformation temperature changes after the ball milling process and to verify whether the quasicrystalline phase would be decomposed in the extrusion process. Three scans were conducted for each of the CL_8, CL_9, CL_10 and C250/200_10 samples. For each of the samples one representative scan was chosen and plotted in Figure 6.6, whereby the peaks show exothermic reactions. There are two main exothermic peaks in the DSC runs for each sample. As discussed in section 4.7.3 in Chapter 4, peak 1 involves Al grain coarsening and intermetallics precipitation, whereas the peak 2 involves mostly quasicrystals decomposition, which leads to further intermetallic precipitation[1]. As discussed in section 4.4 in Chapter 4, Gaussian fits can be applied to separate the overlapping peaks and calculate the peak temperature. The values labelled on Figure 6.6 were the average peak temperatures calculated with three DSC runs. The errors come from the standard deviation. For the C250/200_10 sample, the peak temperature for the left exothermic reaction is 418.2°C, slightly higher than those for the CL_8, CL_9 and CL_10 samples (414.8°C, 414.8°C and 415.0°C respectively). For the right exothermic event, the peak temperature for the C250/200_10 sample is higher, at 478.1°C. The decomposition temperatures of the right peak for the CL_8, CL_9 and CL_10 samples are 468.3°C, 467.6°C and 463.0° respectively. All of these values are lower than that of the C250/200_10 powder.

[1] Peak 1 is the peak at lower temperature in the DSC curve. Peak 2 is the peak at higher temperature in the DSC curve.

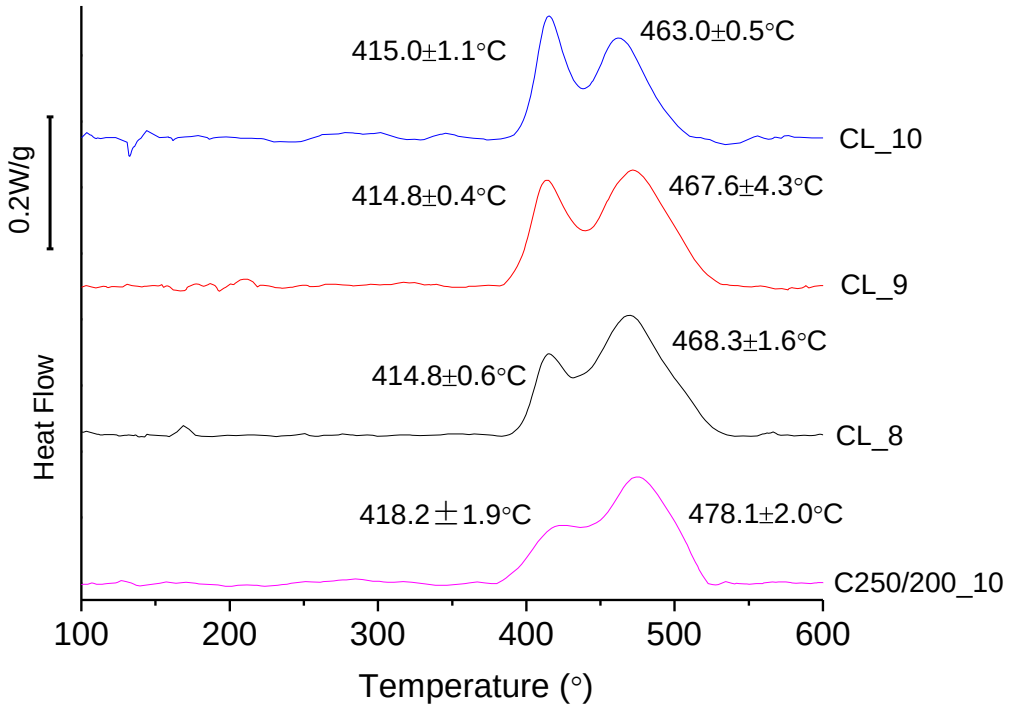

Figure 6.6: DSC scans of the CL batch of powder and the C250/200_10 sample with scanning rate at 40 K/min, showing temperatures corresponding to the main exothermic events

Activation energy values of the transformation corresponding to the two exothermic peaks were estimated for each of the curves for both the CL batch sample and the C250/200 sample using Kissinger plots described in section 3.4.1 in Chapter 3. The values are plotted against the milling time in Figure 6.7. For peak 1, the activation energy values of the CL_9 and C250/200_10 are 140 kJ/mol and 133 kJ/mol, similar to each other, but lower than that of the CL_10 sample (159kJ/mol). For peak 2 the activation energy of the CL_9 sample is 221 kJ/mol, which is higher than those of the CL_10 (177 kJ/mol) and C250/200_10 (168 kJ/mol) samples. The activation energy represents the energy the sample needs to overcome the energy barrier for the phase transformation to occur

(Vaughan 1955). Therefore, peak 2, which mainly involves the decomposition of the quasicrystalline phase (discussed in section 4.7.3 in Chapter 4), should be more difficult for the CL_9 sample.

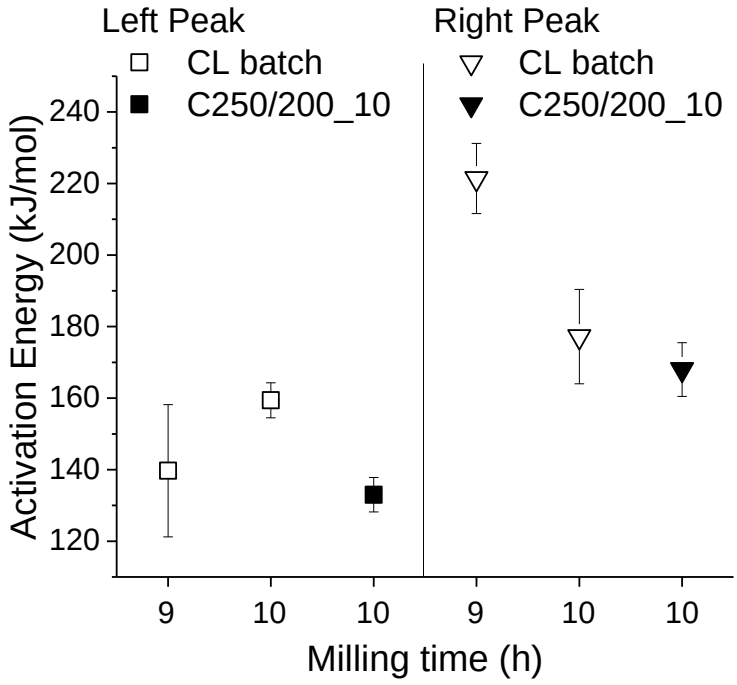

Figure 6.7: Activation values for the CL batch powder and the C250/200_10 powder

6.1.5 Hardness

The Hardness values of the CL_9, CL_10 and C250/200 powder are 472 kg/mm^2, 425 kg/mm^2 and 410 kg/mm^2 respectively, as shown in Figure 6.8.

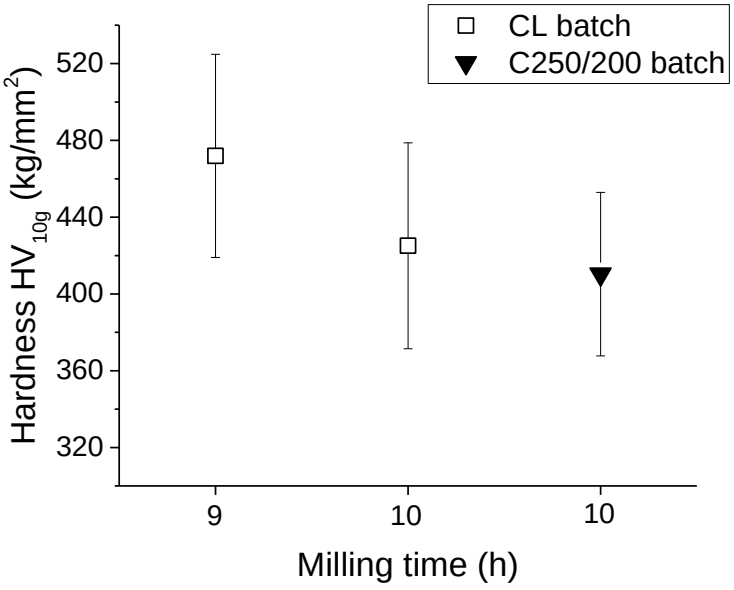

Figure 6.8: Hardness of CL_9, CL_10 and C250/200_10 samples

6.1.6 Final remark

As discussed in 5.6.6 in Chapter 5, several factors are considered when choosing the powders for extrusion: the milling time, the γ-Al_2O_3 distribution level, the decomposition of the quasicrystal, the crystallite size and the hardness. In the current work, a large milling pot (500ml) was used for the purpose of processing powders with a shorter time.

For the even distribution of γ-Al_2O_3, from Figure 6.3, the CL_8 samples contain some γ-Al_2O_3 free regions. In comparison, the CL_10 and the CL_9 powders have relative better γ-Al_2O_3 distribution, which indicates they are more suitable for extrusion. Some researchers report that extrusion can increase the homogeneity of reinforcement distribution. Kalu et al. (Kalu and McNelley 1991) reported that hot extrusion could homogenise the composite buy detaching the reinforcement particle from the clusters and move it to reinforcement free areas. Guo et al. (Guo, Wang et al. 2012) processed a relative homogeneous Mg/SiC nanocomposite from a solidified inhomogeneous composite by cyclic extrusion compression. Therefore, the extruded bar should at least have the same homogeneity level with the raw powder. Compared with CL_10, the CL_9 has higher temperatures and activation energy value for metastable phase transformation, as shown in Figure 6.6 and Figure 6.7.

For processing bulk nanocrystalline alloy or composite, usually the aluminium matrix grains are of nanosize. In the literature, most studies on ball milling used powders with nanosize crystallite sizes for extrusion. *Poirier* et al. (Poirier, Drew et al. 2010) extruded Al-10%Al_2O_3 (4nm) nanocomposites with crystallite size of 90nm and Al-10%Al_2O_3 (80nm) nanocomposites with crystallite size of 180nm. *Flores-Campos* et al. (Flores-Campos, Estrada-Guel et al. 2011) extruded 7075Al matrix carbon coated silver particle

reinforced composites with crystallite size ranging from 30nm to 70nm. In this work, the CL_8, CL_9 and CL_10 have crystallite sizes of 75nm, 50nm and 37nm respectively, which are all of nanosize level. The CL_9 batch powders were chosen to be extruded, as described in section 3.1.4 in Chapter 3.

6.2 Powder consolidation into bulk specimens

6.2.1 Extrusion

The bar extruded was numbered with a letter E. For the cross section, the sample was named as E_C, and for the longitudinal section, the sample was named as E_L. As discussed in section 3.1.4 in Chapter 3, the powders were heat-treated at 430-460°C for 30min before extrusion. The heat-treated powder was named as CL_9_HT. The extrusion conditions were summarised in Table 6.2. Based on the DSC scan in Figure 6.6, the exothermic event corresponding to the right peak of the CL_9 sample occurs from about 400°C to 540°C. This indicates that the metastable phases in the CL_9 powders should be decomposed during the heat treatment or the extrusion process. The maximum pressure between the can and the die during extrusion was 1024MPa. *Hameed* (Hameed 2016) extruded the nanoquasicrystalline $Al_{93}Fe_3Cr_2Ti_2$ powder (the same with the unmilled powder in this thesis) with the same extrusion conditions, except the extrusion temperature was 400°C. The maximum pressure *Hameed* obtained was 1306MPa (Hameed 2016), about 28% higher than current one, even the nanoquasicrystalline $Al_{93}Fe_3Cr_2Ti_2$ powder he used for extrusion had hardness about 130 kg/mm^2, much lower than the value of 472 kg/mm^2 of the CL_9 powder at room temperature.

	Container temperature (°C)			Die temperature (°C)		Force (MPa)	
Extrusion ratio	Aim	Max	Min	Peak	Final	Peak	Final
10.3	450	450	448	302	293	1024	421

Table 6.2: Table summarising the extrusion conditions for the nanocomposite bar

6.2.2 Density measurement

The density of the bottom region in extrude bar is measured to be 2.94g/cm^3 with the Archimedes density method explained in section 3.5.1 in Chapter 3. The theoretical density of the $Al_{93}Fe_3Cr_2Ti_2$ is roughly 2.88g/cm^3 (Rounthwaite 2012), and the density of γ-Al_2O_3 is 3.60g/cm^3 (Inframat Advanced Materials 2017). By applying the rule of mixture (Kim 2000):

$$\boldsymbol{\rho_{the} = \rho_{\alpha} V_{\alpha} + \rho_{\gamma} V_{\gamma}} \quad \text{----------} \quad \text{Equation 1}$$

where ρ_{the} is the theoretical density of the material, ρ_{α} is the density of $Al_{93}Fe_3Cr_2Ti_2$ powder, V_{α} is the volume fraction of the $Al_{93}Fe_3Cr_2Ti_2$ powder, ρ_{γ} is the density of the γ-Al_2O_3, and V_{γ} is the volume fraction of the γ-Al_2O_3. Here ρ is calculated to be 2.97g/cm^3. The relative density can be calculated by (Spierings, Schneider et al. 2011):

$$\boldsymbol{\rho_{rel} = \rho_{mea} / \rho_{the}} \quad \text{----------} \quad \text{Equation 2}$$

Where $\boldsymbol{\rho_{mea}}$ is the measured density through Archimedes method (explained in Chapter section 3.5.1 in Chapter 3) and $\boldsymbol{\rho_{rel}}$ is the material's relative density. $\boldsymbol{\rho_{rel}}$ is calculated to be 99±1%.

6.3 Microstructure of the extruded bar

6.3.1 Alumina distribution

The FIB images of the extruded bar are shown in Figure 6.9. As observed, hardly could any pores be detected. This matches the density measurement in section 6.2.2. In comparison with the CL_9 sample in Figure 6.9(a), the orientation disappears in extruded bar, as shown in Figure 6.9(b) and(c). The cross section and the longitudinal section have similar alumina distribution.

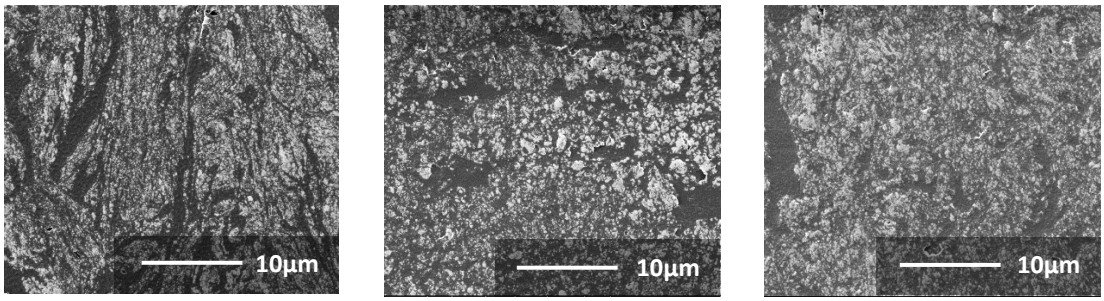

(a) (b) (c)

Figure 6.9: The FIB images of extruded bar and mechanically milled powders **(a)** FIB image of CL_9, **(b)** FIB image of E_C, **(c)** FIB image of E_L

6.3.2 Phase components and crystallite sizes

X-ray diffractograms for the milled powder, the heat-treated powder, the cross section and the longitudinal section of the bars are shown in Figure 6.10(a) with an enlargement of the central section of the scan 35° to 50° for phase identification in Figure 6.10(b). All the phases presented in the powders were indexed as follows. α-Al peaks were identified by indexing the reflections corresponding to the (111), (200), (220), (311), (222) and (400) planes in the 2θ = 20°-100° range at 38.5°, 44.7°, 65.2°, 78.3°, 82.5° and 99.2°. γ-Al_2O_3 was identified by indexing the reflections to the (440) planes at 66.9°. Quasicrystals, with

other intermetallics, including Al_3Ti, $Al_{13}Cr_2$, $Al_{13}Fe_4$ and Al_6Fe were also identified with peak positions listed in Table 6.3. As shown in the spectra, some peaks of the intermetallics overlap with each other. It is expected that the quasicrystals have been fully decomposed during the extrusion.

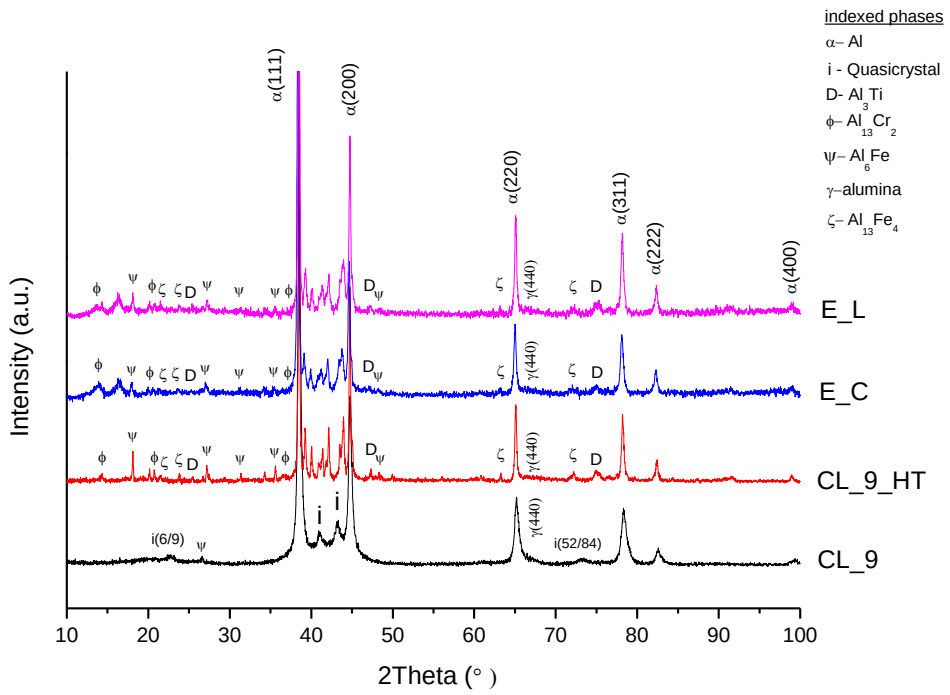

(a)

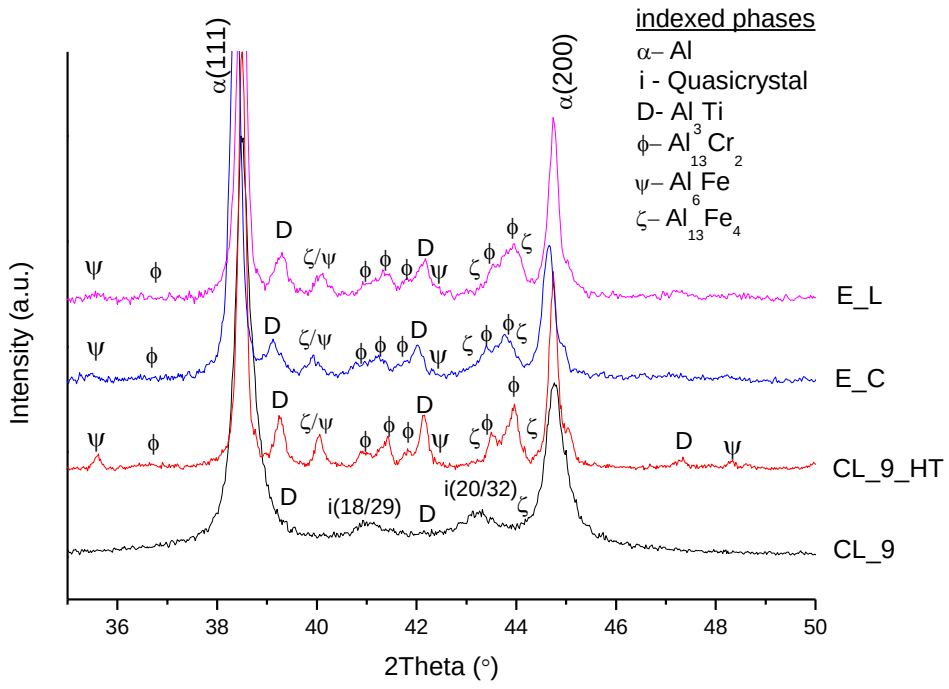

(b)

Figure 6.10: XRD diffractograms of the ball milled powders and the extruded bar, **(a)** 10-100° range, **(b)** 35-50° range

Symbol	Phase	Location of peaks in °(2θ)
i	quasicrystal	22.7, 41.2, **43.3**, 73.1
D	Al_3Ti	25.2, **39.0**, 42.2, 47.3, 75.1
ϕ	$Al_{13}Cr_2$	13.7, 20.7, 36.9, 41.0, 41.3, 43.4, **43.8**
ζ	$Al_{13}Fe_4$	21.5, 23.8, 40.0, **43.3**, 44.0, 63.2, 72.2,
ψ	Al_6Fe	18.1, 27.2, 31.4, 35.6, 40.0, **42.2**, 48.3

Table 6.3: Peak °(2θ) positions for the intermetallic phases in the XRD diffractograms of the heat-treated powders and the extruded bars. (2θ positions corresponding to 100% intensity are in bold)

From the X-ray diffractograms the cross section, the longitudinal section and the heat-treated CL_9 powders have similar relative peak intensities, as shown in Figure 6.11. This indicates the crystallite orientations remain random after extrusion. One possible reason could be the existence of γ-Al_2O_3 inhibits the local Al grain rotations which weakens the amount of major textures. Jiang et al. (Jiang, Galano et al. 2014) processed the Al 6061/SiCp composite through extrusion. In their research, the aluminium grains in SiC free band rotated to typical Brass or Copper orientations. However, the orientations of most grains near the reinforcement particles have continuous gradients due to the inhibition effect of the SiC. Recrystallization, another common behaviour during extrusion process, could lead to nucleation and growth of new grains and cause weak textures (Hutchinson and Wilcox 1973, Humphreys 1979, Bieler, Noebe et al. 1992, Poudens and Bacroix 1996).

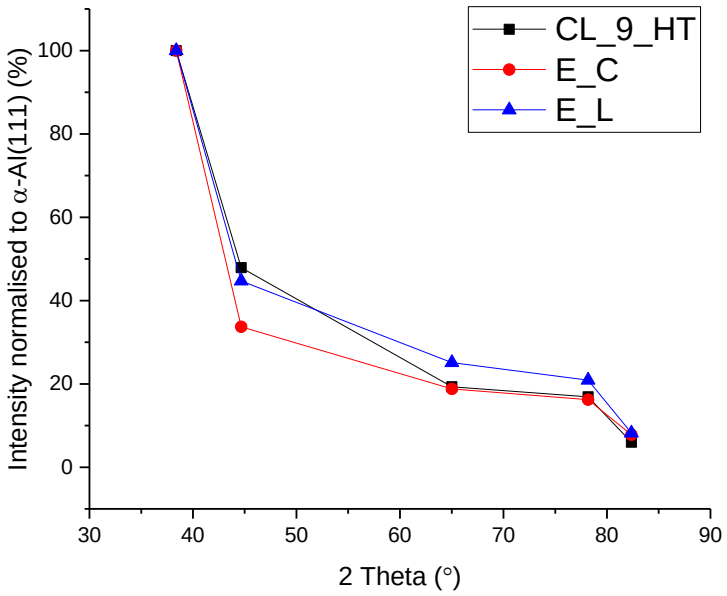

Figure 6.11: Relative intensities of each α-Al reflection plane for the powders and the different sections of the extruded bar

6.3.3 Thermal stability

Small chips from the extruded bar were used for the DSC scans. As shown in Figure 6.12, the metastable phase in the ball milled powder should have been decomposed during the extrusion at 450°C. This matches the X-ray diffractograms in Figure 6.10.

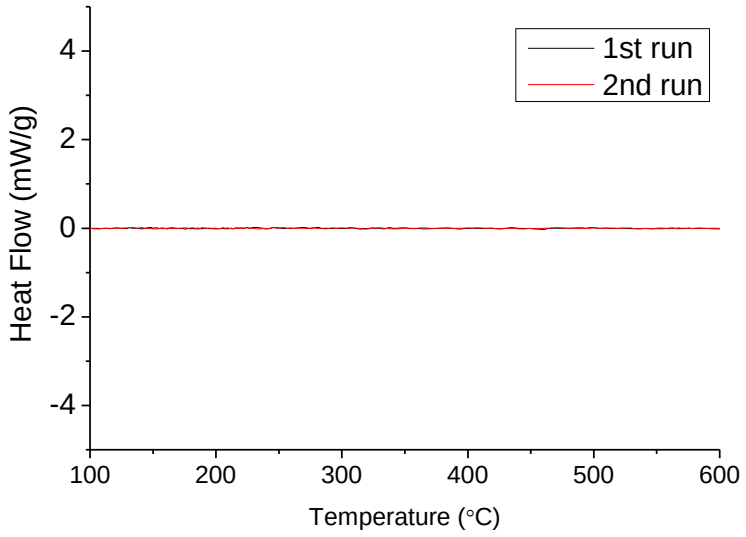

Figure 6.12: the 1st and the 2nd repeated DSC runs for the extruded bar

6.4 Microstructure of the extruded bar

The microstructure of the CL_9, CL_9_HT and E_L powder was characterised using transmission electron microscope (TEM), as shown in Figure 6.13, Figure 6.14 and Figure 6.15 respectively. Particle (1) in Figure 6.13(a) is proved to be a quasicrystal particle with a fivefold convergent beam diffraction patterns (CBDP) being obtained, as shown in Figure 6.13(b). A TEM bright field (BF) image and a scanning transmission electron microscope (STEM) dark field (DF) image obtained from the same area were shown in Figure 6.13(c) and(d). The components were analysed with the EDX mapping of O, Fe, Cr and Ti elements. From the EDX mapping of O element in Figure 6.13(e), the particles with dark contrast in Figure 6.13(d), such as (2), (3) and (4), should be the γ-Al_2O_3 clusters. The transition elements concentrate on certain white particles such as particle (5). These elements can also be detected in the matrix. There are orientations in the CL_9 sample, as shown in Figure 6.13(d). In comparison, in the CL_9_HT sample, no quasicrystalline

phase could be found. Instead, there are some white particles having high concentration of Fe or Cr, such as (1) and (2) in Figure 6.14(b). Most of these intermetallics sit intergranularly among the Al grains. Considering the X-ray diffractograms in Figure 6.10, these intermetallics could be Al_6Fe, $Al_{13}Fe_4$ and $Al_{13}Cr_2$ intemetallics. Some very small particles with diameter less than 50nm but high concentration in Ti were found, as shown in Figure 6.14(f). X-ray diffractogram in Figure 6.10 shows that these intermetallics could be Al_3Ti.

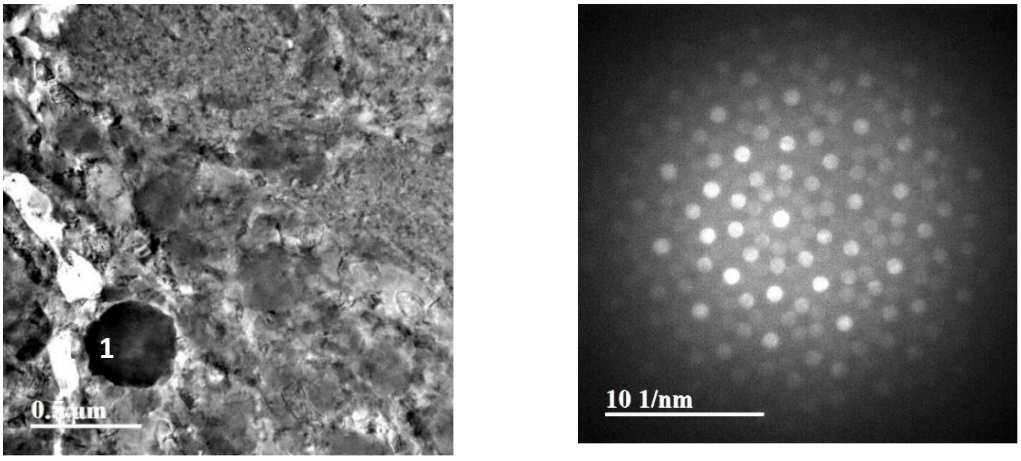

(a) (b)

Figure 6.13: The CL_9 sample **(a)** TEM BF image of CL_9, **(b)** the CBED from particle 1 in (a), **(c)** TEM BF image, **(d)** STEM DF image, **(e)** EDX mapping of O element, **(f)** EDX mapping of Fe element, **(g)** EDX mapping of Cr element, **(h)** EDX mapping of Ti element

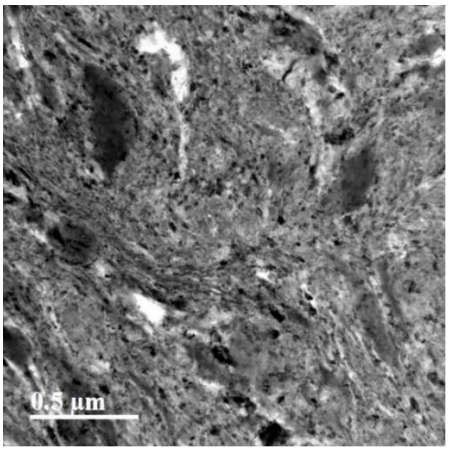

(c)

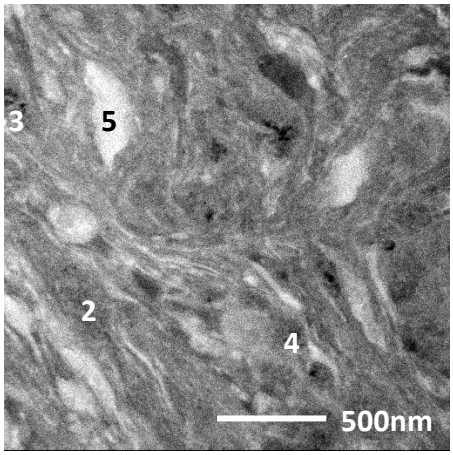

(d)

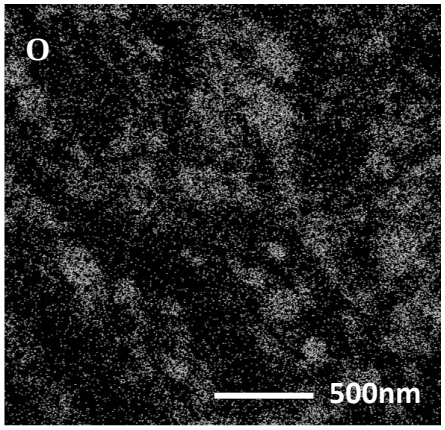

(e)

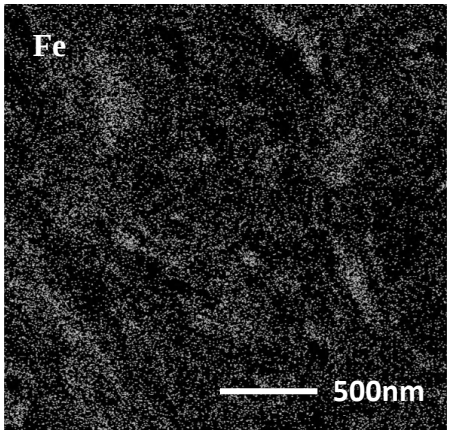

(f)

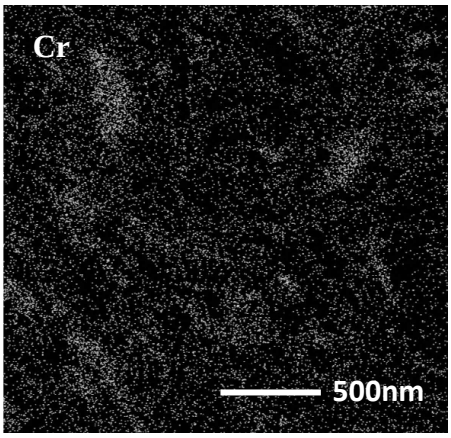

(g)

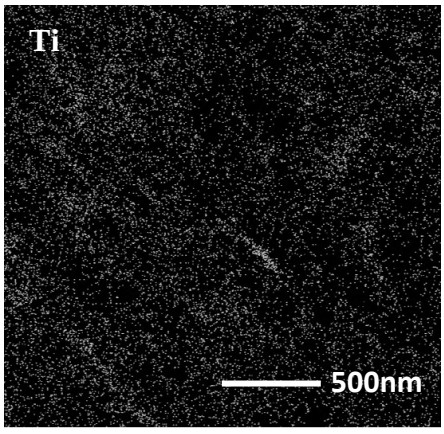

(h)

Figure 6.13: The CL_9 sample **(a)** TEM BF image of CL_9, **(b)** the CBED from particle 1 in (a), **(c)** TEM BF image, **(d)** STEM DF image, **(e)** EDX mapping of O element, **(f)** EDX mapping of Fe element, **(g)** EDX mapping of Cr element, **(h)** EDX mapping of Ti element

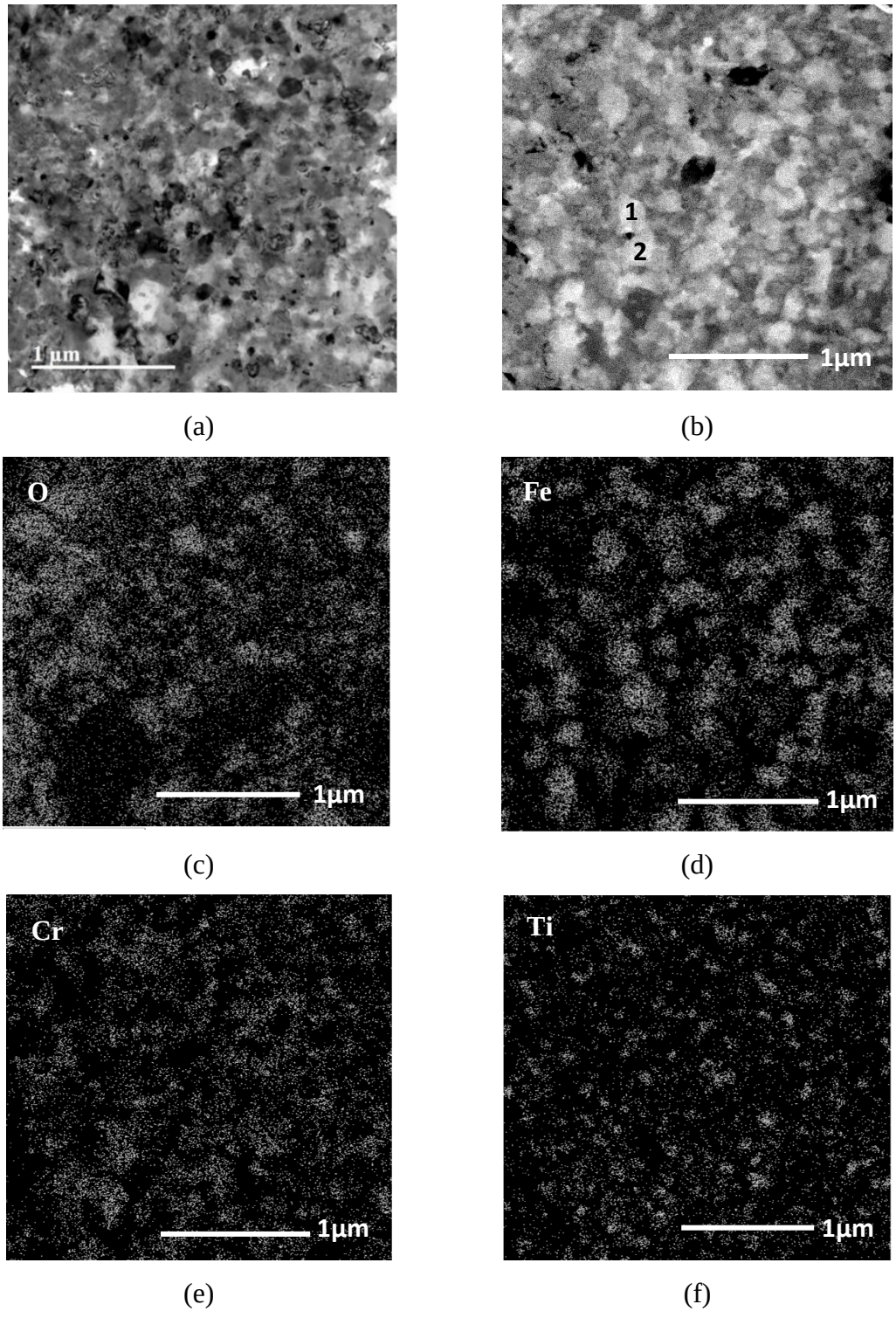

Figure 6.14: Cl_9_HT sample **(a)** TEM BF image, **(b)** STEM DF image, **(c)** EDX mapping of O element, **(d)** EDX mapping of Fe element, **(e)** EDX mapping of Cr element **(f)** EDX mapping of Ti element

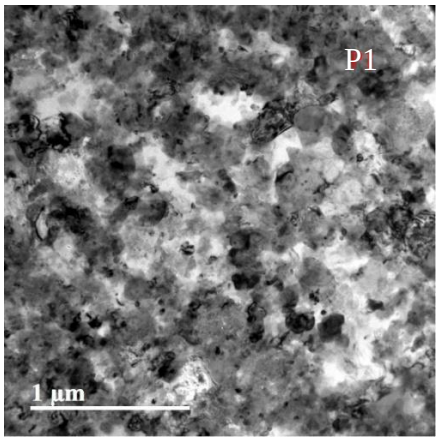

(a)

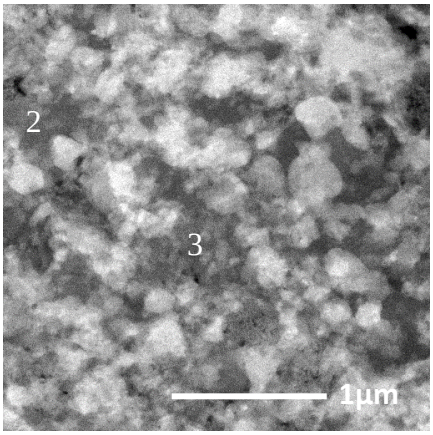

(b)

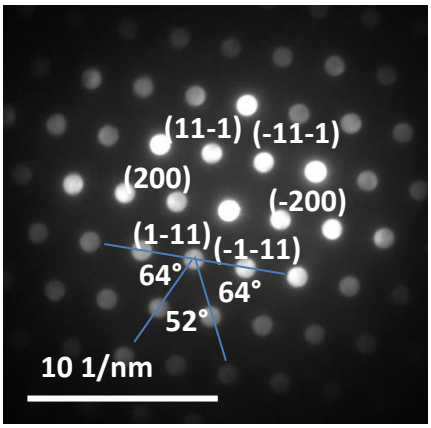

(c)

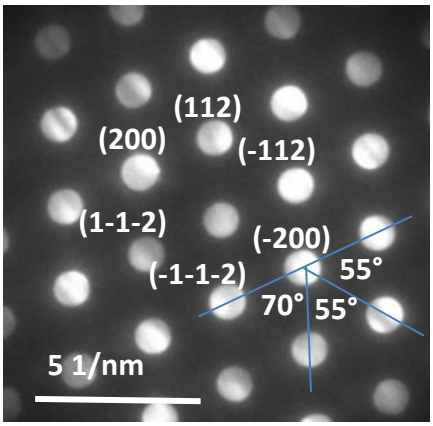

(d)

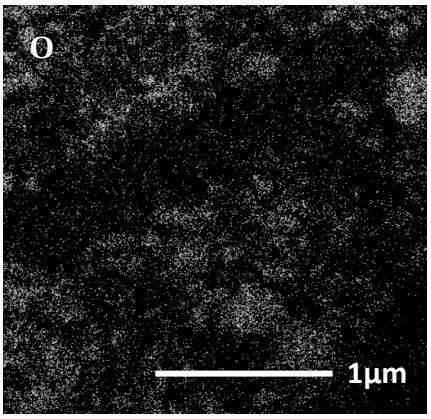

(e)

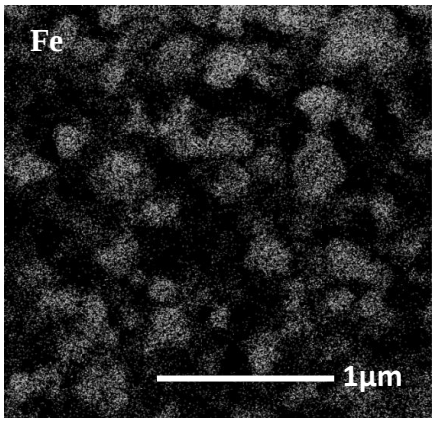

(f)

Figure 6.15: The E_L sample **(a)** TEM BF image, **(b)** STEM DF image, **(c)** CBED of P1, **(d)** CBED of P1, **(e)** EDX mapping of O element, **(f)** EDX mapping of Fe element, **(g)** EDX mapping of Cr element, **(h)** EDX mapping of Ti element

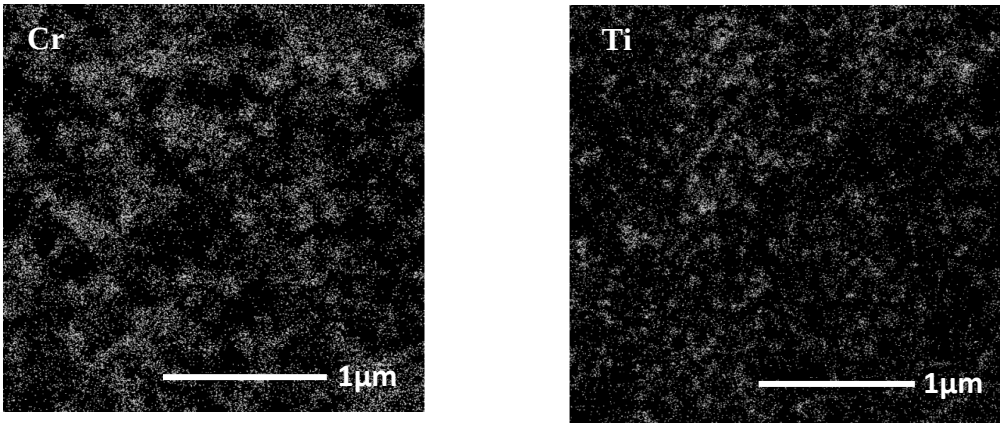

(g) (h)

Figure 6.15: The E_L sample **(a)** TEM BF image, **(b)** STEM DF image, **(c)** CBED of P1, **(d)** CBED of P1, **(e)** EDX mapping of O element, **(f)** EDX mapping of Fe element, **(g)** EDX mapping of Cr element, **(h)** EDX mapping of Ti element

The E_L sample has similar microstructure to the CL_9_HT samples, as shown in Figure 6.15. In general, E_L has three components in the sample, namely the Al grains, the intermetallic particles and the γ-Al_2O_3 reinforcements. The particle P1 in Figure 6.15 was identified to be the Al_6Fe phase with two CBDPs from [011] and [02-1] axes. This is in consistent with the X-ray diffractograms in Figure 6.10. The particle 2 and 3 in Figure 6.15(b) are the Al grains. The EDX could not detect any transition atoms (Fe, Cr, Ti) inside the Al grains.

For the CL_9, CL_9_HT and E_L batch powders, the crystallite sizes were measured using TEM following the same method described in section 4.3.1 in Chapter 4. The crystallite sizes of CL_9, CL_9_HT and E_L are 48±14nm, 154±61nm and 97±46nm respectively, as shown in Figure 6.16. The errors here come from the standard deviation of averaging the measured values from 30 Al crystallites. The crystallite size of CL_9 was also measured using the Williamson-Hall equation from the X-ray diffractogram, and the

result 50±10nm is very close to the one measured using TEM. For the E sample, the crystallite size calculated with Williamson-Hall plot in X-ray diffractogram is 60±4nm, lower than the one calculated using TEM. CL_9_HT has larger crystallite size than the extruded bar. As discussed in section 6.3.2, this may due to the recrystallization.

The intermetallic particle size of E_L sample was measured to be 348±87nm using TEM. The total volume fraction of the intermetallics and γ-Al_2O_3 particles is 0.56, calculated with the equation (Audebert, Prima et al. 2002):

$$\boldsymbol{f = r_p^2/(\lambda/2)^2} \quad \text{----------} \quad \text{Equation 3}$$

Where r_p is the mean planar particle radius and λ is the mean distance between the centres of the planar particles (464±148nm calculated using the STEM images).

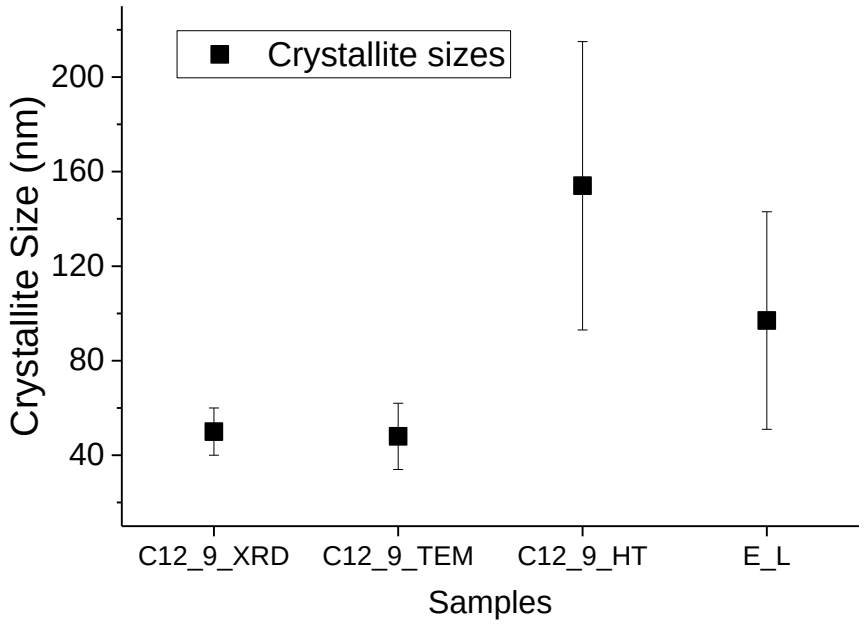

Figure 6.16: Crystallite sizes of the ball milled powders and extruded bar

6.5 Mechanical properties of the extruded bar

The hardness value of the $Al_{93}Fe_3Cr_2Ti_2$/12.9vol.%Al_2O_3 extruded bar was 286±4kg/mm^2, higher than the extruded quasicrystalline $Al_{93}Fe_3Cr_2Ti_2$ alloy (159±1kg/mm^2) (Rounthwaite 2012) and the aluminium nanocomposites reported in literature, such as the $Al_{93}Fe_3Cr_2Ti_2$/8.5vol.%Al_2O_3 nanocomposite obtained by Marsh (226 kg/mm^2) (Marsh 2013). Since the hardness of γ-Al_2O_3 is about 714 to 744 kg/mm^2 (Chou, Nieh et al. 1991, Gallas, Hockey et al. 1994, Mishra, Lesher et al. 1996), it could potentially strengthen the material through the load transfer, as described in section 2.4.7 in Chapter 2:

$$\boldsymbol{H_C = H_A(1 - f) + H_r f} \quad \text{----------} \quad \text{Equation 4}$$

where H_C, H_A, H_r are the hardness values for the composite, the matrix alloy and the reinforcement, respectively. f is the volume fraction of the reinforcements (12.9%). Assuming the hardness of the matrix alloy H_A is 142±18 kg/mm^2, obtained by testing the unmilled powders after heat treatment of 430°C degree for 20min, 445°C for 5min and 460°C for another 5min, H_C is estimated to be 220 kg/mm^2, lower than the tested value 286±4 kg/mm^2. This could be because that the unmilled powder after heat treatment should have micro-size grains, as the unmilled powders already have a grain size of 1.5μm (Table 4.5 in section 4.4 in Chapter 4). Since the average grain size of the extrude bar is only 97nm (Figure 6.16), the underestimation of the hardness is suspected to come from the grain refinement strengthening (Hall 1951, Petch 1953).

For compression, the compliance tests were conducted without any sample being loaded to check the stiffness of the equipment. Compression tests were conducted at both room temperature and at 250 °C with an initial strain rate of 0.001 s^{-1}. The stress-strain curve of compression test at room temperature with displacement compliance subtracted was

shown in Figure 6.17. The compression strength is about 925MPa. The yield strength can be obtained by shifting the linear fitting to the right side by 0.02%, as shown in Figure 6.18. The red crossing point represents the 0.2% strength, 673MPa.

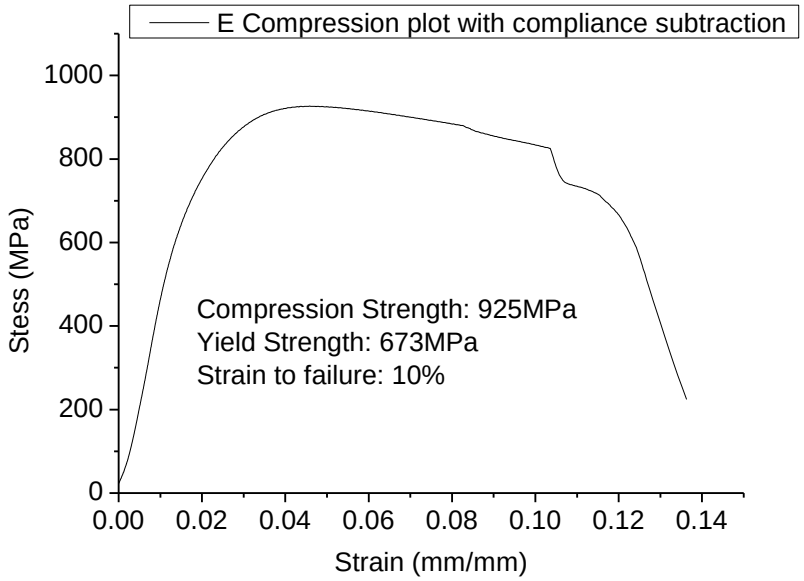

Figure 6.17: Engineering stress-strain curve for the compression sample at room temperature

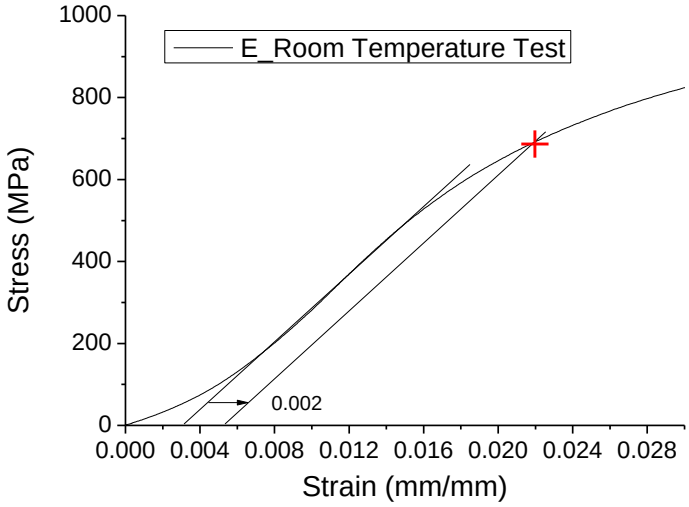

Figure 6.18: Identify the 0.2% yield strength of the compression sample at room temperature

Figure 6.19 shows the fracture surfaces of samples compressed at room temperature. River-band patterns were detected, which indicates a brittle fracture mode. These river markings are caused by the crack moving through the crystal along a number of parallel planes which form a variety of plateaus and connecting ledges (Dieter and Bacon 1986). The directions of the river patterns represent the directions of crack propagations (Dieter and Bacon 1986). The fracture mode depends severely on the volume fraction of the brittle reinforcements. For both aluminium quasicrystalline alloy and nanocomposites, the fracture follows a ductile mechanism when the volume fractions of quasicrystals and reinforcements are low (less than 50% for the quasicrystalline alloys and less than 15vol.% for the ceramic reinforcement particles) (McDanels 1985, Davidson 1989, Kamat, Hirth et al. 1989, Somekawa, Singh et al. 2007, Akbari, Baharvandi et al. 2015, Hameed 2016). In this case, large quantity of dimples could be found in the fractured surface. McDanels (McDanels 1985) reported in the 6061Al/SiC composite, when the volume fracture of SiC is around 20 vol.%, the fracture behaviour underwent a transition, and flat, granular chisel was found on the fracture surface. At reinforcement content of 30 to 40 volume percentage, the fracture surface became totally flat and fracture mode failed in a brittle manner. In the E sample, the volume fraction of the γ-Al_2O_3 is only 12.9vol.%. However, as discussed in section 6.4 in this Chapter, there are about 56% intermetallic particles and γ-Al_2O_3 clusters in total inside the material. These phases are considered to be hard and difficult to deform (Luo, Zhang et al. 2005), and thus are responsible for the brittle failure mode.

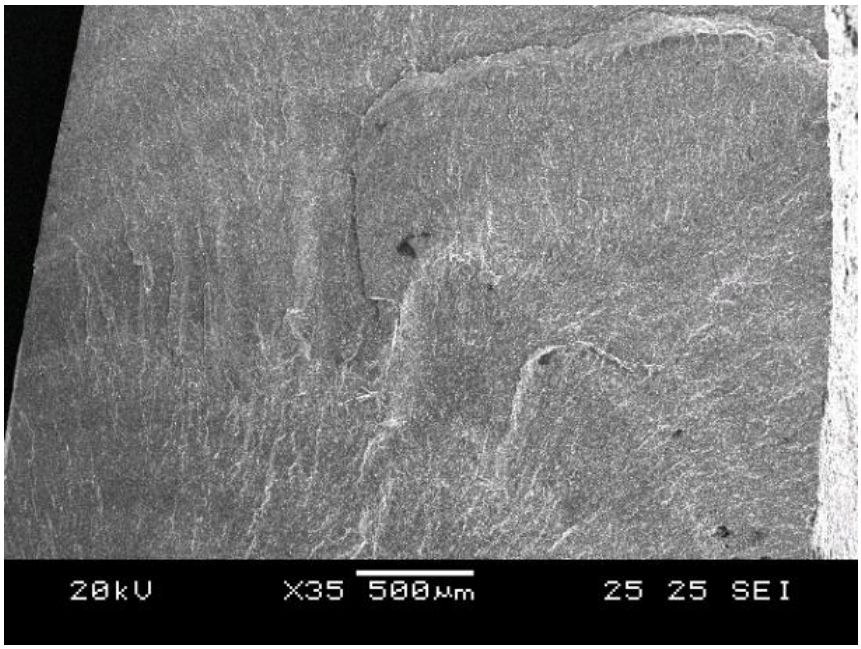

Figure 6.19: Fracture surface of the compression sample tested at room temperature

The extruded bar was also tested at 250°C to verify the high temperature performance, as shown in Figure 6.20. Both the compression strength and the compressive yield stress show a decrease. The strain to failure ratio increases from 10% to 18%. The compressive yield stress of the extruded bar is 424MPa at 250°C. In literature, the compressive yield stress of the $Al_{93}Fe_3Cr_2Ti_2$ alloy at 250°C was not found. However, *Inoue* found that the compressive yield stress of quasicrystalline $Al_{93}Fe_3Cr_2Ti_2$ alloy was 400MPa at 200°C, and decreased with increasing temperature (Inoue 1998). Therefore, the $Al_{93}Fe_3Cr_2Ti_2/\gamma$-$Al_2O_3$ should have higher strength than the $Al_{93}Fe_3Cr_2Ti_2$ alloy at 250°C. The fracture surfaces of the samples are shown in Figure 6.21. The river patterns coming from brittle cleavage of the sample are still observed. The aluminium composite can transfer from brittle fracture to ductile fracture at temperatures high enough. *McDanels* (McDanels 1985) reported the 6061Al/20vol.%SiC composite increased failure strain when tested at 260°C,

but the fracture mode was still transitional (with part of the fracture surface ductile and part brittle). However, the fracture behaviour of their composite changed to ductile when tested at 316°C. Therefore, the brittle behaviour of the E sample may change to ductile if fractured at higher temperatures but further tests are required to verify this hypothesis.

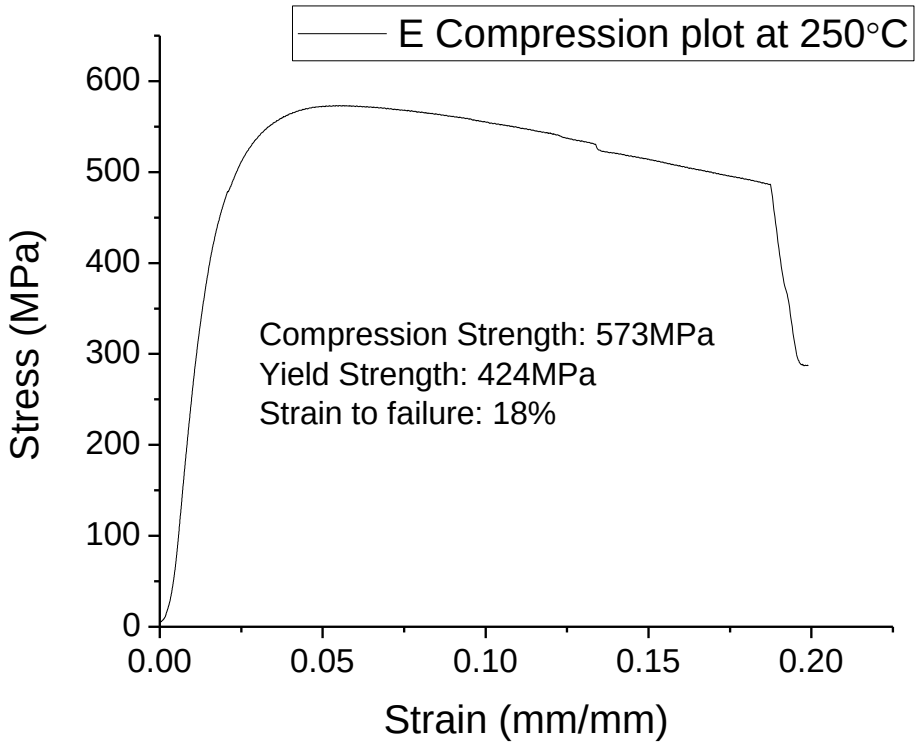

Figure 6.20: Engineering stress-strain curve for the bar tested at 250 °C

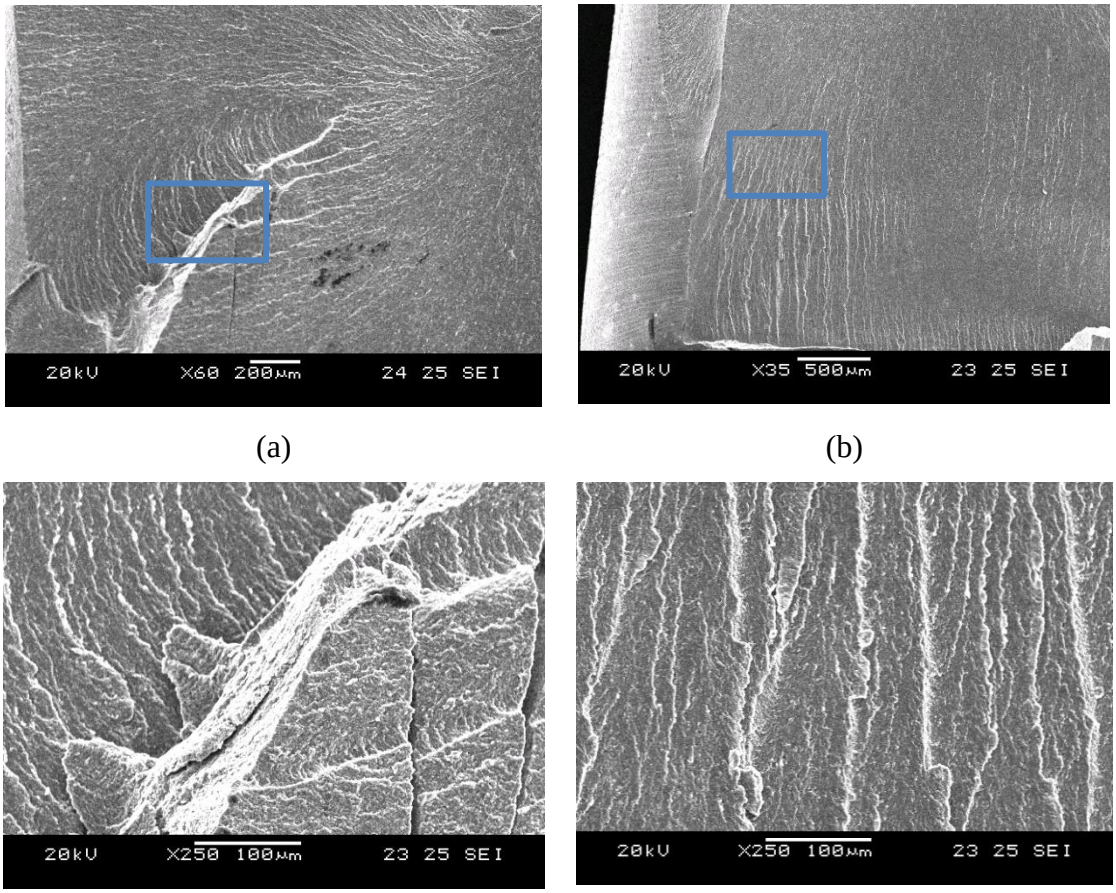

Figure 6.21: Fracture surfaces of the compression sample tested at 250 °C **(a)** river bands, **(b)** river bands, **(c)** a zoom in area from the blue square in (a), **(d)** a zoom in area from the blue square in (a)

It is difficult to test the Young's modulus value through compression test, because the compression tester cannot measure the displacement of the sample accurately. The theoretical Young's modulus value of the nanocomposite bar can be estimated with the rule of mixture (Kim 2000):

$$\boldsymbol{E_C = fE_a + (1-f)E_m} \quad \text{----------} \quad \text{Equation 5}$$

where E_a is the Young's modulus of the γ-Al_2O_3, E_m is the Young's modulus of the aluminium matrix, f is the volume fraction of the reinforcement and E_C is the Young's

modulus of the nanocomposites. Here E_a equals 145GPa (Chou, Nieh et al. 1991), E_m equals to 87.1GPa (Rounthwaite 2012), f is 12.9% and E_C is calculated to be 94.6GPa.

6.6 Conclusion

In this work, $Al_{93}Fe_3Cr_2Ti_2$ nanoquasicrystalline nanocomposite powder was produced with mechanical milling with a 500ml pot. The powders milled at 250rpm up to 4 hours of milling and at 200rpm for the next 5 hours of milling have good γ-Al_2O_3 distribution homogeneity and a crystallite size of 50±10nm, and were extruded at 450°C.

The extruded bar has minor porosities. The reinforcement distribution of the extruded bar is similar to the ball milled powders. The metastable phases have been fully decomposed in either the heat treatment process or the extrusion process. No obvious texture is found, probably because the high volume fractions the reinforcements and the intermetallic particles have an inhibition effect on the reorientation of the grain or because of the recrystallization during extrusion. The Al grain size of the bar is about 97±46nm, measured using TEM.

The hardness of the bar is 286±4kg/mm^2, higher than the extruded nanoquasicrystalline $Al_{93}Fe_3Cr_2Ti_2$ alloy and the aluminium nanocomposites in the literature. The compression tests were conducted at both room and elevated temperatures. At room temperature, the sample has an ultimate compression strength of 925MPa and a strain to failure of 0.10. The compression strength is reduced to 573MPa at 250°C, but the strain to failure increases to 0.18. For both compression tests, the samples fractured in a brittle mode manner. The brittle fracture behaviours should be related with the high fraction of intermetallics and γ-Al_2O_3 particles.

6.7 Reference

Akbari, M. K., et al. (2015). "Tensile and fracture behavior of nano/micro TiB 2 particle reinforced casting A356 aluminum alloy composites." Materials & Design (1980-2015) **66**: 150-161.

Audebert, F., et al. (2002). "Structural characterisation and mechanical properties of nanocomposite Al-based alloys." Materials Transactions **43**(8): 2017-2025.

Bieler, T., et al. (1992). Extrusion Textures in NiAl and Reaction Milled NiAl/AlN Composites. MRS Proceedings, Cambridge Univ Press.

Chou, T., et al. (1991). "Microstructures and mechanical properties of thin films of aluminum oxide." Scripta metallurgica et materialia **25**(10): 2203-2208.

Davidson, D. (1989). "Fracture surface roughness as a gauge of fracture toughness: aluminium-particulate SiC composites." Journal of materials science **24**(2): 681-687.

Dieter, G. E. and D. J. Bacon (1986). Mechanical metallurgy, McGraw-Hill New York.

Flores-Campos, R., et al. (2011). "Microstructure and mechanical properties of 7075 aluminum alloy nanostructured composites processed by mechanical milling and indirect hot extrusion." Materials Characterization **63**(1): 39-46.

Galano, M., et al. (2009). "Nanoquasicrystalline Al–Fe–Cr-based alloys. Part I: Phase transformations." Acta Materialia **57**(17): 5107-5119.

Galano, M., et al. (2015). "Nanoquasicrystalline Al-based matrix/γ-Al_2O_3 nanocomposites." Journal of Alloys and Compounds **643**: S99-S106.

Gallas, M. R., et al. (1994). "Fabrication of Transparent γ-Al_2O_3 from Nanosize Particles." Journal of the American Ceramic Society **77**(8): 2107-2112.

Guo, W., et al. (2012). "Microstructural refinement and homogenization of Mg–SiC nanocomposites by cyclic extrusion compression." Materials Science and Engineering: A **556**: 267-270.

Hall, E. (1951). "The deformation and ageing of mild steel: III discussion of results." Proceedings of the Physical Society. Section B **64**(9): 747.

Hameed, A. (2016). "Microstructural Characterisation and Mechanical Properties of an Extruded Nanoquasicrystalline Aluminium Alloy." DPhil Thesis.

Humphreys, F. (1979). "Recrystallization mechanisms in two-phase alloys." Metal Science **13**(3-4): 136-145.

Hutchinson, W. and B. Wilcox (1973). "The Influence of a Thoria Dispersion on Preferred Orientation in Nickel Alloys." Metal Science Journal **7**(1): 6-11.

Inframat Advanced Materials (2017). "http://www.advancedmaterials.us/26N-0801G.htm." **2017**.

Inoue, A. (1998). "Amorphous, nanoquasicrystalline and nanocrystalline alloys in Al-based systems." Progress in materials science **43**(5): 365-520.

Jiang, X., et al. (2014). "Extrusion textures in Al, 6061 alloy and 6061/SiCp nanocomposites." Materials Characterization **88**: 111-118.

Kalu, P. and T. McNelley (1991). "Microstructural refinement by thermomechanical treatment of a cast and extruded 6061 Al/Al_2O_3 composite." Scripta metallurgica et materialia **25**(4): 853-858.

Kamat, S., et al. (1989). "Mechanical properties of particulate-reinforced aluminum-matrix composites." Acta Metallurgica **37**(9): 2395-2402.

Kim, H. S. (2000). "On the rule of mixtures for the hardness of particle reinforced composites." Materials Science and Engineering: A **289**(1): 30-33.

Luo, H., et al. (2005). "Multi-phase nanocrystalline Al alloy with superior strength and modulus at elevated temperatures." Journal of materials engineering and performance **14**(4): 441-447.

Marsh, A. (2013). Processing of quasicrystalline aluminium matrix nanocomposites. Materials Science. University of Oxford, University of Oxford. **Part 2:** 116.

McDanels, D. L. (1985). "Analysis of stress-strain, fracture, and ductility behavior of aluminum matrix composites containing discontinuous silicon carbide reinforcement." Metallurgical transactions A **16**(6): 1105-1115.

Mishra, R. S., et al. (1996). "High‐Pressure Sintering of Nanocrystalline γ-Al_2O_3." Journal of the American Ceramic Society **79**(11): 2989-2992.

Petch, N. (1953). "The cleavage strength of polycrystals." J. Iron Steel Inst. **174**: 25-28.

Poirier, D., et al. (2010). "Fabrication and properties of mechanically milled alumina/aluminum nanocomposites." Materials Science & Engineering A **527**(29-30): 7605-7614.

Poudens, A. and B. Bacroix (1996). "Recrystallization textures in Al-SiC metal matrix composites." Scripta Materialia **34**(6): 847-855.

Rounthwaite, N. (2012). "Development of bulk nanoquasicrystalline alloys for high strength elevated temperature applications." PhD thesis, University of Oxford.

Somekawa, H., et al. (2007). "High fracture toughness of extruded Mg–Zn–Y alloy by the synergistic effect of grain refinement and dispersion of quasicrystalline phase." Scripta Materialia **56**(12): 1091-1094.

Spierings, A., et al. (2011). "Comparison of density measurement techniques for additive manufactured metallic parts." Rapid Prototyping Journal **17**(5): 380-386.

Swanson, H. E., et al. (1953). "Standard X-ray diffraction powder patterns."

Vaughan, F. (1955). "Energy changes when kaolin minerals are heated." Clay Mineral Bull **2**(13): 265-274.

Williamson, G. and W. Hall (1953). "X-ray line broadening from filed aluminium and wolfram." Acta Metallurgica **1**(1): 22-31.

7. General Discussion

7.1 The mechanisms for the alumina distribution

The γ-Al_2O_3 particle sizes and the fraction of the γ-Al_2O_3 occupied region (explained in section 5.6.2 in Chapter 5) in the matrix powder for all batches powders were plotted together in Figure 7.1. The γ-Al_2O_3 cluster sizes for the C150 batch and C200_10 were not measured, and the reasons were explained in section 5.2 in Chapter 5. It has been widely accepted that in ball milling the reinforcement particles distribute in the matrix homogeneously through flattening, cold-welding and fracturing in mechanical milling (Fogagnolo, Velasco et al. 2003, Zhang, Raynova et al. 2005). This mechanism may be suitable for the C200, C250/200 and C250_II batches powder. For the C150 batches powder, the particle sizes have no significant fluctuations, which indicates there is minor fracturing and cold welding.

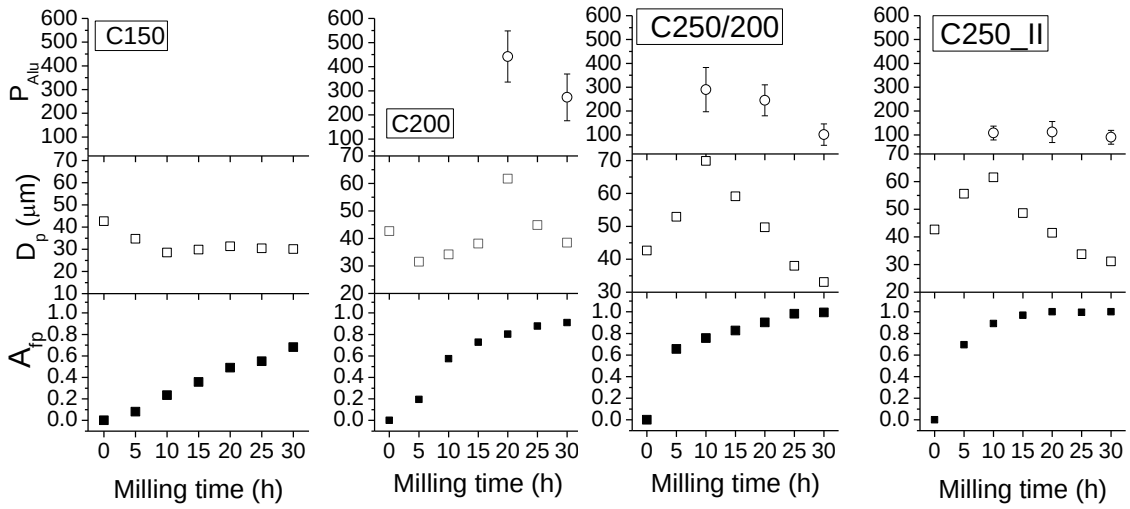

Figure 7.1: The plot of γ-Al_2O_3 cluster size (P_{alu}), peak powder particle size (D_p), and fraction particle occupied region (A_{fp}) in the matrix powder against milling time for **(a)** the C150, **(b)** the C200, **(c)** the C250/200 and **(d)** the C250_II batches of powders

7.1.1 Deformation mechanism

It has been discussed in section 5.6.1 in Chapter 5 that the low milling speed, 150 rpm, cannot cold weld and fracture the quasicrystalline aluminium powder matrix efficiently. Boey et al. (Boey, Yuan et al. 1998) milled Al-Li/SiC_p nanocomposites with Fritsch Pulverisette planetary mill at a milling speed of 150rpm for 2 hours. The matrix powders have no significant particle size changes but suffered severe deformation. This implies deformation is easier to occur compared with cold welding, as cold welding cannot occur without severe deformation (Zhang, Raynova et al. 2005), but deformation does not necessarily lead to cold-welding. However, from 0 to 30 hours of milling, the particle occupied region increased from 0% from ~68%, as shown in Figure 7.1. This implies the γ-Al_2O_3 particles were still distributed into the matrix.

Based on the focus ion beam (FIB) images in Figure 5.9, schematic diagrams were drawn in Figure 7.2. In the schematic diagrams on the left side of Figure 7.2, the spherical shapes represent the matrix powders, and the equiaxed shapes represent the brittle reinforcements. In the FIB images on the right side, the white particles are γ-Al_2O_3 and the grey particles are the nanoquasicrystalline Al matrix powder (Galano, Marsh et al. 2015). The particles highlighted with blue arrows or circles in the FIB images are the nanoquasicrystalline $Al_{93}Fe_3Cr_2Ti_2$ powder matrix, and the particles or clusters marked with red arrows are the γ-Al_2O_3 reinforcements. Stage 1 represents the powders without milling, as shown in Figure 7.2(a). In stage 2, after 5 hours of milling, γ-Al_2O_3 clusters (marked with red arrows) are attached mainly around the surfaces of the matrix powder, as shown in the FIB image in Figure 7.2(b). This stage lasts from 0 to 10 hours of milling. As shown in Figure 7.1(a), the particle sizes will decrease slightly during this period. *Varol* et al. (Varol and

Canakci 2013) claimed that the particle size decrease in the early hours of milling was because the raw powders contain some weak regions which could be easily fractured by ball collisions. In stage 3 in Figure 7.2(c), some γ-Al_2O_3 particles, marked with red arrows, are trapped in the matrix powders with concave shapes. This is probably because mechanical milling is introducing collisions from random directions, and the deformations of the matrix powders are irregular. For instance, if one particle suffered force following the black arrow direction in stage 3 in the schematic diagram in Figure 7.2(c), and then a different force from another direction, as shown with a black arrow in stage 4 in Figure 7.2(d), the matrix could trap some γ-Al_2O_3 particles inside. The stage 3 and 4 are considered to occur from 10 to 30 hours of milling. The particle highlighted by a blue circle in FIB image in Figure 7.2 (d) has a similar microstructure with the matrix powder in the schematic diagram in stage 4. *Romankov* et al. (Romankov, Hayasaka et al. 2009) tried to cold-weld the TiN particles with 50nm in diameter onto soft Al substrates. They observed a morphology very similar to the FIB image in Figure 7.2(c): the soft Al matrix was strongly deformed and the TiN particles were trapped inside.

There are also some band shape γ-Al_2O_3 particles in C150 powders after 20 hours of milling, for example, the band marked with an orange arrow, as shown in Figure 7.2(d). Since ball milling is a dynamic process, the impact energy should have a distribution instead of being a constant value (Zhang 2004). Therefore, it may still be possible for the impact energy to cold weld the powder, yet with a relative low possibility. However, since the average particle size of the C150 batch powder has no significant change, it is suspected that the frequency of cold welding is low.

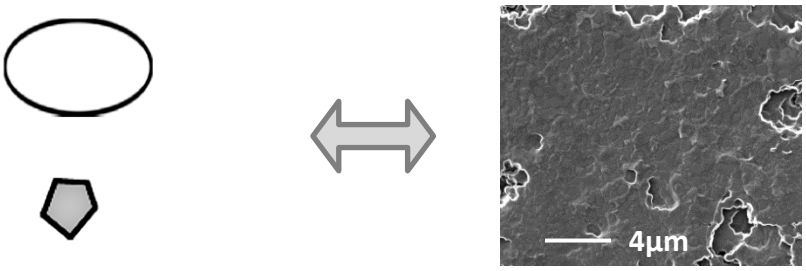

(a) Stage 1

FIB image of unmilled powder

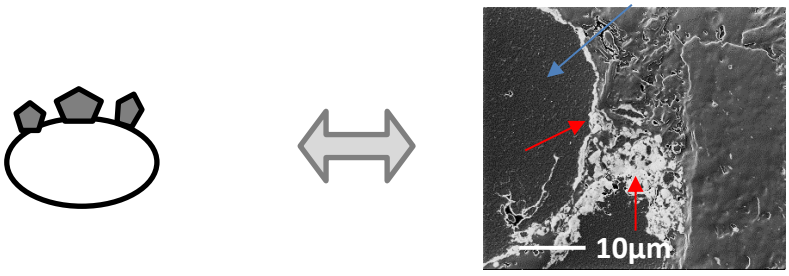

(b) Stage 2

FIB image of C150_5

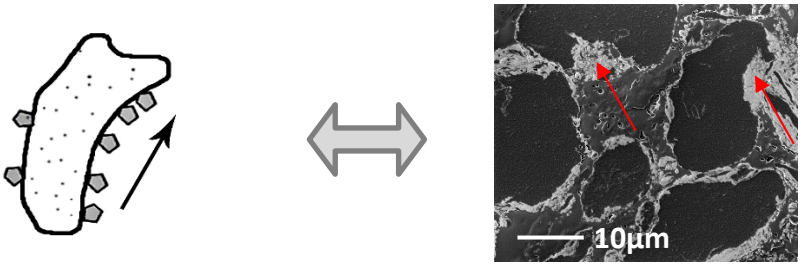

(c) Stage 3

FIB image of C150_10

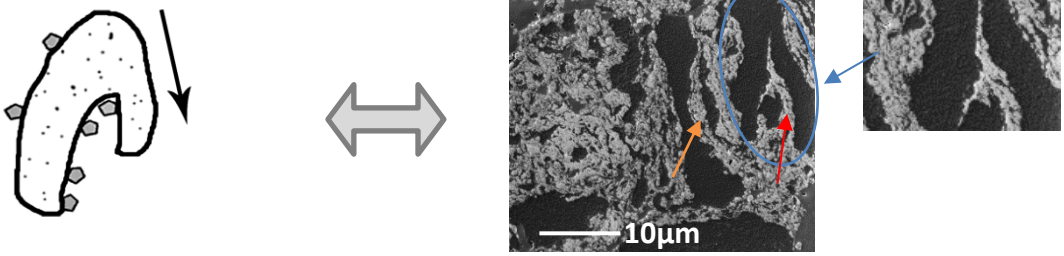

(d) Stage 4

FIB image of C150_20

Figure 7.2: Deformation mechanism in the mechanical milling process **(a)** the sketch diagram of stage 1 and the FIB image of mixed A and γ-Al_2O_3, **(b)** the sketch diagram of stage 2 and the FIB image of C150_5, **(c)** the sketch diagrams of stage 3 and the FIB image of C150_10, (d) the sketch diagram of stage 4 and the FIB image of C150_20. The inset in (d) is a zoom in image of the area in the blue circle

7.1.2 Flattening, fracturing and cold-welding mechanism

For C200, C250/200 and C250 batches, the milling mechanism matches well with the fracturing-cold welding model built up (Fogagnolo, Velasco et al. 2003), which is sketched in Figure 7.3. The FIB images of the C200 batch powder, combined with each other, are used as examples in Figure 7.3 to illustrate this mechanism. Stage 1 represents the powders before milling. In stage 2, the γ-Al_2O_3 particles smear on the surface of the matrix powder. As shown in the FIB image in Figure 7.3(a), the γ-Al_2O_3 particles labelled using a red arrow locate on the surfaces of the Al matrix particles marked with blue circles. The right bottom particle highlighted using blue circle has an elongated shape. This may come from the flattening of the powder. This stage lasts from 0 to 5 hours of milling.

In stage 3, from Figure 7.3(b), the FIB image matches well with the theoretical microstructure sketched. The lamella shape γ-Al_2O_3 bands marked by the red arrows in the FIB image are thought to be trapped in the powder by cold welding of matrix powders (Zhang 2004). Stage 4 is the most crucial step, because homogeneous structure forms through repeated cold welding and fracturing. The homogeneous distribution of reinforcement particles in nanocomposites through fracturing and cold-welding is quite common in literature (Hesabi, Simchi et al. 2006, Tousi, Rad et al. 2009, Mazaheri, Karimzadeh et al. 2010).

For the C200, C250/200 and the C250_II batches powder, the particle occupied region increases fast in early milling hours and then grow gradually. In ball milling, the random fracture keeps generating fresh surfaces of the powder and break the γ-Al_2O_3 clusters (Hussain, Oku et al. 1996). Then the fresh surfaces were cold welded together with reinforcement particles trapped inside. When the particle occupied region is high, its

growing speed is reduced due to that the fracture of the powder is less likely to occur in the particle free region of the powder[1].

[1] The particle occupied region and particle free region are defined in section 5.6.2 in Chapter 5.

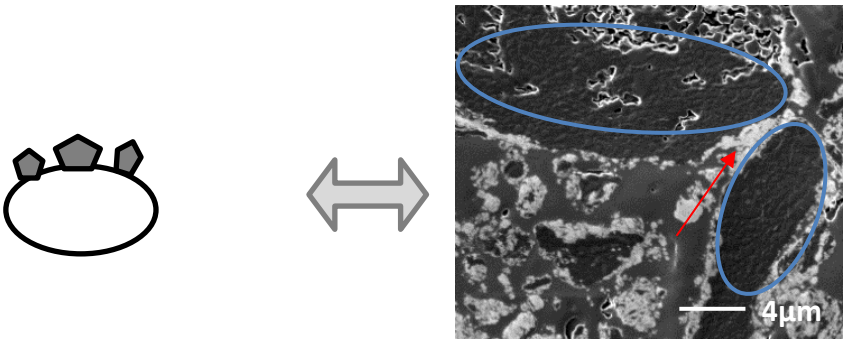

(a) Stage 1 and 2 FIB image of C200_5

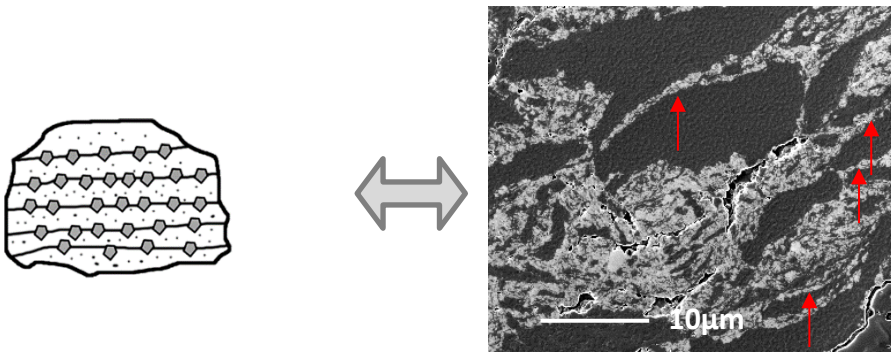

(b) Stage 3 FIB image of C200_10

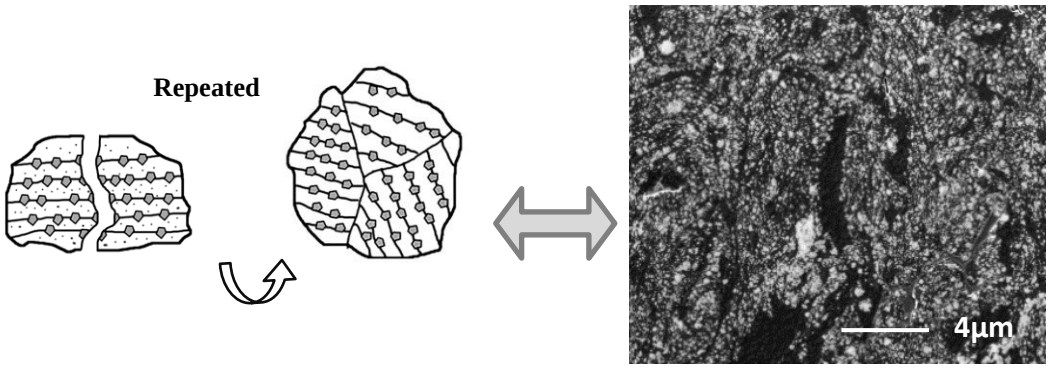

(c) Stage 4 FIB image of C200_30

Figure 7.3: Fracturing-cold welding mechanism in the mechanical milling process **(a)** the sketch diagrams of stage 1 & 2 and the FIB image of C200_5, **(b)** the sketch diagram of stage 3 and the FIB image of C200_10, **(c)** the sketch diagram of stage 4 and FIB image of C200_30

The effects of mechanical milling on the properties and microstructures of the powder were summarised in Figure 7.4. Before milling, all the batches are in stage 1. The orange, blue and red colours represent the 2nd, 3rd, and 4th stages of the milling mechanisms. The γ-Al_2O_3 clusters distribute in the matrix in lamella shape after 20, 10, 5 and 5 hours of milling for the C150, C200, C250/200 and C250_II batches, as shown in Figure 5.13, Figure 5.14 and Figure 5.15 in Chapter 5 respectively. The C150 batch does not reach a homogeneous distribution even after 30 hours of milling: about 32% of the matrix is free of γ-Al_2O_3 particles. For the C250/200, C250_II batches, homogeneous distribution of γ-Al_2O_3 are achieved after 25 and 20 hours of milling, where almost no particle free region could be detected in the powder.

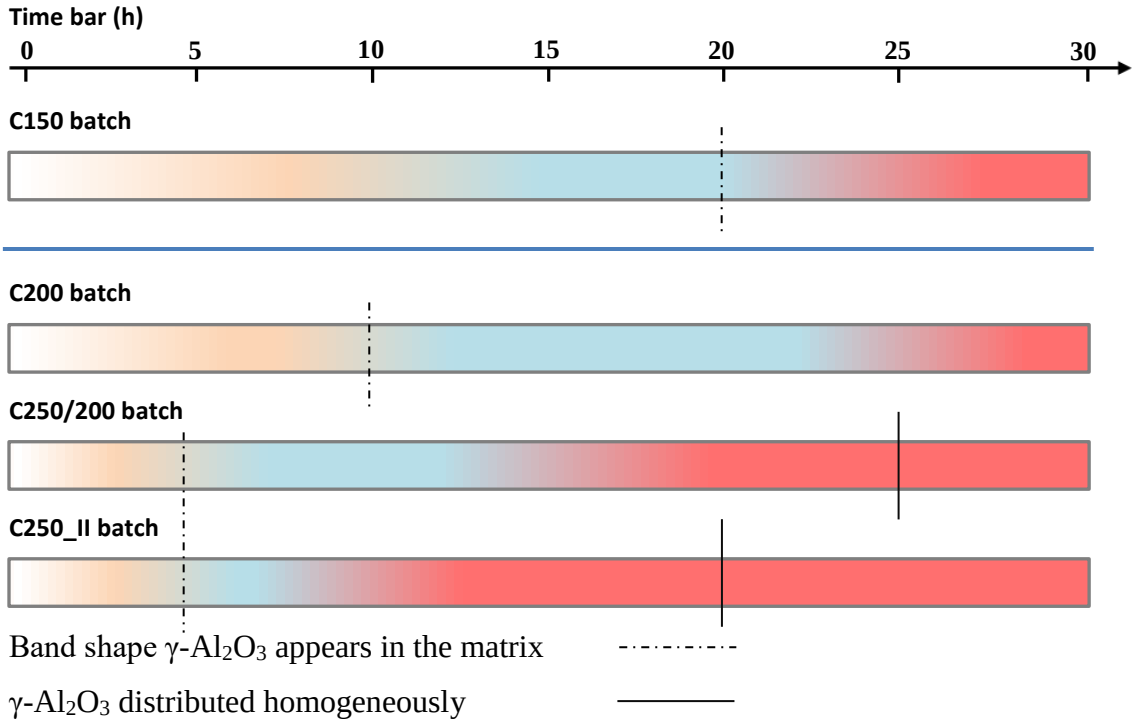

Figure 7.4: The milling stages of C150, C200, C250/200 and C250_II batches of powders. The mixed powder before milling is of stage 1. Orange, blue and red colour represent stage 2, 3 and 4 respectively.

7.2 The effects of ball milling on the Al crystallite sizes

The grain refinement of Al matrix in quasicrystalline alloy can be mainly attributed to (i) the quasicrystals act as a site for particle stimulated in nucleation (Humphreys 1977) (ii) the accumulation of local dislocations by severe deformation improves the formation of subgrains, and the subgrains convert into grains through mechanically driven grain rotation and subgrain boundary sliding (Kamrani, Simchi et al. 2007).

The particle stimulated nucleation has been observed in A250_I_3 in Figure 4.22 (d) and the mechanism has been explained in section 4.7.2 in Chapter 4. The particle stimulated nucleation requires large secondary particle sizes to occur (~400nm as discussed in Chapter 4). Therefore, when the quasicrystalline particles have been fractured into smaller pieces, the contribution of particle stimulated nucleation is limited.

The accumulation of dislocations by severe deformations can occur without hard particles (Ye, Lee et al. 2006, Poirier, Drew et al. 2010). The addition of nanosize reinforcements can increase the dislocation accumulation speed by hindering the movement of dislocations, as discussed in 4.7.2 and 5.6.4. Assuming the homogeneous distribution of reinforcements, the effectivity on the generation of the dislocations from the quasicrystalline and the γ-Al_2O_3 particles can be estimated with the equation (Dieter and Bacon 1986):

$$\lambda = \frac{4(1-f)r}{3f} \qquad \text{----------} \qquad \text{Equation 2}$$

where λ is the mean free path of a dislocation, f is the volume fraction of the particles, and r is the radius of the particles. According to Equation (2), increasing the volume fraction or decreasing the particles size can drop the dislocation mean free path and thus

cause more frequent interactions between the dislocations. The nanoquasicrystalline alloy powder contains 45% of hard quasicrystals homogeneously distributed in the matrix (Inoue and Kimura 1999). With 12.9vol.% γ-Al_2O_3 addition, the nanocomposite contains a high proportion of non-deformable particles. Based on Equation 2, such nanocomposites should have a faster grain refinement speed, compared with the ball milled nanoquasicrystalline alloy.

Table 7.1 is a summary of nanocomposite powders processed with different milling conditions. The Al crystallite sizes for the C250 batch powder after 10, 20, 25 hours of milling are 33nm, 20nm, and 14nm. The smallest crystallite size obtained for the C250 batch with 12.9vol.% γ-Al_2O_3 addition is 14nm after 25 hours of milling, lower than the crystallite size of the ball milled A250 batch powder (22nm), as shown in Table 7.1. *Ye* et al. (Ye, He et al. 2006) milled Al5083 powders as well as Al5083 with 10-25wt.% B_4C (1-7μm) reinforcement powder particles. The smallest crystallite sizes they obtained for all the batch powders are between 24nm and 26nm, as shown in Table 7.1. Similarly, *Fogagnolo* et al. (Fogagnolo, Robert et al. 2006) milled Al6061 alloy powder and Al6061/AlN composites. The milling conditions are summarised in Table 7.1. The smallest crystallite sizes they obtained is 60nm, regardless of the volume percentage of reinforcements addition. *Ye* et al. (Ye, He et al. 2006) explained that micro-size reinforcements were not small enough to provide sufficient interactions with dislocations, i.e., to act as a source of dislocations. Since the grain refinement is determined by the dislocation activity, as discussed in section 4.7.2 and section 5.6.4 in Chapter 4 and 5 respectively, and the micro-sized particles do not interact with dislocations and do not result in more dislocation, the appearance of micro-sized particles does not influence the

formation of the nanocrystalline structure in the matrix (Ye, He et al. 2006). When nanoscale reinforcements are used, the enhancement in the grain refinement for the Al matrix was interpreted with a mechanism based on the interactions between dislocations with nanosize reinforcement particles. *Chung* et al. (Chung, He et al. 2003) processed Al6061 with 1.2 vol.% AlN (2μm) reinforcement particles addition. Though the reinforcements are of micro-size level, fractures of AlN with diameters lower than 20nm were detected in TEM. These tiny particles hinder the movement of dislocations in the material, which results higher dislocation accumulations and finer crystallite sizes (Chung, He et al. 2003). The phenomenon that nanoscale reinforcements can refine the crystallite size of the matrix was also observed by *Hesabi* et al. (Hesabi, Simchi et al. 2006), as shown in Table 7.1. This could potentially explain the lower crystallite size of the C250 batch powders compared with that of the A250 batch powders.

Composition	D[1]	t(h)[1]	ω (rpm)[1]	BPR[1]	d (nm)[1]	Miller Type[2]	Ref.
A250	20-50 nm	25	250	10	22	P6	This work
C250		25	250		14		
C250		20			20		
C250		10			33		
Al5083	/	8	180	32	25.5	UPA	[1]
Al5083+10wt.%B_4C	1-7 µm				24.4		
Al5083+15wt.%B_4C					24.4		
Al5083+20wt.%B_4C					24.4		
Al5083+25wt.%B_4C					24.5		
Al6061	8.0 µm	10	700	6	60	P6	[2]
Al6061+5vol.%AlN					60		
Al6061+15vol.%AlN					60		
Ni	/	8	180	32	132	SAM	[3]
Ni+1.2vol.%AlN	2.0±1.0 µm	8			65		
Ni+5vol.%AlN		8			37		
Ni+5vol.%AlN		20			26		
Ni+5vol.%AlN		8	340		25		
Al	/	24	250	10	303	P	[4]
Al+5vol.%Al_2O_3	1.0 µm				238		
Al+5vol.%Al_2O_3	35nm				129		
Al	/	5	1200	10	110	SP	[5]
Al+1vol.%Al_2O_3	80 nm				110		
Al+2vol.%Al_2O_3					90		
Al+10vol.%Al_2O_3					180		
Al	/	16	250[3]	10	77	P5	[6]
Al+1vol.%SiC	50nm				69		
Al+3vol.%SiC					64		
Al+5vol.%SiC					63		
Al+7vol.%SiC					55		
Al+10vol.%SiC					50		

Table 7.1: The crystallite sizes of ball milled powder with different milling conditions

1. D represents the reinforcement particle size and d represents the crystallite size.

2. The mill types are listed as follows.

P6: FRITSCH Pulverisette 6 mill, UPA: Union Process 1-S attritor mill, SAM: Szegvari attritor model, P: Planetary ball mill, SP: SPEX8000

3. The rotation direction is reversed for these powders

Reference: [1] (Ye, He et al. 2006), [2] (Fogagnolo, Robert et al. 2006) [3] (Chung, He et al. 2003) [4] (Hesabi, Simchi et al. 2006) [5] (Poirier, Drew et al. 2010) [6] (Kamrani, Simchi et al. 2007)

7.3 The effects of ball milling on quasicrystals

One key objective of the current work is to maintain the quasicrystalline phase in the ball milling process. The microstructure of the nanoquasicrystalline alloy powder consists of nanoquasicrystalline icosahedral particles embedded in an FCC-Al matrix. Compared with Al matrix, the quasicrystalline particles have a limited plastic deformation capacity, which will break and decompose in ball milling processes, as discussed in section 4.7.3 and 5.6.4 in Chapter 4 and 5 respectively.

In literature, there is no study on the fractures of the quasicrystals by ball milling. However, there are a few studies showing that the micro-size or sub-microsize ceramic reinforcements are unstable in ball milling, and can be fractured into smaller pieces. *Chung* et al. (Chung, He et al. 2003) processed Al6061 with 1.2 vol.% AlN (2μm) reinforcement particles addition. Fractures of AlN with diameters lower than 20nm were detected in TEM. Similarly, *Poirier* et al. (Poirier, Drew et al. 2010) processed Al nanocomposites with Al_2O_3 (400nm) as reinforcements. After 5 hours of milling, the 400nm Al_2O_3 were broken into pieces with 80nm in diameter. Zhang et al. (Zhang, Liang et al. 2004) processed Ti_3Al/SiC composites with high energy SPEX 8000 mill and relative lower energy planetary mill. The fracture of micro-size SiC powders down to nanometre level was only observed the in the high energy SPEX 8000 mill. They suggested that fracture of micro-size particles required a relative high the impact energy than breaking the nanosize clusters. Considering hard and brittle characteristics of the quasicrystalline phase with a diameter of 400nm~1000nm, it is reasonable to claim the quasicrystals are fractured into nanosize particles distributed in the matrix during ball milling process.

The unmilled quasicrystalline $Al_{93}Fe_3Cr_2Ti_2$ powders have 45% of quasicrystal particles (Inoue and Kimura 1999). The breaking of quasicrystals adds difficulty in measuring the proportions of quasicrystals in ball milled powders using transmission electron microscope (TEM), since it is not possible to identify all the small broken pieces of quasicrystals with diffraction patterns. In the current work, the volume fraction of quasicrystals can be estimated by the enthalpy ratio between the enthalpy involved in the peak 2[2] over the total enthalpy released in the whole exothermic event, as discussed in section 4.7.3 in Chapter 4:

$$f_{NQX} = 0.45 \times \frac{E_2}{E_T} \quad \text{----------} \quad \text{Equation 1}$$

Where f_{NQX} is the fraction of the quasicrystals (0.45), E_2 is the enthalpy value of peak 2, E_T is the sum of the enthalpy values of both peak 1 and peak 2. The proportions of quasicrystals against the milling time were plotted in Figure 7.5. The powders milled at a higher rate suffered heavier quasicrystal decompositions. For the C150 and C250 powders, there is no quasicrystal decomposition after 20 and 5 hours of milling respectively. In this stage, the quasicrystals should still be able to absorb deformations from the milling process, as the milling speeds are relative low. In comparison, For C250/200, C250 and A250 powders, the quasicrystal began to decompose within 5 hours of milling due to the high impact energy.

[2] For the DSC curves with overlapping peaks, peak 1 means the peak at lower temperatures in the DSC curve, and peak 2 means the peak at higher temperatures in the DSC curve.

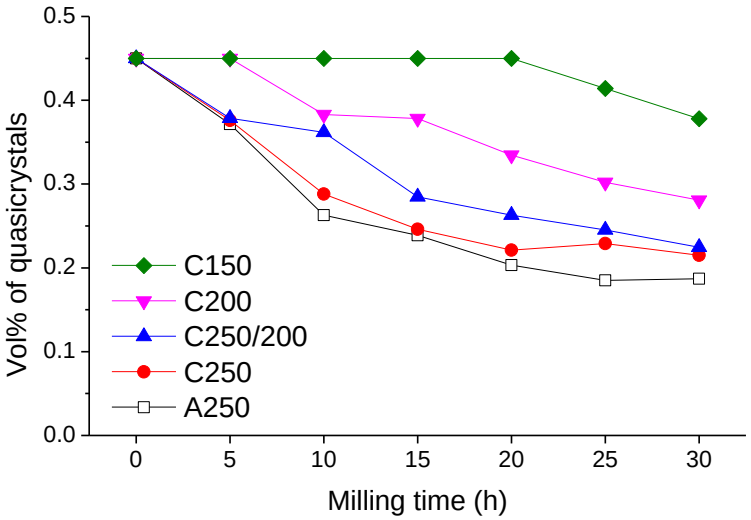

Figure 7.5: Proportions of quasicrystals in the microstructure of the C150, C200, C250/200 and C250 batches of powders

The decomposition of quasicrystals has faster rate at earlier stages of milling, and then slows down, as shown in Figure 7.5. Figure 7.6 plots the volume fraction of quasicrystals and the atom percentage of transition elements in Al grains against the milling time. As observed, the proportion of quasicrystals decreases while the atom percentage of transition elements increases with the milling time. This is because the transition elements are dissolved into the matrix during the milling, as discussed in section 4.7.3 in Chapter 4. When the concentration difference of transition elements between the quasicrystals and the Al grains decreases, the diffusion of the transition atoms is inherited (Mehrer 2007).

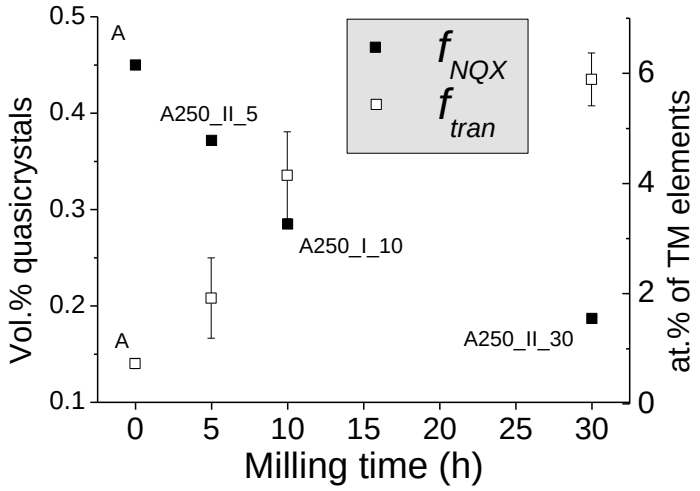

Figure 7.6: The proportions of quasicrystals against the percentage of transition atoms in the Al matrix against milling time, TM represents transition elements. The solid symbols correspond the left-Y axis and the empty symbols correspond to the right-Y axis

7.4 The strengthening mechanisms

7.4.1 Strengthening mechanism for the ball milled powder

The hardness, the crystallites and the strain values of the C150, C200, C250/200 and the C250_II batches are plotted in Figure 7.7. The microhardness increase for the C150 batch is very sluggish, and the microstructure is not homogeneous, as shown in Figure 5.8 in Chapter 5. Therefore, the C150 batch is not going to be investigated in detail in this section.

The hardness value (HV_{A0}) measured on the unmilled nanoquasicrystalline alloy powder includes the contribution of all the strengthening mechanisms related to the nanoquasicrystalline alloy microstructure features. Considering that the volume fraction and the nanosize of quasicrystal/intermetallic precipitates embedded in the

nanoquasicrystalline Al alloy do not change much in long milling hours, the strengthening contribution by the Orowan's mechanism will remain constant with the milling time (Xu, Galano et al. 2016). For high strength alloys in which the particle and grain boundaries mechanisms are the main strengthening mechanisms, the solid solution represents a minor fraction contribution (<5%) and the change in hardness during the milling process due to solid solution changes is even much lower (Leyson, Curtin et al. 2010, Pedrazzini, Galano et al. 2016). The dislocation-dislocation interaction strengthening mechanism is related with the dislocations density and therefore with the strain (Williamson and Smallman 1956). Figure 7.7 shows strain is lower than 1.5% and does not follow a clear trend, which suggests this strengthening mechanism does not contribute further to the hardness change with the milling time. From Figure 7.7, it is also observed that the Al crystallite size strongly decreases while the Vickers hardness increases during the milling from 5 to 30 hours. Finally, it is reasonable to consider that the change in hardness values with the milling time is related mainly to the Al crystallite size refining. This suggests that the increasing of the materials strength should be related to the grain boundaries strengthening mechanism (Hall 1951, Petch 1953).

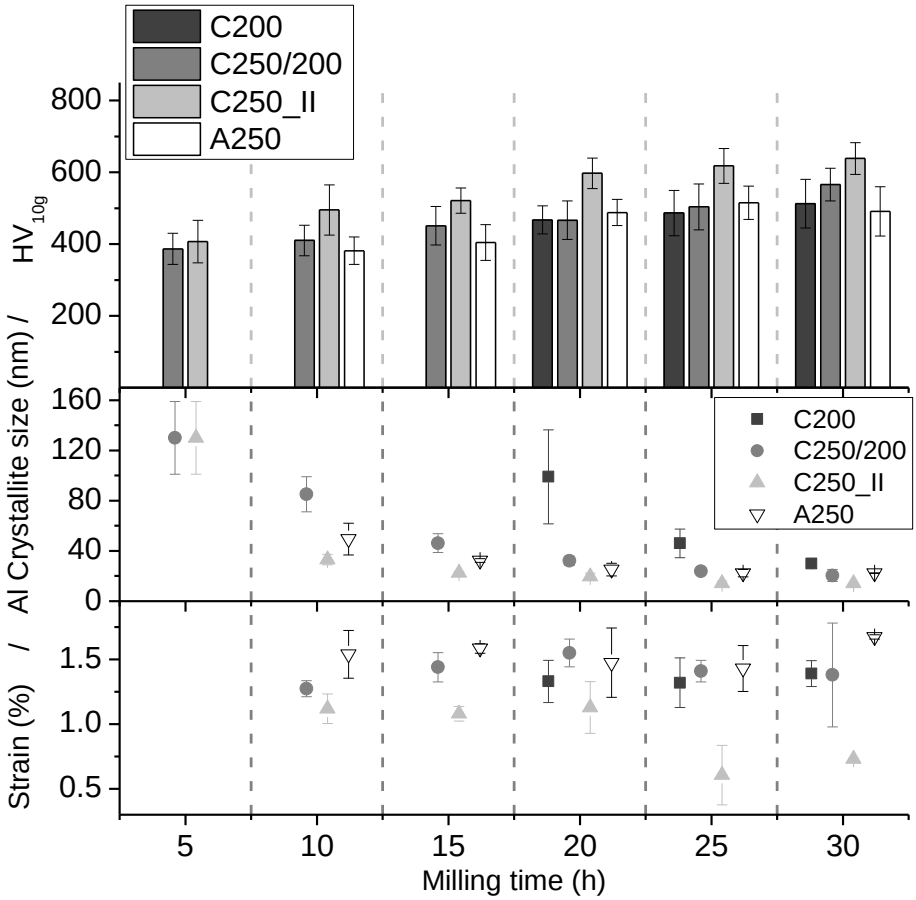

Figure 7.7: The Al crystallite size, the Al crystallite strain and the Vickers hardness values of the ball milled powders against the milling time (Xu, Galano et al. 2016).

The main hardening contributions to the nanoquasicrystalline alloy are the related to the Orowan's mechanism due to the ~45 vol.% of quasicrystals/intermetallic nano-size particles and to the grain boundaries (Hall-Petch) mechanism with an Al grain size of d_0 ~ 1 μm (Audebert, Prima et al. 2002, Galano, Audebert et al. 2009). Then, during the ball milling process, when the Al crystallites are heavily refined, the change of the hardness of the nanoquasicrystalline alloy (A250) will follow a Hall-Petch type relationship as a function of the Al crystallite size. A general expression of hardening as a consequence of the crystallite refining is normally written as:

$$\boldsymbol{H = H_0 + \frac{k}{d^p}} \quad \text{----------} \quad \text{Equation 2}$$

Where H is the hardening due to the crystallite size (d), H_0 is the lattice frictional stress, k is a constant known as "locking parameter", which measures the relative hardening contribution of the grain boundaries (Dieter and Bacon 1986), and p is a constant exponent. This exponent was suggested as $p = 0.5$ by the early works of *Hall* (Hall 1951) and *Petch* (Petch 1953). Deviations of this value have been theoretically proposed and experimentally found in the literature. Very early works by *Mathewson* in 1919 and *Bragg* in 1942 postulate that strength due to the crystallite size is proportional to $d^{-0.25}$ and d^{-1}, respectively (Bragg 1942, Mathewson 1991). Theoretical estimations in the literature for the p value also suggested values as: 1.0, 0.5, 0.33, and 0.25. Each of these values for p is based on different mechanisms and/or models for dislocation-grain boundary interactions. For example, the more common value, $p = 0.5$, is normally related to dislocations pile up at the grain boundaries; and $p = 0.25$ was also found by *Conrad* considering a dislocation forest hardening concept (Conrad 1963, Hirth 1972). Several models considering different dislocation-grain boundaries interactions, crystallite size ranges, boundaries features as porosity and impurities, solute diffusivity, dislocation sources have been proposed leading to different p values and even different complex equations as a function of the crystallite size (Cordero, Knight et al. 2016). The ball milling process introduces several physical changes in the Al lattice and grain boundaries that make it extremely difficult to build up a theoretical approach to propose an equation that accurately describes the hardening mechanism related to the crystallite refining experimentally observed. Thus, the experimental results obtained from the milled alloy and composite powder were fitted following the simple Equation 2, finding an exponent $p = 0.25$ for the best lineal

correlation between measured H values and $\frac{1}{d^p}$, as can be seen in Figure 7.8 for the alloy powder (a) and the composite powder (b). The lineal correlation following a Hall-Petch type relationship suggests that during the milling process of the alloy and the composite the hardening is mainly controlled by the crystallite refining, as was deduced above. Therefore, it is reasonable to suggest that the change of hardness respect to the initial hardness of the unmilled powder can be represented by $\frac{k}{d^p}$. Finally, the hardness value of the milled alloy powder after x hours of milling, H_{Ax}, can be estimated using Equation 3:

$$\boldsymbol{H_{Ax} = (H_{A0} - \frac{kA}{\frac{1}{d_0^4}}) + \frac{kA}{\frac{1}{d_x^4}}} \qquad \text{---------} \quad \text{Equation 3}$$

Where k_A is the "locking parameter" for the alloy, and H_{A0} is the microhardness value of the unmilled nanoquasicrystalline Al-Fe-Cr-Ti alloy powder (measured as 132±10 HV_{10g}) that includes the Al lattice frictional stress, the effects of solutes in the Al solid solution, quasicrystal/intermetallic particles hardening, grain boundaries hardening and other minor contributions. Thus, in order to count only the constant hardening contributions of the microstructure of the milled powders, the grain boundaries contribution for the initial Al grain size (d_0) must be subtracted as: $\frac{kA}{\frac{1}{d_0^4}}$ from H_{A0}. d_x is the Al crystallite size after x hours of milling, which is the main observed microstructural feature that changes during the ball milling process in the nanoquasicrystalline alloy powder. For the unmilled alloy powder, when $d_x = d_0$ Equation 3 provides a hardness value equal to the measured hardness of the unmilled alloy powder, H_{A0}.

For the composite powders, because of the addition of the nano γ-Al_2O_3 particles, other strengthening contributions must be considered. Numerous theoretical models have been developed to correlate the mechanical behaviour of metal matrix composites with their microstructural characteristics. These models might be grouped into three general categories: (1) load transfer models, (2) matrix strengthening models and (3) hybrid models.

(1): The load transfer models

The load transfer models were developed on the basis that the hard, relatively undeformable reinforcements, may carry more load than the relatively soft matrix (Eshelby 1957, Nardone and Prewo 1986, Kim 2000). In this group is included the simplest and well know rule of mixtures (ROM) (Kim 2000), which is characterised for a mathematical expression which gives the homogeneous property of a heterogeneous materials in terms of the properties, quantity and arrangement of its constituents. This model weights the volume average of the component properties in isolation without considering any interactions between reinforcements and matrix. See Equation 4 as applicable for the composite's hardness:

$$\boldsymbol{H_C = H_A(1 - f) + H_r f} \quad \text{----------} \quad \text{Equation 4}$$

where H_C, H_A, H_r are the hardness values for the composite, the matrix alloy and the reinforcement, respectively. f is the volume fraction of reinforcements.

(2): The matrix strengthening models

In the matrix strengthening models, the strengthening effect has been attributed to various microstructural changes experienced by the matrix as a result of the presence of

reinforcement particulates (Poirier, Drew et al. 2010). For example, the stress increment resulting from the difference of the thermal expansion coefficient of matrix and reinforcement when the nanomaterial process involves temperature changes; an increase in strengthening by Orowan's mechanism when the reinforcements are located inside of the matrix grains.

(3): Hybrid model

Other authors proposed hybrid models that combine both approaches of load transfer and effects of the matrix microstructural changes due to the reinforcements addition (Wu and Lavernia 1992, Ramakrishnan 1996, Scudino, Liu et al. 2009).

In the present work, we adopt a hybrid model to evaluate the hardness change with the ball milling time of a composite powder using the Equation 5:

$$\boldsymbol{H_{Cx} = [(H_{A0} - \frac{kc}{\frac{1}{d_0^4}}) + \frac{kc}{\frac{1}{d_x^4}}](1 - f) + H_r f} \quad \text{--------} \quad \text{Equation 5}$$

where H_{Cx} is the hardness of the nanocomposite after x hours of milling, k_C is the "locking parameter" for the composite, f is the volume fraction of the γ-Al_2O_3 reinforcement (12.9%), and H_r is the hardness value of the reinforcement (γ-Al_2O_3 with an average value taken from literature as 730 Kg/mm^2) (Chou, Nieh et al. 1991, Gallas, Hockey et al. 1994, Mishra, Lesher et al. 1996). When no reinforcement is added to the powder alloy (f = 0) Equation 5 becomes Equation 3 giving the hardness values for the milled alloy powders. Equation 5 predicts a theoretical hardness value of the unmilled composite of H_{C0} = 209 kg/mm^2 by the application of the simple rule of mixtures.

It is worth mentioning that in composite systems where the reinforcement particle is much harder than the matrix or the volume fraction of the reinforcement is low, the ROM as given in Equation 4 may not predict the actual hardness of the composite due high plastic deformation around the hard particles that produce a zone of high dislocations density (Kim 2000). For example, for the Ag-Al_2O_3 composites, with a very soft Ag matrix, the experimental values of the hardness are almost the same up to 50 vol.% Al_2O_3 (Greer 2001). However, in the literature, for mechanical milled aluminium composites with about 10-20% volume fraction of ceramic reinforcement particles, the experimental results match the value estimated by the rule of mixtures (Li, Zhao et al. 2009, Mazaheri, Karimzadeh et al. 2010). Equation 5 combines Equation 3 and the rule of mixtures (Equation 4). The mechanical milling and alumina content affects the microstructure of the nanoquasicrystalline Al alloy matrix of the composite. As discussed above in section 7.2, the main observed microstructural features that change with the milling time in the composite are the refining of the Al crystallites in the matrix and a continued homogenisation of alumina distribution. The effect on the alloy matrix introduced by the γ-Al_2O_3 reinforcement is represented in the Equation 5 by the term: $\frac{kc}{d_x^p}(1-f)$ were f considers the quantity of reinforcement in the composite, d_x the size of the crystallite size in the matrix alloy, and the exponent $p = 0.25$, which in this work was obtained by fitting the hardness and Al crystallite size measured on the milled powders. This p value matches with the early model proposed by *Conrad and Hirth* (Conrad 1963, Hirth 1972) that consider a dislocation forest hardening concept. Moreover, the parameter k_C that was fitted for the composite powder is different than the one for the alloy powder (k_A). The "blocking parameter", k, is associated with the stress required to extend dislocations activity into

nearby grains and is very sensitive to the composition of the alloy and composites (Dieter and Bacon 1986, Hayes, Witkin et al. 2004, Vojtěch, Verner et al. 2007, Choi, Lee et al. 2008, Shanmugasundaram, Heilmaier et al. 2010). For example, when adding 4 wt.% of Cu to the pure Al, the k value resulted more than 2 times of the one corresponding to the nanocrystalline pure Al (Choi, Lee et al. 2008, Shanmugasundaram, Heilmaier et al. 2010). In the present work, considering that some γ-Al_2O_3 nanoparticles would be distributed at the Al grain boundaries in the alloy matrix, the hardening behaviour in the alloy and in the composite powders would be different, which lead to different k values that measures the properties of the grain boundaries as a sink and source of dislocations (Li, Ohmura et al. 2005).

In Figure 7.8(a) the slope of the linear fitting for the milled alloy powder resulted as k_A = 1463±183 $kg/mm^2 \cdot nm^{1/4}$ (2551± 319 $MPa \cdot \mu m^{1/4}$). The k_C value for the milled composite powders was also fitted linearly as can be observed in Figure 7.8(b) taken the data for all the composite powder batches, finding a value of the slope as: $k_C(1-f)$ = 938±122 $kg/mm^2 \cdot nm^{1/4}$. Thus, k_C = 1077±140 $kg/mm^2 \cdot nm^{1/4}$ (1878±244 $MPa \cdot \mu m^{1/4}$), which is lower than the obtained for the milled alloy powders showing the effect of the γ-Al_2O_3 nanoparticles on the Al grain boundaries of the alloy matrix.

The values estimated from the linear fitting for the alloy data have larger errors, probably due to the limited number of samples in comparison with the data obtained for the composite powders. The data for the alloy and the composite were statistically evaluated by means of the Chauvenet's criterion (Bevington and Robinson 2003) and only one data point for the alloy has not been taken into account in the fitting; the one corresponded to the A250_15 sample (crossed in Figure 7.8 (a)).

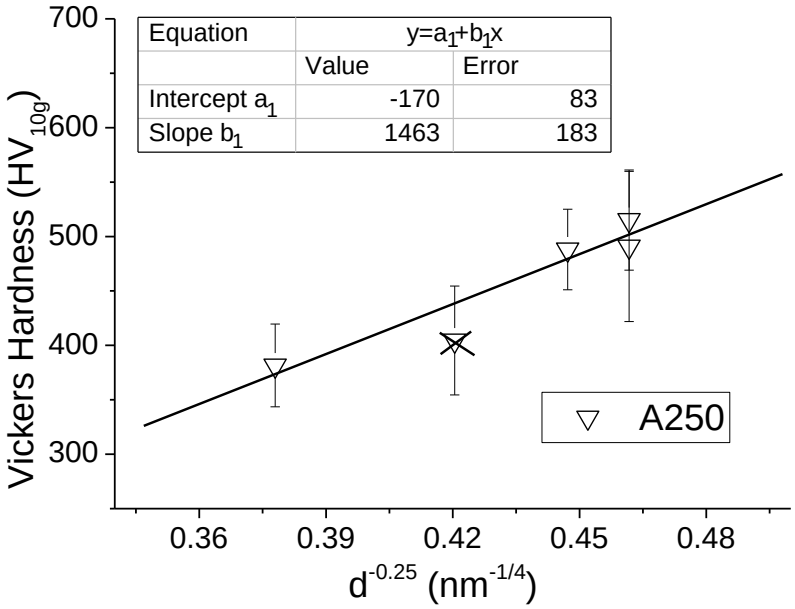

(a)

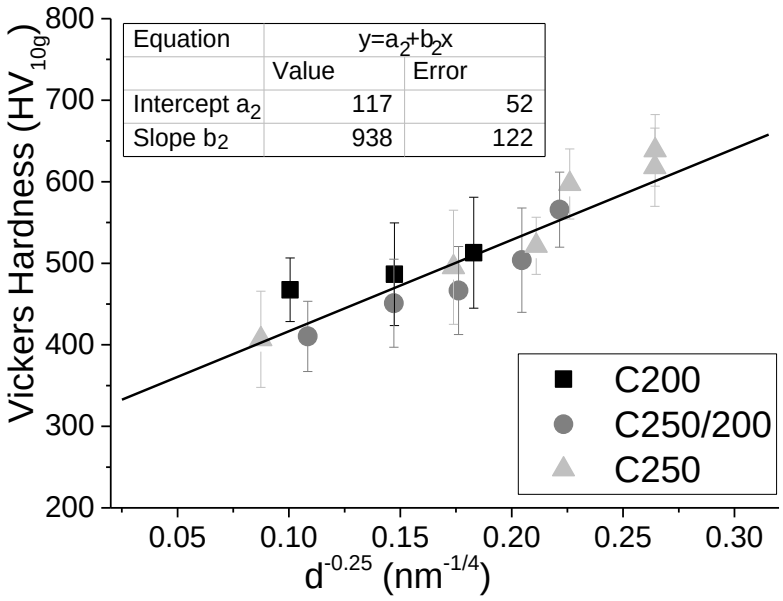

(b)

Figure 7.8: The linear fit model for the **(a)** milled alloy and **(b)** nanocomposite powders. The measured Vickers hardness against d-0.25 (d: Al crystallite size) (Xu, Galano et al. 2016)

The application of the Equations 3 and 5 to predict the hardness value of the milled nanoquasicrystalline Al-Fe-Cr-Ti alloy and for it composites containing 12.9 vol.% γ-Al_2O_3 (20-50 nm) powders provided hardness values slightly lower but inside the error of the measured hardness values.

The hardness values obtained for the nanoquasicrystalline Al-Fe-Cr-Ti alloy matrix/γ-Al_2O_3 particles nanocomposite powders are very high in comparison with the ones found in the literature, which are summarised in Table 2. This can be explained because of the large volume fraction of the quasicrystal nanoparticles embedded in fcc-Al phase, obtained by rapid solidification, produces a high strength alloy which can transfer load to the hard γ-Al_2O_3 reinforcements more efficiently than softer Al-based commercial alloys.

Composite	**d**	**HV**	**Reference**
NQX(25-50μm) + 12.9vol.% γ-Al_2O_3 (20-50nm)	14nm	638±44 HV_{10g}	This work
NQX(25-50μm) + 8.5vol.% γ-Al_2O_3 (20-50nm)	33nm	542±9 HV_{10g}	(Galano, Marsh et al. 2015)
EN AW-2017 Al alloy (100μm) + 15vol.% Al_2O_3 (22μm)	49nm	329±26 HV_{100g}	(Ozdemir, Ahrens et al. 2008)
Al(325mesh) + 10vol.% Al_2O_3(4nm)	90nm	166±4 HV_{50g}	(Poirier, Drew et al. 2010)

Table 7.2: The Al crystallite size and hardness values of ball milled composite powders in literature. NQX is the abbreviation of the nanoquasicrystalline Al alloy

7.4.2 Strengthening mechanisms for the extruded bar

Previous studies on nanoquasicrystalline Al-Fe-Cr-Ti showed that the main mechanisms for the high yield strength were the presence of nanoparticles (quasicrystals and intermetallics) (Audebert, Prima et al. 2002, Vojtěch, Verner et al. 2007, Galano, Audebert et al. 2009), the supersaturations of elements in solid solution (Audebert, Prima et al. 2002, Vojtěch, Verner et al. 2007, Galano, Audebert et al. 2009) and the submicron grain size(Audebert, Prima et al. 2002, Galano, Audebert et al. 2009). For the nanocomposites, the conventional models used in particulate composite strengthening were load transfer, Orowan strengthening and thermal mismatch (Li, Zhao et al. 2009, Poirier, Drew et al. 2010).

For the extruded $Al_{93}Fe_3Cr_2Ti_2$ nanocomposites, the microstructure is complex. The precipitation of the intermetallics and a homogeneous distribution of nanosize γ-Al_2O_3 clusters are observed in the matrix. Among all the mechanisms listed, the strengthening may come from (1) direct strengthening through rule of mixture, (2) the grain refinement (3) the Orowan strengthening from the intermetallic particles and reinforcement particles, (4) thermal mismatch since γ-Al_2O_3 and the Al matrix have different thermal expansion, (5) solid solution strengthening from the transition elements dissolved in the matrix.

Rule of mixture

In the extruded $Al_{93}Fe_3Cr_2Ti_2$ alloy, γ-Al_2O_3 particles distribute in the matrix homogeneously. The load transfer model, known as the continuum approach, is based on the load sharing between the matrix and the reinforcement (Poirier, Drew et al. 2010). Load transfer model has been used for estimating the mechanical properties by a variety of studies (Kok 2005, Li, Zhao et al. 2009, Poirier, Drew et al. 2010).

In the current work, the rule of mixture was used for the load transfer model (Kim 2000):

$$\boldsymbol{\sigma = \sigma_0(1 - f) + \sigma_r f} \qquad \text{---------} \qquad \text{Equation 6}$$

Where σ is the ultimate strength of the composites, σ_0 is the ultimate strength of the matrix alloy and σ_r is the strength of the γ-Al_2O_3 reinforcement, which is equal to 1432MPa (Muller, Seeger et al. 2014). For the matrix alloy, σ_0 should be different from quasicrystalline $Al_{93}Fe_3Cr_2Ti_2$ alloy extruded by other researchers, since the quasicrystalline phase of the E sample has been decomposed into intermetallics. *Luo* et al. (Luo, Shaw et al. 2005, Luo, Zhang et al. 2005) extruded ball milled $Al_{93}Fe_3Cr_2Ti_2$ alloy powder with crystalline elemental powders. The material they processed had $Al_{13}Fe_4$ and Al_3Ti locating intergranularly in the Al grains with a grain size of 80nm. Since the transition element components, the microstructure and the processing routines are very close to the extruded bar in this work, it is expected the σ_0 (ultimate tensile strength of the matrix in sample E) is similar to the ultimate tensile strength of the bar processed by *Luo* et al. (670MPa). The ultimate tensile strength σ estimated with Equation 6 is 768MPa, relative lower than the tested compression strength 925MPa.

Grain refinement:

A general relationship between yield stress and grain size was proposed by Hall (Hall 1951) and extended by Petch (Petch 1953) based on the dislocation pile-up model.

$$\boldsymbol{\Delta\sigma_g = \frac{k}{d^{1/2}}} \qquad \text{----------} \qquad \text{Equation 7}$$

where $\Delta\sigma_g$ is the increased strength by grain refinement, k is a constant relevant to the composition of the sample and d is the grain size. Vojtěch et al. (Vojtěch, Verner et al.

2007) found it was suitable to use 171MPa $\mu m^{1/2}$ for Al-TM[3] alloys as the k value, coming from a similar Al-5Cr-2Zr system (Brahmi, Gerique et al. 1997). d value was 97nm, measured in TEM. The increased strength using the grain refinement model was calculated to be 549MPa.

Orowan strengthening:

Orowan strengthening comes from the resistance of closely spaced hard particles to the passing of dislocations. In the micro-sized particulate-reinforced metal matrix composites, the reinforcement particles are large and the interparticle spacing is large. Therefore, the contribution of Orowan strengthening is neglectable (Lloyd 1994). It has been found that 1% of dispersed nanosized reinforcement particles (~50nm) in a metal matrix can enhance the mechanical property significantly (Kang and Chan 2004), due to the fact that dislocations need to bypass the Orowan bowings (Clyne and Withers 1995, Zhang and Chen 2006), as discussed in section 2.4.2 in Chapter 2. The Orowan looping model can be calculated with the Ashby-Orowan equations (Brown and Ham 1971):

$$\Delta\boldsymbol{\sigma_p} = \boldsymbol{M}\frac{\mathbf{0.4}\boldsymbol{Gb}}{\boldsymbol{\pi}(\mathbf{1}-\boldsymbol{\upsilon})^{\mathbf{1/2}}}\frac{\ln(\frac{\boldsymbol{D_{p,s}}}{\boldsymbol{b}})}{\boldsymbol{\lambda_s}} \quad \text{--------} \quad \text{Equation 8}$$

where $\Delta\sigma_p$ is the particle strengthening contribution value, M is the Taylor factor equal to 3.07 for polycrystalline untextured fcc material (Abbaschian and Reed-Hill 2008), G is the shear modulus 26.4GPa (Poirier, Drew et al. 2010), b is the Burger vector (0.286nm), υ is the Poisson's ratio 0.33 (Köster and Franz 1961), λ_s is the interparticle spacing (464±148nm calculated with STEM images, as explained in 6.4), and $D_{p,s}$ is the mean

[3] TM: transition elements

planar particle diameter which is $\sqrt{2/3}$ times the average particle radius (348±87nm calculated with STEM images, as explained in section 6.4 in Chapter 6). $\Delta\sigma_p$ is calculated to be 54MPa. However, in literature, it is suspected the Orowan mechanism will have effect only when the nanoparticles locate inside the grains (Li, Zhao et al. 2009). As shown in the TEM images in Figure 6.15 in Chapter 6, a large number of intermetallics locate on the grain boundaries. In this case, the $\Delta\sigma_p$ should be less than the estimated value 54MPa. Li et al. suggested (Li, Zhao et al. 2009) a better way for estimating the contribution of Orowan strengthening mechanism should be first randomly selected a number of grains, and then calculate the dispersed particle number and sizes in each grain.

Thermal mismatch:

The difference in the coefficients of thermal expansion between the matrix and reinforcing particles, accompanied with the temperature change in the course of processing, can cause plastic strain in the matrix around the particles, which results a surge of the dislocation density (Arsenault and Shi 1986). Thermal mismatch was modelled using Arsenault equation (Arsenault and Shi 1986) based on the assumption that the reinforcements are of cubic shape. For estimating the dislocation density, an ideal way should be using high resolution transmission electron microscope (HRTEM) to get a number of images in atom resolution. The density can be calculated by counting the numbers in a number of selected locations (Li, Zhao et al. 2009). In this work, the dislocation density is roughly estimated by(Arsenault and Shi 1986, Poirier, Drew et al. 2010):

$$\boldsymbol{\rho = \frac{12 f \varepsilon_{ther}}{b(1-f)t}} \qquad \text{----------} \qquad \text{Equation 9}$$

where b is the Burger's vector, 0.287nm (Kashyap, Ramachandra et al. 2000), t is the reinforcement size assuming the particles are cubic, f is the volume fraction of the sample and ρ is the dislocation density. ε_{ther} is the thermal strain, assuming to be equal to 0.24±0.03% calculated with the Williamson plot in X-ray diffractogram.

The yield strength of the nanocomposite would be (Arsenault and Shi 1986):

$$\Delta\boldsymbol{\sigma} = \boldsymbol{\alpha G \rho^{1/2} b} \qquad \text{----------} \qquad \text{Equation 10}$$

where $\Delta\sigma$ is the increase yield strength, α is a factor equals to about 1 (Li, Zhao et al. 2009), and G is the shear modulus for aluminium (26.4 GPa) (Poirier, Drew et al. 2010). $\Delta\sigma$ is calculated to be 50MPa. For an accurate analysis of thermal mismatch strengthening, HRTEM imaging is needed.

Solid Solution Strengthening:

Strength from solid solution hardening comes from strain fields around each solute atom (Neuhäuser and Schwink 1993). *Vojtěch* et al. suggested that the solid solution strengthening mechanism could be negligible for an $Al_{92.4}Fe_{1.2}Cr_{3.3}Ti_{2.4}Si_{0.7}$ alloy extruded at 450°C. Solid solution always precipitates into intermetallics during the extrusion (Stan-Głowińska, Lityńska-Dobrzyńska et al. 2017). In the current work, the transition elements were not detected in the Al grains in the extruded bar, as explained in Figure 6.15 in Chapter 6. This implicates the solutions strengthening should be minor for the current $Al_{93}Fe_3Cr_2Ti_2$ nanocomposites. Therefore, the contribution to the strength from the solid solution strengthening was not measured in this work.

7.5 Conclusion

For the quasicrystalline $Al_{93}Fe_3Cr_2Ti_2$ nanocomposites milled at 150rpm, the reinforcements were mainly milled into the powder by the deformation of the matrix powder. When the milling speed is increased to 200rpm or 250rpm, the collisions of the ball could cold-weld and fracture the powder efficiently. Therefore, there is an increasing and decreasing trend for the particle sizes of the matrix powders. The reinforcement particles were milled into the matrix powder by cold-welding and distributed homogeneously after repeated cold-welding and fracturing.

The quasicrystalline particles refine the grain size with particle stimulated nucleation, while the γ-Al_2O_3 with 20-50nm in diameter mainly help refining the crystallite size by hindering the movement of dislocations. The quasicrystals were broken and decomposed during ball milling process due to their limited plastic deformation capacity. The higher the milling speed, the faster the decomposition rate. For nanoquasicrystalline nanocomposite powder milled at 250rpm, the volume fraction of quasicrystals dropped from 45% to 21% after 30 hours of milling.

The hardness of the nanoquasicrystalline Al alloy powder is mainly controlled by the refining of the Al crystallite size during the milling process. Thus, the hardness change of the milled nanoquasicrystalline Al alloy powder can be estimated by a simple Hall-Petch type relationship with an exponent of 0.25 in accordance of early models based on dislocation forest hardening concept. The hardness change of the ball milled nanocomposite powder can be estimated by a hybrid model that combines a Hall-Petch type relationship with an exponent of 0.25 and the rule of mixtures.

For the extruded bar, the strength estimated with a load transfer model using the rule of mixture is 768MPa, lower than the tested compressive yield stress 925MPa. The contribution of grain refinement is about 549MPa, estimated using the Hall-Petch equation. HRTEM imaging is required for an accurate quantification of the contribution of Orowan strengthening and thermal mismatch strengthening mechanism.

7.6 Reference

Abbaschian, R. and R. E. Reed-Hill (2008). Physical metallurgy principles, Cengage Learning.

Arsenault, R. and N. Shi (1986). "Dislocation generation due to differences between the coefficients of thermal expansion." Materials Science and Engineering **81**: 175-187.

Audebert, F., et al. (2002). "Structural characterisation and mechanical properties of nanocomposite Al-based alloys." Materials Transactions **43**(8): 2017-2025.

Bevington, P. R. and D. K. Robinson (2003). "Data reduction and error analysis." McGraw-Hill.

Boey, F., et al. (1998). "Mechanical alloying for the effective dispersion of sub-micron SiC p reinforcements in Al–Li alloy composite." Materials Science and Engineering: A **252**(2): 276-287.

Bragg, W. (1942). "A theory of the strength of metals." Nature **149**: 511-513.

Brahmi, A., et al. (1997). "Flow stress of rapidly solidified Al-5Cr-2Zr alloy as a function of processing variables." Scripta Materialia **37**(11): 1623-1629.

Brown, L. and R. Ham (1971). "Dislocation-particle interactions." Strengthening methods in crystals: 9-135.

Choi, H. J., et al. (2008). "Tensile behavior of bulk nanocrystalline aluminum synthesized by hot extrusion of ball-milled powders." Scripta Materialia **59**(10): 1123-1126.

Chou, T., et al. (1991). "Microstructures and mechanical properties of thin films of aluminum oxide." Scripta metallurgica et materialia **25**(10): 2203-2208.

Chung, K. H., et al. (2003). "Mechanisms of microstructure evolution during cryomilling in the presence of hard particles." Materials Science and Engineering: A **356**(1): 23-31.

Clyne, T. and P. Withers (1995). An introduction to metal matrix composites, Cambridge university press.

Conrad, H. (1963). "Effect of grain size on the lower yield and flow stress of iron and steel." Acta Metallurgica **11**(1): 75-77.

Cordero, Z., et al. (2016). "Six decades of the Hall–Petch effect–a survey of grain-size strengthening studies on pure metals." International Materials Reviews **61**(8): 495-512.

Dieter, G. E. and D. J. Bacon (1986). Mechanical metallurgy, McGraw-Hill New York.

Eshelby, J. D. (1957). The determination of the elastic field of an ellipsoidal inclusion, and related problems. Proceedings of the Royal Society of London A: Mathematical, Physical and Engineering Sciences, The Royal Society.

Fogagnolo, J., et al. (2006). "Mechanically alloyed AlN particle-reinforced Al-6061 matrix composites: Powder processing, consolidation and mechanical strength and hardness of the as-extruded materials." Materials Science and Engineering: A **426**(1): 85-94.

Fogagnolo, J., et al. (2003). "Effect of mechanical alloying on the morphology, microstructure and properties of aluminium matrix composite powders." Materials Science and Engineering: A **342**(1): 131-143.

Galano, M., et al. (2009). "Nanoquasicrystalline Al–Fe–Cr-based alloys. Part II. Mechanical properties." Acta Materialia **57**(17): 5120-5130.

Galano, M., et al. (2015). "Nanoquasicrystalline Al-based matrix/γ-Al_2O_3 nanocomposites." Journal of Alloys and Compounds **643**: S99-S106.

Gallas, M. R., et al. (1994). "Fabrication of Transparent γ-Al_2O_3 from Nanosize Particles." Journal of the American Ceramic Society **77**(8): 2107-2112.

Greer, A. L. (2001). "Partially or fully devitrified alloys for mechanical properties." Materials Science & Engineering A **s 304–306**(1): 68-72.

Hall, E. (1951). "The deformation and ageing of mild steel: III discussion of results." Proceedings of the Physical Society. Section B **64**(9): 747.

Hayes, R., et al. (2004). "Deformation and activation volumes of cryomilled ultrafine-grained aluminum." Acta Materialia **52**(14): 4259-4271.

Hesabi, Z. R., et al. (2006). "Structural evolution during mechanical milling of nanometric and micrometric Al_2O_3 reinforced Al matrix composites." Materials Science and Engineering: A **428**(1): 159-168.

Hirth, J. P. (1972). "The influence of grain boundaries on mechanical properties." Metallurgical Transactions **3**(12): 3047-3067.

Humphreys, F. (1977). "The nucleation of recrystallization at second phase particles in deformed aluminium." Acta Metallurgica **25**(11): 1323-1344.

Hussain, M., et al. (1996). "Effects of wet ball-milling on particle dispersion and mechanical properties of particulate epoxy composites." Materials Letters **26**(3): 177-184.

Inoue, A. and H. Kimura (1999). "High elevated-temperature strength of Al-based nanoquasicrystalline alloys." Nanostructured Materials **11**(2): 221-231.

Kamrani, S., et al. (2007). "Effect of reinforcement volume fraction on mechanical alloying of Al–SiC nanocomposite powders." Powder Metallurgy **50**(3): 276-282.

Kang, Y.-C. and S. L.-I. Chan (2004). "Tensile properties of nanometric Al_2O_3 particulate-reinforced aluminum matrix composites." Materials chemistry and physics **85**(2): 438-443.

Kashyap, K., et al. (2000). "Role of work hardening characteristics of matrix alloys in the strengthening of metal matrix composites." Bulletin of Materials Science **23**(1): 47-49.

Kim, H. S. (2000). "On the rule of mixtures for the hardness of particle reinforced composites." Materials Science and Engineering: A **289**(1): 30-33.

Kok, M. (2005). "Production and mechanical properties of Al_2O_3 particle-reinforced 2024 aluminium alloy composites." Journal of Materials Processing Technology **161**(3): 381-387.

Köster, W. and H. Franz (1961). "Poisson's ratio for metals and alloys." Metallurgical Reviews **6**(1): 1-56.

Leyson, G. P. M., et al. (2010). "Quantitative prediction of solute strengthening in aluminium alloys." Nature materials **9**(9): 750-755.

Li, J., et al. (2005). "Evaluation of grain boundary effect on strength of Fe–C low alloy martensitic steels by nanoindentation technique." Materials Transactions **46**(6): 1301-1305.

Li, Y., et al. (2009). "Investigation of aluminum-based nanocomposites with ultra-high strength." Materials Science and Engineering: A **527**(1): 305-316.

Lloyd, D. (1994). "Particle reinforced aluminium and magnesium matrix composites." International Materials Reviews **39**(1): 1-23.

Luo, H., et al. (2005). "On tension/compression asymmetry of an extruded nanocrystalline Al–Fe–Cr–Ti alloy." Materials Science and Engineering: A **409**(1): 249-256.

Luo, H., et al. (2005). "Multi-phase nanocrystalline Al alloy with superior strength and modulus at elevated temperatures." Journal of materials engineering and performance **14**(4): 441-447.

Mathewson, C. H. (1991). "Discussion." Transaction TMS-AIME **60**: 451-455.

Mazaheri, Y., et al. (2010). "Nanoindentation study of Al356-Al_2O_3 nanocomposite prepared by ball milling." Materials Sciences and Applications **1**(04): 217.

Mehrer, H. (2007). Diffusion in solids: fundamentals, methods, materials, diffusion-controlled processes, Springer Science & Business Media.

Mishra, R. S., et al. (1996). "High‐Pressure Sintering of Nanocrystalline γ-Al_2O_3." Journal of the American Ceramic Society **79**(11): 2989-2992.

Muller, P., et al. (2014). "Compression and Breakage Behavior of gamma-Al_2O_3 Granules." Chemie Ingenieur Technik **86**(8): 1284-1293.

Nardone, V. and K. Prewo (1986). "On the strength of discontinuous silicon carbide reinforced aluminum composites." Scripta Metallurgica **20**(1): 43-48.

Neuhäuser, H. and C. Schwink (1993). "Solid solution strengthening." Materials science and technology.

Ozdemir, I., et al. (2008). "Nanocrystalline Al–Al_2O_3p and SiCp composites produced by high-energy ball milling." Journal of Materials Processing Technology **205**(1): 111-118.

Pedrazzini, S., et al. (2016). "Strengthening mechanisms in an Al-Fe-Cr-Ti nano-quasicrystalline alloy and composites." Materials Science and Engineering: A **672**: 175-183.

Petch, N. (1953). "The cleavage strength of polycrystals." J. Iron Steel Inst. **174**: 25-28.

Poirier, D., et al. (2010). "Fabrication and properties of mechanically milled alumina/aluminum nanocomposites." Materials Science and Engineering: A **527**(29): 7605-7614.

Poirier, D., et al. (2010). "Fabrication and properties of mechanically milled alumina/aluminum nanocomposites." Materials Science & Engineering A **527**(29-30): 7605-7614.

Ramakrishnan, N. (1996). "An analytical study on strengthening of particulate reinforced metal matrix composites." Acta Materialia **44**(1): 69-77.

Romankov, S., et al. (2009). "TEM study of TiN coatings fabricated by mechanical milling using vibration technique." Surface and Coatings Technology **203**(13): 1879-1884.

Scudino, S., et al. (2009). "Mechanical properties of Al-based metal matrix composites reinforced with Zr-based glassy particles produced by powder metallurgy." Acta Materialia **57**(6): 2029-2039.

Shanmugasundaram, T., et al. (2010). "On the Hall–Petch relationship in a nanostructured Al–Cu alloy." Materials Science and Engineering: A **527**(29): 7821-7825.

Stan-Głowińska, K., et al. (2017). "Effects of hot-compaction on the structure and properties of Al-Mn-Fe-X alloys strengthened with quasi-crystalline icosahedral phase." Materials & Design **126**: 162-173.

Tousi, S. R., et al. (2009). "Production of Al–20 wt.% Al_2O_3 composite powder using high energy milling." Powder Technology **192**(3): 346-351.

Varol, T. and A. Canakci (2013). "Synthesis and characterization of nanocrystalline Al 2024–B_4C composite powders by mechanical alloying." Philosophical magazine letters **93**(6): 339-345.

Vojtěch, D., et al. (2007). "Properties of thermally stable PM Al–Cr based alloy." Materials Science and Engineering: A **458**(1): 371-380.

Williamson, G. and R. Smallman (1956). "III. Dislocation densities in some annealed and cold-worked metals from measurements on the X-ray debye-scherrer spectrum." Philosophical Magazine **1**(1): 34-46.

Wu, Y. and E. Lavernia (1992). "Strengthening behavior of particulate reinforced MMCs." Scripta metallurgica et materialia **27**(2): 173-178.

Xu, W., et al. (2016). "Nanoquasicrystalline Al-Fe-Cr-Ti alloy matrix/γ-Al_2O_3 nanocomposite powders: The effect of the ball milling process." Journal of Alloys and Compounds.

Ye, J., et al. (2006). "Cryomilling for the fabrication of a particulate B_4C reinforced Al nanocomposite: Part I. Effects of process conditions on structure." Metallurgical and Materials Transactions A **37**(10): 3099-3109.

Ye, J., et al. (2006). "Cryomilling for the fabrication of a particulate B_4C reinforced Al nanocomposite: Part II. Mechanisms for microstructural evolution." Metallurgical and Materials Transactions A **37**(10): 3111-3117.

Zhang, D. (2004). "Processing of advanced materials using high-energy mechanical milling." Progress in materials science **49**(3): 537-560.

Zhang, D., et al. (2004). "Processing Ti_3Al–SiC nanocomposites using high energy mechanical milling." Materials Science and Engineering: A **375**: 911-916.

Zhang, D., et al. (2005). "Consolidation of a Cu–2.5 vol.% Al_2O_3 powder using high energy mechanical milling." Materials Science and Engineering: A **410**: 375-380.

Zhang, Z. and D. Chen (2006). "Consideration of Orowan strengthening effect in particulate-reinforced metal matrix nanocomposites: a model for predicting their yield strength." Scripta Materialia **54**(7): 1321-1326.

8. Conclusions and Future Work

8.1 Conclusions

8.1.1 The unmilled powder

25-50μm $Al_{93}Fe_3Cr_2Ti_2$ alloy (at.%) powders characterisation reveals that the alloy contains mainly the icosahedral quasicrystalline phase particles with some Al_3Ti and Al-Fe intermetallics in aluminium matrix. The [0τ0], [00τ] and [τ00] zone axes of quasicrystalline particles are parallel to the [002], [2-20] and [220] zone axes of Al_3Ti and Al phase respectively for some of the particles. High resolution transmission electron microscope (HRTEM) imaging shows that the quasicrystalline phase may have a coherency relationship with the Al_3Ti intermetallic and the Al grain.

8.1.2 Powder production

Two batches of $Al_{93}Fe_3Cr_2Ti_2$ alloy powders and five batches of $Al_{93}Fe_3Cr_2Ti_2/\gamma$-$Al_2O_3$ nanocomposite powders were produced with ball milling. For the nanocomposite powders processed at a milling speed of 150 rotates per minute (rpm), the particle sizes show a small decrease after 10 hours of milling. This may come from the fracture of weak regions in the unmilled powder. After 10 hours of milling, the particle sizes tend to stay stable. For the nanocomposite powders with milling speeds equal or higher than 200rpm, the powder sizes increase and decrease, which indicates a shift from a cold-welding dominating mechanism to a fracturing dominating mechanism. The morphologies of all the ball milled powders are similar. In the early milling hours of the nanocomposite powders, some γ-Al_2O_3 clusters were found adhered on the matrix powder.

8.1.3 The effects of ball milling on the reinforcement distribution

Two mathematical models, namely the field method model and the particle occupied region model, were introduced to quantify the distribution level of the nanocomposites. Both model showed that the homogeneity increases with milling time and milling speeds. The powders milled at 150rpm do not have a homogeneous distribution of γ-Al_2O_3 even after 30 hours of milling. The nanocomposite powders milled at 250 rpm up to 5 hours of milling and then milled at 200 rpm reach the homogeneous distribution after 25 hours of milling, where almost no γ-Al_2O_3 free region can be found in the matrix in focus ion beam (FIB) images. The nanocomposite powders milled at 250 rpm reach a homogeneous distribution after 20 hours of milling,

The millings speed at 150 rpm cannot cold weld and fracture the $Al_{93}Fe_3Cr_2Ti_2$ efficiently. In this case, the γ-Al_2O_3 particles were milled into the matrix powder by (i) the deformation and wrapping of the matrix powder (ii) the cold-welding of the matrix powder with a low frequency. The nanocomposite powders processed with milling speeds equal or higher than 200 rpm follow a cold-welding and fracturing mechanism. At the beginning, the γ-Al_2O_3 agglomerations were milled into the powder by the cold-welding of the matrix powders. Afterwards, the γ-Al_2O_3 clusters were broken and homogeneous distributed in the matrix through random fracturing and cold welding. The cluster sizes of γ-Al_2O_3 decreases with milling time and milling speeds. The nanoquasicrystalline nanocomposite powders milled at 200rpm, 250/200rpm[1] and 250rpm after 30 hours have minimum γ-Al_2O_3 cluster sizes of 273±97nm, 101±45nm and 90±29nm respectively.

[1] This corresponds to the C250/200 batch powder in Chapter 3, milled at 250 rpm for up to 5 hours of milling and milled at 200 rpm afterwards.

8.1.4 The effects of ball milling on the microstructure

After ball milling, the Al grains were severely refined to nanosize (<100nm) for all the batches of powders at milling speeds equal to 200 rpm or higher than 200rpm. The smallest crystallite sizes for the nanoquasicrystalline $Al_{93}Fe_3Cr_2Ti_2$ nanocomposite powders are 30nm, 20nm and 14nm, obtained with milling speeds at 200 rpm, 250/200 rpm and 250 rpm after 30, 30 and 25 hours of milling respectively. The ball milled nanoquasicrystalline $Al_{93}Fe_3Cr_2Ti_2$ alloy powders reach lowest crystallite size 22nm after 25 hours of milling. The quasicrystalline particles could generate particle stimulated nucleation in the milling process. The nanosize γ-Al_2O_3 particles with diameter 20-50nm could inhibit the movement of the dislocations, which increases the dislocation accumulation speed. The faster dislocation generating causes the transformation to grain boundaries in a shorter time.

The quasicrystalline particles are hard and brittle, and have a low capacity for deformation. They were broken and decomposed during the milling. After 30 hours of milling at 250 rpm, the volume fraction of quasicrystals in the powder is approximately 19%. The lattice diffusion is the most probable control mechanism for the decomposition of quasicrystal before milling during heating. As ball milling introduce defects and cracks, other diffusion mechanism, such as the grain boundary diffusion and the dislocation diffusion are activated.

The ball milling causes supersaturation from the decomposition of the quasicrystals in the Al grains. These supersaturations are metastable and will precipitate into the Al_6Fe, the $Al_{13}Fe_4$, the $Al_{13}Cr_2$ and the Al_3Ti intermetallics during the heat treatment. The solute

contents of Fe, Cr and Ti increases with milling time, which leads to the increase of enthalpy values for the exothermal peak of precipitation.

8.1.5 Mechanical behaviour of the alloy and nanocomposite powders

As milling speed increases, collisions per unit volume of the powder increase; thus distributes the alumina particles, refine the Al crystallite size and increases the hardness of the composites more efficiently.

The hardness of the nanoquasicrystalline Al alloy powder is mainly controlled by the refining of the Al crystallite size during the milling process. Thus, the hardness change of the milled nanoquasicrystalline Al alloy powder can be estimated by a simple Hall-Petch type relationship with an exponent of 0.25 in accordance of early models based on dislocation forest hardening concept. The hardness change of the ball milled nanocomposite powder can be estimated by a hybrid model that combines a Hall-Petch type relationship with an exponent of 0.25 and the rule of mixtures.

The addition of 12.9vol% γ-Al_2O_3 (20-50nm) particles to the nanoquasicrystalline $Al_{93}Fe_3Cr_2Ti_2$ powder processed by ball milling with a ball to powder ratio of 10, at 250 rpm after 30 hours allows to obtain a homogeneous nanocomposite powder with 4.8 times higher hardness (HV_{10g} = 638) than that of the nanoquasicrystalline Al alloy matrix (HV_{10g} = 132).

8.1.6 Extrusion

The powders milled at 250 rpm for up to 4 hours and at 200 rpm from 4 to 9 hours of milling with a 500ml milling vessel were extruded at 450°C. The extruded bar has a relative density of 99% and has no texture. Quasicrystalline phase in the powder has been

fully decomposed during the extrusion. Intermetallics, namely Al_3Ti, Al_6Fe, $Al_{13}Fe_4$ and $Al_{13}Cr_2$ were observed in the bar samples. They have a mean particle size of 348±87nm and an average inner particle distance of 464±148nm. The ultimate compression strength of the bar at room temperature is 925MPa, higher than the value 768MPa estimated with the rule of mixture. As the extruded bar has an ultrafine crystallite size of 97±46nm, one main contribution to the strength should come from the grain refinement strengthening mechanism with a value of 549MPa. The Orowan strengthening, thermal mismatch and solid solution strengthening should also contribute of the strength of the bar, although further experiments are needed to quantify the value.

8.2 Future work

- An HRTEM image and an atom resolution energy dispersive X-ray spectrum mapping from the boundary area of the Al_3Ti and the icosahedral quasicrystal would help the understanding of coherency between these two phases.

- As discussed in section 4.7.4 in Chapter 4, the Al_6Fe, $Al_{13}Cr_2$, $Al_{13}Fe_4$ and Al_3Ti have different onset temperatures and activation energies for precipitation. Conducting differential scanning calorimetry (DSC) runs at lower heating rates with a more sensitive DSC equipment would be helpful in understanding the behaviour of different precipitated intermetallics in the ball milled powders.

- Measuring the dislocation density using HRTEM imaging would be helpful in quantifying the contribution to strength from Orowan strengthening mechanism for the mechanically milled powders, and the increase in strength from Orowan

strengthening mechanism and thermal mismatch strengthening mechanism for the extruded bar.

- In the current work, the powders were extruded at a relative high temperature, 450℃. The quasicrystals have been decomposed during the extrusion. The maximum extrusion pressure was 1024MPa in this work, less than the upper limit pressure the extruder can sustain. It is expected that extruding at lower temperatures would produce a nanocomposite bar containing quasicrystalline phase.

Appendix 1

00-002-1121 Mar 20, 2015 3:04 PM (oums0698)

Status Deleted **QM:** Blank (B) **Pressure/Temperature:** Ambient **Chemical Formula:** Al3 Ti
Empirical Formula: Al3 Ti **Weight %:** Al62.83 Ti37.17 **Atomic %:** Al75.00 Ti25.00
Compound Name: Aluminum Titanium

Radiation: CuKá1 **:** 1.5406Å

SYS: Tetragonal **SPGR:** I4/mmm (139)
Author's Cell [AuthCell a: 3.844Å **AuthCell c:** 8.596Å **AuthCell Vol:** 127.02Å³ **AuthCell Z:** 4.00
AuthCell MolVol: 31.75 **]** **Author's Cell Axial Ratio [c/a:** 2.236 **]** **Dcalc:** 6.738g/cm³
SS/FOM: F(26) = 3.8(0.143, 48)

Space Group: I4/mmm (139) **Molecular Weight:** 128.84
Crystal Data [XtlCell a: 3.844Å **XtlCell b:** 3.844Å **XtlCell c:** 8.596Å **XtlCell :** 90.00° **XtlCell :** 90.00°
XtlCell : 90.00° **XtlCell Vol:** 127.02Å³ **XtlCell Z:** 4.00 **]**
Crystal Data Axial Ratio [c/a: 2.236 **a/b:** 1.000 **c/b:** 2.236 **]**
Reduced Cell [RedCell a: 3.844Å **RedCell b:** 3.844Å **RedCell c:** 5.085Å **RedCell :** 112.21°
RedCell : 112.21° **RedCell :** 90.00° **RedCell Vol:** 63.51Å³ **]**

Crystal (Symmetry Allowed): Centrosymmetric

Pearson: tI16.00 **Subfile(s):** Common Phase, Deleted Pattern, Inorganic, Metals & Alloys
Last Modification Date: 01/11/2011 **Cross-Ref PDF #'s:** 00-026-0039 (Deleted), 04-001-3031

References:

Type	Reference
Primary Reference	Brauer. Z. Anorg. Chem. 242, 4 (1939).

Database Comments: Deleted Or Rejected By: Deleted by 00-026-0039. Unit Cell Data Source: Powder Diffraction.

d-Spacings (27) - 00-002-1121 (Fixed Slit Intensity) - Cu K1 1.54056Å

2	d(Å)	I	h	k	l	*	2	d(Å)	I	h	k	l	*	2	d(Å)	I	h	k	l	*
20.6387	4.300000	40	0	0	2		63.2019	1.470000	20	2	1	3		93.2174	1.060000	10	3	1	4	
25.3538	3.510000	50	1	0	1		65.1846	**1.430000**	80	2	0	4		100.7581	1.000000	20	1	1	8	
32.9015	2.720000	20	1	1	0		68.9967	1.360000	60	2	2	0		106.7150	0.960000	50	4	0	0	
39.3113	**2.290000**	100	1	1	2		73.3273	1.290000	10	2	2	2		110.0589	0.940000	60	2	0	8	
42.1935	2.140000	70	0	0	4		75.0225	1.265000	70	3	0	1		112.3905	0.927000	70	1	0	9	
47.3049	**1.920000**	80	2	0	0		79.0768	1.210000	10	3	1	0		120.5489	0.887000	60	3	0	7	
52.2282	1.750000	20	2	0	2		82.3497	1.170000	75	1	0	7		123.3620	0.875000	60				
54.5807	1.680000	40	2	1	1		82.7806	1.165000	60	3	0	3		127.1904	0.860000	60	0	0	10	
58.7632	1.570000	20	1	0	5		91.5390	1.075000	40	0	0	8		132.0539	0.843000	60	2	2	8	

Status Primary **QM:** Indexed (I) **Pressure/Temperature:** Ambient **Chemical Formula:** Al3 Ti
Empirical Formula: Al3 Ti **Weight %:** Al62.83 Ti37.17 **Atomic %:** Al75.00 Ti25.00
Compound Name: Aluminum Titanium

Radiation: CuKá1 **:** 1.5406Å **d-Spacing:** Guinier **Intensity:** Diffractometer

SYS: Cubic **SPGR:** Pm-3m (221)
Author's Cell [AuthCell a: 3.9720(10)Å **AuthCell Vol:** 62.67Å³ **AuthCell Z:** 1.00 **AuthCell MolVol:** 62.67 **]**
Dcalc: 3.414g/cm³ **SS/FOM:** F(12) = 60.7(0.0094, 21)

Space Group: Pm-3m (221) **Molecular Weight:** 128.84
Crystal Data [XtlCell a: 3.972Å **XtlCell b:** 3.972Å **XtlCell c:** 3.972Å **XtlCell :** 90.00° **XtlCell :** 90.00°
XtlCell : 90.00° **XtlCell Vol:** 62.67Å³ **XtlCell Z:** 1.00 **]** **Crystal Data Axial Ratio [a/b:** 1.000 **c/b:** 1.000 **]**
Reduced Cell [RedCell a: 3.972Å **RedCell b:** 3.972Å **RedCell c:** 3.972Å **RedCell :** 90.00°
RedCell : 90.00° **RedCell :** 90.00° **RedCell Vol:** 62.67Å³ **]**

Crystal (Symmetry Allowed): Centrosymmetric

Pearson: cP4.00 **Prototype Structure:** Cu3 Au **Prototype Structure (Alpha Order):** Au Cu3
Subfile(s): Metals & Alloys, Primary Pattern, Inorganic **Entry Date:** 10/24/1996 **Last Modification Date:** 01/11/2011

References:

Type	Reference
Primary Reference	Braun, **J**., Ellner, M., Predel, B. Z. Metallkd. 85, 855 (1994).

Database Comments: Sample Preparation: Aluminum and titanium were melted together and splat cooled. Unit Cell Data Source: Powder Diffraction.

d-Spacings (12) - 00-049-1446 (Fixed Slit Intensity) - Cu K1 1.54056Å

2	d(Å)	I	h	k	l	*	2	d(Å)	I	h	k	l	*	2	d(Å)	I	h	k	l	*
22.3642	3.972000	35	1	0	0		51.3948	1.776400	5	2	1	0		101.7673	0.992800	5	4	0	0	
31.8542	2.807000	35	1	1	0		66.5304	**1.404300**	80	2	2	0		115.4182	0.911200	50	3	3	1	
39.2560	**2.293100**	100	1	1	1		80.0597	1.197600	80	3	1	1		120.3008	0.888100	50	4	2	0	
45.6398	**1.986100**	80	2	0	0		84.4115	1.146600	50	2	2	2		143.6623	0.810700	35	4	2	2	

Status Primary **QM:** Calculated (C) **Pressure/Temperature:** Pressure (Non-ambient) **Chemical Formula:** Al6 Fe
Empirical Formula: Al6 Fe **Weight %:** Al74.35 Fe25.65 **Atomic %:** Al85.71 Fe14.29
Compound Name: Aluminum Iron

Radiation: CuKá : 1.5418Å **d-Spacing:** Calculated **Intensity:** Calculated

SYS: Orthorhombic **SPGR:** Cmcm (63)
Author's Cell [AuthCell a: 6.46Å **AuthCell b:** 7.44Å **AuthCell c:** 8.78Å **AuthCell Vol:** 421.99Å³
AuthCell Z: 4.00 **AuthCell MolVol:** 105.50] **Author's Cell Axial Ratio [c/a:** 1.359 **a/b:** 0.868 **c/b:** 1.180]
Dcalc: 3.427g/cm³ **SS/FOM:** F(24) = 324.3(0.0031, 24)

Space Group: Bbmm (63) **Molecular Weight:** 217.74
Crystal Data [XtlCell a: 7.440Å **XtlCell b:** 8.780Å **XtlCell c:** 6.460Å **XtlCell :** 90.00° **XtlCell :** 90.00°
XtlCell : 90.00° **XtlCell Vol:** 421.99Å³ **XtlCell Z:** 4.00]
Crystal Data Axial Ratio [c/a: 0.868 **a/b:** 0.847 **c/b:** 0.736]
Reduced Cell [RedCell a: 4.927Å **RedCell b:** 4.927Å **RedCell c:** 8.780Å **RedCell :** 90.00°
RedCell : 90.00° **RedCell :** 98.07° **RedCell Vol:** 210.99Å³]

Crystal (Symmetry Allowed): Centrosymmetric

Pearson: oC28.00 **Prototype Structure:** Mn Al6 **Prototype Structure (Alpha Order):** Al6 Mn
LPF Prototype Structure: Mn Al6,oS28,63 **LPF Prototype Structure (Alpha Order):** Al6 Mn
Subfile(s): Metals & Alloys, Primary Pattern, Inorganic **Entry Date:** 12/01/1995 **Last Modification Date:** 01/11/2011
Cross-Ref PDF #'s: 04-005-5394

References:

Type	Reference
Primary Reference	Putyatin, A., Davydov, V., Nesterenko, S. J. Alloys Compds. 179, 165 (1992).

Database Comments: Sample Preparation: Prepared by quenching from 1800 K to 298 K at 6 GPa pressure.

d-Spacings (24) - 00-047-1433 (Fixed Slit Intensity) - Cu K1 1.54056Å

2	d(Å)	I	h	k	l	*	2	d(Å)	I	h	k	l	*	2	d(Å)	I	h	k	l	*
18.1655	4.879500	53	1	1	0		34.4389	2.602010	9	2	0	2		42.3592	**2.132010**	100	2	2	2	
20.2134	4.389510	22	0	0	2		35.7515	2.509430	26	1	1	3		43.7241	2.068570	2	3	1	0	
20.8149	4.264010	17	1	1	1		36.8201	2.439020	8	2	2	0		44.1845	2.048080	1	1	3	2	
23.9070	3.719040	16	0	2	0		38.2706	2.349850	4	2	2	1		44.9884	2.013330	52	3	1	1	
25.9867	3.425940	6	0	2	1		38.8703	**2.314960**	73	1	3	0		45.2666	2.001600	63	1	1	4	
27.3056	3.263380	31	1	1	2		39.1295	2.300220	48	0	2	3		48.0892	1.890500	9	0	2	4	
27.6005	3.229170	11	2	0	0		40.2475	2.238870	47	1	3	1		48.5536	1.873500	20	2	2	3	
31.5026	2.837520	26	0	2	2		41.0925	2.194760	29	0	0	4		48.6171	**1.871200**	80	3	1	2	

Status Primary **QM:** Calculated (C) **Pressure/Temperature:** Ambient **Chemical Formula:** Al13 Cr2
Empirical Formula: Al13 Cr2 **Weight %:** Al77.13 Cr22.87 **Atomic %:** Al86.67 Cr13.33
Compound Name: Aluminum Chromium

Radiation: CuKá1 **:** 1.5406Å **d-Spacing:** Calculated **Intensity:** Calculated

SYS: Monoclinic **SPGR:** C2/m (12)
Author's Cell [AuthCell a: 25.196Å **AuthCell b:** 7.574Å **AuthCell c:** 10.949Å **AuthCell :** 128.71°
AuthCell Vol: 1630.44Å³ **AuthCell Z:** 6.93 **AuthCell MolVol:** 235.27 **]**
Author's Cell Axial Ratio [c/a: 0.435 **a/b:** 3.327 **c/b:** 1.446 **]** **Dcalc:** 3.21g/cm³
SS/FOM: F(30) = 285.7(0.0017, 63)

Space Group: I2/m (12) **Molecular Weight:** 454.75
Crystal Data [XtlCell a: 20.240Å **XtlCell b:** 7.574Å **XtlCell c:** 10.949Å **XtlCell :** 90.00° **XtlCell :** 103.74°
XtlCell : 90.00° **XtlCell Vol:** 1630.44Å³ **XtlCell Z:** 6.93 **]**
Crystal Data Axial Ratio [c/a: 0.541 **a/b:** 2.672 **c/b:** 1.446 **]**
Reduced Cell [RedCell a: 7.574Å **RedCell b:** 10.949Å **RedCell c:** 10.973Å **RedCell :** 106.25°
RedCell : 110.19° **RedCell :** 90.00° **RedCell Vol:** 815.22Å³ **]**

Crystal (Symmetry Allowed): Centrosymmetric

Pearson: mC103.95 **Prototype Structure:** Al45 V7 **Prototype Structure (Alpha Order):** Al45 V7
LPF Prototype Structure: V7 Al45,mS104,12 **LPF Prototype Structure (Alpha Order):** Al45 V7
Subfile(s): Primary Pattern, Inorganic, Metals & Alloys **Last Modification Date:** 01/11/2011
Cross-Ref PDF #'s: 04-004-2176

References:

Type	Reference
Primary Reference	Technisch Physische Dienst, Delft, Netherlands. ICDD Grant-in-Aid (1975).
Unit Cell	Cooper, **J**. Acta Crystallogr. 13, 257 (1960).

Database Comments: Unit Cell Data Source: Powder Diffraction.

d-Spacings (60) - 00-029-0014 (Fixed Slit Intensity) - Cu K1 1.54056Å

2	d(Å)	I	h	k	l	*	2	d(Å)	I	h	k	l	*	2	d(Å)	I	h	k	l	*
8.4535	10.451000	41	-2	0	1		27.4719	3.244000	2	-4	2	1		38.2173	2.353000	16	1	3	1	
8.9886	9.830000	8	2	0	0		28.9178	3.085000	4	-2	2	2		39.2756	2.292000	7	-3	3	2	
10.3450	8.544000	2	0	0	1		29.7558	3.000000	7	4	2	0		39.5632	2.276000	14	0	2	3	
12.5132	7.068000	2	1	1	0		31.0815	2.875000	2	-1	1	3		40.0770	2.248000	12	-10	0	1	
14.0773	6.286000	20	-4	0	1		32.0299	2.792000	3	-6	2	2		40.2263	2.240000	14	-1	3	2	
14.3457	6.169000	75	-1	1	1		32.6301	2.742000	3	5	1	1		40.4903	2.226000	33	-5	3	2	
16.9518	5.226000	3	-4	0	2		33.5228	2.671000	10	3	1	2		40.6428	2.218000	21	-6	2	4	
17.4844	5.068000	17	2	0	1		34.2896	2.613000	4	-8	0	4		41.1466	2.192000	51	-11	1	3	
17.9815	4.929000	8	1	1	1		34.6175	2.589000	7	-9	1	3		41.3437	2.182000	60	7	1	1	
20.7755	4.272000	12	0	0	2		34.9658	2.564000	5	-6	2	3		41.4630	2.176000	67	-4	2	4	
21.4877	4.132000	29	-5	1	1		35.2640	2.543000	5	4	2	1		41.5629	2.171000	30	-6	0	5	
21.7379	4.085000	3	-1	1	2		35.7431	2.510000	3	-2	2	3		41.9675	2.151000	72	3	3	1	
24.4136	3.643000	6	-4	0	3		35.8317	2.504000	3	1	3	0		42.2763	2.136000	22	0	0	4	
24.9919	3.560000	5	-2	2	1		36.2206	2.478000	4	6	2	0		42.5267	2.124000	19	5	3	0	
25.5015	3.490000	3	5	1	0		36.3725	2.468000	11	-10	0	2		43.2531	2.090000	23	-10	0	5	
25.9400	3.432000	3	4	0	1		36.5565	2.456000	27	-1	3	1		43.7813	**2.066000**	95	-10	2	2	
26.5622	3.353000	3	-2	0	3		37.0249	2.426000	7	-2	0	4		43.8706	**2.062000**	100	8	2	0	
26.6756	3.339000	4	1	1	2		37.1359	2.419000	9	-8	2	2		44.0414	**2.054400**	96	-3	3	3	E
27.1899	3.277000	5	6	0	0		37.9659	2.368000	18	2	0	3		44.0730	2.053000	65	6	0	2	
27.2747	3.267000	5	-5	1	3		38.1500	2.357000	14	-10	0	4		44.1863	2.048000	61	-5	1	5	

Status Deleted **QM:** Indexed (I) **Pressure/Temperature:** Ambient **Chemical Formula:** Al13 Fe4
Empirical Formula: Al13 Fe4 **Weight %:** Al61.09 Fe38.91 **Atomic %:** Al76.47 Fe23.53
Compound Name: Aluminum Iron

SYS: Monoclinic **SPGR:** B2/m (10)
Author's Cell [AuthCell a: 15.489Å **AuthCell b:** 8.0831Å **AuthCell c:** 12.476Å **AuthCell :** 107.72°
AuthCell Vol: 1487.88Å³ **AuthCell Z:** 6.00 **AuthCell MolVol:** 247.98 **]**
Author's Cell Axial Ratio [c/a: 0.805 **a/b:** 1.916 **c/b:** 1.543 **]** **Dcalc:** 3.845g/cm³ **Dmeas:** 3.77g/cm³
SS/FOM: F(29) = 1.5(0.045, 424)

Space Group: P2/m (10) **Molecular Weight:** 574.15
Crystal Data [XtlCell a: 11.327Å **XtlCell b:** 8.083Å **XtlCell c:** 8.336Å **XtlCell :** 90.00° **XtlCell :** 102.89°
XtlCell : 90.00° **XtlCell Vol:** 743.94Å³ **XtlCell Z:** 3.00 **]**
Crystal Data Axial Ratio [c/a: 0.736 **a/b:** 1.401 **c/b:** 1.031 **]**
Reduced Cell [RedCell a: 8.083Å **RedCell b:** 8.336Å **RedCell c:** 11.327Å **RedCell :** 102.89°
RedCell : 90.00° **RedCell :** 90.00° **RedCell Vol:** 743.94Å³ **]**

Crystal (Symmetry Allowed): Centrosymmetric

Pearson: mP51.00 **Subfile(s):** Deleted Pattern, Inorganic, Metals & Alloys **Last Modification Date:** 01/11/2011
Cross-Ref PDF #'s: 00-029-0042 (Primary)

References:

Type	Reference
Primary Reference	Bachmatew. Z. Kristallogr., Kristallgeom., Kristallphys., Kristallchem. 89, 581 (1934).
Unit Cell	Acta Crystallogr. 8, 43 (1955).

Database Comments: Color: Black. Deleted Or Rejected By: Deleted by 00-029-0042. Unit Cell Data Source: Powder Diffraction.

d-Spacings (30) - 00-002-1213 (Fixed Slit Intensity) - Cu K1 1.54056Å

2	d(Å)	I	h	k	l	*	2	d(Å)	I	h	k	l	*	2	d(Å)	I	h	k	l	*
21.9280	4.050000	40	0	2	0		42.6109	2.120000	40	-7	1	1		51.5943	1.770000	10	-4	4	2	
22.4903	3.950000	40					43.2531	**2.090000**	100	-3	2	5		64.1769	1.450000	60	5	4	3	
24.1645	3.680000	60	-3	0	3		43.4716	2.080000	40	-7	1	3		65.1846	1.430000	60	-4	4	6	
25.1354	3.540000	60	2	2	0		43.9154	2.060000	40	6	0	2		66.2268	1.410000	20	7	4	1	
26.7490	3.330000	20	0	2	2		44.3687	**2.040000**	100	-2	3	4		66.7615	1.400000	40	-5	5	3	
27.3344	3.260000	20	1	1	3		44.8318	**2.020000**	100	-4	0	6		68.4228	1.370000	20	-5	0	9	
38.0996	2.360000	10	-1	1	5		45.7884	1.980000	20	0	0	6		69.5811	1.350000	40	-3	5	5	
38.4380	2.340000	60	-3	1	5		47.0450	1.930000	40	-4	3	4		73.3273	1.290000	60	11	0	1	
40.0398	2.250000	40	3	2	3		47.5678	1.910000	20	3	3	3		73.9952	1.280000	20	3	6	1	
41.7844	2.160000	10	1	1	5		50.6730	1.800000	10	8	1	0		74.3341	1.275000	20	-2	5	6	